Interactions of tidal and precessional flows with convection: applications to tidal dissipation in giant planets and stars

Nils Beijing de Vries

Submitted in accordance with the requirements for the degree of

Doctor of Philosophy

The University of Leeds

Department of Applied Mathematics

June 2024

Intellectual Property Statement

The candidate confirms that the work submitted is their own, except where work which has formed part of jointly authored publications has been included. The contribution of the candidate and the other authors to this work has been explicitly indicated below. The candidate confirms that appropriate credit has been given within the thesis where reference has been made to the work of others.

Chs. 1, 2, 3, 4 and 8 contain material from the jointly authored publication (De Vries et al., 2023a):
De Vries, N. B., Barker, A. J., & Hollerbach, R. (2023).
The interactions of the elliptical instability and convection. *Physics of Fluids*, *35* (2), 024116.

Chs. 1, 2, 4, 7 and 8 contain material from the jointly authored publication (De Vries et al., 2023b):
De Vries, N. B., Barker, A. J., & Hollerbach, R. (2023).
Tidal dissipation due to the elliptical instability and turbulent viscosity in convection zones in rotating giant planets and stars. *Monthly Notices of the Royal Astronomical Society*, *524* (2), 2661–2683.

Both of these papers were authored by N. B. de Vries who executed all simulations, performed the analysis and wrote the draft manuscripts above. Contributions of the other authors were through advisory and editorial roles. The SNOOPY code and some NEK5000 scripts were supplied by A. J. Barker. The analysis of the MESA simulations in Ch. 7 and the latter paper was performed jointly by N. B. de Vries and A. J. Barker.

For
Sam Myers

Acknowledgements

First of all, I want to thank my supervisors Adrian Barker and Rainer Hollerbach for excellent guidance, continued assistance, patience and extensive knowledge. This thesis, as well as my skills as a researcher, have been tremendously enhanced by you both. I could not have asked for a better supervisory team.

Furthermore, I would like to thank David Hughes and Gordon Ogilvie for examining my thesis and a fruitful discussion during my viva.

I am grateful for the funding I received from EPSRC studentship 2528559 to complete this research. I also want to extend my thanks to the ARC supercomputer team and ARC4, part of the High Performance Computing facilities at the University of Leeds, itself, which allowed me to perform all the simulations used in thesis. I would also like to thank Thomas Le Reun for kindly supplying his routines in Snoopy that were modified and used to produce the Fourier spectra in Sec. 3.2.3. Additionally, I would like to thank the admin and reception team of the School of Maths.

I've made many great friends during my time at Leeds, all of whom I want to thank for the wonderful adventures and, more importantly, their kindness, be it during badminton, climbing, hikes, trips or just hanging out in cinema sessions or the pub. I hope our friendships will last a lifetime. I would like to specifically thank Christina Pontin for welcoming me to the university when it was still asleep in the months after lockdown lifted, Craig Duguid for the fruitful conversations during the conferences we attended together, Aurélie Astoul for the many wonderful discussions about science, advice for future academic careers, and overall being a great role model, and finally Rob Dymott for being the best office mate I could hope for and my friend through thick and thin.

I would like to thank my parents for supporting me all the way through this journey, even if it meant seeing their only child leave for another country. Finally, I should also thank my two dear friends Emma Griffin and Hannah Osborne for reigniting my passion for astrophysics.

"To reach the unreachable star" - Man of La Mancha

Abstract

Gravitational tidal interactions between two astrophysical bodies can result in evolution of their spins and orbits. These interactions are caused by dissipation of tidal energy and associated transfer of angular momentum. Of particular interest are the close-in giant exoplanets known as Hot Jupiters, because strong tidal dissipation is expected in their own fluid envelopes as well as their host stars.

In the study of tides, the fluid response is often split into an equilibrium tide and a dynamical tide. We will focus on three dissipation mechanisms of the equilibrium tide in convection zones of Hot Jupiters. The first is the action of turbulent convection in damping tidal flows, while the other two are the elliptical and precessional instabilities. Both of these instabilities are parametric in nature and excite inertial waves. The elliptical instability is excited because of the tidal deformation of the body due to the equilibrium tide, while axial precession and the associated precessional flow allows for the precessional instability.

To study these mechanisms we analyse a large number of Boussinesq local Cartesian box simulations covering a wide range of parameters. We have found that the elliptical instability and rotating convection both generate large-scale vortices in the flow, which inhibit the elliptical instability at small tidal amplitudes or strong convective driving. The tidal dissipation due to the precessional instability on the other hand is reduced instead of being inhibited by convection. We find that convective turbulence acts on both flows like an effective viscosity resulting in continuous tidal dissipation. This effective viscosity can be described well using rotating mixing-length theory. Furthermore, we find the effective viscosity to be strongly reduced in the fast tides regime, where the tidal frequency exceeds the convective one, in these rotating simulations.

Finally, we have generated interior models of giant planets, and find that Jupiter and Hot Jupiters are firmly in the fast tides regime. We estimate that both the elliptical and precessional instabilities are efficient for the shortest period Hot Jupiters, and that the effective viscosity of turbulent convection is likely to be negligible in giant planets compared with inertial wave mechanisms.

Contents

List of Figures

List of Tables

Chapter 1

Introduction

1.1 Observational evidence of tides

The tides in Earth's oceans as primarily raised by the Moon's gravity have been studied for many centuries, going back to Newton's theory of gravity and more specifically Laplace's theory of tides in a detailed mathematical context. Although interactions between astrophysical bodies are not limited to just tides and their dissipation, these effects are of immense importance in the evolution of orbits and spins of planets and stars, as well as subsequently affecting their interiors. Furthermore, there are many unknowns still surrounding tides and the dissipation they induce. Within the Solar System one might consider the heat budget and orbital migration of Jupiter's inner moons. Of particular interest outside the Solar System are binary stars and exoplanets at small orbital separations from their host stars, the latter of which has only been unlocked as a class of objects to study within the last 35 years (Wolszczan & Frail, 1992; Mayor & Queloz, 1995). We will now turn to summarise some of the available observational evidence of tides, before examining the way tides arise from the gravitational potential.

1.1.1 Within the Solar System

Starting with the Earth-Moon system, the tides within the oceans and seas are well known (the author recommends finding a nice beach if one requires further evidence). The notable long-term consequences of these tides on the Moon and the Earth themselves resides primarily in evolution of the spin and orbit of the Earth and Moon. The Moon, being the less massive of the two objects, is affected more strongly than the Earth is, and therefore the Moon entered a state of spin-orbit synchronisation a long time ago. This entails that the Moon spins around its axis at the same rate as it orbits Earth, thus continuously showing the same side to the Earth. This effect is also referred to as tidal locking.

Further evidence of the effect of tides on orbits can be found in the semi-major axis of the Moon, which is currently increasing at a rate of about 3.8 cm yr^{-1} (Williams, 2000; Williams & Boggs, 2016). Conservation of angular momentum then implies that

the Earth must be losing spin angular momentum. The Earth must therefore have spun more rapidly in the past, resulting in a shorter Earth day. The number of hours per day obtained from fossil records shown in Fig. 1.1 does indeed attest to an increasing length of the Earth day, and thus a decrease in the Earth's rotation rate.

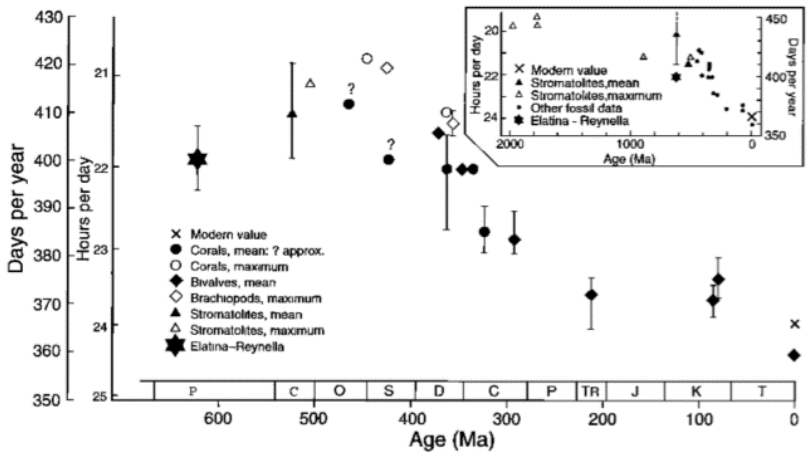

Figure 1.1: Length of an Earth day in hours as obtained from various fossil records. The Earth day was shorter in the past, indicating a larger spin rate, and therefore higher angular momentum. This angular momentum has been and is still being transferred to the Moon, increasing the length of the Earth's day and increasing the orbital period of the Moon. Image reproduced from Williams (2000).

Departing from the comfort of the Earth-Moon system we find additional evidence for tidal effects within the moons of Jupiter and Saturn, although these systems also still contain many open questions. Io in particular, as the closest moon to the massive planet Jupiter, experiences strong tidal effects and as a result it is slowly moving towards Jupiter (Lainey et al., 2009). Io also illustrates the earlier point raised about the subsequent effects of tidal dissipation on interiors. Io experiences very strong, continuous volcanism, which is believed to arise due to the contribution of the dissipated tidal energy to the energy budget of Io (Peale et al., 1979; Lainey et al., 2009). In fact, this result was predicted using tidal theory before it was observed (Peale et al., 1979), illustrating how powerful tidal theory can be.

1.1.2 Outside the Solar System

Outside our Solar System we find many systems with planetary configurations that are in fact quite dissimilar to the orbital architecture we are familiar with. Most notable in this instance are Hot (e.g. surface temperatures as high as 2500 K) Jupiters, which are Jupiter-like planets that are hot due to strong stellar irradiation because they orbit their host stars very closely. This however is a rather loose definition, and instead often it is preferred to introduce a maximum orbital period and minimum mass, the exact values of which are not agreed upon. In this thesis we will work with a maximum orbital period of 10 days and minimum mass of $0.3M_J$. One should potentially also include an upper limit on the mass, which is often set to $13M_J$, to exclude brown dwarfs. Fig. 1.2 shows

all currently confirmed exoplanets in the NASA Exoplanet Archive (2024), here portrayed in planetary mass-orbital period space. Two horizontal dashed lines are included in the figure to denote the minimum and maximum mass respectively, as well as a vertical dashed line to mark the maximum period. The exoplanets within this box are therefore denoted as "Hot Jupiters", except for those exoplanets found through pulsar timing, which are more commonly referred to as "pulsar planets". The colours in the figure indicate the detection method used to find each exoplanet. Further details on these detection methods can be found in Perryman (2018). We will however highlight the transit method, which – as demonstrated by Fig. 1.2 – is very efficient at detecting Hot Jupiters. As the name suggests, the crux of this method is the transit of a planet in front of its host star. This transit will block part of the stellar light and thus result in periodic dips in the brightness of a star. The percentage of light blocked corresponds to the size of the planet in relation to the star, while the periodicity of the dip is used to find the orbital period of the planet.

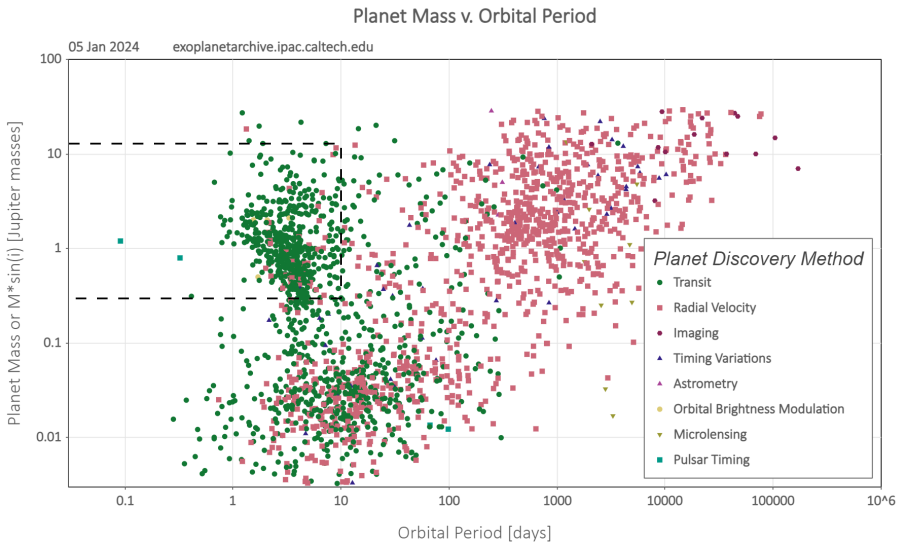

Figure 1.2: Mass–period diagram of all discovered exoplanets. Colours indicate the different detection methods. Two horizontal dashed lines have been added to indicate the minimum and maximum mass of Hot Jupiters at $0.3M_J$ and $13M_J$ respectively, as well as a vertical dashed line at the maximum period of 10 days. The exoplanets within this box are "Hot Jupiters" according to our definitions, except for those exoplanets found through the pulsar timing method, which are more commonly referred to as "pulsar planets" . Colours indicate the methods used to discover these exoplanets. Plot generated using data taken from the NASA Exoplanet Archive (2024).

Many open questions still surround these Hot Jupiters and their origins, particularly in comparison to our own Solar System, since Jupiter is on a much longer 4333 day orbit. There are three hotly debated theories to explain the formation of Hot Jupiters (Dawson & Johnson, 2018). The first, and most simple, is in-situ formation, i.e. the Hot Jupiter forms at a small orbital separation from its host star and stays there (Batygin et al., 2016). Secondly, there is disc migration, where the Hot Jupiter forms at a larger radius, but migrates through the protoplanetary disc due to, for example, gravitational tidal interactions with the disc, to reach its final close-in position (Baruteau et al., 2014). The last theory is that of high-eccentricity migration (Naoz et al., 2011; Wu & Lithwick, 2011;

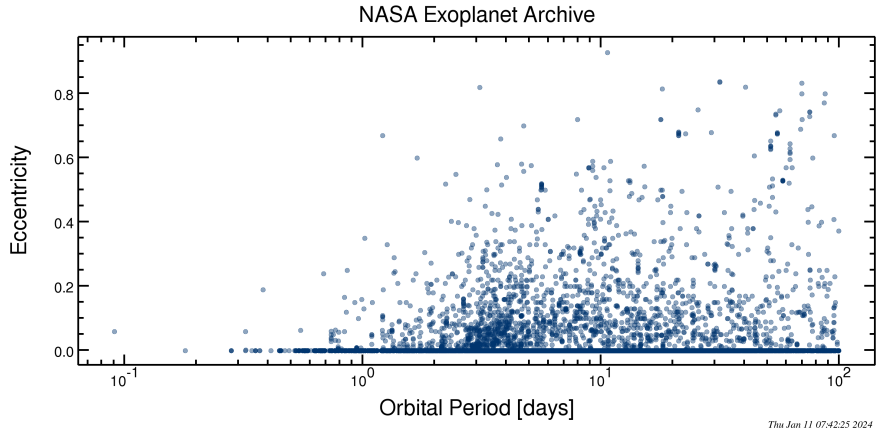

Figure 1.3: Eccentricity distribution of exoplanets with $P_{\rm orb} < 100$ days and masses $M > 0.3 M_J$. Exoplanets with periods $P_{\rm orb} < 3$ days have eccentricities $e < 0.2$, but most of these planets have $e \approx 0$, whereas those with $P_{\rm orb} > 10$ days exhibit a wide range of eccentricities. Plot generated using data taken from the NASA Exoplanet Archive (2024).

Petrovich, 2015; Nelson et al., 2017), where the Hot Jupiter is initially formed with a large orbital separation but obtains a highly eccentric orbit. The Hot Jupiter is scattered into this orbit by, for instance, interactions with other (proto)planets, and then circularises its orbit at the point of periastron, i.e. closest approach to the host star, where the stellar gravity and thus tidal effects are strongest.

The proximity of Hot Jupiters to their host stars results in a strong gravitational pull. In addition, they are primarily composed of gas or fluid and therefore deform more easily under the influence of tides than rock or ice. Therefore, they are likely to experience strong tidal effects and the resulting orbital evolution can possibly be observed. In fact, the eccentricity distribution of these Hot Jupiters as seen in Fig. 1.3 provides indirect evidence of tidal effects operating to circularise their orbits. The orbits of Hot Jupiters with orbital periods $P_{\rm orb} < 3$ days have eccentricities that are tending towards zero. This circularisation is suspected to be due to a tidal effect (primarily by tidal dissipation taking place inside the planets themselves), although there is the possibility that a subset of the population has been formed on circular orbits. This tidal effect seems to only be noticeable for the most close-in planets, which appear to experience sufficiently strong tidal dissipation to circularise their orbits within their host stars' lifetimes.

Finally, there have been clear indications of orbital decay of Hot Jupiters, particularly WASP-12b (Yee et al., 2019; Turner et al., 2021), but also possibly other Hot Jupiters such as WASP-4b and WASP-43b (Hagey et al., 2022). This orbital decay is observed by measuring changes in the transit time of the Hot Jupiter; if the transits occur sooner than expected this could indicate that the period of the orbit is decreasing and thus the orbit is decaying. This orbital decay is expected to result from tidal effects (primarily by tidal dissipation taking place inside the planets' host stars) and demonstrates how influential tides can be if they lead to planets spiralling into their host stars and eventually being

destroyed. As the number of observations increases and the observations themselves become more precise, i.e. less noisy and longer observations, it is likely more Hot Jupiters with a decaying orbit will be identified. One should however consider the possibility that such objects might be rare among the Hot Jupiter population, simply because planets that spiral into their host stars may have already been destroyed. This would imply that Hot Jupiters are found more readily in young systems (Hamer & Schlaufman, 2019).

1.2 Mathematical description of tides

Now, let us turn to the way tides arise from gravity. To this end, we consider a highly simplified two body system, depicted in Fig. 1.4, consisting of body 1 with mass M_1, centre-of-mass position $\boldsymbol{R}_1$ and spin vector $\boldsymbol{\Omega}_s$ and body 2 with mass M_2 and position $\boldsymbol{R}_2$ orbiting around the centre of mass of the system with orbital vector $\boldsymbol{\Omega}_o$. Here we have reduced body 2 to a point mass for simplicity. Therefore we will only consider the gravitational potential of body 2 in body 1, but not vice versa. We define the positions $\boldsymbol{R}_1(t)$, $\boldsymbol{R}_2(t)$ with respect to an arbitrary origin (as indicated within the schematic). The orbital separation between the centres of mass of both bodies is then given by $\boldsymbol{d}(t) = \boldsymbol{R}_2(t) - \boldsymbol{R}_1(t)$. Finally, $\boldsymbol{r}(t)$ is the location at which we examine the gravitational potential and $\boldsymbol{x}(t) = \boldsymbol{r}(t) - \boldsymbol{R}_1(t)$ is the vector between the centre of mass of body 1 and this same location. Note that the bulge depicted in the figure is the bulge raised by tides and we have neglected any rotational/centrifugal distortion effects on body 1.

1.2.1 The tidal potential

The mechanism responsible for raising the tides is simply gravity. To obtain an expression for the tides we can start from the gravitational potential, ψ, raised at a point within body 1 by body 2. The simplest formalism entails treating the secondary body as a point mass like in Fig. 1.4. Some quantitative corrections arise from treating it as body with structure instead for the very closest-in Hot Jupiters (Mathis & Le Poncin-Lafitte, 2009). However, these corrections are often neglected when making heuristic estimates. Thus we can write the gravitational potential as:

$$\psi = -\frac{GM_2}{|\boldsymbol{r} - \boldsymbol{R}_2|}, \tag{1.1}$$

where G is the gravitational constant. We omit the time dependence of the position vectors in this and subsequent expressions, such that they depict a snapshot in time of the system. We can use the vectors $\boldsymbol{d}$ and $\boldsymbol{x}$ introduced above to simplify this expression slightly by writing it as:

$$\psi = -\frac{GM_2}{|\boldsymbol{x} - \boldsymbol{d}|}. \tag{1.2}$$

One can then perform a Taylor expansion around $\boldsymbol{x} = \boldsymbol{0}$, finding:

$$\psi = -\frac{GM_2}{|\boldsymbol{d}|}\left(1 + \frac{2\boldsymbol{d}\cdot\boldsymbol{x}}{|\boldsymbol{d}|^2} + \frac{3(\boldsymbol{d}\cdot\boldsymbol{x})^2 - |\boldsymbol{x}|^2|\boldsymbol{d}|^2}{2|\boldsymbol{d}|^2} + \mathcal{O}\left(\frac{|\boldsymbol{x}|^3}{|\boldsymbol{d}|^3}\right)\right). \tag{1.3}$$

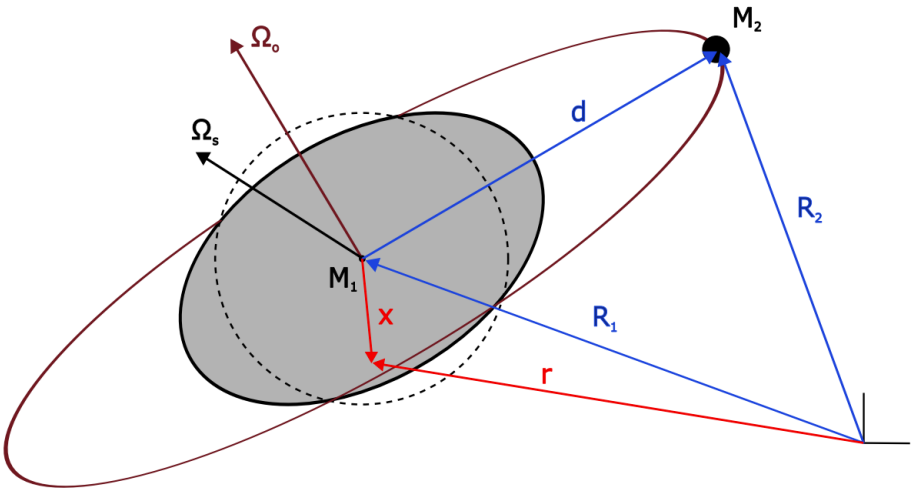

Figure 1.4: Schematic of the tidal interaction between body 1 with mass M_1, position $\boldsymbol{R}_1(t)$ and spin vector $\boldsymbol{\Omega}_s$ and body 2, here represented as a point mass with mass M_2, position $\boldsymbol{R}_2(t)$ and orbital vector $\boldsymbol{\Omega}_o$. Note that the bulge portrayed in the figure is the tidal bulge; the effects of the centrifugal force on the shape of the body have been omitted. Figure adapted from Ogilvie (2014).

This is the full gravitational potential due to body 2, but not all the terms in Eq. (1.3) are responsible for raising tides on body 1. This is readily seen by examining the force generated by each term, remembering that the force can be obtained by taking the gradient with respect to $\boldsymbol{x}$ of the potential multiplied by the mass of the "test particle" experiencing said force. The gradient of the first term in this expansion is simply zero. The gradient of the second term is slightly more complicated, but it can be readily seen that it results in a constant force independent of location within the body $\boldsymbol{x}$. Therefore this term also does not raise a tide; in fact this is the term responsible for the orbital motion of body 1 around body 2. The third and any subsequent terms all produce a force which depends on the location within the planet $\boldsymbol{x}$. It is precisely this difference in forces within body 1 that leads to a tide being raised and a tidal bulge being created. Hence, one can define the tidal potential, Ψ, without the first two terms:

$$\Psi = -\frac{GM_2}{|\boldsymbol{d}|}\left(\frac{3(\boldsymbol{d}\cdot\boldsymbol{x})^2 - |\boldsymbol{x}|^2|\boldsymbol{d}|^2}{2|\boldsymbol{d}|^2} + \mathcal{O}\left(\frac{|\boldsymbol{x}|^3}{|\boldsymbol{d}|^3}\right)\right). \tag{1.4}$$

Often the choice is made to represent this potential as in Eq. (1.4), writing out explicitly the second term and using Big O notation for the subsequent terms. This is done because the potential decreases with powers of $|\boldsymbol{x}|/|\boldsymbol{d}|$, so every term is weaker by several orders of magnitude than the previous term when this is small. Regardless of this choice, the entire tidal potential can be written in a concise way using Legendre polynomials:

$$\Psi = -\frac{GM_2}{|\boldsymbol{d}|}\sum_{l=2}^{\infty}\frac{|\boldsymbol{x}|^l}{|\boldsymbol{d}|^l}P_l\left(\frac{\boldsymbol{x}\cdot\boldsymbol{d}}{|\boldsymbol{x}||\boldsymbol{d}|}\right). \tag{1.5}$$

Here $P_l(x)$ represents the Legendre polynomial of degree l. Further to the above, we can choose a more natural origin for the system than the one chosen in Fig. 1.4 – namely the centre of body 1 – by setting: $\boldsymbol{R}_1 = \boldsymbol{0}$, $\boldsymbol{R}_2 = \boldsymbol{d}$, $\boldsymbol{x} = \boldsymbol{r}$. Additionally, we can define the angle between the vectors $\boldsymbol{d}$ and $\boldsymbol{x}$ to be θ. In this case we can write:

$$\Psi = -\frac{GM_2}{|\boldsymbol{d}|}\sum_{l=2}^{\infty}\frac{|\boldsymbol{x}|^l}{|\boldsymbol{d}|^l}P_l\left(\cos\theta\right). \tag{1.6}$$

For a Keplerian orbit with associated semi-major axis a, orbital eccentricity e and inclination i these Legendre polynomials can be expressed in terms of spherical harmonics (e.g. Ogilvie, 2014):

$$\Psi = \mathrm{Re}\sum_{l=2}^{\infty}\sum_{m=0}^{l}\sum_{n=-\infty}^{\infty}\frac{GM_2}{a}A_{l,m,n}(e,i)\left(\frac{r}{a}\right)^l Y_l^m(\theta,\phi)\mathrm{e}^{-\mathrm{i}n\Omega_o t}, \tag{1.7}$$

with $Y_l^m(\theta,\phi)$ the spherical harmonic of degree l and azimuthal order m. The temporal harmonics of the orbital motion and thus tidal response are given by the integer n. In this expression $A_{l,m,n}(e,i)$ is a complex coefficient that depends on the eccentricity and inclination in a non-trivial way. See Table 1 in Ogilvie (2014) for some values of this coefficient for the quadrupolar $l = 2$ tide, which is often the most important component when $|\boldsymbol{x}|/|\boldsymbol{d}|$ is small. Finally $\Omega_o = \left(\frac{G(M_1+M_2)}{a^3}\right)^{1/2}$ is the mean orbital angular velocity according to Kepler's third law.

In a non-rotating frame the tidal frequency of each component is then given by $\tilde{\omega}_{l,m,n} = n\Omega_o$. In the frame rotating with body 1 the tidal frequency is instead given by $\omega_{l,m,n} = n\Omega_o - m\Omega_s$, which is called the tidal frequency in the fluid frame. The dominant component of the tidal response is typically the $l = m = n = 2$ component, which is referred to as the "asynchronous tide". For this component the tidal frequency is $\omega_{2,2,2} = 2(\Omega_o - \Omega_s)$. Finally, we can absorb all the constants into the $A_{l,m,n}(e,i)$ coefficient and write the full tidal potential in the frame rotating with body 1:

$$\Psi = \mathrm{Re}\sum_{l=2}^{\infty}\sum_{m=0}^{l}\sum_{n=-\infty}^{\infty}\mathcal{A}_{l,m,n}(e,i)\left(\frac{r}{R_1}\right)^l Y_l^m(\theta,\phi)\mathrm{e}^{-\mathrm{i}\omega_{l,m,n}t}, \tag{1.8}$$

where $\mathcal{A}_{l,m,n}(e,i) = \frac{GM_2R_1^l}{a^{l+1}}A_{l,m,n}(e,i)$.

Additionally, one can define the tidal amplitude, ϵ, which is a dimensionless parameter that is used to indicate the strength of tidal effects. It is defined using the quantities M_1, M_2, R_1 and a above:

$$\epsilon = \left(\frac{M_2}{M_1}\right)\left(\frac{R_1}{a}\right)^3, \tag{1.9}$$

such that we can write:

$$\mathcal{A}_{l,m,n}(e,i) = \omega_d^2\epsilon\frac{R_1^l}{a^{l-2}}A_{l,m,n}(e,i), \tag{1.10}$$

Table 1.1: Values of the tidal amplitude ϵ for various bodies within and outside the Solar System. Within the Solar System the values are relatively small for planets due to their moons, however, in the Hot Jupiter WASP-19b the tidal amplitude due to its nearby host star is comparatively very high. Values taken from Ogilvie (2014).

Body 1 and Body 2	Tidal amplitude ϵ
Earth due to the Moon	$6 \cdot 10^{-8}$
Jupiter due to Io	$2 \cdot 10^{-7}$
Saturn due to Titan	$3 \cdot 10^{-8}$
WASP-18 due to WASP-18b	$2 \cdot 10^{-4}$
WASP-19b due to WASP-19	$6 \cdot 10^{-2}$

with $\omega_{\text{dyn}}^2 \sim \frac{GM}{R_1^3}$ the dynamical or free-fall frequency of body 1. Some estimated values of the tidal amplitude taken from Ogilvie (2014) have been reproduced in Table 1.1.

1.2.2 The Love number

We are not just interested in the tide raised in body 1 due to body 2, we would also like to determine the tidal evolution and to this end we must define another parameter: the Love number. The idea for the Love number arises in a very simple way: suppose that body 1 has been deformed under the influence of the tidal forces acting on it, then its mass distribution will have changed from what would have otherwise been expected. Moreover, the perturbed mass distribution will have its own gravitational potential. This additional gravitational potential can be defined as:

$$\Phi' = \text{Re} \sum_{l=2}^{\infty} \sum_{m=0}^{l} \sum_{n=-\infty}^{\infty} \mathcal{B}_{l,m,n} \left(\frac{R_1}{r} \right)^{l+1} Y_l^m(\theta, \phi) \mathrm{e}^{-\mathrm{i}\omega_{l,m,n} t}, \tag{1.11}$$

which arises as a solution to Laplace's equation. This potential has been written using Φ' as it relates to the deformation of body 1's own gravitational potential Φ. The ratio of the coefficients of the gravitational potential of the deformation to the imposed tidal potential for each component (l, m, n) tells us how important the tides are in deforming the planet. If the ratio is small then the tides are relatively unimportant in deforming the planet, and vice versa. This ratio, which is complex in general, is defined as the Love number:

$$k_l^m(\omega_{l,m,n}) = \mathcal{B}_{l,m,n} / \mathcal{A}_{l,m,n}, \tag{1.12}$$

for each tidal component. In general we are interested in the Love numbers with $l = 2$, i.e. the Love numbers corresponding with the quadrupolar tide. The Love numbers we will consider are the $l = m = 2$ and $l = 2$, $m = 1$ components. These are the Love numbers associated with the tidal dissipation mechanisms we wish to study, which we will discuss in Sec. 1.5. A Love number is however an elusive quantity as knowledge about the interior of the body is needed to compute it. For this exact reason we are very much interested in extracting it from observational data because the real and imaginary parts of this Love number contain a wealth of information. The real part, $\text{Re}[k_l^m(\omega)]$, details the amount of deformation, and therefore gives information on the interior. The imaginary

part, $\mathrm{Im}[k_l^m(\omega)]$, describes how misaligned the tidal deformation is with the line connecting the centres of mass of the two bodies, i.e. $\boldsymbol{d}$. The misalignment is directly tied to the tidal torque and tidal dissipation and thus orbital evolution of the system due to tides.

To see how the misalignment of the bulge with the line connecting the two centres of mass connects to the tidal torque and later tidal evolution we can use the most well known example of tidal interaction, namely the Earth-Moon system. In Fig. 1.5 a simple illustration of the Earth-Moon system is presented. In this schematic Earth is treated as the primary with mass M_1, while treating the Moon as the secondary point mass M_2. The tides have acted to deform Earth's surface into a tidal bulge, shown in grey and exaggerated for illustrative purposes. The effects the continents would have on the tides are also omitted.

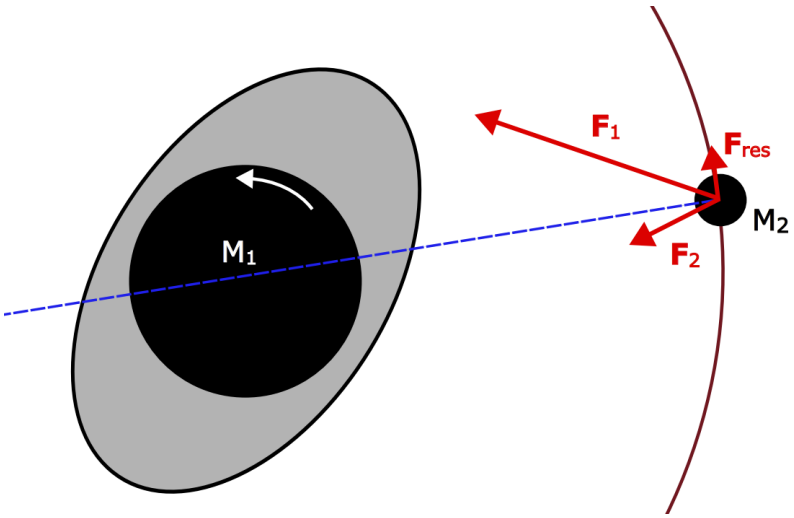

Figure 1.5: Schematic of the Earth (body 1) and Moon (body 2) with an exaggerated misaligned tidal bulge. The Earth rotates faster than the Moon, so the tidal bulge precedes the line connecting the two centres of mass, here illustrated in a blue dashed line. As a result there arise two forces on the Moon, which produce a resultant force that accelerates the Moon, as well as resulting in a torque that transfers angular momentum from the Earth to the Moon.

In the Earth-Moon system the primary has a larger spin rate than the orbital rotation rate of the secondary. Therefore the tidal bulge precedes the line connecting the centres of mass, resulting in a misalignment. This is illustrated in Fig. 1.5. The line connecting the centres of mass is given in dashed-blue. This then results in a gravitational attraction of the Moon to the tidal bulges, as indicated by the red arrows. These forces sum to a total force that acts in the same direction as the direction of travel of the Moon. This force then results in a torque, which leads to a transfer of angular momentum to the Moon from the Earth. Conservation of angular momentum implies that the Earth must lose angular momentum, the only source of which (within this simplified system) is Earth's spin. Thus Earth is expected to slow down over time, while the average distance between the Earth and Moon must increase, exactly as found in Fig. 1.1.

The only question is what causes this misalignment. Perhaps the easiest way of

thinking about this is that there must simply be some friction within the primary. This friction then prevents the tidal bulge from instantaneously sliding back to the line connecting the centres of mass. One can think of viscosity as this friction, but tidal dissipation can additionally be thought to act like a friction in this scenario. Thus tidal dissipation causes a misalignment, which creates a torque. Both the deformation and misalignment, and thus rate of tidal dissipation, should therefore be considered when considering the effect of tides on the orbital evolution.

For Hot Jupiter systems, the opposite configuration should instead be considered. When considering the tide in a Sun-like star due to a Hot Jupiter the star often rotates slowly compared to the very short period orbits of its Hot Jupiter (e.g. the ~ 30 day spin period of the Sun compared to the ~ 1 day orbital period of a Hot Jupiter). This difference is exacerbated as the star ages and slows down due to magnetic braking. In this case the bulge precedes the line connecting the centres of mass, so the forces and resulting torques point in a different direction, therefore acting to reduce the angular momentum and thus semi-major axis or eccentricity of the Hot Jupiter orbit, as well as spinning up the star (though not so much to have a significant impact in most cases, see e.g. Benbakoura et al. 2019).

One can also consider the tide in a Hot Jupiter due to its star, which will be the focus of this work. In this case, one ends up with the reverse transfer, where the tides in the planet compete with those in the star. The tides in the Hot Jupiter contribute to increase the orbital angular momentum of the star, thus increasing the separation distance, whilst slowing down the spin of the Hot Jupiter. However, the Hot Jupiter will achieve spin-orbit synchronisation much faster than the star, which reduces its contribution to tidal dissipation. Additionally, the angular momentum associated with the spin of the Hot Jupiter is small compared to the orbital angular momentum, so even if all its spin angular momentum is transferred to the orbit, it would not have a significant impact. Note that a spin-synchronised Hot Jupiter on an eccentric orbit will however still contribute to tidal evolution, and act to circularise its own orbit in most cases.

In terms of the observational contexts mentioned above, the choice is often made to work with a different quantity to the Love number, namely the tidal quality factor $Q_{l,m,n}$. This prescription of a quality factor takes its inspiration from damped harmonic oscillators, where the quality factor indicates how underdamped a given harmonic oscillator is and thus how fast the oscillations will decay. A larger value of this quality factor implies a slower decay. Following on from this analogy to the damped harmonic oscillator, the quality factor in a tidal context is defined as 2π times the ratio of the maximum total amount of energy stored in the tidal response, $E_{0_{l,m,n}}$, to the energy dissipation rate, $\dot{E}_{l,m,n}$, integrated over one tidal period:

$$Q_{l,m,n} = \frac{2\pi E_{0_{l,m,n}}}{\int \dot{E}_{l,m,n}\,\mathrm{d}t}. \tag{1.13}$$

This is a somewhat counter-intuitive definition, in that it implies that systems which

dissipate tidal energy faster have smaller values of Q. As it turns out, the tidal quality factor is related to the imaginary (and real) part of the Love number:

$$|\mathrm{Im}[k_l^m(\omega_{l,m,n})]|= \frac{\mathrm{Re}[k_l^m(\omega_{l,m,n})]}{Q_{l,m,n}} = \kappa_{l,m,n}. \tag{1.14}$$

Indeed, this implies that knowledge of the tidal quality factor would allow for knowledge of the Love number and vice versa. In general the value of $\mathrm{Re}[k_l^m(\omega_{l,m,n})]$ is close to unity. It depends most strongly on the interior properties of the body and only weakly depends on the values of $\omega_{l,m,n}$ and m. Therefore, the hydrostatic value k_l, independent of $\omega_{l,m,n}$ and m, is often employed instead of $\mathrm{Re}[k_l^m(\omega_{l,m,n})]$. It is also customary to define the modified tidal quality factor $Q'_{l,m,n} = Q_{l,m,n}k_l^{\mathrm{hom}}/k_l$, with $k_l^{\mathrm{hom}} = 3/[2(l-1)]$ for a homogeneous fluid body. Furthermore, since the dominant component of the tidal potential is the $l = 2$ component, often the choice is made to write this relation using this particular component. Thus we obtain:

$$|\mathrm{Im}[k_2^m(\omega_{2,m,n})]|= \frac{k_2}{Q_{2,m,n}} = \frac{3}{2Q'_{2,m,n}}. \tag{1.15}$$

These customary definitions arise from an observational context, rather than theoretical modelling, because values of $Q'_{l,m,n}$ can be indirectly obtained from observations. Observations constrain the amount of tidal dissipation by observing the rate of change of the semi-major axis, spin, eccentricity and obliquity. These rates of change can then be used in analytically derived expressions for these quantities as a function of $Q'_{l,m,n}$, allowing to constrain $Q'_{l,m,n}$ from the observations. These expressions, for small e and i, are (Ogilvie, 2014):

$$\frac{1}{a}\frac{\mathrm{d}a}{\mathrm{d}t} = -\frac{9}{2Q'_{2,2,2}}\frac{M_2}{M_1}\left(\frac{R_1}{a}\right)^5 \Omega_o, \tag{1.16}$$

$$\frac{1}{\Omega_s}\frac{\mathrm{d}\Omega_s}{\mathrm{d}t} = \frac{9}{4Q'_{2,2,2}}\frac{L_o}{L_s}\frac{M_2}{M_1}\left(\frac{R_1}{a}\right)^5 \Omega_o, \tag{1.17}$$

$$\frac{1}{e}\frac{\mathrm{d}e}{\mathrm{d}t} = \frac{9}{32}\left(\frac{4}{Q'_{2,2,2}} - \frac{6}{Q'_{2,0,1}} + \frac{1}{Q'_{2,2,1}} - \frac{49}{Q'_{2,2,3}}\right)\frac{M_2}{M_1}\left(\frac{R_1}{a}\right)^5 \Omega_o, \tag{1.18}$$

$$\frac{1}{i}\frac{\mathrm{d}i}{\mathrm{d}t} = \frac{9}{8}\left[\frac{1}{Q'_{2,2,2}}\left(1-\frac{L_o}{L_s}\right) + \left(\frac{1}{Q'_{2,1,0}} - \frac{1}{Q'_{2,1,2}}\right)\left(1+\frac{L_o}{L_s}\right)\right]\frac{M_2}{M_1}\left(\frac{R_1}{a}\right)^5 \Omega_o, \tag{1.19}$$

where L_o and L_s represent the orbital and spin angular momentum of body 1 and body 2 respectively, given by:

$$L_s = I_1\Omega_s, \qquad L_o = \frac{GM_1M_2(1-e^2)^{1/2}}{\Omega_o a}, \tag{1.20}$$

with I_1 the moment of inertia of body 1. From these equations it is possible to obtain

values of $Q'_{l,m,n}$ if the evolution of a, Ω_s, e, i is known. The unmodified tidal quality factor $Q_{l,m,n}$ cannot be obtained from these equations however, as this would require knowledge of the real part of the Love number and thus the interior properties of the body, which in the case of exoplanets is very unknown (and even for Jupiter and Saturn itself is still not well understood e.g. Stevenson 2020; Helled et al. 2022). For this reason $Q'_{l,m,n}$ is the parameter of choice to report in observational studies. Often, in observational papers a singular Q' without subscripts will be reported, this Q' usually represents that of the $l = m = n = 2$ component as these results are usually obtained from the rate of change of the semi-major axis, which in accordance with Eq. (1.16) only depends on this component.

In practical applications of tidal theory one works backwards. Instead of starting by calculating the Love numbers, calculating all $Q'_{l,m,n}$ and then finally calculating the evolution of the spin and orbit, one often starts from observations which provide constraints on the evolution of a, Ω_s, e and i. From here one can estimate a (maximum) value of all $Q'_{l,m,n}$ or more commonly just Q'. If no evolution is observed a minimum value can be estimated. Then models of tidal theory can be used to find the $Q'_{l,m,n}$ originating from a given tidal dissipation mechanism. Comparing these modelled values of $Q'_{l,m,n}$ to those found from observations can explain which mechanisms are operating to cause certain observed tidal effects, and potentially shed light on the interiors of these objects if both the observational values are very precise and the tidal mechanisms are very well understood. Improving our understanding of these mechanisms is therefore of the essence, not only to explain current observations and make predictions for future tidal evolution of these systems, but also as a pathway to obtain information on the planetary interiors.

1.3 Giant planet interiors

Evidently, if we wish to study the result of tidal deformation and tidal evolution in Hot Jupiters we require information about their interiors. However, we have little to no direct observational knowledge of the interiors of Hot Jupiters. Therefore we turn our attention to the two giant planets whose interiors we do have some knowledge about, namely Jupiter and Saturn.

Prior to the Juno mission the structures of these planets were usually described using a three layer model (Guillot, 1999; Guillot et al., 2004; Militzer et al., 2016). The innermost layer is the solid inner core, which was usually taken to be small and dense, consisting of rock and metal. In this model, a large convection zone spanning most of the interior sits atop the dense inner core. This convection zone was assumed to host efficient convection, i.e. it had homogenised the entropy, and to be under such high pressures that the hydrogen which made up most of its mass was metallic. Atop this metallic hydrogen region sat the third layer, which consisted of molecular hydrogen instead. There were many questions surrounding these models, particularly around the immiscibility of hydrogen and helium, as well as the distribution of the heavier elements.

The Juno mission has provided a wealth of information using gravity measurements,

but it has also revealed that the structure is more complex than previously thought. From these gravity measurements the distribution of mass can be determined, which has indicated that, instead of a small dense solid core, it is possible that the core is instead dilute (Wahl et al., 2017; Stevenson, 2020). A dilute core implies that the metals are not concentrated in one region but are instead spread out throughout the deep interior of Jupiter and Saturn. These results are corroborated by measurements of Saturn's rings (Mankovich & Fuller, 2021), the waves of which are a reflection of those in Saturn's deep interior, and thus allow for constraining said interior. The diluted core might then result in a composition which is stable against convection, commonly referred to as a stable region. Above the dilute core sits a convection zone, followed by a possible "helium rain" layer. In the helium rain layer it is expected that the helium condenses out from the upper parts of the layer and rains down. This difference in composition is thought to possibly result in a second stable region. Above this helium rain layer another small convective region is expected to sit, consisting of molecular hydrogen instead. The deep zonal winds of Jupiter and Saturn penetrate into this layer (Galanti et al., 2019; Gastine & Wicht, 2021). Atop all these regions sits the atmosphere, with its distinct banded cloud structure in the case of Jupiter.

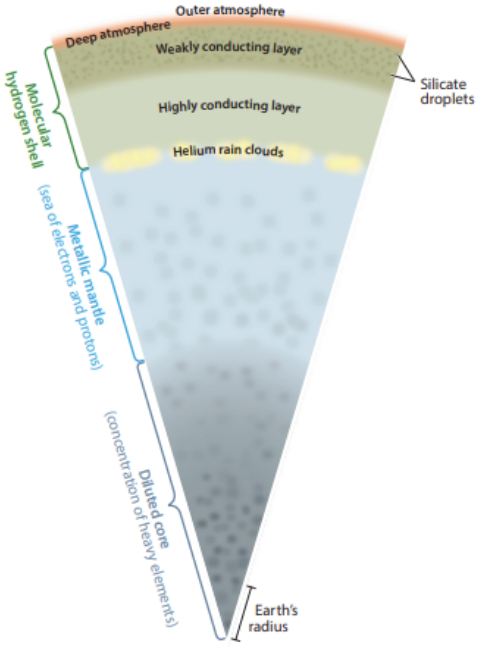

Figure 1.6: Illustration of Jupiter's interior after the Juno mission. A dilute core of large radial extent exists, atop which sits a layer of metallic hydrogen. Above that is the helium rain layer. Atop the helium rain layer sits the molecular hydrogen layer; it is in this layer that the deep zonal winds are located. Atop this all sits the atmosphere, with Jupiter's distinct banded cloud structure. Figure reproduced from Stevenson (2020).

The details of the above dilute core model are still unclear. It is also unclear whether or not such a model is applicable to a Hot Jupiter given that it is much more strongly irradiated by its host star, which might affect its interior. Nevertheless, if we wish to study the tide in these giant planets, studying its interactions with convection is of the essence;

both the 3-layer model and the newer dilute core models feature convective regions and convection is usually thought of as a process that dominates in such a region, particularly if it is efficient enough to homogenise the region.

1.4 The equilibrium and dynamical tide

Before considering the tidal dissipation mechanisms to model in such giant planets and their interactions with convection, we must first describe the convention within tidal theory to split the tidal response within an astrophysical object into two parts, each of which has their own associated tidal dissipation mechanisms. The first of these is the equilibrium or non-wavelike tide, which represents the hydrostatic bulge that has already been portrayed in the schematics in Fig. 1.4 and Fig. 1.5. The second part of the tide is commonly referred to as the dynamical or wavelike tide, which as the name suggests consists of waves excited by the tide. Often it is the rotation and associated acceleration of the equilibrium tide which launches these waves to create the dynamical tide. This distinction is only exact in linear theory, but can still be helpful for our understanding otherwise.

1.4.1 The equilibrium tide

A prescription for the equilibrium tide was first derived by Zahn (1966), who considered a distortion in density and pressure away from the expected value when a tidal potential is imposed. These distortions then allow hydrostatic equilibrium to be achieved again when considering both the imposed tidal potential as well as the distorted gravitational potential of the primary resulting from said distortions. Using hydrostatic equilibrium to derive the tidal response is a good initial approximation when the frequency of the tide is low compared to the dynamical frequency. This entire derivation is based on the instantaneous change of potential, and does not take into account any acceleration or other forces such as the Coriolis force or damping forces when computing it. The corrections that are required when these are taken into account are what excites the dynamical tide.

To follow the derivation in Zahn (1966) we start from hydrostatic equilibrium of the unperturbed uniformly-rotating body:

$$0 = -\frac{1}{\rho}\nabla p - \nabla\Phi, \tag{1.21}$$

with Φ the total potential of the unperturbed primary, which formally consists of both the gravitational potential Φ_g and the centrifugal potential (due to rotation) Φ_c. By taking the curl of this equation we obtain:

$$\begin{aligned} 0 &= -\nabla\frac{1}{\rho} \times \nabla p - \frac{1}{\rho}\nabla \times \nabla p - \nabla \times \nabla\Phi, \\ &= \frac{1}{\rho^2}\nabla\rho \times \nabla p. \end{aligned} \tag{1.22}$$

The latter two terms vanish because the curl of the gradient is zero. This equation implies

that the gradients of ρ and p are parallel, and so must be a function of the same variable. Furthermore, Eq. (1.21) implies that Φ is also of a function of the same variable. We therefore choose that p and ρ are functions of Φ; incidentally, we can also write $\rho = \rho(p)$.

Now we consider the imposed tidal potential Ψ, which satisfies Laplace's equation $\nabla^2\Psi = 0$ within the primary because there is by definition no mass of the secondary within the primary. We consider the linear, i.e. small amplitude, Eulerian perturbations to our defined quantities ρ', p' and Φ' and again consider hydrostatic equilibrium:

$$0 = -\frac{1}{\rho + \rho'}\nabla(p + p') - \nabla\Phi - \nabla\Phi' - \nabla\Psi. \tag{1.23}$$

Upon Taylor expanding the fraction and eliminating all terms that satisfy Eq. (1.21), we find:

$$\begin{aligned} 0 &\approx \frac{\rho'}{\rho^2}\nabla p - \frac{1}{\rho}\nabla p' + \frac{\rho'}{\rho^2}\nabla p' - \nabla\Phi' - \nabla\Psi, \\ &\approx \frac{\rho'}{\rho^2}\nabla p - \frac{1}{\rho}\nabla p' - \nabla\Phi' - \nabla\Psi, \end{aligned} \tag{1.24}$$

where we have linearised the equation in the second expression, as we are considering only linear effects. For ease of calculation we define the quantity W:

$$W = p'/\rho + \Phi' + \Psi, \tag{1.25}$$

using this definition, we can rewrite Eq. (1.24):

$$0 = -\nabla W + (\rho' - \frac{\mathrm{d}\rho}{\mathrm{d}p}p')\frac{1}{\rho^2}\nabla p. \tag{1.26}$$

Repeating the same analysis as above by taking the curl of this equation we deduce that the gradients $\nabla(\rho' - \frac{\mathrm{d}\rho}{\mathrm{d}p}p')$ and ∇p are parallel, which must also be parallel to ∇W. Therefore both of these quantities are again functions of Φ only.

Next, we consider another property of all perturbed quantities: if the tide or the tidal components under consideration are oscillatory then they should all be proportional to $\mathrm{e}^{-i\omega_{l,m,n}t}$, and as such their means over one tidal period should vanish. This includes W and hence:

$$\begin{aligned} W = 0 &= p'/\rho + \Phi' + \Psi, \\ \Rightarrow p' &= -\rho(\Phi' + \Psi), \end{aligned} \tag{1.27}$$

as well as the previously considered quantity $\rho' - \frac{\mathrm{d}\rho}{\mathrm{d}p}p'$:

$$0 = \rho' - \frac{\mathrm{d}\rho}{\mathrm{d}p}p', \tag{1.28}$$

$$\Rightarrow \rho' = \frac{\mathrm{d}\rho}{\mathrm{d}p}p' = -\rho\frac{\mathrm{d}\rho}{\mathrm{d}p}(\Phi' + \Psi). \tag{1.29}$$

Finally, we can combine these in Poisson's equation for the potential:

$$\begin{aligned}\nabla^2(\Phi+\Phi'+\Psi) &= 4\pi G(\rho+\rho'),\\ \Rightarrow \nabla^2(\Phi') &= -4\pi G\rho\frac{\mathrm{d}\rho}{\mathrm{d}p}(\Phi'+\Psi),\end{aligned} \tag{1.30}$$

where we have eliminated the terms that satisfy Poisson's equation for the unperturbed potential Φ and used the fact that $\nabla^2\Psi = 0$ inside the body of the primary. Thus we have obtained a partial differential equation for the perturbed potential Φ' which is valid within the body of the primary. This can be solved if the imposed tidal potential is known, given suitable boundary conditions. These boundary conditions are: regularity at the centre and a free-surface condition at the surface. Upon solving this, the expressions for ρ' and p' can be obtained, and thus the full perturbations due to the equilibrium tide are known.

The tidal flow perturbation associated with the equilibrium tide $\boldsymbol{U}_e$ can be calculated from the tidal displacement $\boldsymbol{\xi}_e$, for which we can obtain an expression starting from the continuity equation:

$$0 = \frac{\partial(\rho+\rho')}{\partial t} + \nabla\cdot((\rho+\rho')\boldsymbol{U}_e) = \frac{\partial(\rho+\rho')}{\partial t} + \nabla\cdot((\rho+\rho')\frac{\partial\boldsymbol{\xi}_e}{\partial t}). \tag{1.31}$$

Again we have perturbed ρ and we treat the tidal flow and displacement as a perturbation, thus we can linearise, taking into account that the hydrostatic background density only depends on Φ, so $\frac{\partial\rho}{\partial t} = 0$:

$$\begin{aligned}0 &= \frac{\partial\rho'}{\partial t} + \nabla\cdot(\rho\frac{\partial\boldsymbol{\xi}_e}{\partial t}),\\ &= \frac{\partial\rho'}{\partial t} + \nabla\cdot(\frac{\partial\rho\boldsymbol{\xi}_e}{\partial t} - \boldsymbol{\xi}_e\frac{\partial\rho}{\partial t}),\\ &= \frac{\partial(\rho' + \nabla\cdot(\rho\boldsymbol{\xi}_e))}{\partial t},\\ \Rightarrow \rho' &= -\nabla\cdot(\rho\boldsymbol{\xi}_e) = -\rho\nabla\cdot\boldsymbol{\xi}_e - \boldsymbol{\xi}_e\cdot\nabla\rho.\end{aligned} \tag{1.32}$$

Equally, assuming adiabatic perturbations we can write from the ideal gas law:

$$\begin{aligned}\frac{p+p'}{(\rho+\rho')^\gamma} &= \text{Constant},\\ \Rightarrow 0 &= \frac{\mathrm{D}}{\mathrm{D}t}\left(\frac{p+p'}{(\rho+\rho')^\gamma}\right),\\ &= \frac{1}{(\rho+\rho')^\gamma}\frac{\mathrm{D}(p+p')}{\mathrm{D}t} + (p+p')\frac{-\gamma}{(\rho+\rho')^{\gamma+1}}\frac{\mathrm{D}(\rho+\rho')}{\mathrm{D}t},\end{aligned} \tag{1.33}$$

where γ represents the adiabatic exponent. Upon using the continuity equation to rewrite

the total derivative with respect to $(\rho + \rho')$ we find:

$$\begin{aligned} 0 &= \frac{1}{(\rho+\rho')^\gamma}\frac{\mathrm{D}(p+p')}{\mathrm{D}t} + (p+p')\frac{-\gamma}{(\rho+\rho')^{\gamma+1}} \cdot -(\rho+\rho')\nabla\cdot\boldsymbol{U}_e, \\ &= \frac{\partial p'}{\partial t} + \boldsymbol{U}_e\cdot\nabla(p+p') + \gamma(p+p')\nabla\cdot\boldsymbol{U}_e, \\ &= \frac{\partial p'}{\partial t} + \frac{\partial \boldsymbol{\xi}_e}{\partial t}\cdot\nabla(p+p') + \gamma(p+p')\nabla\cdot\frac{\partial\boldsymbol{\xi}_e}{\partial t}. \end{aligned} \tag{1.34}$$

This equation we can linearise, and then write everything inside the time derivative once again, which leads to the conclusion:

$$\begin{aligned} 0 &= \frac{\partial p'}{\partial t} + \frac{\partial(\boldsymbol{\xi}_e\cdot\nabla p)}{\partial t} + \frac{\partial(\gamma p\nabla\cdot\boldsymbol{\xi}_e)}{\partial t}, \\ \Rightarrow p' &= -\boldsymbol{\xi}_e\cdot\nabla p - \gamma p\nabla\cdot\boldsymbol{\xi}_e. \end{aligned} \tag{1.35}$$

Using this result together with Eq. (1.28) we can find an expression for the equilibrium tide:

$$\begin{aligned} 0 &= \rho' - \frac{\mathrm{d}\rho}{\mathrm{d}p}p', \\ &= -\rho\nabla\cdot\boldsymbol{\xi}_e - \boldsymbol{\xi}_e\cdot\nabla\rho + \frac{\mathrm{d}\rho}{\mathrm{d}p}\left(\gamma p\nabla\cdot\boldsymbol{\xi}_e + \boldsymbol{\xi}_e\cdot\nabla p\right), \\ &= -\rho\nabla\cdot\boldsymbol{\xi}_e - \frac{\mathrm{d}\rho}{\mathrm{d}p}\boldsymbol{\xi}_e\cdot\nabla p + \frac{\mathrm{d}\rho}{\mathrm{d}p}\left(\gamma p\nabla\cdot\boldsymbol{\xi}_e + \boldsymbol{\xi}_e\cdot\nabla p\right), \\ &= \left(-\rho + \gamma p\frac{\mathrm{d}\rho}{\mathrm{d}p}\right)\nabla\cdot\boldsymbol{\xi}_e. \end{aligned} \tag{1.36}$$

The term in brackets in this last expression is non-zero if the buoyancy frequency N^2 is non-zero (Ogilvie, 2014); an elegant derivation of this fact can be found in Duguid (2020). If this holds true, the tidal displacement and thus tidal velocity are incompressible, i.e. $\nabla\cdot\boldsymbol{\xi}_e = 0$. Finally, we can combine Eq. (1.29) and Eq. (1.32) to obtain:

$$-\rho\frac{\mathrm{d}\rho}{\mathrm{d}p}(\Phi' + \Psi) = -\boldsymbol{\xi}_e\cdot\nabla\rho = -\boldsymbol{\xi}_e\cdot\frac{\mathrm{d}\rho}{\mathrm{d}p}\nabla p, \tag{1.37}$$

$$\Rightarrow \Phi' + \Psi = \boldsymbol{\xi}_e\cdot\frac{1}{\rho}\nabla p. \tag{1.38}$$

It is possible to use $\frac{1}{\rho}\nabla p = -\nabla\Phi = \boldsymbol{g}$ in this final expression to obtain the results in terms of known quantities. Thus the above equation gives us the equilibrium tide displacement in the direction of gravity, i.e. the radial displacement. Then using incompressibility the horizontal displacement can be derived. This is the original equilibrium tide displacement as derived by Zahn (1966).

This derivation of the tidal displacement and associated tidal flow crucially hinges on one argument, namely that $N^2 \neq 0$, or more precisely that $N^2 > \omega^2$. This assumption is typically correct in large portions of stably stratified regions of the planet, or radiative zones in stars. However, in neutrally stratified regions or convection zones where the convection is efficient in homogenising entropy it is in fact expected that $N^2 \approx 0$, i.e. it is

approximately neutrally stratified. This crucial difference was remarked upon in Goodman and Dickson (1998) and Terquem et al. (1998). The tide calculated in approximately neutrally stratified regions has subsequently been referred to as the "non-wavelike tide" (Ogilvie, 2013), although it is often still just called the equilibrium tide. Deriving the tidal flow and displacement in this case starts from the linearised momentum equation (neglecting all forces but the Coriolis force in this example):

$$\frac{\partial \boldsymbol{U}}{\partial t} + 2\boldsymbol{\Omega} \times \boldsymbol{U} = -\nabla W. \tag{1.39}$$

This equation can be decomposed in two parts, one for the non-wavelike tide with subscript nw and one for the wavelike tide with subscript w:

$$\frac{\partial \boldsymbol{U}_{nw}}{\partial t} = -\nabla W_{nw}, \tag{1.40}$$

and

$$\frac{\partial \boldsymbol{U}_{w}}{\partial t} + 2\boldsymbol{\Omega} \times \boldsymbol{U}_{w} = -\nabla W_{w} - 2\boldsymbol{\Omega} \times \boldsymbol{U}_{nw}. \tag{1.41}$$

The philosophy behind this decomposition is to consider the non-wavelike tide as an instantaneous hydrostatic deformation, unaffected by the Coriolis force, and the wavelike tide as the result of the accelerations and other forces acting on said non-wavelike tide and then generating waves. This decomposition follows the idea of the equilibrium and dynamical tide decomposition as introduced by Zahn, except that this derivation is valid in neutrally stratified regions.

From Eq. (1.40) it is clear that the flow $\boldsymbol{U}_{nw}$ (and thus tidal displacement $\boldsymbol{\xi}_{nw}$) is irrotational:

$$\nabla \times \boldsymbol{U}_{nw} = \nabla \times \boldsymbol{\xi}_{nw} = \boldsymbol{0}. \tag{1.42}$$

This allows us to write $\boldsymbol{\xi}_{nw} = \nabla V$, for some potential V, and thus to finally find the following expression by combining Eq. (1.29) and Eq. (1.32) for the non-wavelike tide:

$$\nabla \cdot (\rho \nabla V) = \frac{\mathrm{d}\rho}{\mathrm{d}p} \rho (\Phi' + \Psi). \tag{1.43}$$

This partial differential equation can be solved when suitable boundary conditions are imposed. The equilibrium tide and non-wavelike tide usually result in similar results, although they can quantitatively differ by an $\mathcal{O}(1)$ factor (Barker, 2020).

1.4.2 The dynamical tide

The dynamical tide (or wavelike tide in adiabatically stratified regions) then consists of internal waves in the fluid excited by the tide. The subsequent dissipation of these tidally excited internal waves can be important for tidal evolution. The character of these waves strongly depends on the medium in which they propagate. Of particular importance is the stratification of this medium, as it is hugely influential in determining whether so-called

internal gravity waves can exist. Another highly important factor would be the presence of a magnetic field, which would allow Alfvén waves to exist. In this work however, we do not consider the magnetic field – as is common in tidal studies to date – and limit ourselves to hydrodynamic waves.

Inertial waves

Let us start by considering neutral stratification, which can be crudely thought to represent a convective region with efficient convection that has homogenised the entropy, thus attaining adiabaticity. In these regions internal gravity waves cannot propagate. If the object is rotating on the other hand (which astrophysical objects tend to be) then another possible category of waves arises, namely the inertial waves.

Inertial waves (IWs) are waves restored by the Coriolis force due to the spin of the body. For these waves the classical Cartesian plane wave Ansatz is made: $\mathrm{e}^{i(\boldsymbol{k}\cdot\boldsymbol{x}-\omega t)}$, where $\boldsymbol{k}$ is the wavevector and ω is the frequency of the wave. One can think of this plane wave Ansatz as describing short wavelength waves, such that any constraints from the boundaries are ignored. To derive their dispersion relation, one can start from the linearised Navier-Stokes (or Euler) momentum equation, assuming both constant density and incompressibility while only considering the effects of the Coriolis force:

$$\frac{\partial \boldsymbol{u}}{\partial t} + 2\boldsymbol{\Omega}_s \times \boldsymbol{u} = -\frac{1}{\rho_0}\nabla p. \tag{1.44}$$

Using the Ansatz, choosing the rotation axis to lie along the z-axis and after some algebra one can arrive at the dispersion relation of inertial waves:

$$\omega^2 = \frac{4(\boldsymbol{\Omega}_s \cdot \boldsymbol{k})^2}{k^2} = 4\Omega_s^2 \frac{k_z^2}{k^2}, \tag{1.45}$$

with $k^2 = k_x^2 + k_y^2 + k_z^2$. This dispersion relation has two consequences, inertial waves can only exist with frequencies $|\omega| \leq 2\Omega_s$. If the frequency were to be higher than $2\Omega_s$, this would imply that one or both of the k_x, k_y need to be imaginary and thus that the waves are evanescent. This situation might arise if a wave travels into a region where Ω_s is smaller due to a differential rotation for example. Evidently, these kinds of evanescent waves cannot be directly excited, and thus for all excited waves $|\omega| \leq 2\Omega_s$ is maintained. The second consequence implies that a wave with a given wave number travels in a given direction as long as Ω_s is unchanged. This can be easily seen by defining an angle with respect to the rotation axis, $\tilde{\theta}$ (distinct from the spherical coordinate), in which case $k_z/k = \cos\tilde{\theta}$.

$$\omega^2 = 4\Omega^2 \cos^2\tilde{\theta}. \tag{1.46}$$

Finally, at a given frequency infinitely many waves with different wavenumbers satisfy this relation, precisely because the magnitude does not come into the dispersion relation, but rather the direction.

These waves can exhibit a very interesting phenomenon called a wave attractor

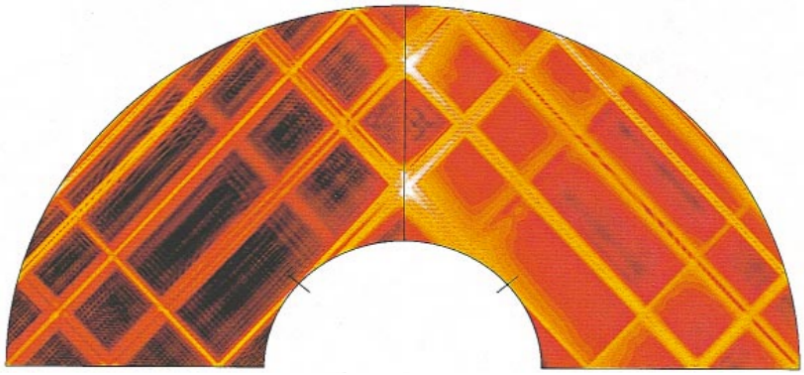

Figure 1.7: Wave attractors of inertial waves in a spherical shell. The solid-body rotation allows for inertial waves which travel on straight paths, the direction of which is fixed by the ratio of the frequency to the rotation rate. For certain frequencies a closed path is found, resulting in focusing of the inertial waves, producing these wave attractors. Figure adapted from Rieutord and Valdettaro (1997).

(Rieutord & Valdettaro, 1997) when one considers the geometry of a planet, i.e. a spherical shell in which to propagate. These attractors arise precisely because the direction of travel of the inertial wave is fixed by the ratio of its frequency and rotation rate. In a planet or star that rotates like a solid body this would allow for certain frequencies to create a closed path as shown in Fig. 1.7, geometrically focusing the inertial waves, potentially leading to rapid dissipation of the highly concentrated energy.

Internal Gravity Waves

If rotation is absent, however, and a stable stratification is present instead, one obtains internal gravity waves (IGWs). This stratification is associated with variations in density, ρ', – or more strictly in entropy – and thus it is important to treat these variations. For ease we utilise the Boussinesq approximation. This approximation assumes that the density variations are small, such that they only need to be taken into account in the buoyancy term, i.e. the term interacting with gravity. This approximation will be presented in more detail in Ch. 2. Using the exact same technique as for the IWs, but this time setting $\Omega = 0$ we can write:

$$\frac{\partial \boldsymbol{u}}{\partial t} = -\frac{1}{\rho_0}\nabla p + B\boldsymbol{g}. \tag{1.47}$$

Here we have introduced a buoyancy parameter, $B = \frac{g/\rho'}{\rho_0}$, to the equation, requiring us to add another equation to solve the system, namely the buoyancy equation. The buoyancy equation arises from a combination of the equation of state of an ideal gas and the fundamental equation of thermodynamics and is given by (in the absence of diffusion):

$$\frac{\partial B}{\partial t} = \boldsymbol{u} \cdot \hat{\boldsymbol{g}} N^2, \tag{1.48}$$

where we have defined the Buoyancy frequency N^2 according to:

$$N^2 \equiv -\boldsymbol{g} \cdot \nabla \left(\frac{s}{c_p} \right) = -\boldsymbol{g} \cdot \nabla \left(\frac{p^{1/\gamma}}{\rho} \right), \tag{1.49}$$

where s is the entropy, c_p is the specific heat capacity at constant pressure and again γ is the adiabatic exponent. The resulting dispersion relation for IGWs is:

$$\omega^2 = \frac{N^2 k_\perp^2}{k^2}, \tag{1.50}$$

with $k_\perp^2 = k_x^2 + k_y^2$. This has the same kinds of consequences as the inertial wave dispersion relation; the IGWs can only exist when $|\omega| \leq N$ and their direction is fixed depending on the given values of ω and $N^2 > 0$. Like Eq. (1.45) we can write this dispersion relation using an angle compared to the z-axis in the system:

$$\omega^2 = N^2 \sin^2 \tilde{\theta}. \tag{1.51}$$

Inertia-Gravity Waves

In case both stratification and rotational effects are to be taken into account, i.e. in stably stratified regions of rotating fluid bodies, one obtains a dispersion relation arising from a combination of the above two dispersion relations:

$$\omega^2 = 4\Omega_s^2 \frac{k_z^2}{k^2} + \frac{N^2 k_\perp^2}{k^2} = 4\Omega_s^2 \cos^2 \tilde{\theta} + N^2 \sin^2 \tilde{\theta}. \tag{1.52}$$

In fact, this dispersion relation is also valid for convective modes in unstably stratified regions. In these regions N^2 can be thought of as negative instead of positive. Thus an inertial wave with a given $k = k_x, k_y, k_z$ will in general have a smaller frequency in convective regions than in neutrally stratified regions, assuming it can exist at all.

Both internal gravity waves and inertia-gravity waves are capable of creating wave attractors in closed domains like the inertial waves. However, while solid body rotation could be a decent approximation to first order for giant planets – ignoring the known differential rotation near the surface of both Jupiter and Saturn – the buoyancy frequency is far from constant, and thus the paths of internal gravity waves and inertia-gravity waves are likely to bend as can be seen in Fig. 1.8, but they can still form closed paths (Dintrans et al., 1999).

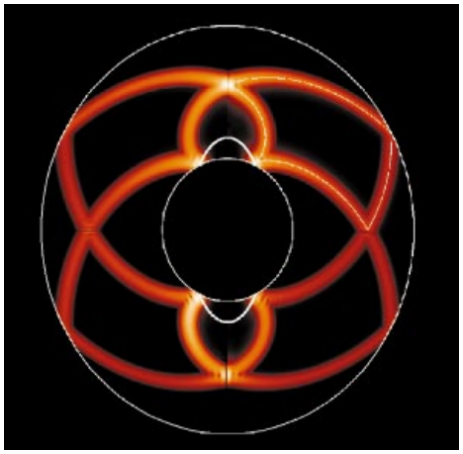

Figure 1.8: Wave attractors of inertia-gravity waves in a spherical shell. The presence of stratification and rotation results in curved wave paths, which can still form closed loops. Figure adapted from Dintrans et al. (1999).

1.5 Dissipation mechanisms of the equilibrium tide

This work will mainly focus on the dissipation of equilibrium tides; therefore we opt to only discuss these mechanisms here. A review of linear and non-linear dissipation mechanisms of the dynamical tide can be found in Ogilvie (2014). The dissipation mechanisms of the equilibrium tide can be further split into linear mechanisms, where the movement of the equilibrium tide flow is resisted by processes like viscosity, and non-linear mechanisms, where the equilibrium tidal flow itself becomes unstable due to resonances with the internal waves described previously. In this context, "non-linear" is used to denote mechanisms which require some finite tidal amplitude to be able to operate, but the instabilities acting upon the tidal flow themselves can be linear ones. The linear mechanism we will discuss in this thesis is the convective turbulence acting like a turbulent effective viscosity (since the microscopic kinematic viscosity is negligible), while the elliptical and precessional instabilities are the two non-linear mechanisms we will discuss.

1.5.1 Turbulent effective viscosity

The first concept of the dissipation of the equilibrium tide is the notion of a turbulent effective viscosity which arises within convective regions in planets and stars. The basic idea is a rather straightforward one: turbulence generated by convection will hinder the propagation of the equilibrium tide because the various rolls and eddies will remove energy from the tide, acting like a frictional process. The idea that it hinders the tide in a rather chaotic way then leads to the idea of parametrising it like a turbulent effective viscosity, or eddy viscosity, instead of trying to make predictions for the chaotic dissipation as a function of time. This idea was first proposed by Zahn (1966) and refined in Zahn (1989) and has been used to explain observations of tidal circularisation and decay. It was particularly successful for explaining binary circularisation in evolved stars (Verbunt & Phinney, 1995).

The idea for the parametrisation of this effective viscosity then arises by considering

a characteristic lengthscale of convection, l_c, and a characteristic velocity of the convective flow, u_c. These can both be estimated using so-called mixing-length theory (MLT), first developed by Prandtl (1925). The principles of MLT consider parcels that travel with this characteristic velocity over this lengthscale before exchanging all their energy to the rest of the flow. In essence, the mixing-length is akin to a mean free path for the parcel. If the lengthscale is short, it means the parcel diffuses rapidly and thus the mean free path is short. Using this parametrisation the effective viscosity is written as:

$$\nu_{\text{eff}} \propto u_c l_c. \tag{1.53}$$

This formula is often derived using dimensional analysis, and usually includes a somewhat arbitrary factor of 1/3. The effective viscosity that is derived in this manner gives rise to very efficient tidal dissipation. It should be noted that the validity of both MLT and the turbulent viscosity to parameterise these chaotic convective processes remains an open question, even though MLT is widely applied in for example 1D stellar evolution models to calculate heat transport and the turbulent viscosity or eddy viscosity is sometimes used to justify large viscosities in simulations. Verifying both of these in detailed studies is therefore of the essence.

Zahn's linear reduction

In addition to the uncertain applicability of the effective viscosity, the effective viscosity as defined in Eq. (1.53) is so large that it predicts orbital evolution on timescales much more rapid than what is currently observed in for example systems featuring planetary orbital decay. Fortunately, Zahn (1966) also devised an explanation why it is too large and should be reduced as a function of the tidal frequency for fast tides. This reduction hinges on the idea that the relevant timescales at play have not been considered in the argument above. One can think of tidal timescales, i.e. the tidal period, to be on the order of days (e.g. for Hot Jupiter orbits), while the convective turnover time, which one might consider as a convective timescale could be on the order of weeks in a star, or even a year or more in a Jupiter-like planet. Consequently, the interaction between the convective turbulence and the tide might be thought to only occur on a tidal timescale instead of the convective timescale. The idea for this reduction in efficiency according to Zahn (1966) can be described using MLT arguments. The idea hinges on the fact that within one tidal timescale, the convective parcel/eddy will only have travelled a distance of $l_c \cdot \tau_{\text{tide}}/\tau_c$. The tidal period τ_{tide} is related to the tidal frequency according to $\omega_{2,2,2} = 2\pi/\tau_{\text{tide}}$. Actually, the $l = m = n = 2$ equilibrium tide is quadrupolar, and as such one should consider the distance travelled in half the tidal timescale $\tau_{\text{tide}}/2$. Thus the considered lengthscale should be reduced according to:

$$\nu_{\text{eff}} \propto u_c l_c \frac{\tau_{\text{tide}}}{2\tau_c} = u_c l_c \frac{\omega_c}{2\omega}, \tag{1.54}$$

where we have defined the tidal frequency $\omega_c = u_c/l_c$ according to mixing-length theory. This is sometimes referred to as Zahn's linear reduction. Finally, the somewhat arbitrary factor of 1/3 is often included as the proportionality factor in these estimates. In summary:

$$\nu_{\text{eff}} = \begin{cases} \frac{1}{3}u_c l_c & \text{if} \quad \omega_c/2\omega > 1, \\ \frac{1}{3}u_c l_c \frac{\omega_c}{2\omega} & \text{if} \quad \omega_c/2\omega < 1. \end{cases} \tag{1.55}$$

The tidal timescales which satisfy the former are often referred to as "slow tides", while those that satisfy the latter are referred to as "fast tides". Expressions for u_c, l_c and ω_c will be derived in Ch. 4 using mixing-length theory and rotating mixing-length theory (RMLT), which is a correction to mixing-length theory in the presence of rotation based on Stevenson (1979).

Goldreich & Nicholson's quadratic reduction

More than a decade after Zahn first proposed his linear reduction, Goldreich and Nicholson (1977) – motivated by tides in Jupiter – produced their own reduction based on tidal and convective timescales. Instead of considering the timescale, lengthscale and velocity of a typical eddy or parcel interacting with the rapid tide, they hypothesised that the eddies with a timescale similar to the tidal timescale are the ones to interact with the tide. This however produces a number of consequences related to the lengthscale and velocity of the eddy. To this end they used Kolmogorov's scaling to state that an eddy with a given lengthscale λ has a velocity u_λ:

$$u_\lambda \sim u_c \left(\frac{\lambda}{l}\right)^{1/3}. \tag{1.56}$$

Furthermore, they stated that the associated frequency $\omega_\lambda = 2\pi/\tau_\lambda$ would be reduced according to:

$$\tau_\lambda \sim \tau_c \left(\frac{\lambda}{l}\right)^{2/3}. \tag{1.57}$$

Combining these two results in:

$$\nu_{\text{eff}} = \nu_\lambda = u_c l_c \left(\frac{\tau_\lambda}{\tau_c}\right)^2. \tag{1.58}$$

The argument above, stating that the eddies with turnover timescales similar to the tidal timescale should be considered then implies that $\tau_\lambda \approx \tau_{\text{tide}}$. This leads to:

$$\nu_{\text{eff}} \approx \begin{cases} \frac{1}{3}u_c l_c & \text{if} \quad \omega_c/2\omega > 1, \\ \frac{1}{3}u_c l_c \left(\frac{\omega_c}{\omega}\right)^2 & \text{if} \quad \omega_c/2\omega < 1. \end{cases} \tag{1.59}$$

This is referred to Goldreich and Nicholson's quadratic reduction. This reduction leads to much less efficient tidal dissipation for fast tides than Zahn's reduction, but recovers the same dissipation for slow tides.

Current consensus

Since large-scale numerical simulations became available, so has our ability to test theories like the crude ones described above. The first attempt to verify these scaling laws was made by Penev et al. (2007, 2009a, 2009b). They considered the interaction of convection with the tidal flow in a local Cartesian box model. In this work they used an oscillatory shear flow in the horizontal direction to represent the tidal flow, with gravity in the vertical direction. Some evidence was found for the linear reduction as predicted by Zahn. It should be noted that the tidal frequencies explored in these works are close to those of the convection, and thus do not allow for a large temporal separation between the tides and the convection.

Subsequently Ogilvie and Lesur (2012) performed an asymptotic analysis on this problem to identify more rigorous results originating from theory and to find scalings in regimes that were still unavailable to simulations. Contrasting to the result found in the simulations by Penev et al. (2009a), Ogilvie and Lesur (2012) obtained the quadratic reduction from their asymptotic analysis. Additionally, they performed simulations in a triply periodic Cartesian box of Boussinesq convection interacting with an oscillatory shear flow, which provided evidence to support a quadratic reduction. Further evidence for this quadratic reduction was found utilising an ABC flow in Braviner (2015).

Note however, that a triply periodic box allows for "elevator modes" (with no vertical variation) to arise within the flow. This is sometimes referred to as homogeneous convection, and is not always considered to be the most physically correct way to model convection. There is an alternative approach for convection, which is the introduction of walls at the top and bottom of the Cartesian box, commonly referred to as Rayleigh-Bénard Convection. This approach could also be considered unphysical, as it neither captures the physical boundaries of a spherical object properly, nor models a small section of a convection zone accurately, since there is a distinct absence of walls within convection zones of gaseous objects such as giant planets and stars. Nevertheless, this, in combination with stress-free boundary conditions, is often used in local approaches of convection modelling for simplicity and because it produces convection with well-behaved properties.

The effective viscosity was later revisited by Duguid et al. (2019, 2020) in non-rotating local Cartesian models using an oscillatory shear flow to represent the tidal flow and incorporating Rayleigh-Bénard Convection. They performed an extensive sweep of parameter space for both the convective driving as well as the tidal frequency. At high tidal frequencies evidence for the quadratic reduction was obtained, but an intermediate scaling was also retrieved when $\omega \approx \omega_c$, with a reduction according to $\omega^{-0.5}$. Incidentally, this work also analysed which size of eddy was most important in contributing to the effective viscosity. According to the Goldreich and Nicholson (1977) arguments, which these non-rotating works agree with in terms of scaling behaviour of the turbulent effective viscosity, the small-scale "resonant" eddies should be contributing most strongly. It was found however that it was in fact the large scales which most strongly contributed to the effective viscosity. So even though the end result of Goldreich and Nicholson (1977)

was confirmed, the arguments as to why are still up for debate – in terms of real understanding as opposed to asymptotic theory. Below we reproduce the scalings with fitted proportionality constants and regimes in which they are applicable as found in Duguid et al. (2020):

$$\nu_{\text{eff}} = \begin{cases} 5u_c l_c & \frac{|\omega|}{\omega_c} \lesssim 10^{-2}, \\ \frac{1}{2}u_c l_c \left(\frac{\omega_c}{\omega}\right)^{\frac{1}{2}} & \frac{|\omega|}{\omega_c} \in [10^{-2}, 5], \\ \frac{25}{\sqrt{20}}u_c l_c \left(\frac{\omega_c}{\omega}\right)^{2} & \frac{|\omega|}{\omega_c} \gtrsim 5. \end{cases} \tag{1.60}$$

At the same time, the effective viscosity was also revisited in the context of a global, idealised Boussinesq spherical model in Vidal and Barker (2020a, 2020b), both to avoid the choice of convective model and to allow a more realistic geometry and tidal flow. The trade-off of a global model is however that they are often more demanding in terms of computational resources, and therefore the parameter sweeps cannot be as extensive. Nevertheless, these global simulations also found evidence for the quadratic reduction with tidal frequency for fast tides. It should be noted however that for simulations where $\omega \approx \omega_c$ a reduction similar to the linear reduction was found, although possibly the exponent in these simulations was more in the range of $0.5 - 1$.

An alternate hypothesis

An alternative hypothesis on the topic of the effective viscosity damping equilibrium tides has been put forward in recent years by Terquem (2021). Motivation for this alternative hypothesis arises because the weak dissipation of equilibrium tides predicted by the Goldreich and Nicholson (1977) reduction for fast tides is unable to explain observations of binary circularisation. This hypothesis essentially flips the picture of frequency reductions above on its head. Instead of considering the timescale separation above to indicate the tidal flow as the rapid main flow, which is acted upon by convection on its slower timescale, this hypothesis postulates that the convective flow is the main flow based on a Reynolds decomposition based on timescales, i.e. the convection is the mean flow through which the tide flows as a fast perturbation. The tidal dissipation resulting from this theory is large (but not unreasonably large) and should therefore be considered as a mechanism worth exploring, to see whether the theory is correct and the mechanism is viable.

Note however that this hypothesis is very much in early development stages, akin to the heuristic arguments by Zahn (1966) and Goldreich and Nicholson (1977) above when these results were first published, since there are many unknowns still (particularly surrounding the temporary anti-dissipation which is reported on). Moreover, this mechanism is entirely absent from the works of Duguid et al. (2019, 2020) and Vidal and Barker (2020a, 2020b) due to the setup of their models. As such no detailed simulations have as of yet been done to confirm these results, except in Barker and Astoul (2021), which finds the term to be much less relevant than claimed by Terquem (2021) by several orders of

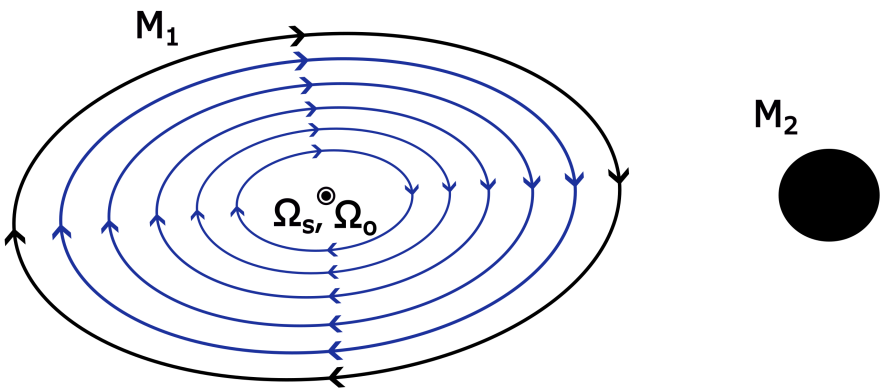

Figure 1.9: Schematic of the elliptical flow in body 1 viewed from above due to the tidal deformation in body 1 as a result of the tidal potential of body 2. Body 1 takes the shape of a triaxial ellipsoid due to the tidal deformation. The flow is constrained to surfaces parallel to the equator and the resulting stream lines shown in blue take elliptical shapes. These elliptical shapes of the flow allow for the elliptical instability. The effect of centrifugal distortion has been omitted in this schematic.

magnitude, such that it cannot act to significantly enhance dissipation of the equilibrium tides.

1.5.2 The elliptical instability

On the topic of non-linear tidal mechanisms – remembering that this refers to tidal mechanisms which require a finite tidal amplitude to operate – we start by discussing the elliptical instability (Kerswell, 2002). In the context of astrophysical tides, this instability arises because the $l = m = n = 2$ component of the equilibrium tide with associated tidal frequency $\omega_{2,2,2} = 2\Omega_o - 2\Omega_s$ takes an ellipsoidal shape around the planet, which rotates to follow the companion. As a result the flow and thus streamlines of the tidal flow around the planet are ellipses. This is demonstrated in the schematic of the tidally deformed planet in Fig. 1.9. The parameter to define the shape of this ellipsoid is in fact (proportional to) the tidal amplitude ϵ in Eq. (1.9). However, in the context of the elliptical instability it is referred to as the ellipticity.

In this thesis the elliptical instability will be studied in the context of astrophysics, but the elliptical instability itself has a long history of being studied simply as a fluid dynamical instability, both theoretically and experimentally. The first discovery in this direction was made by Crow (1970), who considered the three-dimensional stability of interacting vortices. In this work the Crow instability was discovered, which is an instability related to the elliptical instability. Simply put, the Crow instability requires two interacting vortices and produces a long wavelength in the axial direction (on the order of several vortex diameters) instability caused by the strain field of one vortex on the other. The elliptical instability on the other hand is more localised, concerned with disturbances in the vortex core of a strained vortex that has taken an elliptical shape, producing elliptical streamlines (Leweke et al., 2016). Shortly after the work of Crow (1970), Widnall et al. (1974) theorised that the elliptical instability could exist and Moore et al. (1975)

subsequently discovered it. At around roughly the same time, Gledzer et al. (1976) performed an experiment in a rotating elliptical cylinder, studying the vortex dynamics of such an elliptically deformed vortex. The instability observed in this study turned out to be exactly the one found theoretically in Moore et al. (1975), and was subsequently named the elliptical instability.

Later development considered the ideal model of an unbounded, inviscid, strained, i.e. elliptically deformed, vortex and the instabilities associated with it (Bayly, 1986; Pierrehumbert, 1986), which is exactly the type of flow shown in Fig. 1.9 (ignoring the boundaries in the schematic). The modification of the elliptical instability due to the introduction of viscosity was examined in Landman and Saffman (1987), who found inhibition at large wavenumbers, but no inherent modification of the instability. An important contribution came from Waleffe (1990), who elucidated the responsible mechanism: the elliptically deformed streamlines excite pairs of inertial waves through parametric resonances (e.g. Waleffe, 1990; Kerswell, 2002), in which the elliptical flow acts like a parent wave, transferring energy to the inertial waves as its two daughter waves. This leads to exponential growth of the amplitude of the inertial waves. Upon considering this instability in a tidal context, the energy transferred to the inertial waves is at the expense of energy in the tidal flow, and therefore at the expense of orbital or rotational energy (e.g. Barker et al., 2016). To allow this interaction – which is nothing more than a triadic resonance – the difference of the frequencies and wavenumbers of the daughter waves must add up to the frequency of the tidal "wave". As long as any retarding processes such as viscous damping can be overcome, an arbitrarily small elliptical deformation can then lead to instability (depending on γ – which we define in Ch. 2).

Later, progress started being made on understanding the non-linear evolution of the instability. The instability was observed to emerge in experiments, showing the expected inertial waves. Once saturation of the linear instability was reached the excited inertial waves started producing smaller and smaller scale waves and finally collapsed to rotating turbulence. The turbulence typically dissipates over time, leading to the flow becoming unstable again (e.g. Malkus, 1989; Le Bars et al., 2010; Schaeffer & Le Dizès, 2010; Barker & Lithwick, 2013, 2014; Favier et al., 2015; Barker, 2016a; Le Reun et al., 2017, 2019). It was found in numerical simulations that inertial waves are always unstable (D. Mason & Kerswell, 1999)[1], and will continue collapsing to smaller and smaller scales. The collapse to turbulence either occurs via weak "inertial wave turbulence" (Malkus, 1989; Barker & Lithwick, 2014; Le Reun et al., 2017, 2019), or rotating turbulence involving large-scale geostrophic vortices or zonal flows (Barker & Lithwick, 2013; Favier et al., 2015; Barker, 2016a; Grannan et al., 2017; Le Reun et al., 2017, 2019). The inertial wave turbulence (involving a sea of weakly interacting inertial waves) may occur when the forcing amplitude is weak (Le Reun et al., 2019; Astoul & Barker, 2022), or when geostrophic modes are

[1]There are two works we will cite in this thesis, one with first author D. Mason, which is the work cited here, the other with first author R. Mason, both with second author Kerswell. These works are on very similar topics and published very soon after one another, so it would be easy to think they have the same first author based on in-text citations alone. For clarification we will include the first initial of the first author in the in-text citations of these works.

suppressed, either by artificial frictional damping (Le Reun et al., 2017) or via an external process such as the imposition of a magnetic field (Barker & Lithwick, 2014).

As mentioned above, the elliptical instability finds application as a possible tidal dissipation mechanism in stars and planets (Rieutord, 2004; Cébron et al., 2010; Le Bars et al., 2010; Cébron et al., 2012; Barker & Lithwick, 2013; Cébron et al., 2013; Ogilvie, 2014; Barker, 2016a), extracting energy from the equilibrium tide. This however requires careful consideration of the dynamics of the elliptical instability, particularly the properties of the turbulence which is expected, as well as its interaction with other processes in the system, such as magnetic fields or (stable or unstable) stratification (Le Reun et al., 2018).

The elliptical instability has been studied previously in simulations using a local Cartesian box model both with (Barker & Lithwick, 2014) and without (Barker & Lithwick, 2013) weak magnetic fields. The latter study found that the elliptical instability leads to "bursty" behaviour, involving the interaction of instability-generated inertial waves with geostrophic columnar vortical flows produced by their non-linear interactions. Irregular cyclic "predator-prey behaviour" was obtained in which the elliptical instability first excited inertial waves, these interacted non-linearly to produce vortices that inhibited further growth of waves until these vortices were damped sufficiently by viscosity, thereby enabling further growth of the waves. Similar behaviour features in global hydrodynamical simulations of the elliptical instability (Barker, 2016a), where zonal flows take the place of columnar vortices in the predator-prey dynamics. Upon taking magnetic fields into account in the local model, the behaviour changed from bursts to a sustained energy input into the flow, as magnetic fields served to break up or prevent formation of strong vortices (Barker & Lithwick, 2014). Similar sustained behaviour is observed if the vortices are damped by an artificial frictional force mimicking Ekman friction on no-slip boundaries (Le Reun et al., 2017).

The elliptical instability and convection

The elliptical instability was analysed in the convective regions of planetary (or stellar) interiors, but did not incorporate convection explicitly (except perhaps by motivating a choice of viscosity if this is due to turbulence). However, convection can potentially interact with the elliptical instability in a number of ways. Firstly, we might imagine that smaller-scale turbulent convective eddies could act like an effective viscosity not just on the equilibrium tide but also on these larger-scale inertial waves, damping them and inhibiting or reducing the growth rate of the elliptical instability. Secondly, convection under the influence of rotation is known to generate mean flows (zonal flows or vortices), and these flows could also interact with those generated by the elliptical instability.

This interaction of the elliptical instability with convection has been studied within linear theory (e.g. Kerswell, 2002; Le Bars & Le Dizès, 2006), experimentally in cylindrical containers (Lavorel & Le Bars, 2010) and using idealised laminar global simulations in a triaxial ellipsoid (Cébron et al., 2010). These studies illustrate that the elliptical instability can modify heat transport, though they did not focus on the dissipation of tidal flows which

is one of our primary aims. The dimensionless heat transport is usually represented by the Nusselt number (Nu), which is a measure of the ratio of the total heat flux to the conductive flux (i.e. with no transport by fluid motions), as a function of the Rayleigh number (Ra), the dimensionless ratio of buoyancy driving to viscous and thermal damping, which measures the strength of convective driving. The Nusselt number was observed to be increased by the elliptical instability for Rayleigh numbers close to and below the value required for onset of convection. It was also observed to be larger than one even with stable stratification ($\mathrm{Ra} < 0$), indicating that the elliptical instability can contribute to heat transport in this regime also.

1.5.3 The precessional instability

The precessional instability, like the elliptical instability, is a non-linear tidal dissipation mechanism that arises due to an instability associated with a component of the equilibrium tide. However, for the precessional instability it is not the tidal deformation as a result of the $l = m = n = 2$ component of the tide that generates a flow that becomes unstable. Instead, a centrifugally deformed planet with misaligned rotation axis to the orbital axis results in gravitational forces (i.e. tidal forces) that cause the spin axis to rotate around a secondary rotation axis. This spin-orbit misalignment, also called obliquity, is responsible for two more components of the tide: $l = 2,\ m = 1,\ n = 0$ and $l = 2,\ m = 1,\ n = 2$ with associated tidal frequencies $\omega_{2,1,0} = -\Omega_s$ and $\omega_{2,1,2} = 2\Omega_o - \Omega_s$. The former is static in the inertial frame, i.e. the frame not rotating with the planet, and essentially causes bulk precessional motion of the star or planet. It is this component of the obliquity tide that we will focus on. These precessional flows within solid boundaries are described by the laminar flow solution known as the Poincaré solution (Poincaré, 1910). This laminar solution is unstable to the precessional instability, which allows turbulence to arise (Kerswell, 1993).

This instability is excited because the precessional tidal flow is confined to planes inclined to the equator with an angle which depends on the rotation rate of precession, misalignment angle and oblateness of the body. Because the body is oblate this results in two interesting consequences which can be seen in the schematic in Fig. 1.10. Firstly, the planes inclined with respect to the equator in an oblate body are elliptical in shape, thus this flow can be unstable to the elliptical instability itself. The inclination of the planes can be quite small however, and the oblateness is usually presumed small as well, e.g. the largest known oblateness within the Solar System is that of Saturn with a value of 0.098, so this effect is typically quite weak. Secondly, the line connecting the centres of these planes is not perpendicular to the planes and therefore the centres of these planes are sheared with respect to one another. This oscillatory shear results in a shearing instability (Kerswell, 1993) which, like the elliptical instability, can excite inertial waves through a parametric resonance. It is in fact this part of the instability that is usually considered to be the most relevant, especially for objects with small oblateness.

The behaviour of the precessional instability is very similar to that of the elliptical instability, so much so that they are often mentioned together (Kerswell, 2002; Le Bars

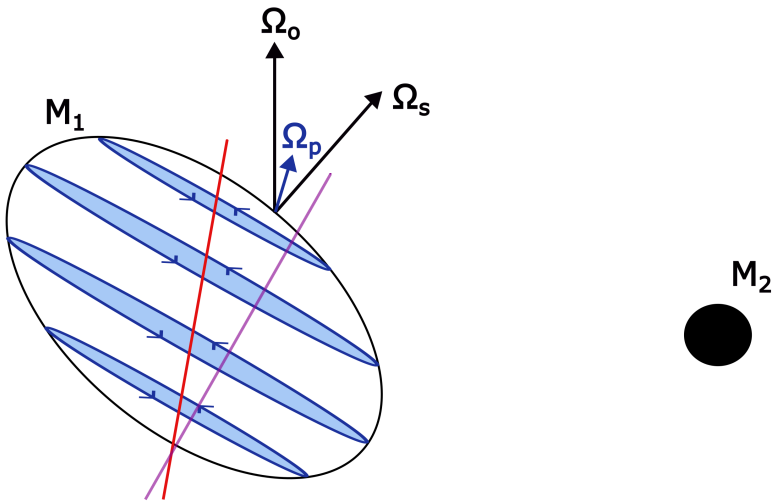

Figure 1.10: Schematic of the flow in body 1 due to the precession of its spin axis as a result of the tidal potential of body 2. Body 1 takes the shape of an oblate spheroid due to centrifugal distortion caused by its own rotation. The spin-orbit misalignment present in the system then causes the spin axis to precess about the orbit normal. The resulting precessional flow is portrayed in blue; these flows are inclined with respect to both the precession and spin axis, as indicated by the normal to the surfaces in purple. These flows take an elliptical shape because they cut through the oblate spheroid at an angle inclined to the equator. The line connecting the centres of these flow surfaces is indicated in red, and demonstrates a shear between the flow surfaces. The tidal deformation which is responsible for the elliptical instability has been omitted in this schematic for illustrative purposes.

et al., 2015). The precessing flow, like the elliptical flow, excites pairs of inertial waves through a parametric resonance, and these inertial waves grow exponentially. The linear instability saturates, producing small-scale inertial waves which finally collapse to rotating turbulence after which the cycle starts anew like the elliptical instability. This effect has been observed in simulations of the precessional instability executed in a Cartesian shearing box model with periodic boundaries (Barker, 2016b) and in spheroidal shells with stress-free boundaries (Lorenzani & Tilgner, 2003).

Precession and the associated precessional instability has received a fair share of attention as it was found to produce sustained turbulence in the fluid in realistic spherical (Tilgner & Busse, 2001) or spheroidal geometries (Lorenzani & Tilgner, 2001, 2003). As such it is thought that the precessional instability could power a dynamo in for example the Earth's core (Malkus, 1968; Kerswell, 1996; Tilgner, 2005; Wu & Roberts, 2008; Le Bars et al., 2015). Furthermore, it has application as a tidal mechanism as it is thought to result in spin-orbit alignment, i.e. evolution of the spin-orbit angle so that the equatorial and orbital planes coincide (Le Bars et al., 2015; Barker, 2016a). The shearing instability part of the precessional instability can be studied in isolation by considering a local box approach in which the streamlines are circular, but vertically sheared. The entire box is rotating around the spin axis and the rotation of precession is represented by a secondary rotation perpendicular to the spin axis, with rotation rate $\Omega_p = \mathrm{Po}\Omega_s$. The parameter Po is the Poincaré number and indicates how fast precession occurs compared to the spin

rotation; in analogy to the elliptical instability this parameter is sometimes also denoted by ϵ. This unbounded approach is documented in Kerswell (1993), presenting an initial linear instability analysis. This local shearing instability approach to precession has been taken in various papers (Barker, 2016b; Pizzi et al., 2022; Kumar et al., 2024) reproducing some of the results found in spheroidal geometries: it excites inertial waves, like the elliptical instability, generates vortices, like the elliptical instability, and as a result sees intermittent activation. Its exact operation was examined numerically in Pizzi et al. (2022), studying the transfers of energy. They identified two different regimes, one where the vortex is completely dominant in the simulation at low Poincaré number, and one where the inertial waves contribute meaningfully at higher Po. Furthermore, the precessional instability was studied in tandem with weak magnetic fields as well, which show that just this aspect of the precessional flow and its instability can indeed act as a dynamo (Barker, 2016b; Kumar et al., 2024).

Intriguingly, work has been done to study the possibility of wave attractors arising due to precession. It was found that indeed the inertial waves as generated from these instabilities in a spherical shell can generate wave attractors (Hollerbach & Kerswell, 1995; Noir et al., 2001). The chosen geometry is therefore of importance to the precessional instability, and one can expect it to be equally important to the elliptical instability.

The precessional instability and convection

The precessional instability interacting with convection has received less attention than the elliptical instability interacting with convection. The interaction was however studied using a linear stability analysis in cylindrical geometry in Benkacem et al. (2022), and using simulations in spheroidal objects in Wei and Tilgner (2013). The former found that the instability is slightly enhanced for weak convection, and is suppressed for strong convection. The latter found that indeed the precessional instability is enhanced for weak convection, allowing it to onset where it previously could not. Furthermore, it was found that convection can onset at weaker convective driving when weak precession is present. With strong precession it requires stronger convective driving to onset. Finally, in a similar fashion to the elliptical instability it was found that the precession can cause additional heat transport compared to convection in isolation.

In terms of the local Cartesian box approach, this interaction has not yet been studied. However, the evolution of the precessional instability in isolation together with walls in the vertical direction has been studied in R. Mason and Kerswell (2002)[2] and Wu and Roberts (2008), finding that the introduction of these walls imposes a mode selection constraint on the precessional instability. In fact this mode selection constraint forces a distinct growth rate on each set of inertial waves which are able to resonate and grow and reduces the maximum growth rate compared to expectations from the unbounded analysis.

[2]The second of the papers with first author Mason, second author Kerswell; this one with first author R. Mason

One might then expect a number of interesting effects similar to the elliptical instability. Again an effective viscosity might arise to damp the inertial waves; the convective mean flows might interact with the instability. Furthermore, in this particular geometry, the presence of convection, or stratification in general, might affect the mode selection constraint. The most unstable modes could become a function of the buoyancy frequency and rotation rate. Moreover, it is highly likely the growth rate of the instability will be affected by the stratification based on the linear analysis of Benkacem et al. (2022) even though their model does not include walls. Finally, at high enough values of the Poincaré number, it is possible that this additional precessional rotation axis influences the convection and modifies or even prevents the formation of mean flows.

1.6 Research Aims

The effectiveness of the above tidal mechanisms is still poorly understood, particularly when considering the interaction of the elliptical and precessional instabilities with convection. There is strong motivation to study these interactions because these instabilities are expected to arise in convective regions. Indeed, we wish to study these interactions in a clear and concise manner, without any effects due to for example a spherical geometry. Therefore we take the local box approach for both instabilities with stress-free walls at the top and bottom of our model to accommodate Rayleigh-Bénard convection.

There are numerous questions that then arise from the introduction of convection to the elliptical and precessional instabilities. We have outlined some of these questions below:

- Will convection act to enhance the elliptical/precessional instability, or will it suppress it?
- Can the elliptical/precessional instability influence convection and modify the heat transport?
- How will the changes in behaviour impact our predictions for tidal dissipation and tidal quality factors in Hot Jupiters and binary stars? Can we derive scaling laws to make estimates about real astrophysical systems?

Additionally, we wish to study the effective viscosity described above, which interacts with our tidal flows. Questions which we hope to answer are:

- Will the interactions of the convection with the tidal flow, that can be parameterised with a turbulent effective viscosity, arise in our simulations?
- Does the effective viscosity match Zahn's linear reduction or Goldreich and Nicholson's quadratic reduction?
- Can we use (R)MLT to derive scaling laws for the convective velocity, lengthscale and turnover time in our simulations?

- Will the effective viscosity match the (R)MLT predictions applied to the effective viscosity reduction in the simulations?
- Will the extrapolated effective viscosity contribute meaningfully to tidal dissipation in giant planets or will it be inefficient as previously predicted?

To answer these questions we will execute numerous simulations, which will be verified using linear stability analyses. The setup of our local Cartesian box model with stress-free impermeable walls at the top and bottom will be detailed in Ch. 2. In addition to the setup of the model, we will detail the properties of the elliptical instability and, for the first time, derive the linear growth rate of the elliptical instability after the introduction of walls at the top and bottom of the local Cartesian box. Furthermore, we will detail Rayleigh-Bénard convection in this chapter. In Ch. 3 we will study the behaviour of the elliptical instability interacting with the convection in the numerical simulations. Here we will endeavour to answer the questions related to the behaviour of the elliptical instability in the presence of convection as well as examining whether the convection acts as a turbulent effective viscosity on the tidal flow in these simulations. Following on from the studies on the behaviour of the interactions, in Ch. 4 we will attempt to quantify the dissipation in our simulations due to both the elliptical instability under the influence of convection as well as the turbulent effective viscosity, should it be present, and derive scaling laws for both as well as the relevant convective quantities, i.e. the convective velocity, lengthscale and frequency.

In Ch. 5 we pivot to the precession problem. In this chapter we will detail the properties of the precessional instability, as well as presenting, for the first time, the associated linear stability analysis in the presence of stratification after the introduction of the walls. In Ch. 6 we will study the interactions of the precessional instability with convection in our simulations, attempting to constrain how the precessional instability and the precession itself interact with the convection. In addition, we will seek to derive scaling laws for the tidal dissipation due to the precessional instability and effective viscosity, if present. Having obtained the scaling laws for the tidal dissipation due to both the elliptical and precessional instability and effective viscosity, if present, we will apply these to 1D models of the interiors of (Hot) Jupiter-like planets to derive timescales of tidal evolution in Ch. 7. Finally, in Ch. 8 we will summarise all our findings.

Chapter 2

Theoretical background of the elliptical instability and convection

Before we can start answering the research questions regarding the elliptical instability interacting with convection posed in Ch. 1, we must dive a little deeper into the origins of the elliptical instability. To this end we first discuss the form the background tidal flow takes in a local model of a giant planet or star. Next, we present the linear stability analysis of the elliptical instability with walls at the top and bottom and deduce the characteristics of the instability, such as the most unstable mode and growth rate. We will then discuss rotating convection and its associated linear stability analysis. Finally we derive the quantities of interest in our system such as the kinetic energy and tidal energy injection rate. From here we detail the SNOOPY code utilised for this work and the numerical methods employed. Once these have been covered we test that we do indeed retrieve the linear growth rates as expected in the simulations. Finally, we discuss the parameters we will vary in this study as well as the resolutions we employ for the simulations.

2.1 The elliptical instability

2.1.1 The background tidal flow

The elliptical instability originates from the elliptical streamlines of the tidal flow corresponding to the "asynchronous tide", i.e. the $l = m = n = 2$ component of the tide, within a rotating planet or star. This component of the tide is quadrupolar, and therefore the tidal frequency is twice the rotation rate of the tidal flow, because the equivalent to "high tide" passes by an observer located on the body twice during one rotation period of the flow. The tidal frequency is $\omega_{2,2,2} = 2(\Omega_o - \Omega_s)$, and thus the rotation rate of this flow, in what is known as the bulge frame, is given by $\gamma = (\Omega_o - \Omega_s)$. In the literature for the elliptical instability the orbital rotation rate is sometimes denoted by n while the spin rotation rate is denoted by Ω, and $\gamma = \Omega - n$ (Barker & Lithwick, 2013), which differs by a minus sign compared to the previous definition of $\gamma = (\Omega_o - \Omega_s)$. We will adopt

the conventions used in Barker and Lithwick (2013) in the rest of this thesis. Using these definitions, the bulge frame is the frame rotating at the rate n about the axis of rotation of the planet. The tidal flow, which we treat as a background flow $\tilde{\boldsymbol{U}}_0$ present in our system, in this frame takes the form (Barker & Lithwick, 2013):

$$\tilde{\boldsymbol{U}}_0 = \gamma \begin{pmatrix} 0 & -(1+\epsilon) & 0 \\ 1-\epsilon & 0 & 0 \\ 0 & 0 & 0 \end{pmatrix} \tilde{\boldsymbol{x}}, \tag{2.1}$$

where $\tilde{\boldsymbol{x}}$ represents the position vector from the centre of the planet. In the frame rotating with the planet at the rate Ω, it can be written alternatively as:

$$\boldsymbol{U}_0 = \mathrm{A}\boldsymbol{x} = -\gamma\epsilon \begin{pmatrix} \sin(2\gamma t) & \cos(2\gamma t) & 0 \\ \cos(2\gamma t) & -\sin(2\gamma t) & 0 \\ 0 & 0 & 0 \end{pmatrix} \boldsymbol{x}, \tag{2.2}$$

where $\boldsymbol{x}$ now represents the position vector from the centre of the planet in the frame rotating with the planet. This description represents the exact $l = m = n = 2$ component of the equilibrium tide of a uniformly rotating incompressible fluid body perturbed by a companion on a circular aligned orbit (Chandrasekhar, 1967; Barker et al., 2016), but approximates the main features of the equilibrium tide in more realistic models described previously (Terquem et al., 1998; Ogilvie, 2013; Barker, 2020). We choose to work in the frame rotating with the planet, so that Eq. (2.2) describes the tidal flow. As described briefly in Sec. 1.5.2, the elliptical instability operates because the background flow given in Eq. (2.2) acts like a parent wave with zero wavenumber, i.e. a steady oscillator that oscillates with an amplitude of $\gamma\epsilon$, that can achieve a triadic resonance with two daughter inertial waves, resulting in a parametric instability.

2.1.2 Governing equations and setup of the problem

In this work we have chosen to work in a local Cartesian box model – which can be thought to represent a small patch of a planet or star (see Fig. 2.1) – and we will build upon the previous works of Barker and Lithwick (2013, 2014) and Le Reun et al. (2017) to study the interaction of the elliptical instability with convection in this model, focusing on the resulting tidal dissipation. Our local model allows for higher resolution studies, which in turn allows us to reach more turbulent regimes than e.g. Cébron et al. (2010) and Lavorel and Le Bars (2010), as well as providing the cleanest way to study the instability with minimal effects from the chosen boundaries of the container.

We model the convective instability using Rotating Rayleigh-Bénard Convection (RRBC). RRBC is chosen as it is the simplest model of rotating convection (Chandrasekhar, 1961) which allows us to study its interaction with the elliptical instability. In this setup two impermeable walls are introduced at the top and bottom of the local box, to avoid "homogeneous convection". At these walls or plates the temperature is fixed and in the case of convection the bottom plate is hotter while the top plate is cooler. This

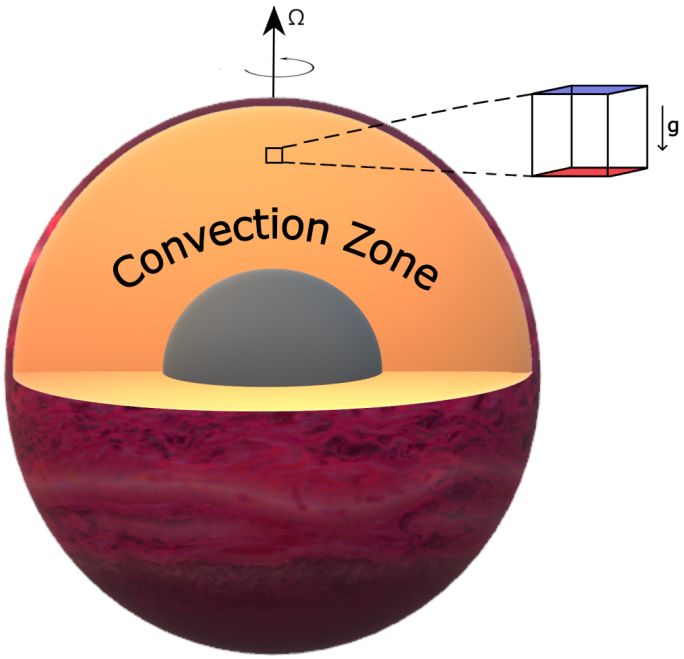

Figure 2.1: Location of the local box in the convection zone of a Hot Jupiter, indicating the rotation axis and the temperature gradient represented by the red (hot) and blue (cold) sides of the box. Gravity is chosen in the vertical direction in the box.

introduces a vertical temperature difference and therefore a density difference to the flow. Upon choosing the direction of gravity, which is chosen to be the vertical direction, we find that gravity will act on this density difference, generating a buoyancy force and thus allowing convective motions to occur.

In addition to modelling convection using RRBC, we employ the Boussinesq approximation (Spiegel & Veronis, 1960). The crux of this approximation is to consider small density variations – compared to some reference density – in the studied system. In particular, the density variations are neglected in every term bar the buoyancy term. The philosophy behind this choice is that the buoyancy force generated by gravity acting on the density variations can still be large, even if the density variations themselves are small. Using the Boussinesq approximation is justified if and only if the two required conditions are satisfied: 1) flows are much slower than the sound speed, $u \ll c_s$, which is a condition that is also present in the anelastic approximation and 2) the vertical size of the domain d is much smaller than a pressure or density scale height, $d \ll H_p$. A local system that only considers a small section of the astrophysical body can justifiably use this approximation, as density is not expected to change much if the size of the chosen system is small enough. Any large-scale variations of the properties of a planet, such as density and temperature, as a function of radius cannot be captured when this approximation is employed. Moreover, large-scale circulations spanning a full convection zone of multiple density scale heights cannot be modelled using this approximation. The advantage of this approximation is however that computation and analysis is massively eased, both because density variations can be neglected and because the continuity equation is reduced to the

incompressibility condition, eliminating sound waves in the system:

$$\nabla \cdot \boldsymbol{u} = 0. \tag{2.3}$$

In addition to choosing the temperature gradient and gravity in the vertical direction, we also choose the rotation axis to be vertical, as indicated in Fig. 2.1. The box in the current setup thus represents a polar region, because the local rotation and gravity vectors are either aligned or anti-aligned (depending on the sign of Ω). The dimensions of this box are $[L_x, L_y, d]$ with $L_x = L_y = Ld$. The boundary conditions in the horizontal directions are periodic, while in the vertical direction they are impermeable, $u_z(z = 0) = u_z(z = d) = 0$, and stress-free, $\partial_z u_x(z = 0) = \partial_z u_x(z = d) = \partial_z u_y(z = 0) = \partial_z u_y(z = d) = 0$. The combination of the Boussinesq approximation and the stress-free impermeable walls implies that this local model thus represents a single convection cell (or mixing-length) in the vertical. Boundary conditions in the vertical for the temperature perturbation are assumed to be perfectly conducting, i.e., $\theta(z = 0) = \theta(z = d) = 0$.

We start from the full Navier-Stokes equations for RRBC under the Boussinesq approximation. In these equations we represent the total velocity $\boldsymbol{U} = \boldsymbol{U}_0 + \boldsymbol{u}$ as the addition of the background flow and the velocity perturbation $\boldsymbol{u} = (u_x, u_y, u_z)$ and the total pressure $P_{\rm tot} = P(z) + p$ as the background pressure $P(z)$ obtained from hydrostatic balance, with a contribution from background flow to be steady, and the pressure perturbation p. This equation is presented together with the heat equation – with total temperature $T_{\rm tot} = T(z) + \theta$ as the addition of the background temperature profile $T(z)$ and the temperature perturbation θ – and the incompressibility condition:

$$\frac{\mathrm{D}\boldsymbol{U}}{\mathrm{D}t} + 2\Omega\hat{\boldsymbol{z}} \times \boldsymbol{U} = -\frac{1}{\rho_0}\nabla P_{\rm tot} + \alpha g T_{\rm tot}\hat{\boldsymbol{z}} + \nu\nabla^2\boldsymbol{U} + \boldsymbol{\mathcal{F}}, \tag{2.4}$$

$$\frac{\mathrm{D}T_{\rm tot}}{\mathrm{D}t} = \kappa\nabla^2 T_{\rm tot}, \tag{2.5}$$

$$\nabla \cdot \boldsymbol{U} = 0, \tag{2.6}$$

where

$$\frac{\mathrm{D}}{\mathrm{D}t} \equiv \frac{\partial}{\partial t} + \boldsymbol{U} \cdot \nabla. \tag{2.7}$$

In these equations ρ_0 is the reference density, g is the local gravitational acceleration (assumed constant), α is the (constant) thermal expansion coefficient, ν is the viscosity, κ is the thermal diffusivity and $\boldsymbol{\mathcal{F}}$ is the tidal forcing responsible for perfectly maintaining the background flow $\boldsymbol{U}_0$. If we consider a local box of vertical dimension d the conduction state or background temperature profile $T(z)$ can be derived by considering the heat equation in a background stationary state ($\boldsymbol{u} = 0,\ \partial_t T = 0$) and employing the boundary

conditions that $T(z=0)=T_0$ and $T(z=d)=T_0-\Delta T$:

$$\begin{aligned}\boldsymbol{U}_0\cdot\nabla T &= \kappa\nabla^2 T,\\ \Rightarrow 0 &= \frac{\mathrm{d}^2}{\mathrm{d}z^2}T.\end{aligned} \tag{2.8}$$

The term $\boldsymbol{U}_0\cdot\nabla T$ vanishes because $\boldsymbol{U}_0$ is purely horizontal. The resulting temperature profile can then be written, using the boundary conditions, as:

$$T(z)=T_0-\frac{\Delta T}{d}z. \tag{2.9}$$

Without loss of generality T_0 is set to zero, so the temperature at the bottom (hot plate, typically) is $T(z=0)=0$, while the temperature at the top (cold plate) is $T(z=d)=N^2/(\alpha g)$, such that the temperature difference is $\Delta T=-N^2/\alpha g$ and the temperature gradient is:

$$T=\frac{N^2}{\alpha g d}z. \tag{2.10}$$

A negative value of N^2 corresponds to a positive ΔT and thus a hot plate at the bottom and a cold plate at the top, which is the setup that can be unstable to convection, and is referred to as unstable stratification. When choosing N^2 as positive, corresponding to the hot plate at the top and cold plate at the bottom, this is referred to as stable stratification instead as it is stable to convection.

Now considering the above governing equations and eliminating all terms that satisfy the background state we are left with:

$$\frac{\mathrm{D}\boldsymbol{u}}{\mathrm{D}t}+\boldsymbol{u}\cdot\nabla\boldsymbol{U}_0+2\Omega\hat{\boldsymbol{z}}\times\boldsymbol{u}=-\frac{1}{\rho_0}\nabla p+\alpha g\theta\hat{\boldsymbol{z}}+\nu\nabla^2\boldsymbol{u}, \tag{2.11}$$

$$\frac{\mathrm{D}\theta}{\mathrm{D}t}-u_z\frac{\Delta T}{d}=\kappa\nabla^2\theta, \tag{2.12}$$

$$\nabla\cdot\boldsymbol{u}=0, \tag{2.13}$$

where

$$\frac{\mathrm{D}}{\mathrm{D}t}\equiv\frac{\partial}{\partial t}+\boldsymbol{U}_0\cdot\nabla+\boldsymbol{u}\cdot\nabla. \tag{2.14}$$

We can now non-dimensionalise by scaling all instances of a lengthscale in the above equations with the vertical domain size d (distance between the plates), scaling all timescales using the corresponding thermal timescale d^2/κ, thus scaling velocities with κ/d, pressures with $\rho_0\kappa^2/d^2$, and finally scaling temperature with ΔT (i.e. by the temperature difference between the plates). The governing equations for the dimensionless velocity and temperature perturbations $\boldsymbol{u}$ and θ to the background flow $\boldsymbol{U}_0$ and conduction state temperature profile $T(z)$ in the Boussinesq approximation, in a frame rotating at the rate Ω about the z-axis, are then:

$$\frac{\mathrm{D}\boldsymbol{u}}{\mathrm{D}t} + \boldsymbol{u}\cdot\nabla\boldsymbol{U}_0 + \frac{\mathrm{Pr}}{\mathrm{Ek}}\hat{\boldsymbol{z}}\times\boldsymbol{u} = -\nabla p + \mathrm{RaPr}\theta\hat{\boldsymbol{z}} + \mathrm{Pr}\nabla^2\boldsymbol{u}, \tag{2.15}$$

$$\nabla\cdot\boldsymbol{u} = 0, \tag{2.16}$$

$$\frac{\mathrm{D}\theta}{\mathrm{D}t} - u_z = \nabla^2\theta. \tag{2.17}$$

In these equations we have introduced multiple non-dimensional parameters to describe our system, which are the Rayleigh number:

$$\mathrm{Ra} = \frac{\alpha g\Delta T d^3}{\nu\kappa}, \tag{2.18}$$

which describes the ratio of convective driving to viscous and thermal diffusive effects, the Ekman number (ratio of viscous to Coriolis terms):

$$\mathrm{Ek} = \frac{\nu}{2\Omega d^2}, \tag{2.19}$$

and the Prandtl number:

$$\mathrm{Pr} = \nu/\kappa, \tag{2.20}$$

which describes the ratio of viscosity to thermal diffusivity. Note that we can relate the dimensional buoyancy frequency N^2 to the Rayleigh number according to $N^2 = -\mathrm{Ra}\,\mathrm{Pr}\,\kappa^2/(\alpha g d^4)$, so that when $\mathrm{Pr} = 1$, the dimensionless value (in thermal time units, where $d^2/\kappa = 1$) is $N^2 = -\mathrm{Ra}$. The background tidal flow also introduces the dimensionless ellipticity ϵ and the tidal rotation rate γ in our chosen units. We will fix the Prandtl number in the rest of this thesis to reduce the number of executed parameter sweeps and thus computational costs. We choose to set $\mathrm{Pr} = 1$ for consistency with the previous works we will build on e.g. Cébron et al. (2010), Wei and Tilgner (2013), Barker et al. (2014), and Guervilly et al. (2014).

2.1.3 Analytical derivation for the linear growth rate

From these governing equations we can determine the growth rates of the two instabilities present within the system: the elliptical instability and the convective instability. The growth rate of the elliptical instability is well known in isolation (Kerswell, 2002), and that of rotating convection in our chosen geometry is well studied (Chandrasekhar, 1961). We will treat the derivation of these instabilities in isolation; it is expected, from previous works, that the influence of one instability on the other is to slightly modify the growth rate but not to lead to any fundamental changes (Kerswell, 2002). What might however lead to changes of the behaviour of the elliptical instability is the introduction of stress-free walls. As such, we will derive the growth rate of the elliptical instability in this geometry. To this end, we adapt the method described in R. Mason and Kerswell (2002), which was originally employed to derive the growth rate of the precessional instability in the same geometry, which we will summarise in Ch. 5.

The elliptical instability in the presence of stress-free walls

The elliptical instability is a parametric instability and so one can not simply find the dispersion relation and deduce the growth rate of the instability from there; instead we must employ asymptotics to find how the two daughter inertial waves grow from the resonance between the tidal flow $\boldsymbol{U}_0$ and these waves. One can think of the tidal flow as a "wave" with frequency 2γ, as seen from Eq. (2.2), completing the three way interaction, known as a triadic resonance, needed for this parametric instability. We start from the momentum equation Eq. (2.11), neglecting all temperature terms:

$$\frac{\partial \boldsymbol{u}}{\partial t} + \boldsymbol{U}_0 \cdot \nabla \boldsymbol{u} + \boldsymbol{u} \cdot \nabla \boldsymbol{U}_0 + \boldsymbol{u} \cdot \nabla \boldsymbol{u} + 2\Omega \hat{\boldsymbol{z}} \times \boldsymbol{u} = -\nabla p + \nu \nabla^2 \boldsymbol{u}. \tag{2.21}$$

We linearise this equation and set the viscosity to 0. We know that the main effect of viscosity is to introduce a reduction to the final growth rate of $-\nu k^2$, where k is the wavenumber magnitude (Kerswell, 2002), thus we can safely omit it from this calculation and include the reduction later. All terms containing the small parameter ϵ, in this case contained within $\boldsymbol{U}_0$, are moved to the RHS of the equation and all terms without ϵ to the LHS:

$$\frac{\partial \boldsymbol{u}}{\partial t} + 2\Omega \hat{\boldsymbol{z}} \times \boldsymbol{u} + \nabla p = -\boldsymbol{U}_0 \cdot \nabla \boldsymbol{u} - \boldsymbol{u} \cdot \nabla \boldsymbol{U}_0. \tag{2.22}$$

We can work out the products $\boldsymbol{U}_0 \cdot \nabla \boldsymbol{u}$ and $\boldsymbol{u} \cdot \nabla \boldsymbol{U}_0$ and write them both in matrix form. For clarity and brevity we write $\mathcal{C} \equiv \cos(2\gamma t)$, $\mathcal{S} \equiv \sin(2\gamma t)$:

$$\begin{aligned} -\boldsymbol{U}_0 \cdot \nabla \boldsymbol{u} &= \gamma\epsilon \begin{pmatrix} \mathcal{S}x + \mathcal{C}y \\ \mathcal{C}x - \mathcal{S}y \\ 0 \end{pmatrix} \cdot \begin{pmatrix} \partial_x \\ \partial_y \\ \partial_z \end{pmatrix} \boldsymbol{u}, \\ &= \gamma\epsilon \begin{pmatrix} (\mathcal{S}x + \mathcal{C}y)\partial_x + (\mathcal{C}x - \mathcal{S}y)\partial_y & 0 & 0 \\ 0 & (\mathcal{S}x + \mathcal{C}y)\partial_x + (\mathcal{C}x - \mathcal{S}y)\partial_y & 0 \\ 0 & 0 & (\mathcal{S}x + \mathcal{C}y)\partial_x + (\mathcal{C}x - \mathcal{S}y)\partial_y \end{pmatrix} \boldsymbol{u}, \end{aligned} \tag{2.23}$$

$$\begin{aligned} -\boldsymbol{u} \cdot \nabla \boldsymbol{U}_0 &= \gamma\epsilon (u_x \partial_x + u_y \partial_y + u_z \partial_z) \begin{pmatrix} \mathcal{S}x + \mathcal{C}y \\ \mathcal{C}x - \mathcal{S}y \\ 0 \end{pmatrix}, \\ &= \gamma\epsilon \begin{pmatrix} \mathcal{S}u + \mathcal{C}v \\ \mathcal{C}v - \mathcal{S}v \\ 0 \end{pmatrix} = \gamma\epsilon \begin{pmatrix} \mathcal{S} & \mathcal{C} & 0 \\ \mathcal{C} & -\mathcal{S} & 0 \\ 0 & 0 & 0 \end{pmatrix} \boldsymbol{u} = -\mathrm{A}\boldsymbol{u}. \end{aligned} \tag{2.24}$$

These can be rewritten using Euler's formula:

$$\sin(2\gamma t) = -\frac{\mathrm{i}}{2}(\mathrm{e}^{\mathrm{i}2\gamma t} - \mathrm{e}^{-\mathrm{i}2\gamma t}), \qquad \cos(2\gamma t) = \frac{1}{2}(\mathrm{e}^{\mathrm{i}2\gamma t} + \mathrm{e}^{-\mathrm{i}2\gamma t}),$$

obtaining for the RHS of Eq. (2.22):

$$-\boldsymbol{U}_0 \cdot \nabla \boldsymbol{u} - \boldsymbol{u} \cdot \nabla \boldsymbol{U}_0 = \epsilon \left(\mathrm{e}^{\mathrm{i}2\gamma t} \mathcal{L} + \mathrm{e}^{-\mathrm{i}2\gamma t} \mathcal{L}^* \right) \boldsymbol{u}, \tag{2.25}$$

with

$$\mathcal{L} = \frac{\gamma}{2} \begin{pmatrix} -\mathrm{i} + (-\mathrm{i}x + y)\partial_x + (x + \mathrm{i}y)\partial_y & 1 & 0 \\ 1 & \mathrm{i} + (-\mathrm{i}x + y)\partial_x + (x + \mathrm{i}y)\partial_y & 0 \\ 0 & 0 & (-\mathrm{i}x + y)\partial_x + (x + \mathrm{i}y)\partial_y \end{pmatrix}. \tag{2.26}$$

We rewrite Eq. (2.22) as:

$$\frac{\partial \boldsymbol{u}}{\partial t} + 2\Omega\hat{\boldsymbol{z}} \times \boldsymbol{u} + \nabla p = \epsilon \left(\mathrm{e}^{\mathrm{i}2\gamma t}\mathcal{L} + \mathrm{e}^{-\mathrm{i}2\gamma t}\mathcal{L}^*\right)\boldsymbol{u}, \tag{2.27}$$

together with incompressibility condition $\nabla \cdot \boldsymbol{u} = 0$ and the boundary conditions: $u_z(z = 0) = u_z(z = 1) = 0$. Setting $\epsilon = 0$ returns the inertial wave problem (Greenspan, 1968). Using our chosen boundary conditions the real part of the eigenmodes of inertial waves takes the form:

$$\begin{bmatrix} u_x \\ u_y \\ u_z \\ p \end{bmatrix} = \begin{bmatrix} k^2(k_x\lambda - 2\mathrm{i}k_y\Omega)\cos(n\pi z)/4\Omega^2k_\perp^2 \\ k^2(k_y\lambda + 2\mathrm{i}k_x\Omega)\cos(n\pi z)/4\Omega^2k_\perp^2 \\ -\mathrm{i}k_z\sin(n\pi z)/\lambda \\ \cos(n\pi z) \end{bmatrix} \mathrm{e}^{\mathrm{i}(k_x x + k_y y + \lambda t)}, \tag{2.28}$$

where the amplitude of the pressure perturbation is chosen as 1 without loss of generality. The total, horizontal and vertical wavenumber of each eigenmode are given by $k^2 = k_x^2 + k_y^2 + k_z^2$, $k_\perp^2 = k_x^2 + k_y^2$ and $k_z = n\pi$ respectively, which satisfy the dispersion relation for the frequency λ:

$$\lambda = \pm\frac{2\Omega k_z}{k}. \tag{2.29}$$

This dispersion relation is the same as presented in Eq. (1.45) and it, together with the eigenmodes, tells us how the daughter waves behave, but does not shed any light on the growth of their amplitudes due to the elliptical instability. To study the amplitude growth we examine the behaviour at $\mathcal{O}(\epsilon)$ instead. We follow R. Mason and Kerswell (2002) and, using the method of multiple timescales, introduce a slow timescale $\tau = \epsilon t$ such that variables are assumed to depend on the fast timescale t_0 and slow timescale τ, i.e. $\boldsymbol{u} = \boldsymbol{u}(t_0, \tau)$. The time derivative becomes:

$$\frac{\partial}{\partial t} = \frac{\partial}{\partial t_0} + \epsilon\frac{\partial}{\partial \tau}. \tag{2.30}$$

Like R. Mason and Kerswell (2002) we will consider the linear combination of two inertial waves A and B, each with its own k_x, k_y, k_z and thus λ. These waves each have associated amplitudes A and B, which should only grow on the slow timescale τ. We can thus represent the perturbation velocity field $\boldsymbol{u}$ as these two inertial waves in addition to an unspecified correction $\boldsymbol{u}_1$ at $\mathcal{O}(\epsilon)$:

$$\boldsymbol{u} = A(\tau)\boldsymbol{u}_A(\boldsymbol{x})\mathrm{e}^{\mathrm{i}\lambda_A t} + B(\tau)\boldsymbol{u}_B(\boldsymbol{x})\mathrm{e}^{\mathrm{i}\lambda_B t} + \epsilon\boldsymbol{u}_1(\boldsymbol{x}, t) + \mathcal{O}(\epsilon^2). \tag{2.31}$$

Using this expression in Eq. (2.27) and keeping only terms of $\mathcal{O}(\epsilon)$ we find:

$$\begin{aligned} \frac{\partial \boldsymbol{u}_1}{\partial t_0} + 2\Omega\hat{\boldsymbol{z}} \times \boldsymbol{u}_1 + \nabla p_1 =& A\left(\mathrm{e}^{\mathrm{i}(\lambda_A+2\gamma)t}\mathcal{L} + \mathrm{e}^{\mathrm{i}(\lambda_A-2\gamma)t}\mathcal{L}^*\right)\boldsymbol{u}_A(\boldsymbol{x}) \\ &+ B\left(\mathrm{e}^{\mathrm{i}(\lambda_B+2\gamma)t}\mathcal{L} + \mathrm{e}^{\mathrm{i}(\lambda_B-2\gamma)t}\mathcal{L}^*\right)\boldsymbol{u}_B(\boldsymbol{x}) \\ &- A_\tau\boldsymbol{u}_A\mathrm{e}^{\mathrm{i}\lambda_A t} - B_\tau\boldsymbol{u}_B\mathrm{e}^{\mathrm{i}\lambda_B t}, \end{aligned} \tag{2.32}$$

where p_1 is the correction to the pressure at $\mathcal{O}(\epsilon)$, $A_\tau = \frac{\mathrm{d}A}{\mathrm{d}\tau}$ and $B_\tau = \frac{\mathrm{d}B}{\mathrm{d}\tau}$. Then we define the inner product under which these inertial waves are orthogonal (R. Mason & Kerswell, 2002):

$$\langle \boldsymbol{u}, \boldsymbol{v} \rangle \equiv \lim_{L\to\infty} \frac{1}{L^2} \int_{-L/2}^{L/2} \int_{-L/2}^{L/2} \int_0^1 \boldsymbol{u}^* \cdot \boldsymbol{v} \, \mathrm{d}z \, \mathrm{d}y \, \mathrm{d}x. \tag{2.33}$$

We then take the inner product of Eq. (2.32) with the first wave $\boldsymbol{u}_A$: $\langle A\boldsymbol{u}_A \mathrm{e}^{\mathrm{i}\lambda_A t}, \text{Eq. (2.32)} \rangle$. This inner product with the LHS of Eq. (2.32) leads to secular growth, and thus we demand non-secularity, therefore obtaining an expression similar to the one found in R. Mason and Kerswell (2002) for precession:

$$\begin{aligned} 0 = \langle \boldsymbol{u}_A, & A\left(\mathrm{e}^{\mathrm{i}(\lambda_A-\lambda_A+2\gamma)t}\mathcal{L} + \mathrm{e}^{\mathrm{i}(\lambda_A-\lambda_A-2\gamma)t}\mathcal{L}^*\right)\boldsymbol{u}_A(\boldsymbol{x}) \\ & + B\left(\mathrm{e}^{\mathrm{i}(\lambda_B-\lambda_A+2\gamma)t}\mathcal{L} + \mathrm{e}^{\mathrm{i}(\lambda_B-\lambda_A-2\gamma)t}\mathcal{L}^*\right)\boldsymbol{u}_B(\boldsymbol{x}) \\ & - A_\tau \boldsymbol{u}_A \mathrm{e}^{\mathrm{i}(\lambda_A-\lambda_A)t} - B_\tau \boldsymbol{u}_B \mathrm{e}^{\mathrm{i}(\lambda_B-\lambda_A)t} \rangle. \end{aligned} \tag{2.34}$$

Again, any secular term must vanish, therefore upon removing all terms that are time-dependent, we retain:

$$A_\tau \langle \boldsymbol{u}_A(\boldsymbol{x}), \boldsymbol{u}_A(\boldsymbol{x}) \rangle = B \langle \boldsymbol{u}_A(\boldsymbol{x}), \left(\mathrm{e}^{\mathrm{i}(\lambda_B-\lambda_A+2\gamma)t}\mathcal{L} + \mathrm{e}^{\mathrm{i}(\lambda_B-\lambda_A-2\gamma)t}\mathcal{L}^*\right)\boldsymbol{u}_B(\boldsymbol{x}) \rangle. \tag{2.35}$$

Thus if we want a non-trivial solution we require that $\lambda_B = \lambda_A \pm 2\gamma$. Choosing $\lambda_B = \lambda_A + 2\gamma$ and continuing to follow the same derivation pattern as in R. Mason and Kerswell (2002) yields:

$$A_\tau \langle \boldsymbol{u}_A(\boldsymbol{x}), \boldsymbol{u}_A(\boldsymbol{x}) \rangle = B \langle \boldsymbol{u}_A(\boldsymbol{x}), \mathcal{L}^* \boldsymbol{u}_B(\boldsymbol{x}) \rangle, \tag{2.36}$$

$$B_\tau \langle \boldsymbol{u}_B(\boldsymbol{x}), \boldsymbol{u}_B(\boldsymbol{x}) \rangle = A \langle \boldsymbol{u}_B(\boldsymbol{x}), \mathcal{L} \boldsymbol{u}_A(\boldsymbol{x}) \rangle. \tag{2.37}$$

There exist growing solutions of the form $(A, B) = (A_0, B_0)\mathrm{e}^{\sigma\Omega\epsilon t}$, which implies that $(A_\tau, B_\tau) = \sigma\Omega(A, B)$ with growth rate:

$$\sigma^2\Omega^2 = \frac{\langle \boldsymbol{u}_A(\boldsymbol{x}), \mathcal{L}^*\boldsymbol{u}_B(\boldsymbol{x}) \rangle \langle \boldsymbol{u}_B(\boldsymbol{x}), \mathcal{L}\boldsymbol{u}_A(\boldsymbol{x}) \rangle}{\langle \boldsymbol{u}_A(\boldsymbol{x}), \boldsymbol{u}_A(\boldsymbol{x}) \rangle \langle \boldsymbol{u}_B(\boldsymbol{x}), \boldsymbol{u}_B(\boldsymbol{x}) \rangle}. \tag{2.38}$$

We start working out these inner products by calculating $\langle \boldsymbol{u}_A(\boldsymbol{x}), \mathcal{L}^*\boldsymbol{u}_B(\boldsymbol{x}) \rangle$:

$$\boldsymbol{u}_A^*(\boldsymbol{x}) \cdot \mathcal{L}^*\boldsymbol{u}_B(\boldsymbol{x}) = \boldsymbol{u}_A^* \cdot \frac{\gamma}{2} \begin{pmatrix} \mathrm{i}u_{B,x} + (\mathrm{i}x + y)\partial_x u_{B,x} + (x - \mathrm{i}y)\partial_y u_{B,x} + u_{B,y} \\ u_{B,x} - \mathrm{i}u_{B,y} + (\mathrm{i}x + y)\partial_x u_{B,y} + (x - \mathrm{i}y)\partial_y u_{B,y} \\ (ix + y)\partial_x u_{B,z} + (x - \mathrm{i}y)\partial_y u_{B,z} \end{pmatrix}, \tag{2.39}$$

$$\begin{aligned} = \frac{\gamma}{2} \Big[& \mathrm{i}u_{A,x}^* u_{B,x} + \mathrm{i}k_{B,x}(\mathrm{i}x + y)u_{A,x}^* u_{B,x} + \mathrm{i}k_{B,y}(x - iy)u_{A,x}^* u_{B,x} \\ & + u_{A,x}^* u_{B,y} + u_{A,y}^* u_{B,x} - \mathrm{i}u_{A,y}^* u_{B,y} \\ & + \mathrm{i}k_{B,x}(\mathrm{i}x + y)u_{A,y}^* u_{B,y} + \mathrm{i}k_{B,y}(x - \mathrm{i}y)u_{A,y}^* u_{B,y} \\ & + ik_{B,x}(\mathrm{i}x + y)u_{A,z}^* u_{B,z} + \mathrm{i}k_{B,y}(x - \mathrm{i}y)u_{A,z}^* u_{B,z} \Big]. \end{aligned} \tag{2.40}$$

From this expression we see that the products between $\boldsymbol{u}_A^*$ and $\boldsymbol{u}_B$ take five general forms: $u_{A,x}^* u_{B,x}$, $u_{A,x}^* u_{B,y}$, $u_{A,y}^* u_{B,x}$, $u_{A,y}^* u_{B,y}$ and $u_{A,z}^* u_{B,z}$. In the first four of these products the integral over z will take the form of:

$$\int_0^1 \cos(n_A \pi z)\cos(n_B \pi z)\,\mathrm{d}z = \begin{cases} 1/2 & \text{if } n_A = \pm n_B, \\ 0 & \text{else.} \end{cases} \tag{2.41}$$

Thus these terms vanish unless $n_A = n_B$ or $n_A = -n_B$. The fifth term $u_{A,z}^* u_{B,z}$ takes the form of:

$$\int_0^1 \sin(n_A \pi z)\sin(n_B \pi z)\,\mathrm{d}z = \begin{cases} 1/2 & \text{if } n_A = n_B, \\ -1/2 & \text{if } n_A = -n_B, \\ 0 & \text{else.} \end{cases} \tag{2.42}$$

Clearly, these integrals enforce $n_A = |n_B|$ on all terms, providing information about the required vertical wavenumbers for resonance. Additionally, for this computation they all introduce a factor of $\frac{1}{2}$. The x and y dependence of all components of $\boldsymbol{u}(\boldsymbol{x})$ are equal and therefore the integrals over x and y under consideration are:

$$\frac{1}{2L^2}\int_{-L/2}^{L/2}\int_{-L/2}^{L/2} \mathrm{e}^{-\mathrm{i}(k_{A,x}x + k_{A,y}y)}\mathrm{e}^{\mathrm{i}(k_{B,x}x + k_{B,y}y)}\,\mathrm{d}y\,\mathrm{d}x = 1/2, \tag{2.43}$$

$$\frac{1}{2L^2}\int_{-L/2}^{L/2}\int_{-L/2}^{L/2} x\mathrm{e}^{-\mathrm{i}(k_{A,x}x + k_{A,y}y)}\mathrm{e}^{\mathrm{i}(k_{B,x}x + k_{B,y}y)}\,\mathrm{d}y\,\mathrm{d}x = 0, \tag{2.44}$$

$$\frac{1}{2L^2}\int_{-L/2}^{L/2}\int_{-L/2}^{L/2} y\mathrm{e}^{-\mathrm{i}(k_{A,x}x + k_{A,y}y)}\mathrm{e}^{\mathrm{i}(k_{B,x}x + k_{B,y}y)}\,\mathrm{d}y\,\mathrm{d}x = 0. \tag{2.45}$$

Integrating these three expressions will always reduce to zero unless $k_{A,x} = k_{B,x}$ and $k_{A,y} = k_{B,y}$, in which case all exponentials cancel, which is what we have assumed in Eq. (2.43). If the exponentials cancel, the last two integrals still vanish because an odd function is integrated over a symmetric interval. The volume integrals therefore always reduce to a factor $\pm 1/2$ provided the required resonance conditions of the daughter waves are satisfied: (1) $n_A = \pm n_B$, (2) $k_{A,x} = k_{B,x} = k_x$ and $k_{A,y} = k_{B,y} = k_y$, (3) $\lambda_B = \lambda_A + 2\gamma$. Requirements (1) and (2) together result in further conditions $k_{A,\perp} = k_{B,\perp} = k_\perp$ and $k_A = k_B = k$. Furthermore, requirements (1) and (2) imply that $\lambda_B = -\lambda_A$ and thus combined with requirement (3) $\lambda_B = -\lambda_A = \gamma$. Combining all this, we know that the only terms in Eq. (2.40) that are non-zero after integration are:

$$\langle \boldsymbol{u}_A(\boldsymbol{x}), \mathcal{L}^*\boldsymbol{u}_B(\boldsymbol{x})\rangle = \frac{1}{2}\left(\mathrm{i}\hat{u}_{A,x}^*\hat{u}_{B,x} - \mathrm{i}\hat{u}_{A,y}^*\hat{u}_{B,y} + \hat{u}_{A,x}^*\hat{u}_{B,y} + \hat{u}_{A,y}^*\hat{u}_{B,x}\right), \tag{2.46}$$

where the hatted quantities denote only the constant factors of the inertial wave eigenmodes in Eq. (2.28). Upon working out this product and a little algebra:

$$\langle \boldsymbol{u}_A(\boldsymbol{x}), \mathcal{L}^*\boldsymbol{u}_B(\boldsymbol{x})\rangle = \frac{k^4\gamma}{64\Omega^4 k_\perp^4}\left(-2k_x k_y + \mathrm{i}[k_y^2 - k_x^2]\right)(3\Omega - n)^2. \tag{2.47}$$

Likewise we find for the other inner product in the numerator:

$$\langle \boldsymbol{u}_B(\boldsymbol{x}), \mathcal{L}\boldsymbol{u}_A(\boldsymbol{x})\rangle = \frac{k^4\gamma}{64\Omega^4 k_\perp^4}\left(-2k_xk_y - \mathrm{i}[k_y^2 - k_x^2]\right)(3\Omega - n)^2, \tag{2.48}$$

which is the complex conjugate of Eq. (2.47). We retrieve the same expressions for the terms in the denominator as obtained in R. Mason and Kerswell (2002):

$$\langle \boldsymbol{u}_A(\boldsymbol{x}), \boldsymbol{u}_A(\boldsymbol{x})\rangle = \frac{k^4}{4\Omega^2 k_\perp^2}, \qquad \langle \boldsymbol{u}_B(\boldsymbol{x}), \boldsymbol{u}_B(\boldsymbol{x})\rangle = \frac{k^4}{4\Omega^2 k_\perp^2}, \tag{2.49}$$

Combining Eq. (2.47), Eq. (2.48) and Eq. (2.49), we find for the growth rate:

$$\sigma^2\Omega^2 = \gamma^2\frac{9^2}{16^2}\frac{(3\Omega - n)^4}{9^2\Omega^4}. \tag{2.50}$$

Finally we obtain for the growth rate:

$$\sigma\Omega = \frac{9}{16}\gamma\frac{(3\Omega - n)^2}{9\Omega^2} = \frac{9}{16}\gamma\frac{(3\gamma + 2n)^2}{9(\gamma + n)^2}. \tag{2.51}$$

The growth rate in this final expression is the same as that of the elliptical instability in the triply periodic case (Kerswell, 2002) and thus the introduction of walls has not modified the growth rate of the elliptical instability. From our definitions of $\boldsymbol{u}_A$ and $\boldsymbol{u}_B$ we can then write that the velocity field grows according to:

$$\boldsymbol{u} = (A_0\boldsymbol{u}_A\mathrm{e}^{-\mathrm{i}\gamma t} + B_0\boldsymbol{u}_B\mathrm{e}^{\mathrm{i}\gamma t})\mathrm{e}^{\sigma\Omega\epsilon t}. \tag{2.52}$$

Note that the expression obtained in Eq. (2.51) is multiplied by ϵ to obtain the growth rate of the amplitude. The elliptical instability is always active – if such waves exist that satisfy the resonance conditions – in the absence of viscosity; there is no critical value of ϵ that must be exceeded for it to operate. This however is in the inviscid limit; upon including viscosity one finds an additional leading order correction to the growth of the velocity of $\mathrm{e}^{-\nu k^2 t}$ (Kerswell, 2002), which can be readily seen by rederiving the eigenmodes in Eq. (2.28) starting from the governing equations with viscosity included. The solution for the velocity perturbation $\boldsymbol{u}$ at this order with viscosity included is given by:

$$\boldsymbol{u} = (A_0\boldsymbol{u}_A\mathrm{e}^{-\mathrm{i}\gamma t} + B_0\boldsymbol{u}_B\mathrm{e}^{\mathrm{i}\gamma t})\mathrm{e}^{(\sigma\Omega\epsilon - \nu k^2)t}. \tag{2.53}$$

Rotating convection

We can also find the growth rate of the convective instability; this however is a better known problem than the elliptical instability and therefore we only highlight the key details. We start from the dispersion relation of rotating convection (Chandrasekhar,

1961):

$$s^3 + As^2 + Bs + C = 0, \tag{2.54}$$

where A, B, C are given by:

$$A = (2\mathrm{Pr} + 1)k^2, \tag{2.55}$$

$$B = k^4\mathrm{Pr}(\mathrm{Pr} + 2) - \mathrm{RaPr}\frac{k_\perp^2}{k^2} + \mathrm{Pr}^2\frac{k_z^2}{l^2\mathrm{Ek}^2}, \tag{2.56}$$

$$C = (-\mathrm{Ra}a^2 + \frac{k_z^2}{\mathrm{Ek}^2} + k^6)\mathrm{Pr}^2. \tag{2.57}$$

This dispersion relation is cubic and will therefore allow three real solutions for s, those solutions with a positive real part are convectively unstable and will have growing amplitudes, or one real and two complex solutions. If the solutions are complex the behaviour is referred to as oscillatory. We are interested in the real solutions, because – at our chosen $Pr = 1$ – the associated steady modes become unstable first and are the fastest growing.

Onset of the convective instability is achieved when $s = 0$, which implies that C must be zero. From this one can determine the criterion for instability for a perturbation with a given wavenumber:

$$\mathrm{Ra} = \frac{(k_z^2 + k_\perp^2)^3 + \frac{k_z^2}{\mathrm{Ek}^2}}{k_\perp^2}, \tag{2.58}$$

with $k_\perp^2 = k_x^2 + k_y^2$ the horizontal wavenumber and $k_z = n\pi$ the vertical wavenumber. The minimal value of this Rayleigh number for instability in our local box model can be obtained by setting $k_z = \pi$ and minimising with respect to $k_\perp$. One then obtains in the asymptotic limit $\mathrm{Ek} \ll 1$:

$$k_{\perp,c} \sim \left(\frac{\pi^2}{2}\right)^{\frac{1}{6}} \mathrm{Ek}^{-\frac{1}{3}}, \qquad \mathrm{Ra}_c \sim 3\left(\frac{\pi^2}{2}\right)^{\frac{2}{3}} \mathrm{Ek}^{-\frac{4}{3}}, \tag{2.59}$$

with $k_{\perp,c}$ the critical perpendicular wavenumber for which the critical Rayleigh number, Ra_c, of the instability is minimised. However, as Ra is increased beyond this critical value the most unstable mode will change away from the critical wavenumber. We must instead numerically solve the dispersion relation in Eq. (2.54) to find the most unstable mode and subsequent growth rate of the instability at every value of Ra. Equally, if the Ekman number is not very small, the relations in Eq. (2.59) above are not accurately satisfied and instead Eq. (2.58) is minimised directly and solved to obtain the critical Rayleigh number.

2.1.4 Known properties of the elliptical instability and convection

The linear properties of the elliptical instability have been reviewed by Kerswell (2002), but are also illustrated by the linear instability analysis performed above. The instability operates when two inertial waves have frequencies which differ by approximately the tidal frequency 2γ, represented by the condition that $\lambda_B = \lambda_A \pm 2$. In the short wavelength limit, this occurs for two waves with frequencies $\lambda = \pm\gamma$. The two inertial waves must

also have the same vertical and horizontal wavenumbers. Finally, the inertial waves in question must, by definition, each satisfy the dispersion relation for inertial waves. This leads to the further constraint that $\gamma = \pm 2\Omega k_z/k$, in the absence of stratification.

The elliptical instability is further influenced by de-tuning of the most unstable modes as well as convection. The effects of these on the elliptical instability in the unbounded case can also be found in the review by Kerswell (2002). De-tuning is used to refer to any waves that do not satisfy the resonance conditions exactly, which reduces the maximum growth rate. De-tuning of the waves also interacts with the effects of viscosity, and the reduction of the growth rate due to both effects together could be enhanced or reduced compared to either effect in isolation. Finally, if an (un)stable stratification (aligned with the rotation axis) is present the expression for the growth rate of the unbounded elliptical instability – for small ϵ – is further modified according to (Kerswell, 2002):

$$\sigma\Omega = \frac{9}{16}\gamma\frac{4(3\gamma+2n)^2(\gamma^2-N^2)}{9\gamma^2(4(\gamma+n)^2-N^2)}. \tag{2.60}$$

Both the effects of unstable stratification (negative N^2) and stable stratification (positive N^2) can be computed using this equation. We observe that stable stratification typically inhibits the linear growth of the elliptical instability, but that unstable stratification typically enhances the growth rate. One can consider the dispersion relation of inertia-gravity waves in Eq. (1.52) to determine which combinations of N^2, γ and Ω are allowed such that inertia-gravity waves can exist. Upon requiring that $\omega = \gamma$ in the dispersion relation, as these are the frequencies of the waves excited by the elliptical instability, one finds that three cases arise. If $4\Omega^2 > \gamma^2$, the dispersion relation requires that $N^2 \leq \gamma^2$ and thus $N^2 < 4\Omega^2$. Next, if $4\Omega^2 < \gamma^2$, it requires that $N^2 \geq \gamma^2$ and thus $N^2 > 4\Omega^2$. Finally, if $4\Omega^2 = \gamma^2$ there are no constraints on N^2. The first two cases imply that the growth rate obtained from Eq. (2.60) is always positive, and the latter case implies that the growth rate becomes independent of the buoyancy frequency when $4\Omega^2 = \gamma^2$ because $4(\gamma+n)^2 = 4\Omega^2 = \gamma^2$. All three cases ensure that the growth rate in Eq. (2.60) does not go to infinity.

In an astrophysical context, in the absence of stratification, the elliptical instability is furthermore affected by the rotation of the primary body around the companion, and thus the rotation of the elliptical bulge, because it modifies the growth rate depending on the rotation speed n (Craik, 1989). The growth rate is decreased for most values of n (e.g. see Fig. 1 in Barker & Lithwick, 2013), and it cannot operate in the interval $n = [-\frac{3}{2}\gamma, -\frac{1}{2}\gamma]$. In this interval no inertial waves exist that satisfy the dispersion relation. In the interval $n = [-\frac{1}{2}\gamma, 0]$ the growth rate is increased, though everywhere else it is decreased, over the case with $n = 0$. For clarity of presentation $\gamma = \Omega$ is chosen in the rest of this work, resulting in $n = 0$, strictly representing the unphysical scenario where the body in question is not rotating around its companion which causes the tidal effects. This implies that the bulge is therefore not rotating around the body. As a result of setting $\gamma = \Omega$

the dispersion relation of the most unstable mode reduces to $k_z/k = \pm\frac{1}{2}$. The elliptical instability then grows at a rate proportional to $\gamma\epsilon$. Although this scenario is unphysical indeed, it turns out that for simulations the only linear effects of choosing a different value of Ω, and therefore a non-zero value of n, would be to modify the growth rate of the elliptical instability (Barker & Lithwick, 2013) as well as the wavenumber of the most unstable mode (Barker & Lithwick, 2014).

As previously described, the non-linear evolution of the elliptical instability – in the absence of magnetic fields – results in large geostrophic vortices in the flow in local Cartesian box models such as ours. Thus we expect that our non-linear simulations should show these large geostrophic vortices if the elliptical instability operates. Interestingly, in RRBC simulations in a local Cartesian box model large-scale vortex (LSV) structures also emerge in the flow when rotation dominates (Favier et al., 2014b; Guervilly et al., 2014; Rubio et al., 2014). This LSV emerges with stress-free impermeable walls at the top and bottom, i.e. our chosen boundary conditions, and grows to the size of the box in the horizontal. One of the effects of this convectively-generated LSV is to reduce heat transport, as the vertical convective motions are suppressed by such a vortex (Guervilly et al., 2014). An additional reason to study convective LSVs is that the elliptical instability is naturally suppressed by the presence of its own non-linearly generated large vortex (Barker & Lithwick, 2013). The convective LSV might suppress the elliptical instability in the same manner, potentially preventing it from operating efficiently.

2.1.5 Energetic analysis of simulations

To analyse the energy of the flow and determine the quantities of interest in our simulations we derive a kinetic energy equation by taking the scalar product with $\boldsymbol{u}$ of Eq. (2.15) and then averaging over the box. We define our averaging operation on a quantity X here as $\langle X\rangle = \frac{1}{L^2 d}\int_V X \,\mathrm{d}V$. Note that this definition is different compared to the one in Eq. (2.33). We obtain:

$$\frac{\mathrm{d}}{\mathrm{d}t}K = -\langle \boldsymbol{u}\cdot(\boldsymbol{u}\cdot\nabla\boldsymbol{U}_0)\rangle - \langle \boldsymbol{u}\cdot(\boldsymbol{U}_0\cdot\nabla\boldsymbol{u})\rangle + W_B - D_\nu. \tag{2.61}$$

The term associated with the Coriolis force has vanished because $\boldsymbol{u}\cdot(\hat{\boldsymbol{z}}\times\boldsymbol{u}) = 0$, the well known result that the Coriolis force does no work. In addition we have defined the mean kinetic energy:

$$K \equiv \frac{1}{2}\langle|\boldsymbol{u}|^2\rangle, \tag{2.62}$$

the work done by buoyancy:

$$W_B \equiv \mathrm{PrRa}\langle\theta u_z\rangle, \tag{2.63}$$

and the mean viscous dissipation rate

$$D_\nu \equiv -\mathrm{Pr}\langle\boldsymbol{u}\cdot\nabla^2\boldsymbol{u}\rangle. \tag{2.64}$$

These three terms are well known as they arise from considering the energy equation of rotating convection. The two remaining terms which are newly introduced due to the background flow on the RHS of Eq. (2.61) shall be individually addressed, starting with the $-\langle \boldsymbol{u} \cdot (\boldsymbol{u} \cdot \nabla \boldsymbol{U}_0) \rangle$ term, which we will rewrite by using Eq. (2.24):

$$I \equiv -\langle \boldsymbol{u} \mathrm{A} \boldsymbol{u} \rangle = -\langle \boldsymbol{u} \cdot (\boldsymbol{u} \cdot \nabla \boldsymbol{U}_0) \rangle, \tag{2.65}$$

where we have defined this term as the energy injection rate or more generally the energy transfer rate I. This term is the one responsible for injecting energy from the tidal flow to the local inertial waves (and vice versa) and therefore allowing the elliptical instability to operate. Equally, if there is a contribution of the tidal flow acting on the convection or the convection acting on the tidal flow that energy transfer will also be contained within this term.

The second term on the RHS of Eq. (2.61) can be rewritten using various vector calculus identities:

$$\langle -\boldsymbol{u} \cdot (\boldsymbol{U}_0 \cdot \nabla \boldsymbol{u}) \rangle = -\langle \boldsymbol{U}_0 \cdot \frac{1}{2} \nabla |\boldsymbol{u}|^2 \rangle = -\langle \frac{1}{2} [\nabla \cdot (\boldsymbol{U}_0 |\boldsymbol{u}|^2) - |\boldsymbol{u}|^2 (\nabla \cdot \boldsymbol{U}_0)] \rangle. \tag{2.66}$$

The second term on the RHS vanishes due to incompressibility and we are left with:

$$-\frac{1}{V} \int \frac{1}{2} [\nabla \cdot (\boldsymbol{U}_0 |\boldsymbol{u}|^2)] \, \mathrm{d}V = -\frac{1}{2V} \int \boldsymbol{U}_0 |\boldsymbol{u}|^2 \cdot \hat{\boldsymbol{n}} \, \mathrm{d}S = 0, \tag{2.67}$$

where we have applied the divergence theorem. By definition $\boldsymbol{U}_0$ has no z component, so on the top and bottom walls $\boldsymbol{U}_0 \cdot \hat{\boldsymbol{n}} = 0$ and the contribution to the surface integral vanishes there. The horizontal boundary conditions are periodic, and the contribution on these boundaries will thus be cancelled, because $\hat{\boldsymbol{n}}$ has opposite signs on each side. Therefore Eq. (2.67), and by extent the second term on the RHS of Eq. (2.61), vanishes. From this derivation we know that like the Coriolis force this term does not produce any net work; it is however an important part of the elliptical instability and required for its operation. Finally, we can then write the kinetic energy equation:

$$\frac{\mathrm{d}}{\mathrm{d}t} K = I + W_B - D_\nu. \tag{2.68}$$

To obtain an equation for the thermal (potential) energy when the stratification is convectively unstable, i.e. $\mathrm{Ra} > 0$, we multiply Eq. (2.17) by $\mathrm{PrRa}\theta$ and average over the box to obtain in a similar manner:

$$\frac{\mathrm{d}}{\mathrm{d}t} P = W_B - D_\kappa, \tag{2.69}$$

where we have defined the mean thermal energy P and the mean thermal dissipation rate

D_κ as:

$$P \equiv \mathrm{PrRa}\frac{1}{2}\langle\theta^2\rangle, \quad D_\kappa \equiv -\mathrm{PrRa}\langle\theta\nabla^2\theta\rangle. \tag{2.70}$$

The total energy is $E = K + P$, which thus obeys:

$$\frac{\mathrm{d}}{\mathrm{d}t}E = I + 2W_B - D_\nu - D_\kappa = I + 2W_B - D, \tag{2.71}$$

where $D = D_\nu + D_\kappa$ is the total dissipation rate. In a steady state, i.e. no change in time of the total energy, it is expected that the (time-averaged value of the) energy injected together with the buoyancy work balances the total dissipation. Because of the presence of the buoyancy work term, the total dissipation cannot be used directly to infer tidal dissipation rates. However, the energy injected by the tide must be dissipated if a steady state is to be maintained. Therefore, to interpret the tidal energy dissipation rate we examine the tidal energy injection rate I. If we instead consider stable stratification, i.e. $\mathrm{Ra} < 0$, we must multiply Eq. (2.17) by $-\mathrm{PrRa}\theta$, such that it has the same sign as $\mathrm{PrRa}\theta$ when the Rayleigh number is positive. Upon averaging over the box we obtain:

$$\frac{\mathrm{d}}{\mathrm{d}t}P = -W_B - D_\kappa, \tag{2.72}$$

where we have redefined the mean thermal energy P and the mean thermal dissipation rate D_κ as:

$$P \equiv -\mathrm{PrRa}\frac{1}{2}\langle\theta^2\rangle, \quad D_\kappa \equiv \mathrm{PrRa}\langle\theta\nabla^2\theta\rangle. \tag{2.73}$$

Note the minus sign differences compared to the definitions in Eq. (2.70), which ensure that thermal energy and thermal dissipation rate maintain the same sign as before. As a result the energy is maintained as a positive definite quantity. We have not redefined the buoyancy work term W_B so as to maintain consistency with the kinetic energy equation in Eq. (2.68). The total energy is again $E = K + P$, which thus obeys:

$$\frac{\mathrm{d}}{\mathrm{d}t}E = I + W_B - W_B - D_\nu - D_\kappa = I - D, \tag{2.74}$$

thus we are only left with I and D in Eq. (2.74), such that in steady state $I \approx D$.

The quantity I is therefore of tremendous interest to the determination of the tidal dissipation due to the elliptical instability. As a result, we wish to derive at least some estimates regarding how this quantity should scale with the parameters in the system. To this end we can first consider the saturation of the elliptical instability as involving a single most unstable mode whose amplitude saturates when its growth rate balances its non-linear cascade rate (Barker & Lithwick, 2013). We can think of the growth rate (ignoring viscosity) as the inverse of a growth timescale:

$$\frac{1}{t_{\mathrm{grow}}} \sim \sigma\Omega\epsilon \sim \gamma\epsilon. \tag{2.75}$$

We have used the knowledge that $\sigma\Omega$ is proportional to γ as can be readily inferred from

Eq. (2.51). Equally, we can define a damping timescale, or rather a cascade timescale due to secondary instabilities, according to:

$$\frac{1}{t_{\text{damp}}} \sim ku, \tag{2.76}$$

where k is again the wavenumber magnitude and u is the velocity amplitude. If the instability is saturated, this would imply that the growth and damping timescales are the same, and thus:

$$u \sim \epsilon\gamma/k. \tag{2.77}$$

The total dissipation rate D therefore scales as:

$$D \sim u^2/t_{\text{damp}} \sim \epsilon^3\gamma^3 k^{-2}. \tag{2.78}$$

Thus, in such a statistically steady state the dissipation and energy injection rate are expected to scale as:

$$D = I \propto \epsilon^3, \tag{2.79}$$

which is consistent with some local and global simulations (Barker & Lithwick, 2013; Barker, 2016a) as well as the scaling found for related instabilities like the precessional instability with its own small parameter (Barker, 2016b; Pizzi et al., 2022). We are interested in exploring whether convection could lead to a different result, and potentially change this steep ϵ scaling.

Since we know both the elliptical instability (Barker & Lithwick, 2013) and convection (e.g. Guervilly et al., 2014) in isolation can produce geostrophic flows such as vortices, we want to introduce further diagnostics to analyse these flows and the roles they play in the simulations. To do this, we decompose the total energy injection from the background flow into:

$$I = I_{2D} + I_{3D}, \tag{2.80}$$

where we have defined $I_{2D} = -\langle \boldsymbol{u}_{2D} \mathrm{A} \boldsymbol{u}_{2D} \rangle$ and $I_{3D} = -\langle \boldsymbol{u}_{3D} \mathrm{A} \boldsymbol{u}_{3D} \rangle$. I_{2D} and $\boldsymbol{u}_{2D}$ are defined to include all (geostrophic) modes where the wavevector has only non-vanishing x and y components, with $k_z = 0$, and I_{3D} and $\boldsymbol{u}_{3D}$ includes all the modes with $k_z \neq 0$. Thus we have decomposed the total energy injection rate into energy injection into the barotropic ($k_z = 0$) and baroclinic ($k_z \neq 0$) flow.

One can also think of this decomposition as one into geostrophic vortex modes (I_{2D}) and waves (I_{3D}). A pure inertial wave with $k_z = 0$ would have zero frequency, i.e. it is not a wave, so any energy injection into inertial waves would thus automatically be contained within I_{3D}. In convectively unstable simulations, which is the main focus of this work, the inertia-gravity waves with $k_z = 0$ also cannot exist, and therefore one can again crudely think of all energy injected into such inertia-gravity waves being contained within I_{3D}. In the case of stable stratification inertia-gravity waves could exist with $k_z = 0$. In these

stably stratified cases some of the energy injection into waves is contained within I_{2D}, but the majority will still be injected into the inertia-gravity waves, i.e. I_{3D}. Any modes which are not waves, such as the geostrophic, i.e. vertically invariant, vortex modes must by definition have $k_z = 0$ and thus any energy injected by the elliptical instability directly into these modes is contained within I_{2D}. Finally, convective eddies are expected to have vertical variation and therefore energy injected into these by interaction with the tidal flow, i.e. essentially the interaction of the convective flow with the tides as a turbulent viscosity, will also fall under the I_{3D} component.

It was found previously that the time-averaged energy input into the vortical motions I_{2D} is approximately zero or small (Barker & Lithwick, 2013), but that the input into the waves I_{3D} is on average non-zero (which it must be when the elliptical instability operates) and clearly demonstrates any bursty behaviour observed. The total kinetic energy K is also split up into a 2D and 3D component in a similar manner by defining K_{2D} and K_{3D}, so as to allow us to determine which components dominate the flow:

$$K = K_{2D} + K_{3D}. \tag{2.81}$$

To be able to study the turbulent effective viscosity we need to convert the energy injection rates I and I_{3D} to the energy dissipated by such a turbulent effective viscosity, which we dub ν_{eff} and $\nu_{\text{eff},3D}$ respectively. In particular, this is a useful comparison to quantify the rate at which turbulent convection could damp our tidal flow, if this interaction behaves like a turbulent viscosity. This is a scalar representation of the turbulent effective viscosity, instead of the tensor representation employed in Penev et al. (2009a, 2009b). It was found in Penev et al. (2009a) that the effective viscosity is only mildly anisotropic, and hence subsequent works (Ogilvie & Lesur, 2012; Duguid et al., 2019, 2020; Vidal & Barker, 2020a, 2020b) have examined the turbulent effective viscosity using the scalar representation. For consistency with these studies we have also opted to use the scalar representation of the effective viscosity throughout this thesis. These studies were however conducted in the absence of rotation, and in our rapidly rotating system with an anisotropic LSV, it is possible that the effective viscosity should instead be treated as an anisotropic tensor. Analysing such a tensor effective viscosity is left to future work. To define the effective viscosity, we equate the work done by the tidal flow on the convective flow with the viscous dissipation rate of the tidal flow, assuming this is due to a constant kinematic viscosity ν_{eff}, following Goodman and Oh (1997), Ogilvie and Lesur (2012), Braviner (2015), Duguid et al. (2019), and Vidal and Barker (2020b). The work done by the tidal flow is given by our energy injection term I. We also define the strain rate tensor for the tidal flow as $e^0_{ij} \equiv \frac{1}{2}(\partial_i U_{0,j} + \partial_j U_{0,i})$:

$$e^0 = -\gamma\epsilon \begin{pmatrix} \sin(2\gamma t) & \cos(2\gamma t) & 0 \\ \cos(2\gamma t) & -\sin(2\gamma t) & 0 \\ 0 & 0 & 0 \end{pmatrix}, \tag{2.82}$$

such that the rate at which energy is dissipated is given by:

$$\frac{2\nu_{\text{eff}}}{V}\int_V e^0_{ij}e^0_{ij}\,\mathrm{d}V = 4\nu_{\text{eff}}\gamma^2\epsilon^2. \tag{2.83}$$

Upon equating this expression to I we can define the effective viscosity according to:

$$\nu_{\text{eff}} = I/(4\gamma^2\epsilon^2). \tag{2.84}$$

Because the effective viscosity is expected to be independent of ϵ (for small enough ϵ), this implies that, if the interaction of turbulence acting on the tidal flow can be parametrised as a turbulent effective viscosity, it should scale as (for small enough ϵ):

$$D = I \propto \epsilon^2. \tag{2.85}$$

The different scaling laws of the energy injection with ϵ in Eq. (2.80) and Eq. (2.85) have immediately provided us with a good diagnostic for the sources of energy injection into the flow. If the energy injection in the simulations appears to scale as ϵ^2, it implies that the dominant dissipation mechanism is like that of the convection interacting with the tidal flow like an effective viscosity. If we however see a scaling with ϵ^3, this implies that the elliptical instability is likely to be the dominant mechanism in the simulations. It is possible that both mechanisms are operating at the same time, at which point the interaction may be some combination of ϵ^2 and ϵ^3 behaviour. The second diagnostic we can use in the simulations to tell the difference lies in the time series of the energy injection itself in a single simulation. If there is bursty behaviour present, the elliptical instability has maintained the same kind of behaviour as before the introduction of convection. If, however, the simulations show continuous energy injection, that may be the result of turbulence acting like an effective viscosity. An alternative option would be that the elliptical instability behaviour has significantly changed upon the introduction of convection, like it was upon the introduction of magnetic fields (Barker & Lithwick, 2014).

One final note on the energy injection: the injection terms represent energy being transferred from the background flow to the perturbations or vice versa. This, by definition, impacts the energy in these flows. The evolution of the tidal flow $\boldsymbol{U}_0$, however, is not explicitly accounted for in our model; we treat it as a fixed (but time-dependent) background flow. The tidal flow possesses much more energy than the perturbations, so we treat it as an infinite reservoir in our simulations. These results therefore give us only a snapshot at a certain point in time of the evolution of the astrophysical system, which is reasonable because tidal evolutionary processes usually occur very slowly relative to convective or rotational timescales.

Finally, because the convective LSVs impact the heat transport in the simulations, it is possible that the vortex generated by the elliptical instability would also affect the heat transport. Therefore we wish to study the heat transport in our simulations. To this

end we compute the Nusselt number, which we define as:

$$\mathrm{Nu} = 1 + \mathrm{RaPr}\langle\theta u_z\rangle. \tag{2.86}$$

The Nusselt number is a commonly studied quantity to investigate heat transport. It is the ratio of the total heat flux to the conductive flux, and is one by definition in the absence of any flow (i.e. heat transported purely by conduction). In essence, if the flow is convecting heat, than this quantity will be larger than one; the larger the Nusselt number the more important the flow is at transporting heat. We would thus expect that the introduction of strong vortices due to the elliptical instability will hinder heat transport, and therefore reduce the Nusselt number.

2.2 The Snoopy code

The simulations of the interactions of the elliptical instability and convection are executed using an adapted version of the Snoopy code (Lesur & Longaretti, 2007). Snoopy implements a Fourier pseudo-spectral method in a Cartesian box. It was originally designed for local models of accretion disks, in which the Keplerian velocity profile was represented as a background shear flow. To accommodate this background shear flow the code was set up with so-called shearing waves. For this reason the Snoopy code is – after suitable modifications – also well-equipped to study our system with a background tidal flow in a local box.

2.2.1 Shearing waves

The Fourier pseudo-spectral method that is utilised within the code uses a series of Fourier modes (i.e. sines and cosines) as its basis to expand the relevant parameters in the simulation, namely the velocity field, pressure and temperature perturbation. A single Fourier mode with associated velocity, pressure and temperature perturbation is given by:

$$\begin{aligned}
\boldsymbol{u} &= \mathrm{Re}[(\hat{u}_x(t)\cos(k_z z), \hat{u}_y(t)\cos(k_z z), \hat{u}_z(t)\sin(k_z z))^T \, \mathrm{e}^{\mathrm{i}\boldsymbol{k}_\perp(t)\cdot\boldsymbol{x}}], \\
p &= \mathrm{Re}[\hat{p}(t)\cos(k_z z)\, \mathrm{e}^{\mathrm{i}\boldsymbol{k}_\perp(t)\cdot\boldsymbol{x}}], \\
\theta &= \mathrm{Re}[\hat{\theta}(t)\sin(k_z z)\, \mathrm{e}^{\mathrm{i}\boldsymbol{k}_\perp(t)\cdot\boldsymbol{x}}],
\end{aligned} \tag{2.87}$$

where $\boldsymbol{k}_\perp(t) = (k_x(t), k_y(t), 0)$ is the horizontal part of the wavevector. Summing over all Fourier modes returns the total velocity field, pressure and temperature perturbations in the simulations. The vertical dependence of these quantities is expressed using sines or cosines to satisfy the relevant boundary conditions on the walls at the top and bottom (Cattaneo et al., 2003).

The horizontal wavevectors are time-dependent in this setup, which is an approach referred to as shearing waves. This is a necessity to be able to use the horizontally periodic boundary conditions in tandem with our background flow (Waleffe, 1990; Kerswell, 2002). Shearing waves allow us to automatically follow the stretching and rotation of waves due

to a background flow, such as the equilibrium tide in our simulation. The idea is simply this, the term:

$$\boldsymbol{U}_0 \cdot \nabla \boldsymbol{u} = -\gamma\epsilon[(\mathcal{S}x + \mathcal{C}y)\partial_x + (\mathcal{C}x - \mathcal{S}y)\partial_y]\boldsymbol{u}, \tag{2.88}$$

contains both the x and y coordinate. Therefore, because we have opted for periodic boundary conditions in the horizontal, these terms will have discontinuities on the boundaries. This leads to a numerical, but not physical, issue in the simulation. Fortunately, by utilising shearing waves, one can cancel this term, at the cost of needing to take into account the time-evolution of the wavevectors. This is readily seen by considering the consequence of time-dependent wavevectors in the momentum equation, as it modifies the time derivative term by introducing a second term according to the product rule:

$$\frac{\partial \boldsymbol{u}}{\partial t} = \frac{\partial \hat{\boldsymbol{u}}}{\partial t} \mathrm{e}^{\mathrm{i}\boldsymbol{k}_\perp(t)\cdot\boldsymbol{x}} + \hat{\boldsymbol{u}} \frac{\partial}{\partial t}\left[\mathrm{e}^{\mathrm{i}\boldsymbol{k}_\perp(t)\cdot\boldsymbol{x}}\right]. \tag{2.89}$$

The former term is unchanged compared to non-shearing wave descriptions, but the latter term arises precisely because of the introduction of shearing waves. We will equate the latter term to the term in Eq. (2.88) to eliminate both:

$$-\mathrm{i}\dot{\boldsymbol{k}}_\perp(t) \cdot \boldsymbol{x}\ \boldsymbol{u} = -\gamma\epsilon[(\mathcal{S}x + \mathcal{C}y)\partial_x + (\mathcal{C}x - \mathcal{S}y)\partial_y]\boldsymbol{u}. \tag{2.90}$$

Because we want to eliminate the term in Eq. (2.88), we have introduced a minus sign on the LHS of Eq. (2.90). Equating coefficients in x, y, z reveals that $\dot{k}_z = 0$ and as such k_z is independent of time. This is an important realisation as it allows us to satisfy the boundary conditions on the walls at the top and bottom using the choice of sines and cosines in Eq. (2.87). For k_x, k_y we find:

$$\mathrm{i}\dot{k}_x = \gamma\epsilon(\mathrm{i}\mathcal{S}k_x + \mathrm{i}\mathcal{C}k_y), \tag{2.91}$$

$$\mathrm{i}\dot{k}_y = \gamma\epsilon(\mathrm{i}\mathcal{C}k_x - \mathrm{i}\mathcal{S}k_y), \tag{2.92}$$

which can be presented in a neat and concise way by writing:

$$\dot{\boldsymbol{k}}_\perp = -A^T \boldsymbol{k}_\perp, \tag{2.93}$$

with A as defined in Eq. (2.2). This is a system of coupled ODEs. For ease of calculation we will again employ asymptotic analysis, writing $\boldsymbol{k}(t) = \boldsymbol{k}_0 + \epsilon\boldsymbol{k}_1(t)$. The equations at $\mathcal{O}(1)$ are trivial and tell us that $\boldsymbol{k}_0$ is constant. The equations at $\mathcal{O}(\epsilon)$ read:

$$\dot{k}_{x_1}(t) = \gamma(\mathcal{S}k_{x_0} + \mathcal{C}k_{y_0}), \tag{2.94}$$

$$\dot{k}_{y_1}(t) = \gamma(\mathcal{C}k_{x_0} - \mathcal{S}k_{y_0}). \tag{2.95}$$

Solving this is straightforward and we find for the wavevector to $\mathcal{O}(\epsilon)$:

$$\boldsymbol{k}(t) = \begin{pmatrix} k_{x,0} + \frac{\epsilon}{2}(-\mathcal{C}k_{x,0} + \mathcal{S}k_{y,0}) \\ k_{y,0} + \frac{\epsilon}{2}(\mathcal{S}k_{x,0} + \mathcal{C}k_{y,0}) \\ k_{z,0} \end{pmatrix}. \tag{2.96}$$

This description of the shearing waves also works for the temperature perturbation and eliminates the $\boldsymbol{U}_0 \cdot \nabla\theta$ term in the heat equation. This is the same basis of shearing waves as those used in Barker and Lithwick (2013).

Originally, the Snoopy code was set up for a triply periodic system but this is easily converted to a system with walls in one direction when using the Fourier basis by implementing a sine-cosine decomposition. The idea behind the simplest implementation of this sine-cosine decomposition is to double the domain in the direction that the walls are imposed in as shown in Fig. 2.2. The solid box indicates the Cartesian model we wish to study, while the dotted rectangle with double the domain in z is what we simulate when employing the sine-cosine decomposition. Using this double domain one can utilise the same triply periodic code, but only use the results of the bottom half of the domain. The chosen boundary conditions are then automatically enforced in the part of the domain we study because of the choice of sines and cosines in Eq. (2.87). The sines, depicted in blue on the left-hand side of the schematic, employed in the z-direction in the expressions for u_z and θ automatically enforce the impermeable and fixed temperature boundary conditions, as the sines are by definition zero on the boundaries. This holds true not only for the doubled rectangular domain, but also the square domain we wish to study. Additionally, by making this choice the system is no longer periodic, as there is no flow through the boundaries by definition, and thus the two halves of the rectangle can be considered in isolation. Note that by necessity of satisfying the boundaries no cosines are employed in the expressions for u_z and θ. Equally, the cosines, depicted in grey on the right-hand side of the schematic, employed in the z-direction in the expressions for u_x, u_y and p automatically satisfy the stress-free conditions on the boundaries, as their derivatives go to zero. An alternative approach to the sine-cosine decomposition, using sine and cosine transforms directly, can also be employed (Cattaneo et al., 2003).

In practical terms, this means the vertical resolution of the simulation is effectively halved, as we only consider one half of the domain. The vertical resolutions reported in this work represent the effective vertical resolution of the domain which we wish to simulate, not that of the full double domain. A 3rd-order explicit Runge-Kutta scheme is used for the time-stepping of all terms except the diffusion term, which is dealt with by using an integrating factor. The Courant-Friederichs-Lewy (CFL) safety factor is used to ensure the timesteps are small enough to accurately capture non-linear effects, usually set to 1.5 (which is smaller than the stability limit of $\sqrt{3}$). The de-aliasing in the code uses the standard 2/3 rule (Boyd, 2001).

Since our flow is likely to be rotationally dominated due to our choice of Ekman

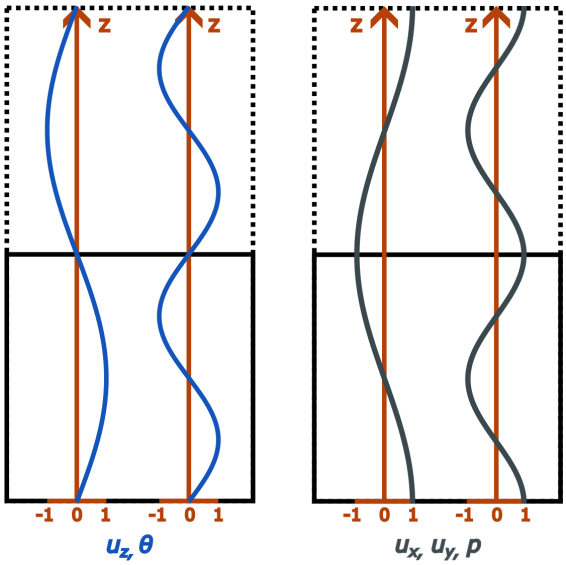

Figure 2.2: Schematic of the sine-cosine decomposition employed in the Snoopy code. We wish to study the solid-black square with impermeable stress-free walls at the top and bottom and so we need to double the domain to the dotted-black rectangle in the direction in which we employ the sine-cosine decomposition. The sines (in blue) in the expressions for u_z and θ automatically satisfy the fixed temperature, impermeable boundary conditions, while the cosines (in grey) in $u_x, u_y, \boldsymbol{p}$ automatically satisfy the stress-free conditions.

number and computationally feasible Rayleigh numbers, a default box size of $L_x = L_y = 4$, $L_z = 1$ was chosen that would capture this LSV. The box size in this work is always the default, unless otherwise specified. The question remains however what effect changing the aspect ratio of the box would have on the interactions presented, as the aspect ratio L/d (the ratio of horizontal length of the box to its vertical length) influences the ratio of the vertical to total kinetic energy (e.g. Guervilly et al., 2014).

2.2.2 Benchmarking

To verify that Snoopy is capturing the instabilities correctly, we calculate the growth rate of the kinetic energy in our simulations and compare it to the predicted growth rate given in Eq. (2.60). Since we have adopted the RRBC setup with impermeable walls in z, we must determine how this affects the growth rate of instability, although we expect it remains unchanged as we have demonstrated analytically. Hence, we performed multiple test simulations analysing the linear growth rates of both the elliptical and convective instabilities. We initialised them with random noise and the non-linearities were switched off, thus leading to a continuous exponential growth, allowing for easy extraction of the growth rate. Fits were performed to the mean kinetic energy on a log-scale to determine σ, by noting that if velocity components grow as $\exp(\sigma t)$, then $K \propto \exp(2\sigma t)$.

The results, along with the theoretical growth rate predictions for both instabilities, are plotted in Fig. 2.3. The top panel shows the growth rate of the elliptical instability as a function of ϵ (when $n = 0$), where we have adopted a time unit γ^{-1}, equivalent to using $\gamma = 1$, for the purposes of this figure. It can be concluded that the modelling

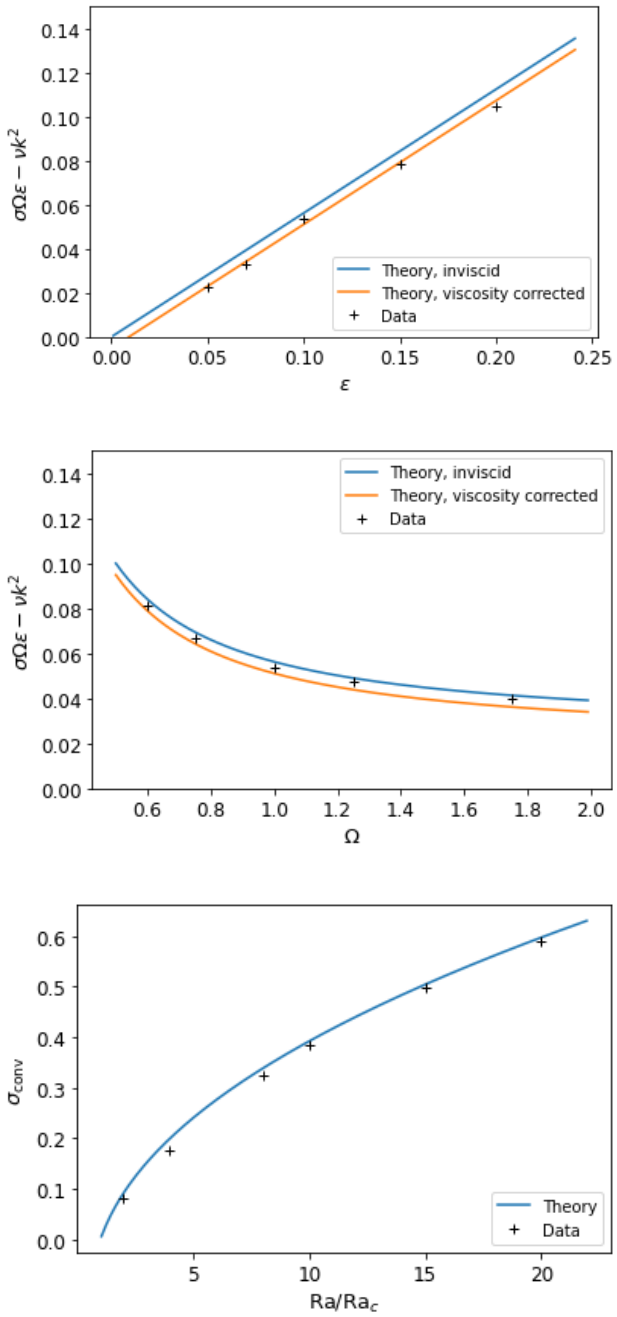

Figure 2.3: Growth rates of the elliptical instability and convection studied in isolation. Top left: growth rate of the elliptical instability (σ with time units of γ^{-1}) showing simulations compared with the theoretical prediction based on Eq. (2.51), as a function of ϵ ($n = 0$, $\gamma = \Omega = 1$) with and without the reduction of viscosity, and Eq. (2.51) as a function of Ω (keeping $\gamma = 1$) in the top right panel. The simulations are in good agreement, with a slight reduction due to the combined effects of viscosity and de-tuning. Bottom: growth rate of rotating convection, compared with the theoretical prediction of RRBC for the fastest growing mode (σ in thermal time units) with $\mathrm{Ek} = 5 \cdot 10^{-5.5}$.

of the inviscid growth rate is approximately correct. We also accounted for the leading effects of viscous damping by including the viscous decay rate so that the total growth rate is $\sigma - \nu k^2$ (where k is the wavevector magnitude of the mode), which is in excellent agreement with our simulations. We obtain values that are very slightly smaller than the theoretical prediction though, even when taking into account viscosity, which is likely due to the de-tuning effect discussed previously (i.e. that the mode does not precisely satisfy $k_z/k = 1/2$). In numerical simulations this de-tuning arises because of the finite number of grid points, which, in addition to a chosen aspect ratio, prohibits the waves from precisely satisfying the resonance conditions. However, because this condition does not stipulate the size of the wavenumbers, instead stipulating their ratio, and as such direction, the fastest growing mode that dominates the volume-averaged energy will be as large-scale as possible while still adequately satisfying the resonance condition in order to reduce the viscosity correction. This means that it should be unaffected by resolution, instead being controlled by the aspect ratio of the box. The effect on the growth rate of this de-tuning in these benchmark tests is represented by the difference between the markers and the viscosity corrected growth rate. At the aspect ratio corresponding to the top panel of Fig. 2.3 and the other simulations in this work, with $\gamma = \Omega = 1$, the maximum absolute value reduction of the growth rate is determined numerically to be ≈ 0.002, which is small.

The growth rate of the elliptical instability as a function of Ω, keeping $\gamma = 1$ and fixing $\epsilon = 0.1$, is shown in the middle panel of Fig. 2.3, and also follows the theoretical prediction well, but is again slightly lower for the same reasons. The viscosity correction is based on the mode that best satisfies the resonance conditions at $\Omega = 1$. The growth rate of the convective instability for $\mathrm{Ek} = 5 \cdot 10^{-5.5}$ is shown in the bottom panel of Fig. 2.3, now using thermal time units, and this is also in very good agreement with the linear convective growth rate for the fastest growing mode as expected. We can therefore be confident that both instabilities have been captured correctly.

2.2.3 Parameter variations

To examine our quantities of interest, namely the kinetic energy, energy injection and heat transport, the latter of which is represented by the Nusselt number, we will execute a large parameter sweep. We will vary the Rayleigh number, Ekman number and ellipticity to be able to independently vary the convective driving, rotational constraint and driving of the elliptical instability.

Some simulations will be performed with Rayleigh numbers in the stably stratified regime, i.e. with $\mathrm{Ra} < 0$. The values of the Rayleigh number are typically reported as $R = \mathrm{Ra}/\mathrm{Ra}_c$ for clarity, where Ra_c is the onset critical Rayleigh number (determined numerically by solving Eq. (2.54)) and R is the supercriticality. The range of this ratio studied at $\mathrm{Ek} = 5 \cdot 10^{-5.5}$ is $R \in [2, 20]$ and $R \in [-10, 0.8]$, in the convectively unstable and stable regimes, respectively. We consider ellipticities in the interval $\epsilon \in [0.01, 0.20]$ and Ekman numbers in the interval $\mathrm{Ek} \in [5 \cdot 10^{-4.5}, 5 \cdot 10^{-6}]$. When varying the Ekman number we either fix the Rayleigh number itself to be $\mathrm{Ra} = 1.3 \cdot 10^8$, corresponding to

Table 2.1: Table of resolutions used in the SNOOPY simulations to study the elliptical instability with different Rayleigh numbers, Ekman numbers, and horizontal box size $L_x = L_y = 4$ (unless otherwise specified). The same resolution was used for all ellipticities. The square brackets indicate all entries within are multiplied by the factor 5 in front.

$\mathrm{Ek} = 5 \cdot 10^{-5.5}$	n_x, n_y	n_z
$R = -6, -4, -3, -1, -0.8, 0.3, 0.8, 2, 3, 4, 5, 6$	256x256	96
$R = 7, 8$	256x256	128
$R = -10, 9, 10, 11, 12, 15$	256x256	160
$R = 20$	256x256	224
$\mathrm{Ra} = 1.3 \cdot 10^8$	n_x, n_y	n_z
$\mathrm{Ek} = 5 \cdot [10^{-5.6}, 10^{-5.7}, 10^{-5.8}, 10^{-5.9}]$	256x256	96
$\mathrm{Ek} = 5 \cdot 10^{-5.4}$	256x256	128
$\mathrm{Ek} = 5 \cdot [10^{-5.2}, 10^{-5.3}]$	256x256	160
$\mathrm{Ek} = 5 \cdot [10^{-5}, 10^{-5.1}]$	256x256	196
$\mathrm{Ek} = 5 \cdot [10^{-4.5}, 10^{-4.6}, 10^{-4.7}, 10^{-4.8}, 10^{-4.9}]$	256x256	128
$R = 6$	n_x, n_y	n_z
$\mathrm{Ek} = 5 \cdot [10^{-5.6}, 10^{-5.7}, 10^{-5.8}, 10^{-5.9}, 10^{-6}]$	256x256	96
$\mathrm{Ek} = 5 \cdot [10^{-5.0}, 10^{-5.1}, 10^{-5.4}]$	256x256	128
$\mathrm{Ek} = 5 \cdot [10^{-5.2}, 10^{-5.3}]$	256x256	160
$R = 6$, $\epsilon = 0$, $L_x = 2$ (to determine l_c)	n_x, n_y	n_z
$\mathrm{Ek} = 5 \cdot [10^{-5}, 10^{-5.1}, ..., 10^{-5.8}, 10^{-5.9}, 10^{-6}]$	512x512	128
$\mathrm{Ra} = 1.3 \cdot 10^8$, $\epsilon = 0$, $L_x = 2$ (to determine l_c)	n_x, n_y	n_z
$\mathrm{Ek} = 5 \cdot [10^{-4.5}, 10^{-4.6}, ..., 10^{-5.8}, 10^{-5.9}, 10^{-6}]$	512x512	128

$R = 6$ at $\mathrm{Ek} = 5 \cdot 10^{-5.5}$, or we fix it to $R = 6$.

A table of the parameters in our simulations, as well as the associated resolution of the simulations is given in Table 2.1. High Rayleigh number simulations were carried out with higher vertical resolutions, so as to ensure the heat flux is fully resolved. Simulations with higher ellipticities in the range we considered were not found to require higher resolutions. In addition, in some simulations it is our aim to resolve the heat flux spectrum in excess of the very smallest-scale fluctuations, where we opted to use a 2-by-2-by-1 ($L = 2$) box without the elliptical instability, as indicated in the bottom two columns of Table 2.1.

2.3 Summary

We have discussed the elliptical instability and convective instability in rotating systems. Our linear stability analysis of the elliptical instability indicates that the introduction of walls does not modify the inviscid growth rate of the elliptical instability.

Furthermore, from the non-dimensionalised governing equations, with $\mathrm{Pr} = 1$, we have found both the parameters that we can vary within our simulations, namely the ellipticity, ϵ, Ekman number, Ek and Rayleigh number, Ra, as well as the quantities which we wish to analyse, namely the kinetic energy, K, Nusselt number, Nu, and energy injection rate from the tidal flow, I. We can decompose the energy injection and kinetic energy into its geostrophic (or vortex) modes with $k_z = 0$, referred to as I_{2D} and K_{2D},

and waves and eddies with $k_z \neq 0$, referred to as I_{3D} and K_{3D}. In previous work (Barker & Lithwick, 2013) it was shown that the energy injection rate I is rapidly oscillating as a function of time in the simulations. The I_{2D} component of this energy injection rate is responsible for these rapid oscillations, which were found to cancel on average. The I_{3D} component of the energy injection rate does not cancel on average however, and it is this component which is responsible for the energy injection into the inertial waves. Therefore we will the I_{3D} term instead of the full energy injection rate I.

We have found – using a crude argument which considers the saturation of a single mode – that this energy injection term may scale with the ellipticity parameter ϵ according to $I \propto \epsilon^3$ if the elliptical instability operates. If however the energy injection or tidal dissipation of the flow is by action of the convective turbulence on the tidal flow like an effective viscosity, independent of ϵ, it was found that the energy injection should scale as $I \propto \epsilon^2$. These two different scalings are a useful way to examine which mechanism is likely to be active in the flow, both being motivated by prior work. If both tidal dissipation mechanisms are operating at the same time it might be expected that the energy injection could be a combination of the two scalings.

We have detailed the Snoopy code used to execute our simulations, as well as deriving the shearing waves necessary to accommodate the background tidal flow with periodic boundary conditions. We have verified that the code captures both the instabilities properly by examining the growth rate of the kinetic energy in linear test simulations, comparing these growth rates with the theoretical predictions and finding good agreement.

Now that we have demonstrated that Snoopy accurately reproduces the instabilities in our setup we can be confident moving on to analyse non-linear simulations of the elliptical instability and Rayleigh-Bénard convection.

Chapter 3

Interactions of the elliptical instability and convection

In the following two chapters we will explore the interactions of the elliptical instability and convection. In this chapter we will examine the overall behaviour of the interactions, without deriving quantitative scaling laws, which we will do in Ch. 4. All simulations considered in this chapter were executed with fixed $\mathrm{Ek} = 5 \cdot 10^{-5.5}$. We will first look at some snapshots of the flow in these simulations as well as the patterns in the time series of the kinetic energy, energy injection and Nusselt number. Afterwards, we will study the interaction by analysing the flow in both real and spectral space. Finally, we study if and how the growth rate of the elliptical instability in our simulations is modified by the presence of a convective large-scale vortex (LSV).

3.1 Time series analysis of the interactions

3.1.1 Qualitative analysis of illustrative simulations

We will begin our discussion of the simulation results by presenting the z-averaged vertical vorticity $\langle \omega_z \rangle_z$ of the flow in Fig. 3.1. The snapshot of the flow in the left-hand panel was taken at $t = 0.08$ (in thermal diffusion times) in a simulation with $\epsilon = 0.1$, $\mathrm{Ra} = 0$. At these parameters only the elliptical instability and its associated non-linear dynamics are present. A snapshot at time $t = 0.08$ was chosen such that the flow has evolved far beyond the initial saturation of the instability and an LSV has formed. This LSV is generated by non-linear interactions between the inertial waves linearly excited by the elliptical instability. The cyclonic vortices that emerge in this and subsequent snapshots have been centred for clarity. A smaller and weaker anticylonic vortex emerges at the corners in this snapshot, but note our periodic boundaries. This anticyclonic vortex emerges because the vertical vorticity of the flow is conserved.

In the right-hand panel of Fig. 3.1 we present a snapshot of a simulation with $\epsilon = 0.1$, $\mathrm{Ra} = 6\mathrm{Ra}_c$, in which both the elliptical instability and the convective instability, as well

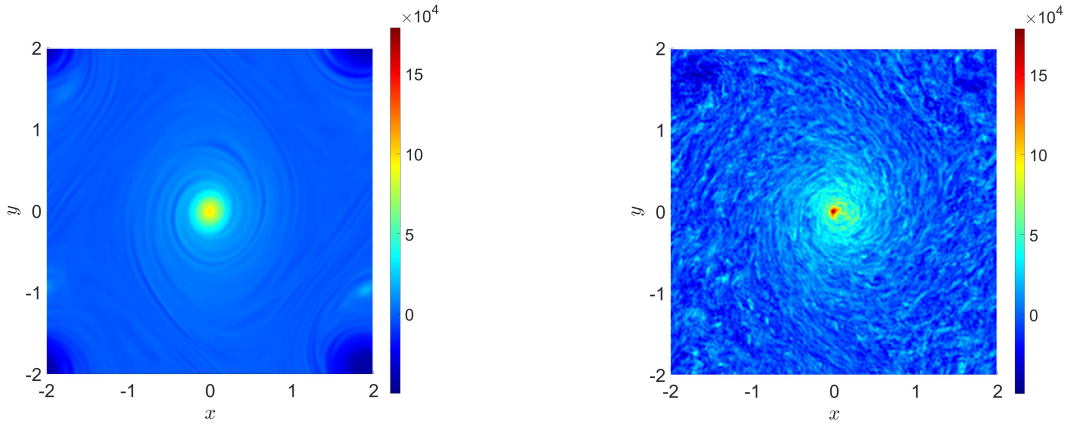

Figure 3.1: The vertical vorticity averaged over z ($\langle\omega_z\rangle_z$) of the flow at $t = 0.08$ (in thermal diffusion times). The cyclonic vortex is centred for clarity in both images. Left: elliptical instability in isolation with $\epsilon = 0.1$, Ra $= 0$. Right: elliptical instability and convection with $\epsilon = 0.1$, Ra $= 6\text{Ra}_c$.

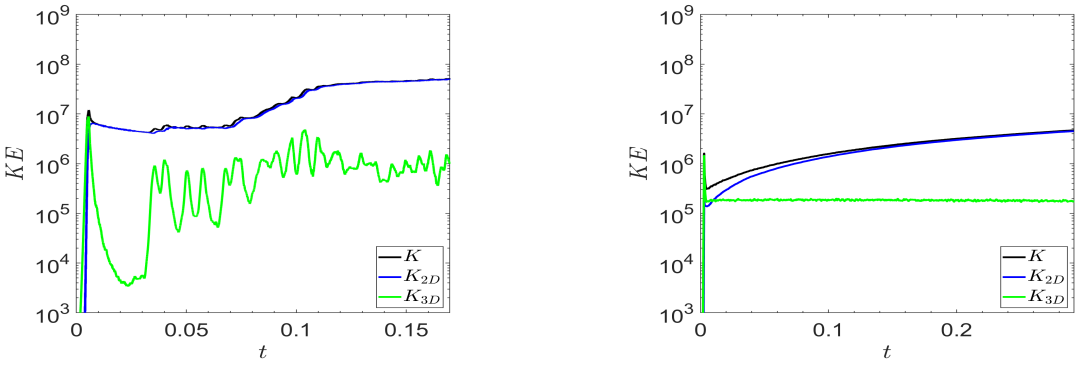

Figure 3.2: Kinetic energy of simulations of the elliptical instability in isolation (left) with $\epsilon = 0.1$, Ra $= 0$ and convection in isolation (right) with $\epsilon = 0$, Ra $= 4\text{Ra}_c$. The 2D (blue) and 3D (green) components of the energy represent the energy in the vortical motions, and the waves and convective eddies, respectively. The total kinetic energy is plotted as the black line.

as their associated non-linear dynamics, are present. This snapshot, like the one in the left-hand panel, was taken at $t = 0.08$. In this simulation the convection dominates the flow and as such a single cyclonic convective LSV arises, with a primarily anticyclonic background. The vorticity in the centre of this vortex is larger than the vorticity in the centre of the one in the left-hand panel. In the right-hand panel, small-scale convective eddies are present throughout the box, making the flow appear much noisier compared to the elliptical instability in isolation. Note that with our chosen aspect ratio and Ekman number the convective LSV emerges when Ra $\gtrsim 3\text{Ra}_c$. Thus it emerges at a similar value of the Rayleigh number as the convective LSV in Guervilly et al. (2014), which is readily seen from their criterion to indicate when the LSV emerges: $\tilde{\text{Ra}} = \text{RaEk}^{4/3} \gtrsim 20$. Using the expression for the critical Rayleigh number in the rapidly rotating regime in Eq. (2.59): $\text{Ra}_c \approx 8.7\text{Ek}^{-4/3}$, this can be rewritten as: Ra $\gtrsim 20\text{Ek}^{-4/3} \approx 2.5\text{Ra}_c$.

Turning our attention to the time-evolution of the quantities of interest, we study the volume-averaged kinetic energy of a simulation with the elliptical instability in isolation, as well as a simulation with the convective instability in isolation, in Fig. 3.2. The left-hand panel of Fig. 3.2 shows the former simulation with $\epsilon = 0.1$, $\mathrm{Ra} = 0$. The vortex observed previously in a 1-by-1-by-1 box by Barker and Lithwick (2013) dominates the flow to an even greater extent in the 4-by-4-by-1 box, as we can see by the dominance of the energy in the 2D component of the flow (K_{2D}) at all times after the initial saturation. The 2D, or geostrophic, modes have energies much larger than the inertial waves (quantified by the energy in the 3D modes, K_{3D}), but the inertial waves undergo transient bursts temporarily increasing their energy, though K_{2D} remains dominant unlike in the 1-by-1-by-1 case in Barker and Lithwick (2013). Each burst in the 3D energy later results in an increase in the 2D energy, indicating energy transfers from inertial waves to vortices. The vortex slowly decays viscously. The bursts of inertial wave energy are sufficient to compensate this lost energy, enhancing it further until a quasi-steady state is reached after $t \sim 0.1$. Meanwhile, the right-hand panel of Fig. 3.2 shows the clear dominance of the LSV in a purely convective simulation with $\epsilon = 0$, $\mathrm{Ra} = 4\mathrm{Ra}_c$, as the 2D energy of the LSV, and by extension the LSV itself, continuously grows for all times plotted. The LSV will continue to grow until it reaches either the horizontal box scale, its growth is balanced by viscous dissipation, it has back reacted on the flow in such a way to inhibit its further growth, or possibly some combination of these. A steady level of 3D energy is present in this simulation after the initial saturation, representing the energy in the convective eddies, which appears to be only weakly affected by the growing LSV.

The interaction of convection and the elliptical instability varies according to the parameters chosen. Here, we start by presenting a simulation with weak convection but strong ellipticity in Fig. 3.3, with $\epsilon = 0.1$ and $\mathrm{Ra} = 4\mathrm{Ra}_c$. The convection in this simulation leads to an LSV which results in continuous growth of the 2D modes. This however does not inhibit the elliptical instability, and a multitude of bursts is observed. The elliptical instability in fact enhances the energy in the 2D modes by at least one order of magnitude compared to the purely convective simulation in the right-hand panel of Fig. 3.2, as the bursts input more energy into the LSV. There is a continuous decrease of the 2D energy, from $t = 0.1$ to $t = 0.17$. In this period of time neither the bursts, weakened by the strong vortex, nor the convective eddies, provide enough energy to compensate the viscous dissipation. From $t = 0.17$ onwards the energy in the LSV seems to stabilise and bursts of the elliptical instability reappear from $t = 0.21$, once the LSV has been sufficiently weakened.

In the right-hand panel of Fig. 3.3 the energy injection corresponding to the simulation of the elliptical instability in isolation in the left-hand panel of Fig. 3.2 with parameters $\epsilon = 0.1$, $\mathrm{Ra} = 0$ is plotted in black. The increase in 3D energy in the left-hand panel of Fig. 3.2 is a result of a direct energy injection into those modes. The 2D injection (I_{2D}, not shown) is oscillatory in sign and has a small average value consistent with 0. The energy injection corresponding to the simulation in the left-hand panel of Fig. 3.3 is also plotted

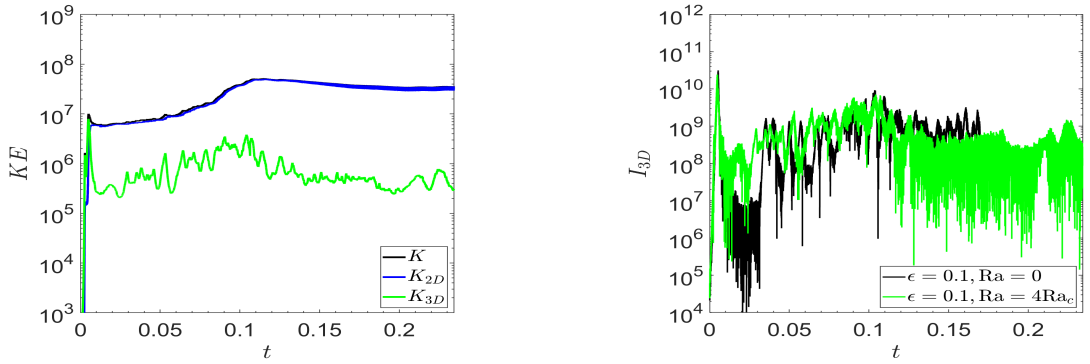

Figure 3.3: Kinetic energy (left) of the elliptical instability and convection interacting with $\epsilon = 0.1$, $\mathrm{Ra} = 4\mathrm{Ra}_c$. The 2D (blue) and 3D (green) components are plotted in addition to the total kinetic energy. The energy injection (right) of both simulations with $\epsilon = 0.1$, $\mathrm{Ra} = 0$ (black) and $\epsilon = 0.1$, $\mathrm{Ra} = 4\mathrm{Ra}_c$ (green).

in the right-hand panel of Fig. 3.3 in green and roughly matches the energy injection of the purely elliptical simulation, although it is initially maintained at a higher value. From $t = 0.11$ onwards, when the LSV has reached its strongest value, the behaviour gradually changes from bursts to an almost continuous energy injection. From $t = 0.21$, once the LSV has been sufficiently weakened, bursts in the energy injection rate are again observed, as expected from the time-evolution of the kinetic energy.

3.1.2 Varying the strength of convective driving and the ellipticity

Next we vary the strength of the convective driving and ellipticity to study what the effects these (and their combination) have on the behaviour in the simulations. In Fig. 3.4 and Fig. 3.5 we present results for a range of values of ϵ and $\mathrm{Ra}/\mathrm{Ra}_c$. The figures on the left show the time-evolution of the kinetic energy components, and those on the right the energy injection term I_{3D}. Fig. 3.4a and Fig. 3.4b show a simulation with $\epsilon = 0.2$ and $\mathrm{Ra} = 2\mathrm{Ra}_c$. Barker and Lithwick (2013) observed a change in behaviour at $\epsilon \gtrsim 0.15$, seeing a sharp increase in the frequency and strength of the elliptical instability bursts. The 3D component of the kinetic energy is maintained at a higher level in this case compared to previous cases, but is still lower than the energy in the 2D component. The energy injection features many bursts in a short timeframe, with multiple bursts injecting energy at the same rate as the initial burst in linear growth phase. The increased burst frequency also leads to a continuous energy injection throughout the simulation. There appears to be a secondary transition around $t = 0.045$ where the energy injection increases steeply and maintains a significant energy injection much larger than the initial burst. We observe a correspondingly higher minimum level of the 3D component of the energy during this simulation.

The kinetic energy in Fig. 3.4c shows that increasing the Rayleigh number, i.e. making the convection stronger compared to the elliptical instability, results in fewer visible bursts of energy injection into the 3D component in the first half of the simulation

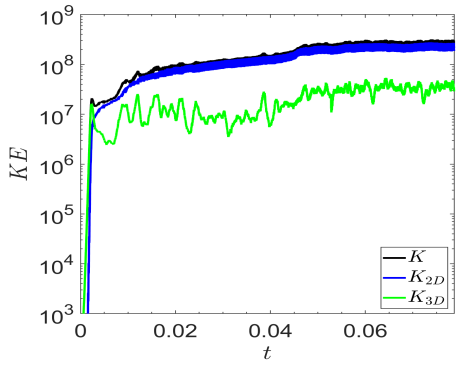

(a) K of the simulation with $\epsilon = 0.2$, Ra $= 2\text{Ra}_c$.

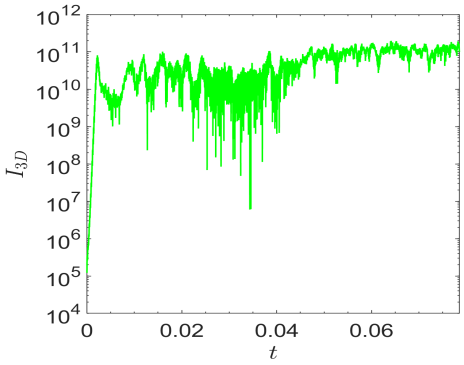

(b) I_{3D} of the simulation with $\epsilon = 0.2$, Ra $= 2\text{Ra}_c$.

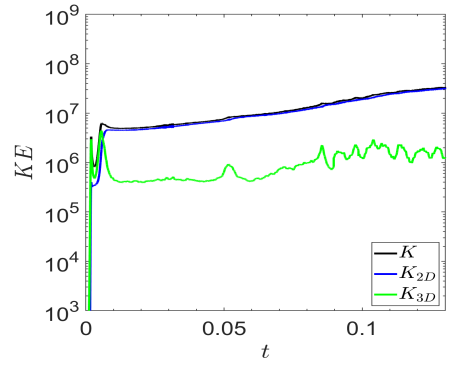

(c) K of the simulation with $\epsilon = 0.1$, Ra $= 6\text{Ra}_c$.

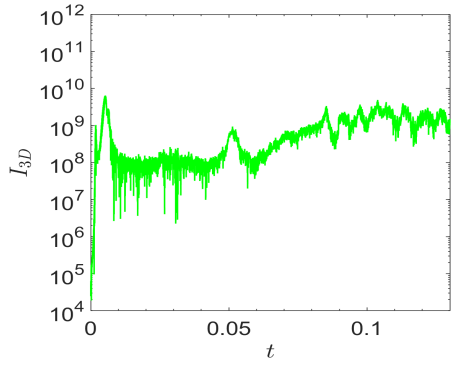

(d) I_{3D} of the simulation with $\epsilon = 0.1$, Ra $= 6\text{Ra}_c$.

Figure 3.4: Kinetic energy (left) and the energy injection contribution I_{3D} (right) for two simulations with an operating elliptical instability. Convection results in a sustained energy input into the flow from the tidal flow, allowing for sustained tidal dissipation in addition to the bursts of the elliptical instability.

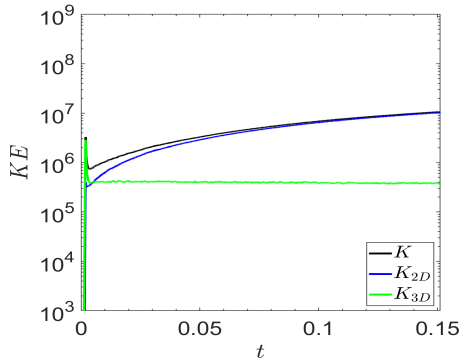

(a) K of the simulation with $\epsilon = 0.05$, Ra $= 6\text{Ra}_c$.

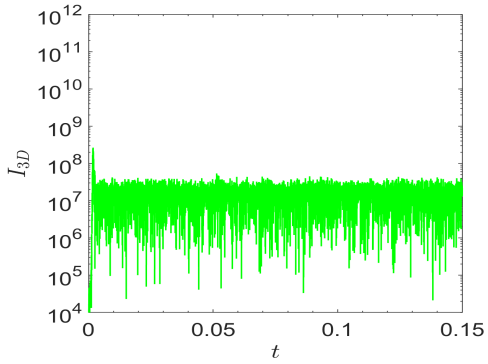

(b) I_{3D} of the simulation with $\epsilon = 0.05$, Ra $= 6\text{Ra}_c$.

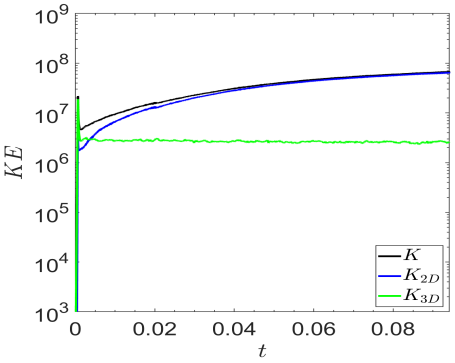

(c) K of the simulation with $\epsilon = 0.1$, Ra $= 20\text{Ra}_c$.

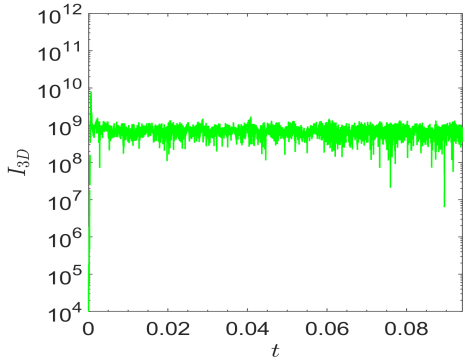

(d) I_{3D} of the simulation with $\epsilon = 0.1$, Ra $= 20\text{Ra}_c$.

Figure 3.5: Kinetic energy (left) and the energy injection contribution I_{3D} (right) for two simulations without an operating elliptical instability. The convection is sufficiently strong in these simulations compared to the elliptical instability, so that it can suppress the bursts leaving only the sustained energy injection.

compared with the left-hand panel of Fig. 3.3, and the total kinetic energy is further dominated by the 2D component. The increased convection strength, and therefore (for our parameters) stronger LSV, drowns out most of the bursts from the elliptical instability. The reduced presence of the elliptical instability is also clearly visible from the I_{3D} term in Fig. 3.4d, showing considerably fewer bursts in the first half of the simulation, decreasing the tidal dissipation. On the other hand, a "floor value" corresponding to a non-zero continuous energy injection arises, which is most clearly visible in between bursts. This sustained energy injection arises from the interaction between the convection and the equilibrium tidal flow.

Fig. 3.5a and especially Fig. 3.5b confirm this sustained injection occurs as the convection is strengthened relative to the elliptical instability. The ellipticity has been reduced to $\epsilon = 0.05$, thus weakening the elliptical instability (whose growth rate is proportional to ϵ). As a result, the bursts from the elliptical instability have vanished, with only a short initial burst remaining, after which a continuous injection arises. These simulations suggest there is a point at which the convection, with both its LSVs and its resulting action to damp the inertial modes, overpowers the elliptical instability such that the bursts are

completely suppressed.

Increasing the Rayleigh number to $\mathrm{Ra} = 20\mathrm{Ra}_c$ and maintaining $\epsilon = 0.1$ instead of decreasing ϵ in Fig. 3.5c and Fig. 3.5d leads to similar behaviour, with no bursty behaviour for the elliptical instability and instead a sustained energy injection. Thus, increasing the Rayleigh number inhibits bursts even if they were present at lower values of Ra with the same ellipticity. Additionally, the sustained injection term has increased by a factor of about 20 compared to Fig. 3.5b. The sustained energy injection therefore increases with Ra and ϵ. Thus, introducing convection has two effects: 1) the bursts of elliptical instability are suppressed by the convective LSV, the extent of which increases as the strength of convection increases relative to the strength of the elliptical instability, and 2) a sustained energy injection arises from the interaction between convection and the background tidal flow.

3.1.3 Heat transport modification by elliptical instability

A further effect of the elliptical instability is to modify heat transport. The inertial waves excited by the elliptical instability are capable of transporting heat in the system (Cébron et al., 2010; Lavorel & Le Bars, 2010). Because the elliptical instability can occur in both stably stratified and convectively unstable fluids (see Eq. (2.60)), it is of interest to study how the heat transport is modified as the Rayleigh number is varied. We start by studying the heat transport in a simulation with stable stratification in Fig. 3.6a with $\epsilon = 0.1$, $\mathrm{Ra} = -4\mathrm{Ra}_c$ in red, compared to the result with $\epsilon = 0$, $\mathrm{Ra} = -4\mathrm{Ra}_c$ in black. In the absence of the elliptical instability in a stably stratified fluid no heat is transported except by conduction, and thus the Nusselt number equals one by definition. If the elliptical instability is operating, here represented by the simulation in red, the inertia-gravity waves excited during bursts of the elliptical instability will transport heat, and therefore the Nusselt number intermittently exceeds one. In those same bursts the elliptical instability can also transport heat in the opposite direction to the conduction state, reducing the Nusselt number below one.

In the convectively unstable simulation in Fig. 3.6b, with $\epsilon = 0.1$, $\mathrm{Ra} = 2\mathrm{Ra}_c$ in red and $\epsilon = 0$, $\mathrm{Ra} = 2\mathrm{Ra}_c$ in black, heat is transported by convection regardless of the presence of the elliptical instability and thus the black line is maintained above $\mathrm{Nu} = 1$. The bursts of the elliptical instability contribute on top of this heat transport, and in general increase the Nusselt number and therefore enhance the heat transport. They can however temporarily decrease the heat transport compared to the purely convective case.

The simulation in Fig. 3.6c with $\epsilon = 0.1$, $\mathrm{Ra} = 6\mathrm{Ra}_c$ in red and $\epsilon = 0$, $\mathrm{Ra} = 6\mathrm{Ra}_c$ in black shows a secondary effect of the elliptical instability on the heat transport. The bursts increase heat transport, temporarily increasing the Nusselt number. The enhanced cyclonic vortex, as a result of the elliptical instability, on the other hand, slightly decreases the heat transport compared to the purely convective case. A similar reduction is observed in the presence of purely convective LSVs by Favier et al. (2014b) and Guervilly et al. (2014), which they proposed occurs because cyclonic vortices act to effectively increase

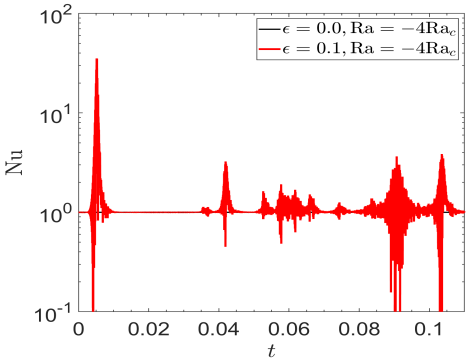

(a) Nu of the simulation with $\epsilon = 0$ (black) and $\epsilon = 0.1$ (red), $\mathrm{Ra} = -4\mathrm{Ra}_c$.

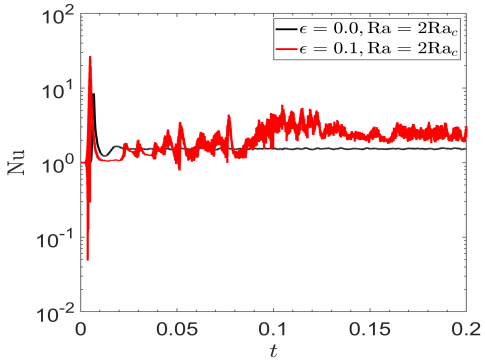

(b) Nu of the simulation with $\epsilon = 0$ (black) and $\epsilon = 0.1$ (red), $\mathrm{Ra} = 2\mathrm{Ra}_c$.

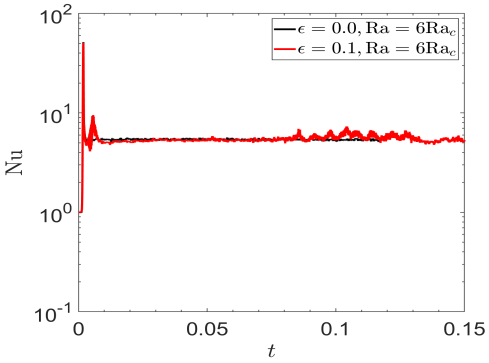

(c) Nu of the simulation with $\epsilon = 0$ (black) and $\epsilon = 0.1$ (red), $\mathrm{Ra} = 6\mathrm{Ra}_c$.

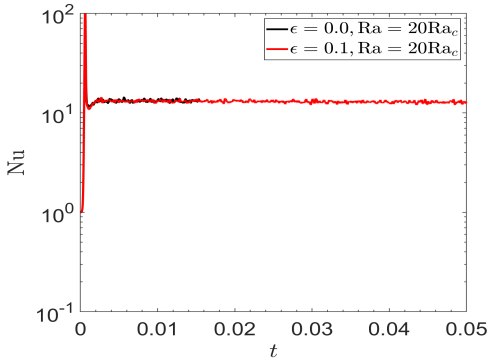

(d) Nu of the simulation with $\epsilon = 0$ (black) and $\epsilon = 0.1$ (red), $\mathrm{Ra} = 20\mathrm{Ra}_c$.

Figure 3.6: Nusselt number as a function of time at various Rayleigh numbers with the background tidal flow with $\epsilon = 0.1$ (red) and without the background tidal flow (black). Inertial (or inertia-gravity for $\mathrm{Ra} < 0$) waves excited during bursts of the elliptical instability transport heat and therefore temporarily increase the heat transport. The increased energy in the vortex modes suppresses the heat transport further compared to the simulations with $\epsilon = 0$.

the rotation in a significant fraction of the domain, thus further constraining the vertical motions, and as a consequence the heat transport, according to the Taylor-Proudman theorem (e.g. Currie et al., 2020).

Finally, no bursts of the elliptical instability appear present in the simulation in Fig. 3.6d with $\epsilon = 0.1$, $\mathrm{Ra} = 20\mathrm{Ra}_c$ in red and $\epsilon = 0$, $\mathrm{Ra} = 20\mathrm{Ra}_c$ in black. In fact, there seems to be a slight reduction of the Nusselt number in the simulation with $\epsilon = 0.1$. The sustained energy injection from the interaction of convection and the equilibrium flow slightly enhances the 2D energy of the vortex, which slightly diminishes the total heat transport.

The effects of the elliptical instability on heat transport can be further quantified using time-averages of the Nusselt number shown in Fig. 3.7, for simulations performed with $\epsilon = 0$ and $\epsilon = 0.1$. Due to the absence of bursts of the elliptical instability, there is no observable enhancement to the heat transport when the convection is strong. The inhibition of the heat transport as a result of the more energetic LSV is possibly supported

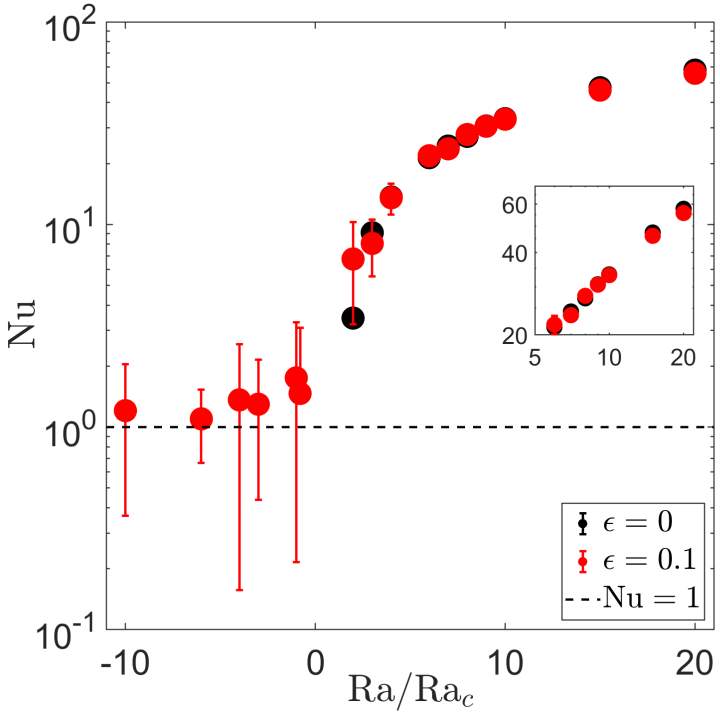

Figure 3.7: Time-average of the Nusselt number with (orange) and without (blue) the elliptical instability. The elliptical instability results in heat transport when it operates, even in the stably stratified regime ($\mathrm{Ra} < 0$). When it does not operate the enhanced energy in the convective LSV results in reduced heat transport for $\mathrm{Ra} > 0$, see inset. $\mathrm{Nu} = 1$ means there is no net heat transport by fluid motions (black dashed line).

by the inset at $\mathrm{Ra} = 15\mathrm{Ra}_c$ and $\mathrm{Ra} = 20\mathrm{Ra}_c$, where the Nusselt number is slightly reduced in the $\epsilon = 0.1$ case compared to the $\epsilon = 0$ case. At low positive Rayleigh numbers, the elliptical instability plays a major role in enhancing or hindering the heat transport as a function of time. For very weak convection, in which there is no convectively-generated LSV, the elliptical instability enhances the net heat transport strongly, while at stronger convective driving it cancels or slightly decreases the heat transport. Finally, the elliptical instability does indeed produce heat transport in stably stratified fluids, although the additional heat transport is highly variable in time, only occurring during a burst in energy injection of the elliptical instability, and decreases as the stratification increases (i.e., $-\mathrm{Ra}$ increases). This is represented by the Nusselt number tending towards one on average as the fluid becomes more stably stratified, where we note that the elliptical instability is linearly unstable in all plotted cases. Hence the elliptical instability could potentially play a role in heat transport in regions of planets that are nearly neutrally stratified.

3.2 Analysis of the sustained tidal energy injection

We have found that the elliptical instability can be inhibited by the convective LSV in our simulations, instead allowing a sustained energy injection to arise within the flow. Therefore, it is of interest to test at which parameter values this occurs and to make an

attempt to identify the leading cause of this effect. We will examine the 3D component of the flow in both real and spectral, i.e. Fourier, space. To this end we have performed a range of simulations in which ϵ and Ra are varied, again at constant $\mathrm{Ek} = 5 \cdot 10^{-5.5}$ to determine when sustained energy injection (versus burstiness) is obtained.

3.2.1 Parameter regime for sustained tidal energy injection

First, a "phase diagram" was created based on these simulations, plotted in Fig. 3.8, which indicates in which simulations we observe bursts of the elliptical instability, and in which we observe sustained energy injection. Simulations containing any bursts of the elliptical instability – even when it is a solitary burst at the start of the simulation – have been labelled "bursty" (orange markers), while simulations containing no such bursts have been labelled "sustained" (blue markers). Bursty simulations may still feature a sustained energy injection, however, in the interests of determining where the bursts of the elliptical instability still exist we have classified them as bursty here. Some of the simulations are very difficult to tell by eye whether they are bursty or sustained, and have therefore been labelled as "uncertain" (yellow markers). The transition between the two "phases" is likely situated close to these markers. Finally, one point has been labelled "neither", namely the point corresponding to the simulation with $\epsilon = 0.02$, $\mathrm{Ra} = 2\mathrm{Ra}_c$. This simulation features no bursts as the elliptical instability is too weak to operate at this level of convection. However, it also does not display any sustained energy injection. Of further note is that at this supercriticality ($\mathrm{Ra}/\mathrm{Ra}_c$) the LSV is absent, which was also observed by Guervilly et al. (2014), and they observed this absence to be independent of Ekman number. Clearly the suppressive effects of the convective LSV are very important to the elliptical instability in the local box model, as the elliptical instability in simulations with ellipticities up to $\epsilon = 0.1$ can be suppressed by relatively low supercriticalities, at this chosen Ekman number. The suppressive effects of the LSV in the phase diagram appear most important at low ellipticity, as the "phase transition" seems to follow a sub-linear curve. One explanation for this sub-linear curve could be the relative importance of viscous effects at low ellipticity. The growth rate of the elliptical instability is low, and therefore any applied viscous effects are comparatively more important than at high ellipticity. As such the reductive effects the convective LSV might have are exacerbated at these low ellipticities.

To explain the absence of bursts of elliptical instability we investigate the 3D modes in the flow in both real space and Fourier space. The 3D modes should contain only the inertial waves excited by the elliptical instability and convective eddies. By studying these modes we should be able to identify whether the elliptical instability has ceased operation completely or the sustained energy injection obfuscates the bursts of the elliptical instability instead.

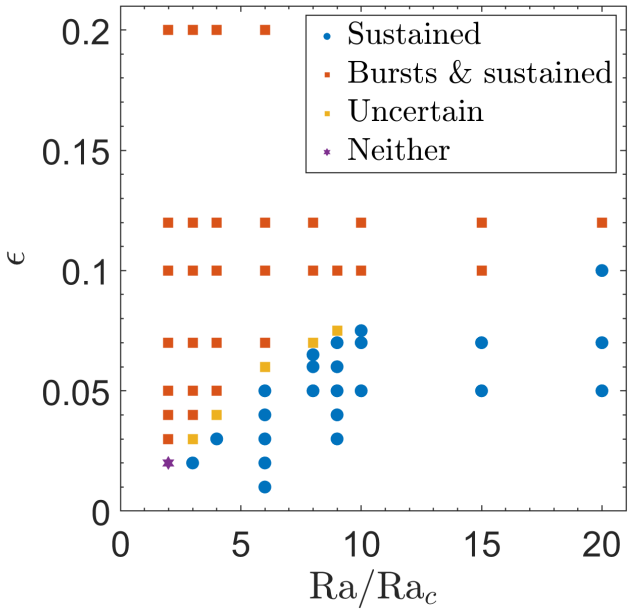

Figure 3.8: "phase diagram" showing the observed behaviour in our simulations. Simulations where sustained behaviour but no bursts of elliptical instability are observed are marked in blue, those with clear bursts of the elliptical instability (and possible additional sustained behaviour) are marked in orange. The "uncertain markers" represent simulations close to where the regime transition is likely situated. The case $\epsilon = 0.02$, Ra $= 2\text{Ra}_c$ is marked in purple, as it shows neither sustained injection nor bursts of elliptical instability.

3.2.2 Velocity magnitude analysis

In real space we employ a method akin to the one used in Favier et al. (2019) to determine the 3D flow. The 3D velocity components are obtained by taking the difference between the total velocity and the z-averaged horizontal (or 2D) velocity components:

$$\begin{aligned} u_{x,3D} &= u_x - \langle u_x \rangle_z, \\ u_{y,3D} &= u_y - \langle u_y \rangle_z, \\ u_{z,3D} &= u_z. \end{aligned} \tag{3.1}$$

Here, $\langle u_x \rangle_z$,$\langle u_y \rangle_z$ are the depth-averaged x and y components of the velocity, respectively, i.e. the horizontal velocity components. From this, the magnitude of the 3D velocity, $|\boldsymbol{u}_{3D}|$, is calculated. Favier et al. (2019) showed that the convective LSV suppresses 3D motions, resulting in a region with lower 3D velocities inside the vortex. Since we observe similar LSVs, such a suppression of 3D modes might contribute to the suppression of the elliptical instability.

First, we examine a case of convection in isolation using this method in Fig. 3.9a, with parameters $\epsilon = 0$, Ra $= 6\text{Ra}_c$. We show results for $|\boldsymbol{u}_{3D}|$ at $t = 0.1$ at the mid-plane ($z = d/2$). The convective LSV is centred in the figure. The 3D velocity magnitude is reduced under the convective vortex compared to the edges of the figure. Thus our results

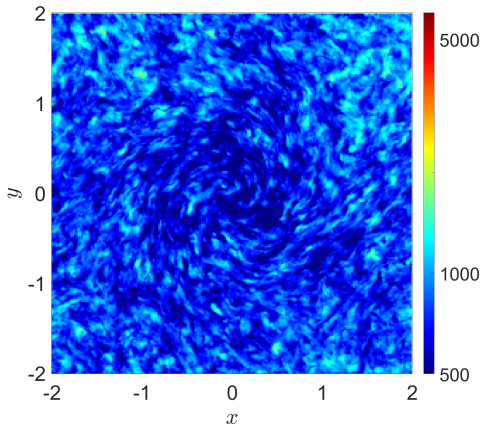

(a) $t = 0.1$, $\epsilon = 0$, Ra $= 6$.

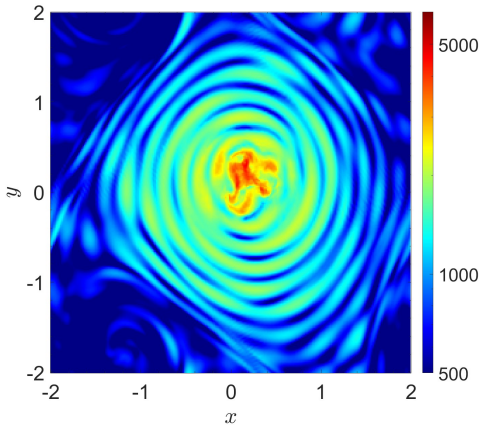

(b) $t = 0.05$, $\epsilon = 0.1$, Ra $= 0$.

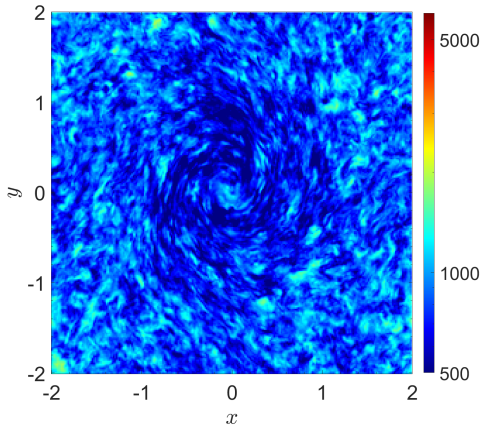

(c) $t = 0.04$, $\epsilon = 0.1$, Ra $= 6$.

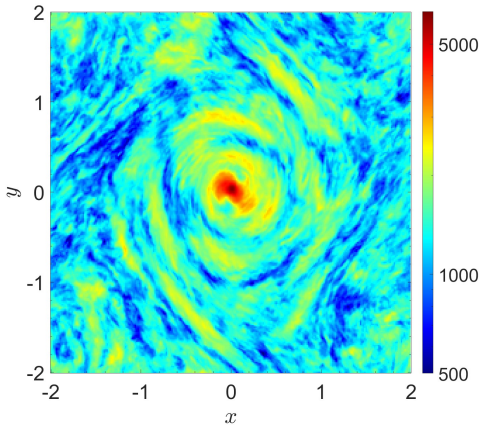

(d) $t = 0.1$, $\epsilon = 0.1$, Ra $= 6$.

Figure 3.9: The magnitude of the 3D velocity, $|\boldsymbol{u}_{3D}|$, showing its localisation within the vortices. (a) Elliptical instability in isolation. (b) Convection in isolation. (c) Elliptical instability and convection in the absence of a burst. (d) Elliptical instability and convection in the presence of a burst. The convective LSV suppresses 3D motions. If the elliptical instability is operating, the energy in the 3D motions is concentrated in the vortex core. The vortices are centred for clarity.

agree with those of Favier et al. (2019).

Next, we examine a case of the elliptical instability in isolation using this method in Fig. 3.9b, with parameters $\epsilon = 0.1$, $\mathrm{Ra} = 0$. The time-evolution of the kinetic energy of this simulation can be found in the left-hand panel of Fig. 3.2. We show results at $t = 0.05$ during a burst of instability, after vortices have formed following initial saturation. The largest velocities during a burst are located in the vortex core, as expected for the elliptical instability (Leweke et al., 2016). The 3D velocity magnitudes are much larger than those in the purely convective case, because the elliptical instability transfers large amounts of energy to inertial waves.

In Fig. 3.9c we show a result from a simulation with both the elliptical instability and convection, using the parameters $\epsilon = 0.1$, $\mathrm{Ra} = 6\mathrm{Ra}_c$, the kinetic energy of which is given in Fig. 3.4c. This snapshot was taken at $t = 0.04$, which corresponds to the absence of a burst, as well as having been a significant amount of time since the initial burst. However, the sustained energy injection has been operating during the entire simulation, as was shown in Fig. 3.4d. Indeed, as there is no burst of the elliptical instability, the figure is very similar to that of the purely convective simulation in Fig. 3.9a.

Finally, in Fig. 3.9d, we show a result from the same simulation with the elliptical instability and convection, using the parameters $\epsilon = 0.1$, $\mathrm{Ra} = 6\mathrm{Ra}_c$ during a burst of the elliptical instability at $t = 0.1$. We again observe that the highest velocities are concentrated in the centre of the vortex, but the energy appears to be more spatially spread out than in the simulation with the elliptical instability in isolation.

Bursts of the elliptical instability are thus primarily concentrated in the centre of the cyclonic portion of the LSVs. The LSV is therefore expected to have a strong effect on the growth of the elliptical instability, as the free inertial waves existing within these vortices will differ from those of the original flow, thus acting as a constraint to potentially de-tune the elliptical instability. Furthermore, one might expect that if no concentration of excess energy is observed inside the vortex core in a simulation, like in our simulations which show only sustained energy injection and no bursts, then the elliptical instability is not, or is only very weakly, operating in said simulation.

3.2.3 Frequency-wavenumber spectrum analysis

We now present further analysis of our simulations using the approach devised by Le Reun et al. (2017) by computing the frequency-wavenumber spectrum of the flow to identify the inertial waves and the convection. This Fourier space analysis shown in Fig. 3.11 uses two properties of the elliptical instability to be able to identify its operation in the spectrum: 1) the excited inertial waves have a preferred direction (wavevector orientation) and 2) the dispersion relation of the inertial waves relate each direction to a particular frequency.

Analysis in Fourier space is done by considering the power or squared amplitude of each Fourier mode instead of examining the power at a physical location in the flow, as in the previous section. To this end, we use the Fourier transformed versions of the flow

fields above. We define the direction of a Fourier mode as the angle the wavevector makes with the rotation axis, which we denote by θ. This angle can then be determined from the ratio $k_z/k = \cos\theta$. The power in each velocity component, i.e. $u_x,\ u_y,\ u_z$, associated with a specific wavevector can be put into a bin corresponding to its angle and wavenumber (wavevector magnitude) at every output timestep in the simulation. We use 60 bins for the angle θ, with $\theta = [0, \pi/2]$; likewise we have chosen bins of size $\pi/2$ for the k-bins and enough of these to cover all values allowed by the spatial resolution of the simulation. By binning like this we produce a 2D contour plot of power in each wavevector bin versus angle, and by outputting this data at every output timestep in the simulation we generate a $\theta - k - t$ matrix.

We are, however, predominantly interested in obtaining a spectrum as a function of the frequency and angle, because this allows us to compare to the dispersion relation of inertial waves and thus identify if (and which) inertial modes are excited in the simulation. Therefore we sum over the k-bins, resulting in the total power per velocity component in each wavevector angle bin, at each timestep. Equal timesteps of size 10^{-6} are used, such that the highest frequency inertial waves, with periods $\pi \cdot 10^{-4.5}$ can be properly captured. The Fourier transform in time of all three velocity components produces the frequency spectrum of each velocity component. We then multiply the transformed velocities with their complex conjugates and add all three components to obtain the energy in each ω and θ bin. We consider the interval of wavenumber bins $[2, 50]$, i.e the wavenumbers $k \in [\pi, 25\pi]$, to avoid the contribution of small-scale motions which contain little energy. The geostrophic modes with $\theta = \pi/2$ strongly dominate the energy, so for clarity we set the rightmost column at $\theta = \pi/2$ to zero on these plots since we wish to analyse the waves.

We want to identify the inertial modes in our simulations, and so we plot the dispersion relation of inertial waves on the $\theta - \omega$ energy spectra. We opt to plot the dispersion relation of pure inertial waves given in Eq. (1.45) (in the absence of vortices and stratification) as a solid black line on all $\theta - \omega$ energy spectra. This choice is suitable for the Rayleigh numbers plotted, because convection tends to reduce the magnitude of the buoyancy frequency in the bulk of the box, leading to an effective buoyancy frequency: $N^2_{\text{eff}} > N^2$ (keeping in mind that N^2 is negative). This is most readily seen by considering the horizontally-averaged temperature profile in a simulation.

In Fig. 3.10 the conduction profile, T, as given by Eq. (2.10), is plotted in dashed-grey, corresponding to a simulation with $\epsilon = 0.1,\ \text{Ra} = 4\text{Ra}_c$. Allowing the temperature perturbation, θ, to evolve in these simulations results in the partial homogenisation of the temperature profile. The horizontally-averaged total temperature profile, represented by the sum of the conduction profile and the temperature perturbation, at time $t = 0.1$, is plotted in the same figure in solid-black. The profile in the bulk as a function of z has become less steep, but thermal boundary layers at the top and bottom of the simulation domain have appeared. Upon plotting an effective temperature profile in the bulk in solid-red, we find that it is well represented by an effective temperature gradient of $\Delta T_{\text{eff}} \propto 1.5\text{Ra}_c$. In this simulation the effective buoyancy frequency, and thus effective

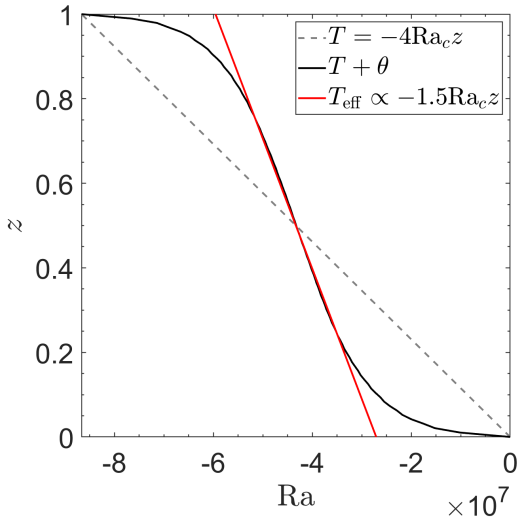

Figure 3.10: The horizontally-averaged temperature profile of the simulation in Fig. 3.3 with $\epsilon = 0.1, \mathrm{Ra} = 4\mathrm{Ra}_c$ at $t = 0.1$. The background conduction state profile is plotted in dashed-grey, while the partially homogenised total temperature profile is plotted in solid-black. The temperature gradient in the bulk has decreased, while the boundary layer temperature profile is steeper. The effective temperature gradient in the bulk has been approximated as roughly $\Delta T_{\mathrm{eff}} = 1.5\mathrm{Ra}_c$, plotted in solid-red.

Rayleigh number, are therefore adjusted to $N^2_{\mathrm{eff}} = -\mathrm{Ra}_{\mathrm{eff}} \approx -1.5\mathrm{Ra}_c$. At the other examined Rayleigh numbers of $\mathrm{Ra} = 6\mathrm{Ra}_c$ and $\mathrm{Ra} = 8\mathrm{Ra}_c$ the respective effective buoyancy frequencies are: $N^2_{\mathrm{eff}} \approx -2.5\mathrm{Ra}_c$ and $N^2_{\mathrm{eff}} \approx -3\mathrm{Ra}_c$. This implies that $N^2_{\mathrm{eff}}/\Omega^2 \sim \mathcal{O}(10^{-2})$ at the Rayleigh numbers used in these simulations; thus the second term in the dispersion relation of inertia-gravity waves in Eq. (1.52) is close to zero, only affecting the dispersion relation around $\theta \approx \pi/2$. We conclude that the usage of the pure inertial waves dispersion relation is a good approximation.

The initial bursts of the elliptical instability on the $\theta - \omega$ energy spectra are expected to be located at their preferred angle of $\theta = \arccos(1/2) = \pi/3$ (when $\gamma = \Omega$). Combined with the dispersion relation, the fastest growing mode of the elliptical instability is expected to be located at $\theta = \pi/3$, $\omega = \Omega$ on these figures. An example where we can clearly identify these inertial modes excited by the elliptical instability is given in Fig. 3.11a, computed from the linear growth phase of the simulation with $\epsilon = 0.05$, $\mathrm{Ra} = 0$. All modes with non-negligible energy during the linear growth phase are shown to be centred on this point, as well as at $\theta = \pi/3$, $\omega = 3\Omega$, where the latter result from secondary "non-linear" interactions between the background tidal flow with frequency 2Ω (and wavenumber zero) and the dominant modes at $\omega = \Omega, \theta = \pi/3$.

The spectrum of the same simulation as Fig. 3.11a directly after the linear growth phase is shown in Fig. 3.11b. Most of the power is concentrated around the initial fastest growing modes, however the energy is also spread throughout the figure, away from the dispersion relation, i.e. the resulting energy is no longer solely contained in inertial waves. This is likely to represent the turbulent motions arising after the collapse of inertial waves.

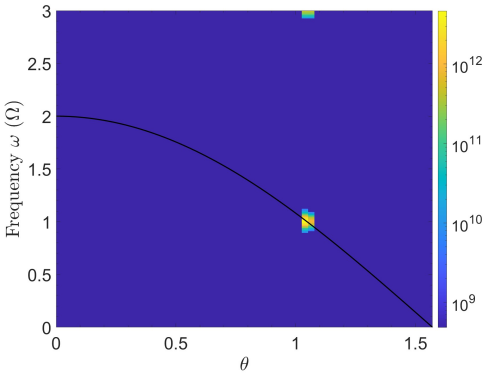

(a) Linear growth phase of the simulation with $\epsilon = 0.05$, $\mathrm{Ra} = 0$.

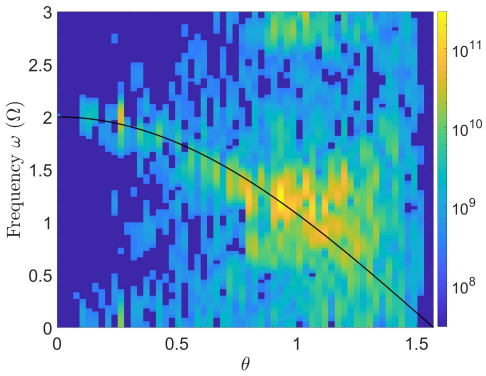

(b) Inertial wave breakdown of the simulation with $\epsilon = 0.05$, $\mathrm{Ra} = 0$.

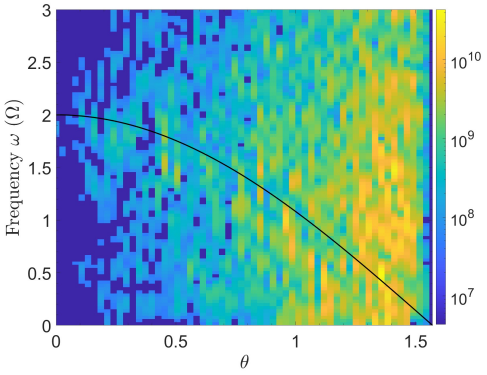

(c) $t = 0.11 - 0.13$ of the simulation with $\epsilon = 0$, $\mathrm{Ra} = 6\mathrm{Ra}_c$.

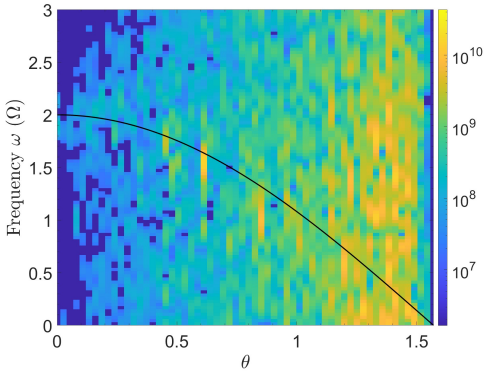

(d) $t = 0.11 - 0.13$ of the simulation with $\epsilon = 0.05$, $\mathrm{Ra} = 6\mathrm{Ra}_c$.

Figure 3.11: Various $\theta - \omega$ energy spectra obtained by Fourier transforming the $t - \theta$ spectrum, where ω is given in units of Ω. The interval of wavenumber bins used is: $[2, 50]$, i.e. $k \in [\pi, 25\pi]$. The black solid line shows the dispersion relation for free inertial waves. For visibility the rightmost column containing the geostrophic modes which would otherwise dominate is set to zero.

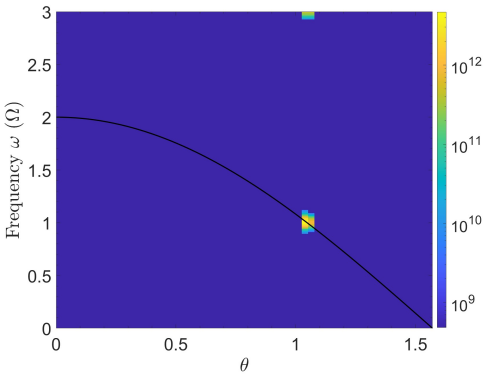

(a) Linear growth phase of the simulation with $\epsilon = 0.05$, Ra $= 0$.

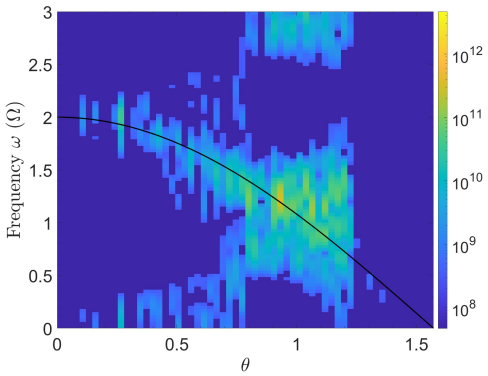

(b) Inertial wave breakdown of the simulation with $\epsilon = 0.05$, Ra $= 0$.

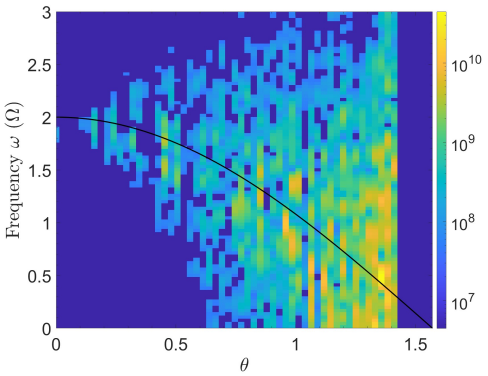

(c) $t = 0.11 - 0.13$ of the simulation with $\epsilon = 0$, Ra $= 6\text{Ra}_c$.

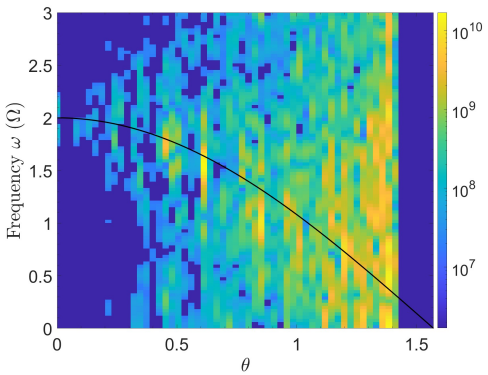

(d) $t = 0.11 - 0.13$ of the simulation with $\epsilon = 0.05$, Ra $= 6\text{Ra}_c$.

Figure 3.12: Same as Fig. 3.11, except the interval of wavenumber bins is reduced to $[2, 12]$, i.e. $k \in [\pi, 6\pi]$. This removes most convective modes from the RHS of the figure, allowing for clearer visibility of the inertial waves. The black solid line is the dispersion relation. The geostrophic modes which dominate the flow are set to zero for visibility of other modes.

There is also energy in the geostrophic modes ($\theta \sim \pi/2$, omitted for clarity) as well as the "mirrored dispersion relation", given by: $\omega = -2\Omega\cos\theta + 2\Omega$, from secondary non-resonant interactions of the waves with the tidal flow (Le Reun et al., 2017).

Fig. 3.11c shows the spectrum of a simulation of rotating convection without the elliptical instability, with $\epsilon = 0$, Ra $= 6\text{Ra}_c$ from $t = 0.11$ to $t = 0.13$. Convection is shown to introduce modes at high values of θ. This can be understood from linear growth rate predictions, where we can show that convective instability of the conduction state requires $\theta \approx [1.4, \pi/2]$ for $n = 1$ modes at this Rayleigh number. The dominant modes are indeed concentrated in convective modes at $\theta \approx [1.4, \pi/2]$ in this figure. Convective modes at onset are steady, so they should have $\omega \sim 0$ and be concentrated at the bottom of this figure. Instead, it appears that a host of convective eddies with non-zero frequencies are generated. Some of these eddies have frequencies below the rotational frequency, as we would expect because the convective turnover frequency is smaller than the rotational frequency. On the other hand, a significant number of eddies are generated with frequencies

that are larger than the rotational frequency, indicating numerous shorter-lived eddies in the convectively unstable simulations. The power away from these modes, i.e. outside the range $\theta \approx [1.4, \pi/2]$, broadly follows the dispersion relation. We might therefore speculate that the turbulence generated by convection is swept up by rotation into inertial waves, explaining the frequency of these modes. Inertial waves in rotating convection are expected to arise from oscillatory convective modes if $\mathrm{Pr} < 1$ (technically for $\mathrm{Pr} < 0.677$) (Chandrasekhar, 1961), and have previously been observed in simulations (Lin, 2021) at $\mathrm{Pr} < 1$. Supporting our argument for inertial waves arising due to rotating convection at $\mathrm{Pr} \geq 1$ is the detection of inertial waves at $\mathrm{Pr} > 1$ in spherical shell simulations of rotating convection (Bekki et al., 2022).

Spectra featuring both the elliptical instability and convection would be expected to look like a combination of these features, although it is likely to be difficult to distinguish the turbulent phases of the elliptical instability from the convective motions. However, the location of the elliptical instability bursts should shed some light on whether the sustained energy injection contains a weak (overshadowed) burst or whether the elliptical instability is absent entirely. The spectrum of the simulation with $\epsilon = 0.05$, $\mathrm{Ra} = 6\mathrm{Ra}_c$ analysed from $t = 0.11$ to $t = 0.13$ is shown in Fig. 3.11d. This shows the expected convective modes, but no enhanced power at the expected location of the elliptical instability. Similar spectra produced at other times in the simulation produce similar results. Thus we conclude that the operation of the elliptical instability has been inhibited by convection at these parameters.

Convective motions are expected to be small-scale motions, based on the visible fluctuations in Fig. 3.1, Fig. 3.9d and on the linear theoretical analysis of convection, which at these parameters predicts unstable modes in the interval of wavenumber bins $[30, 50]$. Meanwhile, the energetically dominant inertial waves are likely to be large-scale. This is a direct consequence of the elliptical instability being directional, and therefore scale-free, and thus choosing the mode with the smallest viscous effects (the largest possible modes, which also have the longest non-linear cascade times). Therefore we have reproduced the plots in Fig. 3.11 with the limited range of wavenumber bins $[2, 12]$, i.e. $k \in [\pi, 6\pi]$, in Fig. 3.12. One effect of the limited wavenumber range, combined with our finite grid, is that a number of columns on the right will contain no energy. Only higher wavenumbers can have these angles. The limited range of k does not affect the linear growth spectrum in Fig. 3.12a as the power is concentrated in wavenumbers within our adopted range. During the inertial wave breakdown in Fig. 3.12b we can clearly see the power concentrated along the inertial wave dispersion relation, as well as the mirrored dispersion relation representing the secondary non-resonant interactions between the waves and the background tidal flow (Le Reun et al., 2017). In the convective simulations in the bottom two panels there is indeed power along the dispersion relation where inertial waves are expected, providing another tentative hint for inertial waves in rotating convection. There is however still no clear energy located at the location where we would expect energy injection if the elliptical instability is operating in Fig. 3.12d.

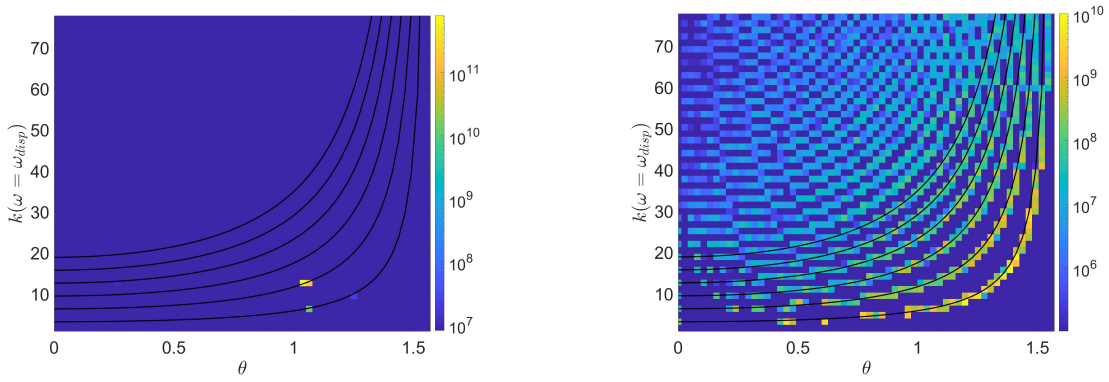

Figure 3.13: Energy in each wavenumber as a function of θ on the dispersion relation, i.e. all wavenumbers have a frequency ω which satisfies $\omega = 2\Omega\cos\theta$. The solid black curves are given by $k = n_z\pi/\cos\theta$, for $n_z = 1, 2, 3, 4, 5, 6$. The finite vertical resolution implies power must be along one of these curves. Left: during the linear growth phase for $\epsilon = 0.05$, $\mathrm{Ra} = 0$. Right: $t = 0.11 - 0.13$ for $\epsilon = 0.05$, $\mathrm{Ra} = 6\mathrm{Ra}_c$.

Using the Fourier spectrum we can determine the wavenumbers that contain the most energy in the simulation as a function of θ at a given ω. To this end, we do not sum over all wavenumbers k, but instead construct a $\theta - k$ spectrum in Fig. 3.13. We are interested in the wavenumber magnitudes that are active on the pure inertial wave dispersion relation. Therefore we have done a Fourier transform on the original $\theta - k - t$ matrix, resulting in a $\theta - k - \omega$ matrix. Slices of this matrix on the dispersion relation were taken by considering the energy in all k-values at a combination of ω and θ that satisfy the dispersion relation.

The left-hand panel of Fig. 3.13 shows the same simulation as Fig. 3.11a, i.e. pure elliptical instability during its linear growth phase. The power here is concentrated along various black solid curves defined by the relation between θ, the vertical wavenumber, $k_z = n_z\pi$, and total wavenumber, k: $\theta = \arccos(k_z/k)$. Each curve has a different integer vertical wavenumber n_z, with $n_z = 1$ the lowest curve, $n_z = 2$ the one above, etc. The curves with $n_z = 1, 2, 3, 4, 5, 6$ are plotted. In this simulation the energy of the elliptical instability burst is concentrated in modes with $n_z = 2$, $k = 4\pi$. The mode corresponding to this with horizontal wavenumber integers $n_x = n_y$ is the $(5, 5, 2)$ mode. This method of analysis is powerful as it clearly shows which inertial modes are growing in the simulation. In the right-hand panel of Fig. 3.13 this method is applied to the same simulation as in Fig. 3.11d of both convection and the elliptical instability in the sustained regime. This panel shows that there is less power on the $(5, 5, 2)$ mode. Instead, we see power concentrated on the $n_z = 1$ curve, and concentrated towards higher wavenumbers and higher angles, as we would expect of convective motions. So indeed, we observe no clear sign of the elliptical instability during this simulation, but do observe convective eddies which are inertial wave-like.

To examine the effect of different box sizes, we have run the simulation of the elliptical instability on its own in a 1-by-1-by-1 box. To accommodate the smaller box

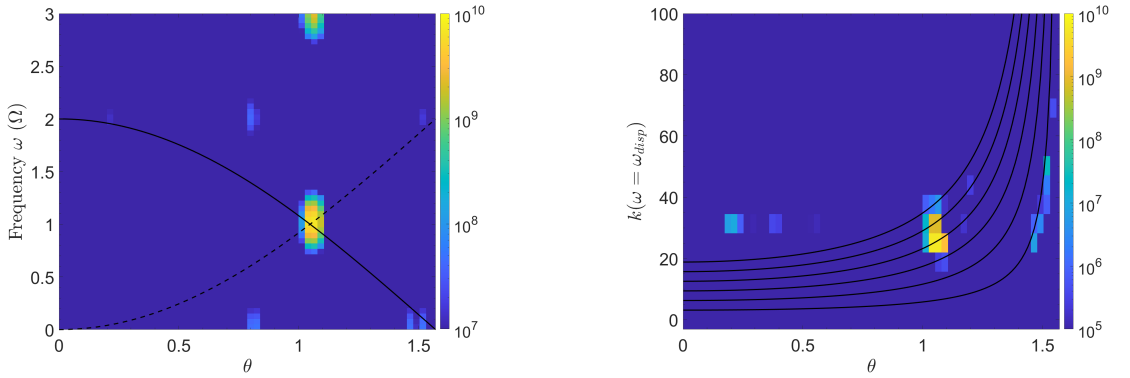

Figure 3.14: Energy in a $\theta - \omega$ spectrum and $\theta - k$ spectrum on the dispersion relation in a 1-by-1-by-1 box during the linear growth phase. Left: the location of the energy in the inertial waves is unchanged, as expected. Right: The smaller box size results in larger horizontal wavenumber and thus larger vertical wavenumbers to satisfy the resonance condition. The larger wavenumber results in a stronger reduction of the growth rate due to viscosity.

size, the wavenumber bin size has been increased to 2π, and we again consider the interval of wavenumber bins $[2, 50]$. The left-hand panel of Fig. 3.14 shows the $\theta - \omega$ spectrum of the energy of a simulation with parameters $\epsilon = 0.1$, $\mathrm{Ra} = 0$. This simulation captures the behaviour during the linear growth phase of the elliptical instability. The reduced horizontal box size changes the available modes, but the power is still concentrated at the expected value of $\theta = \pi/3$, $\omega = \Omega$. The right-hand panel of Fig. 3.14 shows the $\theta - k$ spectrum on the dispersion relation of the same simulation. These are the linearly most unstable modes. The dominant k modes lie on lines of $n = 4$ and $n = 5$. These larger values of k imply larger decay rates $-\nu k^2$, and therefore a decreased growth rate due to viscosity. This suppresses the elliptical instability for larger ϵ when the box is smaller. The suppression of the elliptical instability is thus artificially enhanced (reduced) by the choice of a smaller (larger) box. Upon extrapolating this effect to a full planet, and assuming that a planet-scale mode is excited, one might expect the viscosity suppression of the elliptical instability to be weak.

Finally, we are interested in analysing further the energy injection term I_{3D}. The 3D component is any component that is not in the rightmost column of these $\theta - \omega$ spectra (since that column has $\theta = \pi/2$, implying that $n_z = 0$). Therefore to study I_{3D} we just set the rightmost column to zero, which was already done for visibility in the above plots. I_{3D} is calculated from the Reynolds stress components $u_x u_y$, u_x^2 and u_y^2. After calculation, this quantity is Fourier transformed, and its real part is then plotted here. The colourbar minimum has been increased compared to previous figures to reduce the impact of convective noise on the figure. In the panel on the left of Fig. 3.15 we show just the elliptical instability, for the same simulation as Fig. 3.11a with $\mathrm{Ra} = 0$, $\epsilon = 0.05$, during the linear growth phase. We see that the energy injection is into the resonant inertial waves during this initial burst. It seems two frequency bins in particular contain

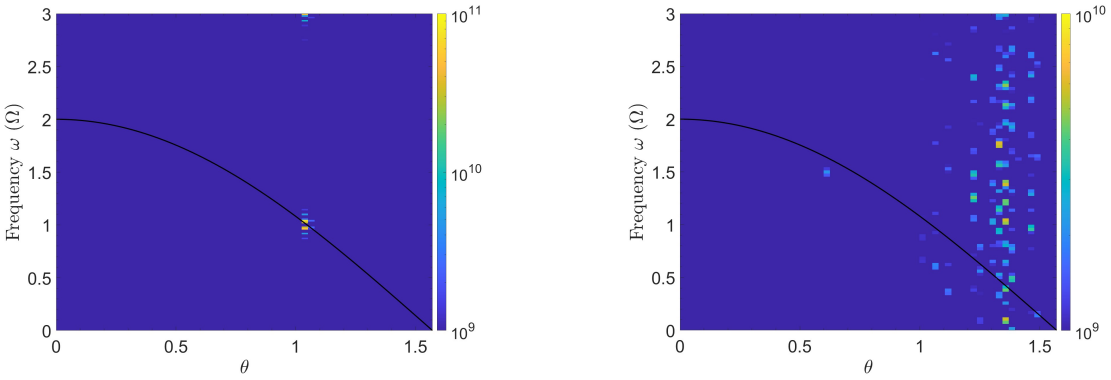

Figure 3.15: The $\theta - \omega$ I_{3D} spectrum obtained by calculating I_{3D} and taking the real part of the Fourier transform of the $\theta - t$ spectrum; ω is given in units of Ω. The interval of wavenumber bins is $[2, 50]$. The black solid line is the dispersion relation. For visibility the rightmost column containing the geostrophic modes which dominate the flow is set to zero. Left: linear growth phase of $\epsilon = 0.05$, $\mathrm{Ra} = 0$. Right: $t = 0.11 - 0.13$ of $\epsilon = 0.05$, $\mathrm{Ra} = 6\mathrm{Ra}_c$.

the majority of the energy injection, one of these bins is located on the dispersion relation and the other on the mirrored dispersion relation. To compare, I_{3D} of the same simulation as Fig. 3.11d with $\mathrm{Ra} = 6\mathrm{Ra}_c$, $\epsilon = 0.05$ is plotted in the right-hand panel of Fig. 3.15. Energy injection is present predominantly in the range $\theta \approx [1.4, \pi/2]$ and is no longer concentrated along the dispersion relation, suggesting the energy injection is primarily into convective motions, instead of the inertial waves of the elliptical instability. This would be consistent with treating the energy transfer between tidal and convective flows as being interpretable as a turbulent effective viscosity from the convective motions.

3.2.4 The elliptical instability on a convective background

Based on the real space analysis in Sec. 3.2.2 we concluded that the convective flow and its resulting LSV modifies subsequent growth of the elliptical instability, similar to the modification of the LSV resulting from the elliptical instability. Furthermore, based on the Fourier space results in Sec. 3.2.3 we found that the elliptical instability is largely inhibited by the convective flow (and its LSV) for lower values of ϵ.

To further examine the effects of convection on the elliptical instability, we analyse the growth rate of bursts of the elliptical instability on a convective background. First we measured the growth rates in simulations without convection ($\mathrm{Ra} = 0$) as a reference. We split the results of each simulation into the initial burst and any further bursts. The initial burst should then be close to the linear prediction, although it is likely that for large values of ϵ the non-linear saturation, and thus end of the linear growth phase, is reached before the theoretical largest linear growth rate is achieved. Subsequent bursts are affected by non-linear effects, such as the LSV, and thus are expected to have reduced growth rates. The growth rate of the bursts of the elliptical instability is obtained from (half) the growth rate of K_{3D}, and our results after normalisation with $\gamma\epsilon$ are shown in

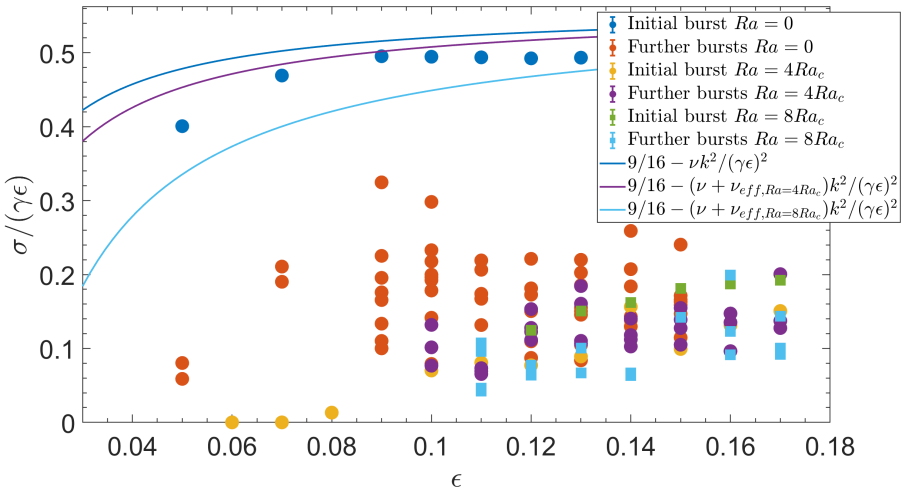

Figure 3.16: Growth rate of the initial burst and further bursts of the elliptical instability measured in simulations without convection Ra = 0 (blue and orange), and simulations restarted from a turbulent purely convective state (with an LSV) at Ra = 4Ra$_c$ (yellow and purple) and Ra = 8Ra$_c$ (green and cyan). The theoretical prediction for the inviscid linear growth rate without convection is plotted as a blue line, while predictions assuming an effective viscosity (with damping rate $-\nu_{\text{eff}}k^2$) from convection at Ra = 4Ra$_c$ and Ra = 8Ra$_c$ are plotted as purple and cyan lines, respectively. This figure implies that the reduction in the growth rate originates from something other than a simple effective viscosity, as the prefactor of the growth rate is changed, indicated by the growth rates tending to a value lower than 9/16 as ϵ is increased.

Fig. 3.16. The growth rates of the initial burst without convection (blue diamonds) lie close to the linear theoretical prediction, $(9/16)\epsilon\gamma$, plotted as the solid blue line. Further bursts of these simulations (orange diamonds), however, substantially deviate from this prediction. A large reduction of the growth rate is found, likely due primarily to the LSV created by the initial burst. Note that these growth rates reduce further as the simulation continues and the energy in the LSV grows.

To compare these with similar results in the presence of convection, we ran new simulations which have been initialised with the flow and temperature fields from a purely convective simulation long after saturation of the initial instability. We started several simulations with various ellipticities $\epsilon > 0.05$ from our simulation with Ra = 4Ra$_c$, $\epsilon = 0$, and several with $\epsilon > 0.1$ from our simulation with $\epsilon = 0$, Ra = 8Ra$_c$. These results are shown in Fig. 3.16 using yellow circles for the initial burst and purple circles for further bursts at Ra = 4Ra$_c$ and green and cyan squares at Ra = 8Ra$_c$, respectively. Focusing first on Ra = 4Ra$_c$, we see that the suppression of the initial burst of the elliptical instability occurs for $\epsilon \lesssim 0.07$. Our previous results and phase diagram (Fig. 3.8) indicated bursts of instability for $\epsilon \gtrsim 0.05$. These results also show that the growth rate is strongly affected by the convection, as the markers are substantially below the theoretical growth rate. The further bursts show a wide spread of growth rates. The highest measured growth rates overlap with those of the simulations of the pure elliptical instability. This implies that the convective LSV inhibits the elliptical instability in the same way as the LSV generated

by the elliptical instability itself, but can inhibit it even more strongly.

Our results for the case of more turbulent convection with $\mathrm{Ra} = 8\mathrm{Ra}_c$ show higher growth rates than at $\mathrm{Ra} = 4\mathrm{Ra}_c$, particularly at $\epsilon > 0.14$. This is possibly indicative of a reduced suppression of the elliptical instability or an enhancement of the growth rate as the convection becomes stronger. A possible explanation for the enhanced growth rate could lie in the linear growth rate of the elliptical instability presented in Eq. (2.60). Increasing the Rayleigh number increases $-N^2$ for the conduction state. However, at $\mathrm{Ra} = 8\mathrm{Ra}_c$ the growth rate is only increased by a factor of ≈ 1.13 compared to $\mathrm{Ra} = 0$, and even at $\mathrm{Ra} = 20\mathrm{Ra}_c$ the increase is only a factor of ≈ 1.3 compared to $\mathrm{Ra} = 0$. Furthermore, this factor is likely to be less important than this would predict, as convection acts to reduce $-N^2$ as we have shown in Fig. 3.10, and the efficiency of rotating convection increases with the Rayleigh number (Currie et al., 2020).

We compare these results with predictions for the linear growth rate in Fig. 3.16 after subtraction of the viscous damping rate. To this end, we first identify other simulations we have run with equal Rayleigh number to those under consideration in Fig. 3.16 but with sufficiently low ellipticity so that only sustained energy injection arises in the simulation. We then convert the sustained energy injection I_{3D} from these simulations to an effective viscosity ν_{eff} using Eq. (2.84). The effective viscosity obtained in this way is strictly parametrising the action of convection on the tidal flow rather than the inertial waves, but is at this moment the best estimate of the effective viscosity acting on the inertial waves. We add this effective viscosity to the fluid viscosity ν to obtain the "total viscosity", which is used to compute a viscous damping rate $-(\nu+\nu_{\mathrm{eff}})k^2$. Predictions for the growth rate after introduction of an effective viscous damping rate corresponding with $\mathrm{Ra} = 4\mathrm{Ra}_c$ and $\mathrm{Ra} = 8\mathrm{Ra}_c$ are plotted in purple and cyan lines, respectively, assuming the dominant wavenumbers and resonance conditions are unchanged. Incorporating the microscopic viscosity and/or effective viscosity decay rates are both inconsistent with the numerically-obtained growth rates. Indeed, results from simulations with just the elliptical instability imply that the suppression by an LSV is much stronger than would be predicted by this effective viscosity. Furthermore, the slope of the growth rate as a function of ϵ for simulations initialised on a convective background deviates from the 9/16 prediction in a similar manner with and without the convective background. To modify this 9/16 value there must be some change in the resonance conditions and the dominant wavenumbers, due to either de-tuning as previously remarked upon in this work, or the phases of the inertial waves, to explain the bursty behaviour.

We investigate the dominant wavenumber in each simulation, to examine if weakening of the elliptical instability occurs because the LSV changes this dominant wavenumber, using the approach described in Sec. 3.2.3. The $\theta - k$ spectrum for inertial modes following the dispersion relation is shown with $\epsilon = 0.15$ for two values of the Rayleigh number in Fig. 3.17. This shows that there is indeed a modification of the dominant wavenumber of the initial burst when initialising on a convective background. The $\theta - k$ spectrum in the left-hand panel shows the first elliptical instability burst in the simulation with

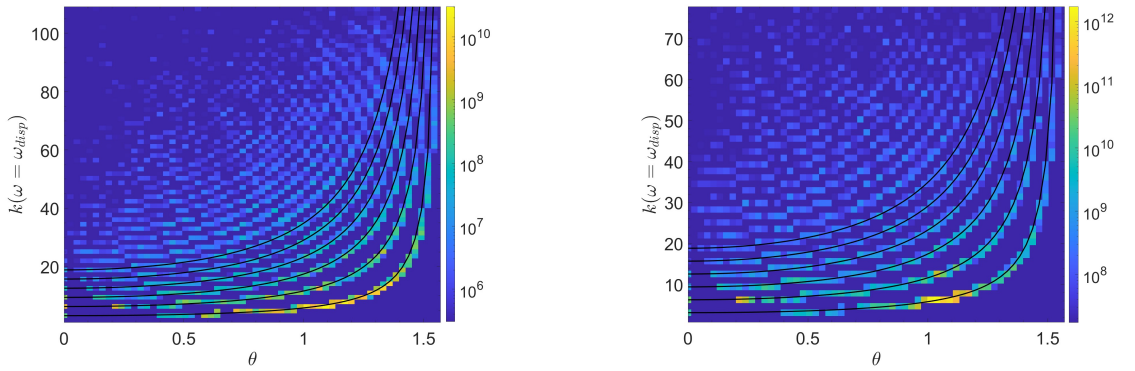

Figure 3.17: Same as Fig. 3.13 for simulations initialised from a convective simulation. Left: initial burst of $\epsilon = 0.15$, $\mathrm{Ra} = 4\mathrm{Ra}_c$, initiated from $\epsilon = 0$, $\mathrm{Ra} = 4\mathrm{Ra}_c$. Right: initial burst of $\epsilon = 0.15$, $\mathrm{Ra} = 8\mathrm{Ra}_c$, initiated from $\epsilon = 0$, $\mathrm{Ra} = 8\mathrm{Ra}_c$.

$\epsilon = 0.15$, $\mathrm{Ra} = 4\mathrm{Ra}_c$. The energetically dominant wavenumber is no longer the $(5, 5, 2)$ mode satisfying the ideal resonance condition without convection, and instead the power is concentrated at $n_z = 1$ with θ close to but larger than the ideal value $\theta = \pi/3$. In the right-hand panel of Fig. 3.17 we show the same for the first elliptical instability burst, but with $\epsilon = 0.15$, $\mathrm{Ra} = 8\mathrm{Ra}_c$. At both values of the Rayleigh number the subsequent inertial wave breakdown results in power in larger wavenumbers, including the (5,5,2) mode, which is viscously dissipated but otherwise maintained until the next burst. The availability of the (5,5,2) mode in the subsequent bursts results in higher growth rates compared to the initial burst, but still far below the ideal linear prediction. However, we observe power at the expected $k_z/k = 1/2$ and $\omega = \gamma$, therefore apparently arguing against the hypothesis that de-tuning the dominant resonance is responsible for most of the reduction in growth rate. This leaves the perturbed phase argument originally proposed by Barker and Lithwick (2013) to potentially explain the observed change of the growth rate prefactor.

3.3 Conclusions

In this chapter we have investigated the interactions of the elliptical instability and rotating Rayleigh-Bénard convection in a Cartesian model using pseudo-spectral hydrodynamical numerical simulations involving horizontal shearing waves. First, we simulated the elliptical instability without convection in wide boxes, and found the non-linear evolution of the instability to produce geostrophic vortices that dominate the flow to an even greater extent than in cubical boxes. The introduction of convection leads to a suppression of the elliptical instability that we find to be primarily the result of the convectively-generated LSV. It also gives rise to a sustained energy injection into the flow (i.e. transfer from the elliptical/tidal flow), which can be interpreted as the convection operating as an effective viscosity (approximately independent of ϵ, as we will show in Ch. 4) in damping the tidal flow.

Finally, we also found that the inertial waves excited by the elliptical instability can

transport heat; when the elliptical instability is weak relative to convection or suppressed this has little effect on the Nusselt number, but when the elliptical instability is comparable in strength to convection, it can significantly enhance transport. If the elliptical instability is suppressed however, the sustained energy injection from the tidal flow into the system results in a more energetic LSV, which then acts to suppress the heat transport. The Nusselt number therefore appears to be reduced at strong convective driving. The elliptical instability can also result in heat transport in stably stratified regimes, but this weakens as the stratification becomes stronger until the elliptical instability is no longer linearly unstable due to the stabilising effects of the stratification.

The suppression of the elliptical instability by convection was investigated in detail using numerous approaches. Measuring the 3D motions, which are weakened by the LSV, we found that during a burst of the elliptical instability the largest 3D velocities are found in the centre of the vortex. If the elliptical instability cannot operate, the vortex instead reduces the 3D velocities. We also presented a detailed analysis of the frequency and wavenumber Fourier spectra of the energy in our simulations to clearly identify inertial modes and convective flows. We observed that the elliptical instability (and energy injection into inertial modes more generally) is indeed inhibited by convective flows. Furthermore, we have found that rotating convection also weakly excites inertial modes, which are identified as power in modes along the dispersion relation, in the absence of the elliptical instability.

When initialising simulations of the elliptical instability from a convective turbulent state including an LSV it was found that this LSV reduces the growth rate of the elliptical instability compared with the inviscid or viscous growth rate prediction. It is also reduced compared with the prediction modified by crudely adopting the effective turbulent viscosity. The reduction of the growth rate by the LSV indicates that the dominant resonances are de-tuned by it or that there are significant perturbations in the phases of the waves by the LSV. Our Fourier space analysis showed that the identity of the fastest growing mode is unaltered by the presence or absence of an LSV for all bursts of elliptical instability. Because the fastest growing mode is unchanged from before, this should not result in a de-tuning effect for free inertial waves. The perturbation of the phases of the inertial waves by the convective vortex might therefore be more applicable as an explanation.

Chapter 4

Scaling laws for the elliptical instability and effective viscosity

In Ch. 3 we focused on exploring the fluid dynamical interactions of the elliptical instability and convection. Here we will quantify the tidal dissipation that arises from the elliptical instability, as well as the effective viscosity of the convection acting on the equilibrium tide.

The simulations studied in this work necessarily use dimensionless parameters that are far from the astrophysical ones, except perhaps for ϵ for the hottest of Hot Jupiters, for which the values we use are appropriate. Hence, we wish to obtain scaling laws for the energy injection due to the elliptical instability, as long as it operates, as well as the effective viscosity of convection acting on the equilibrium tide. For the latter we will use mixing-length theory and rotating mixing-length theory to interpret key convective quantities such as the vertical convective velocity, lengthscale and frequency and combine these to find an expression for the effective viscosity. We will attempt to verify that these quantities agree with our simulation results as well as testing whether they can be used to retrieve the three empirically-obtained regimes for the effective viscosity in Duguid et al. (2020). To ensure that our scalings are indeed applicable for the relevant dimensionless parameters, we extend the range of parameters surveyed by varying the Ekman number in addition to the Rayleigh number and ellipticity.

4.1 Scaling laws for the energy injection

When the flow is sufficiently turbulent and is not dominated by large-scale vortices that inhibit wave driving, the time-averaged value of the energy injection rate into the 3D modes, I_{3D}, due to the elliptical instability on its own scales consistently with ϵ^3 (Barker & Lithwick, 2013, 2014). However, the energy injection we observe in our simulations does not result from the elliptical instability alone. In fact, because the simulations indicate that the elliptical instability is inhibited by the convective LSV, we expect regions of parameter space where the energy injection is not the result of the elliptical instability

but rather solely the result of the convection interacting with the tidal flow. In Fig. 4.1 the time-averaged value of the energy injection I_{3D} as a function of ϵ for various values of Ra with fixed $\mathrm{Ek} = 5 \cdot 10^{-5.5}$ is plotted. The error bars on these data points are obtained by calculating the standard deviation of these time series. These standard deviations tend to be large because the bursty behaviour of the elliptical instability results in large differences in the energy injection as a function of time, sometimes even resulting in a standard deviation that is larger than the time-average. Furthermore, at very small ellipticities the energy injection is so small such that even the fluctuations present in the sustained energy injection are larger than the time-average, again resulting in standard deviations that are larger than the time-averages. We have plotted the full error bars on the burgundy circles to illustrate which simulations display these fluctuations in the time series, but omitted the downward part of the other markers for clarity.

Fig. 4.1 can be divided into two regimes by a vertical dashed line. To the left of this line, the elliptical instability is absent, and only the action of turbulent convection on the tidal flow is responsible for energy injection and thus tidal dissipation. To the right of this line the elliptical instability is present, possibly modified by the convection, in addition to the interaction of turbulent convection with the background tidal flow. In the figure this vertical dashed line is located at $\epsilon = 0.08$, corresponding to the transition for the arbitrarily chosen value of $\mathrm{Ra} = 6\mathrm{Ra}_c$, the energy injection of which is represented by the burgundy data points. If the Rayleigh number is lower (higher) – and thus the convective driving is weaker (stronger) – this line is expected to move to smaller (larger) values of ϵ.

We know that the energy injection associated with the effective viscosity scales with the Rayleigh number from comparing the time series in Fig. 3.4d and Fig. 3.5d. Therefore we choose to fit the energy injection at a fixed Rayleigh number, in this case the arbitrarily chosen $\mathrm{Ra} = 6\mathrm{Ra}_c$, using an ϵ^2 scaling. The data agrees very well with this scaling for ϵ to the left of the vertical dashed line, i.e. below the transition value of ϵ, indicating that the energy injection can indeed be interpreted as an effective viscosity that is independent of ϵ here. Moreover, the effective viscosity fit is expected to move up or down proportional to the chosen fitted Rayleigh number because the energy injection scales with the Rayleigh number. We will justify both of these observations further in Sec. 4.2.1.

The simulations corresponding to data points on the right of the vertical dashed line feature bursts of the kinetic energy and energy injection rates, indicating that the elliptical instability operates in this regime. The operation of the elliptical instability appears to be in addition to the effective viscosity resulting from convective turbulence, but the energy injection rate due to the elliptical instability is much larger, as is illustrated by the strong departure of these points from the black ϵ^2 line. We fit these data points with our (naive) theoretically predicted ϵ^3 fit (solid-blue line), and an ϵ^6 fit (solid-red line, as previously observed in Barker & Lithwick, 2013). Both fits are consistent with the data on the right hand side (over a narrow range of ϵ), and are inconsistent with data on the left. Furthermore, the data and fits are consistent at all values of Ra, indicating that this scaling is likely independent of the Rayleigh number, particularly further from the transition line.

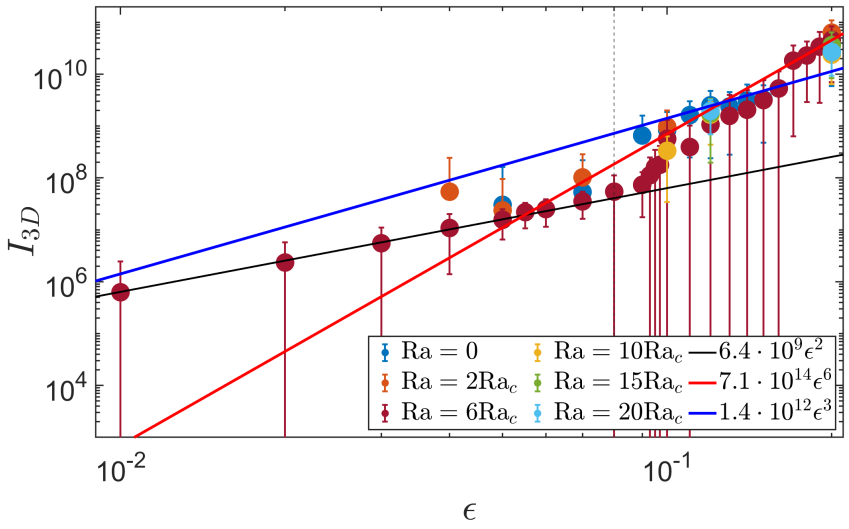

Figure 4.1: Time-averaged values of the energy injection rate (into 3D modes) I_{3D} as a function of ϵ for various Rayleigh numbers. The vertical dashed line at $\epsilon = 0.08$ marks the transition at $\mathrm{Ra} = 6\mathrm{Ra}_c$ between sustained behaviour on the left, and bursts in addition to sustained behaviour on the right. The large error bars on the right are introduced because the strong fluctuations in the energy injection, due to the burstiness of the elliptical instability, lead to a large variance. We have included the full error bars for the burgundy circles to illustrate this, but omitted the downward part of the error bars of all other markers for clarity. Three lines are fitted to the data at $\mathrm{Ra} = 6\mathrm{Ra}_c$. The sustained behaviour is consistent with an ϵ^2 scaling for $\epsilon \lesssim 0.08$, represented by the black line. Bursts of the elliptical instability contribute on top of this sustained energy injection, resulting in a much larger energy injection for larger ϵ. The energy injection at larger ϵ featuring both bursts and sustained behaviour is fitted using an ϵ^3 fit in blue, and an ϵ^6 fit in red.

Upon extrapolating the energy injection rate of the elliptical instability with an ϵ^3 scaling we find that it is greater than that of the effective viscosity due to convection for $\epsilon \gtrsim 0.01$, at the fixed Ekman number and Rayleigh number of $\mathrm{Ek} = 5 \cdot 10^{-5.5}$ and $\mathrm{Ra} = 6\mathrm{Ra}_c$ respectively.

Following Barker and Lithwick (2014), we use the theoretical prediction in Eq. (2.79) to obtain a proportionality "factor" χ from our fit to the data shown in Fig. 4.1 such that $I_{3D} \equiv \chi\epsilon^3\gamma^3$. The reasoning for introducing this proportionality factor is the intermittent and imperfect operation of the elliptical instability. In theory, if the elliptical instability were operating continuously, and exciting box-scale modes, this proportionality factor would be of order unity, but because it is only operating some of the times, it needs to be reduced. The proportionality factor can therefore also be thought of as an efficiency factor for a particular large-scale mode, which is selected by the box aspect ratio.

We find $\chi \approx 0.044$ for the plotted blue line, with $\chi \approx 0.18$ as an upper estimate when fitting to the top right clump of data points. If instead we follow the previously observed fit with ϵ^6 in Barker and Lithwick (2013) we can naively define $I_{3D} \propto \chi_2\epsilon^6\gamma^3$; we obtain $\chi \equiv \chi_2\epsilon^3 \approx 22.45 \cdot \epsilon^3$. To illustrate the (in)efficiency of this ϵ^6 scaling we insert

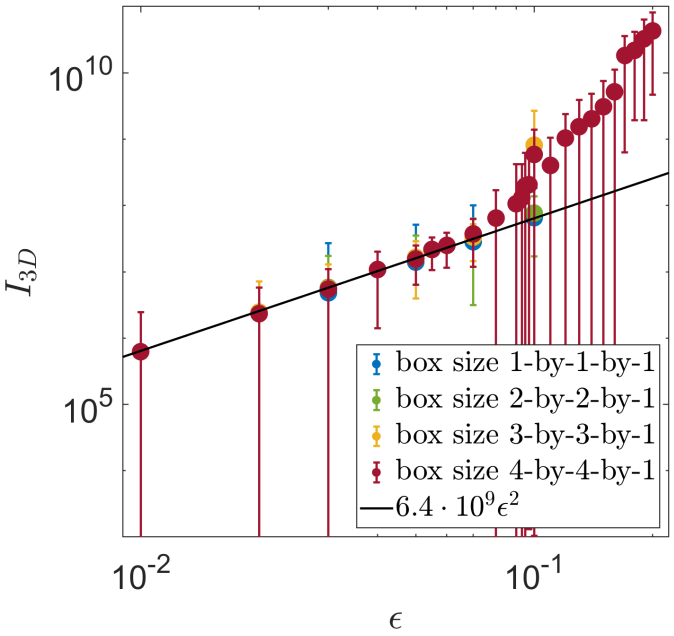

Figure 4.2: Same as Fig. 4.1, but showing time-averaged values of I_{3D} for different box sizes. For clarity we have omitted the downward part of the error bars on all markers except the burgundy circles. Changing the box size has no impact on the sustained energy injection. Smaller boxes do result in the elliptical instability being suppressed at larger values of ϵ; larger wavenumbers are required to satisfy the resonance condition in these smaller boxes and thus the suppressive effects of viscosity are more important.

the highest-inferred ellipticity of a Hot Jupiter, $\epsilon = 0.06$, and find $\chi = 4.8 \cdot 10^{-3}$. Hence, the elliptical instability is considerably weaker if this steeper scaling applies in realistic astrophysical objects. The ϵ^3 scaling can thus be viewed as an "upper bound" on the energy transfer rates resulting from the elliptical instability for small ϵ.

We additionally wish to test the effects of different box sizes on energy transfers. To this end, we ran multiple sets of simulations with different box sizes; in each set of simulations we fixed the Rayleigh and Ekman numbers at $\mathrm{Ra} = 6\mathrm{Ra}_c$ and $\mathrm{Ek} = 5 \cdot 10^{-5.5}$ respectively, while varying the value of ϵ. We have plotted I_{3D} as a function of ϵ with different markers denoting different box sizes in Fig. 4.2. The blue, green, yellow and burgundy markers represent results in 1-by-1-by-1, 2-by-2-by-1, 3-by-3-by-1 and 4-by-4-by-1 boxes respectively. The time-averaged energy injection in the sustained regime is shown to be independent of box size, and all markers follow the same ϵ^2 scaling. The main difference between the box sizes resides in the value of ϵ at which the elliptical instability is able to operate. The simulations in the 4-by-4-by-1 box become bursty at $\epsilon \geq 0.08$. Simulations with smaller horizontal box sizes do not become bursty at this value; simulations in the 3-by-3-by-1 box only indicate burstiness at $\epsilon \geq 0.1$, while the flows in 2-by-2-by-1 and 1-by-1-by-1 boxes remain in the sustained regime beyond $\epsilon = 0.1$.

The enhanced suppression of the elliptical instability can be explained by the variation of the allowed values of $k_\perp$ as the box size is varied. For smaller horizontal box

sizes at the same resolution, the values of $k_\perp$ and hence k that fit in the box increase, while the values of k_z that fit in the box are maintained at the same value. The increasing wavenumber effect from choosing a larger box is compounded by the requirement to satisfy the resonance with $k_z/k \approx \pm 1/2$; the discreteness of the method forces the instability to select larger values of both k and therefore also larger values of k_z (even if smaller ones are available) to achieve resonance, as was seen in the right-hand panel of Fig. 3.14. The increased values of k then result in a stronger suppression of the elliptical instability by viscosity at a chosen value of ϵ, which – in tandem with the suppressive effects of the LSV – results in stronger inhibition of the elliptical instability in smaller boxes. The effects of viscosity must consequently become less important in larger boxes for fixed Ek. One might then expect that the effects of viscosity can be considered as unimportant when extrapolating to planets.

4.2 Scalings of the effective viscosity

We have found that turbulent convection acts to damp the equilibrium tidal flow like an effective viscosity (independently of ϵ). The three regimes of the effective viscosity were previously presented in Eq. (1.60), as obtained from Duguid et al. (2020), and are reproduced below for convenience:

$$\nu_{\text{eff}} = \begin{cases} 5 u_c l_c & \frac{|\omega|}{\omega_c} \lesssim 10^{-2}, \\ \frac{1}{2} u_c l_c \left(\frac{\omega_c}{\omega}\right)^{\frac{1}{2}} & \frac{|\omega|}{\omega_c} \in [10^{-2}, 5], \\ \frac{25}{\sqrt{20}} u_c l_c \left(\frac{\omega_c}{\omega}\right)^2 & \frac{|\omega|}{\omega_c} \gtrsim 5. \end{cases} \tag{4.1}$$

These scalings depend on the convective velocity u_c, the convective lengthscale l_c and the ratio of the tidal frequency $\omega = \omega_{2,2,2} = 2\gamma$, for this tidal component, to the convective frequency ω_c. The reported (upper-bound by-eye fit) numerical coefficients from Duguid et al. (2020) were reproduced in Eq. (4.1), but the introduction of rotation and our different background flow might modify these, even if the scaling laws themselves hold. More importantly, the choice of scaling laws for the convective quantities u_c, l_c and ω_c will depend on properties of the system like rotation (and perhaps magnetic fields etc.). Therefore, before we can apply the above scalings, we must derive appropriate scaling laws for these quantities depending on which regime the flow is in and verify that these regimes apply in our numerical simulations. To this end we will use mixing-length theory (MLT, Prandtl, 1925; Böhm-Vitense, 1958).

4.2.1 Scalings of convective quantities using mixing-length theory

In non-rotating simulations, it is reasonable to think of the appropriate convective lengthscale as the vertical size of the box, and therefore set $l_c = d$, pretending that d is the Boussinesq equivalent of a pressure scale height (or mixing-length, which is usually taken as a multiple of the pressure scale height). One should then consider the vertical veloci-

ties of the parcel when deriving an expression for the convective velocity. However, it is not clear whether this is appropriate for rapid rotation. Rapidly rotating Rayleigh-Bénard convection is confined to thin columns or vortices, and the width of these is thought to represent the dominant convective lengthscale. Therefore, the shorter horizontal lengthscale for l_c might be more appropriate than the vertical size of the box in the rapidly rotating regime. One might then also consider the horizontal velocity instead of the vertical velocity to represent the convective velocity. Choosing a shorter lengthscale and altered velocity will affect the turbulent viscosity, but how strong these effects are will depend on the regime the effective viscosity is in. Finally, the appropriate arguments and thus scalings may change with the intended application, because the effective viscosity is not a property of the fluid, but rather a way to model the interaction between a particular fluid flow and convective flow. Nevertheless, we will apply mixing-length theory to predict the scaling laws of convective properties such as convective velocities, lengthscales, frequencies and effective viscosities. MLT has been applied to non-rotating cases previously (e.g. Zahn, 1966; Duguid et al., 2019, 2020) and verified in simulations, but our cases are sufficiently rapidly rotating that we must account for modifications of convective properties by rotation as outlined above. To do so, we use rotating mixing-length theory (RMLT; Stevenson, 1979) to predict scaling laws for rotating convection, following the approach of e.g. Barker et al. (2014), Mathis et al. (2016), and Currie et al. (2020), who have verified the applicability of RMLT in Boussinesq simulations.

Within RMLT the horizontal convective velocity on the relevant scales (i.e. for the modes that dominate heat transport) is expected to be roughly equal to the vertical convective velocity (Stevenson, 1979) and is given by:

$$u_c \sim d^{1/5} F^{2/5} \Omega^{-1/5}, \tag{4.2}$$

where F is the vertical heat flux (more specifically a buoyancy flux with units of L^2T^{-3}). We may write this in terms of the standard dimensionless numbers by relating the vertical heat flux to the Rayleigh number via the Buoyancy frequency:

$$\mathrm{Ra} \sim N^2 d^4 \nu^{-1} \kappa^{-1} \sim F^{2/5} d^{8/5} \kappa^{-1} \nu^{-1/5} \mathrm{Ek}^{-4/5}, \tag{4.3}$$

since $N^2 \sim F^{2/5} \Omega^{4/5} d^{-4/5}$ according to RMLT. Converting to the Rayleigh number (based on a fixed temperature gradient or N^2) from the fixed heat flux F entails a switch from flux-based scalings to temperature-based (and by extension N^2-based) scalings. This switch is necessary as the simulations are executed using a constant temperature difference in the model, i.e. they are temperature-based rather than flux-based. After this switch, RMLT predicts for the dimensional convective velocity:

$$u_c \sim \mathrm{RaEk} \frac{\kappa}{d}. \tag{4.4}$$

Furthermore, the dominant horizontal lengthscale of convection is predicted to scale as:

$$l_c \sim \Omega^{-3/5} F^{1/5} d^{3/5} \sim \frac{\mathrm{Ra}^{1/2}\mathrm{Ek}}{\mathrm{Pr}^{1/2}} d. \tag{4.5}$$

Finally, the convective turnover frequency (based on the horizontal lengthscale) according to RMLT is:

$$\omega_c \sim \frac{u_c}{l_c} \sim \mathrm{Ra}^{1/2}\mathrm{Pr}^{1/2}\frac{\kappa}{d^2}. \tag{4.6}$$

These are the RMLT scalings written in terms of Rayleigh, Ekman and Prandtl numbers. These scalings agree with those found in Guervilly et al. (2019) and Aurnou et al. (2020), and with many others, indicating that the results found from the Coriolis-Inertia-Archimedean (CIA) balance are in agreement with the predictions of RMLT following Stevenson (1979). The three effective viscosity scaling laws in Eq. (4.1) can be written using these predictions from RMLT as:

$$\nu_{\mathrm{eff}} \propto \begin{cases} \mathrm{Ra}^{3/2}\mathrm{Ek}^2\mathrm{Pr}^{-1/2}\kappa & \text{low frequency,} \\ \mathrm{Ra}^{7/4}\mathrm{Ek}^2\mathrm{Pr}^{-1/4}\kappa^{3/2}d^{-1}\omega^{-1/2} & \text{intermediate frequency,} \\ \mathrm{Ra}^{5/2}\mathrm{Ek}^2\mathrm{Pr}^{1/2}\kappa^3 d^{-4}\omega^{-2} & \text{high frequency.} \end{cases} \tag{4.7}$$

The first of these regimes occurs when the tidal frequency is low, while the rotation rate is high (so that we use RMLT rather than MLT). Naively, this situation seems counter-intuitive because the tidal frequency is related to the rotation rate, but it can occur if the body is close to spin-orbit synchronisation. We have not supplied ranges of ω/ω_c for which these apply as we will determine these based on our simulations. Instead we elect to refer to these regimes qualitatively as the low, intermediate and high frequency regimes, where the frequency in question is the tidal frequency (compared with the convective frequency). The low frequency regime can be thought to correspond to the "slow tides" and the high frequency regime to the "fast tides". Note that these regimes have not been previously verified with simulations of rotating convection interacting with tidal flows (unlike in the non-rotating case).

We can use the expressions in Eqs. (4.4), (4.5) and (4.7) to analyse our results as a function of both Rayleigh and Ekman numbers, in regimes attainable by simulations. To analyse our simulation results in terms of the Ekman number we use two approaches: fixing the Rayleigh number and fixing the supercriticality $R = \mathrm{Ra}/\mathrm{Ra}_c$. The second approach modifies the power of the Ekman number scaling, because the critical Rayleigh number scales as $\mathrm{Ra}_c \approx 3(\pi^2/2)^{2/3}\mathrm{Ek}^{-4/3}$ for rapid rotation, which results in $u_c \sim R\mathrm{Ek}^{-1/3}\kappa d^{-1}$ and $l_c \sim R^{1/2}\mathrm{Ek}^{1/3}\mathrm{Pr}^{-1/2}d$. This leads to the following changes to ν_{eff} scalings:

$$\nu_{\mathrm{eff}} \propto \begin{cases} R^{3/2}\mathrm{Ek}^0\mathrm{Pr}^{1/2}\kappa & \text{low frequency,} \\ R^{7/4}\mathrm{Ek}^{-1/3}\mathrm{Pr}^{-1/4}\kappa^{3/2}d^{-1}\omega^{-1/2} & \text{intermediate frequency,} \\ R^{5/2}\mathrm{Ek}^{-4/3}\mathrm{Pr}^{1/2}\kappa^3 d^{-4}\omega^{-2} & \text{high frequency.} \end{cases} \tag{4.8}$$

For completeness, since some of our simulations might enter the regime where rotation is no longer rapid, we include here the scalings of the relevant quantities using non-rotating MLT, in the temperature-based formulation, i.e. in terms of Rayleigh and Prandtl numbers:

$$u_c \sim \mathrm{Ra}^{1/2}\mathrm{Pr}^{1/2}\frac{\kappa}{d}, \tag{4.9}$$

and the relevant lengthscale in this regime is likely to be comparable with the vertical lengthscale d:

$$l_c = d. \tag{4.10}$$

It follows that:

$$\omega_c \sim \mathrm{Ra}^{1/2}\mathrm{Pr}^{1/2}\frac{\kappa}{d^2}, \tag{4.11}$$

which is the same scaling obtained previously using RMLT. The three regimes we expect for the effective viscosity using MLT are then:

$$\nu_{\mathrm{eff}} \propto \begin{cases} \mathrm{Ra}^{1/2}\mathrm{Pr}^{1/2}\kappa & \text{low frequency,} \\ \mathrm{Ra}^{3/4}\mathrm{Pr}^{3/4}\kappa^{3/2}d^{-1}\omega^{-1/2} & \text{intermediate frequency,} \\ \mathrm{Ra}^{3/2}\mathrm{Pr}^{3/2}\kappa^{3}d^{-4}\omega^{-2} & \text{high frequency.} \end{cases} \tag{4.12}$$

The high frequency regime within non-rotating MLT is unlikely to occur in our simulations as that regime only applies when the tidal frequency is high, yet the rotation rate is low. It is however likely to be important in reality, for example inside spun-down Hot Jupiter host stars, due to for example magnetic braking (e.g. Benbakoura et al., 2019). If a Hot Jupiter host star is spun down, and is thus slowly rotating, but there is a large orbital frequency due to the short-period Hot Jupiter companion, the tidal frequency is also high (and in the fast tides regime), indicating that this regime is relevant there (e.g. Barker, 2020; Duguid et al., 2020).

It should be noted at this point that all the scalings obtained in this regime are in fact diffusion-free, i.e. the microscopic viscosity and thermal diffusivity drop out of the obtained expressions when writing them out in full instead of using dimensionless numbers. We have, however, written them using the standard dimensionless numbers for ease of understanding and comparison to previous works.

From the multitude of obtained scalings a new question arises: for a given system, which scalings (if any!) are the correct ones? This question in reality consists of two separate questions. The first part of the question is related to whether MLT or RMLT (or neither) predictions should be used, and the second part relates to which tidal frequency regime is applicable. One of our key aims is to test these scalings and to determine the appropriate ones for astrophysical extrapolation. We can start by quantifying the transition from MLT to RMLT using the convective Rossby number:

$$\mathrm{Ro}_c \equiv \left(\frac{u_c}{2\Omega l_c}\right) = \left(\frac{\omega_c}{2\Omega}\right), \tag{4.13}$$

which is based on the spin of the planet, and the convective velocities and frequencies. Fortunately, using these temperature-based definitions, regardless of whether the regime in question is MLT or RMLT, the expression for the Rossby number in terms of the diffusion-free scalings is the same because ω_c has the same form in both regimes. This useful result was also found previously (e.g. Aurnou et al., 2020), and leads to the expression for the convective Rossby number:

$$\mathrm{Ro}_c \sim \mathrm{Ra}^{1/2}\mathrm{Pr}^{-1/2}\mathrm{Ek}. \tag{4.14}$$

On the other hand, the transitions between the different frequency regimes for ν_{eff} depend on the ratio ω/ω_c, which we can write as:

$$\frac{\omega}{\omega_c} = \frac{\omega}{u_c/l_c} = \frac{1}{2}\frac{2\omega l_c}{u_c} \equiv \frac{1}{2}\mathrm{Ro}_\omega^{-1}. \tag{4.15}$$

We have defined this quantity as a "tidal convective Rossby number", Ro_ω. The two Rossby numbers are related via the factor Ω/ω. In this work, the two Rossby numbers differ by a factor of 1/2, because $\Omega = \gamma = \frac{1}{2}\omega$ is set for the simulations with a given Ek. The regime transitions are thus expected to occur at roughly the same value of the rotation rate. Using the tidal frequency transitions obtained in Duguid et al. (2020), where the transition from intermediate to high frequency regimes occurs around $\frac{\omega}{\omega_c} \approx 5$, this may be expected to occur here at $\mathrm{Ro}_\omega \approx 0.1$. The transition from MLT to RMLT on the other hand is likely to start at $\mathrm{Ro}_c \approx 0.1$ (e.g. Fig. 4 of Barker et al., 2014).

4.2.2 Verification of rotating mixing-length theory scaling laws

To verify the usage of the RMLT scaling laws we will compare the observed values of the convective velocity and lengthscale in the simulations with our predictions. We choose parameters predominantly in the strongly rotationally-constrained regime, which are, because of the model setup with $\Omega = \gamma$, generally located in the fast tides regime. We expect to observe the RMLT scalings for the convective frequency and lengthscale in our simulations, and the high frequency regime of the effective viscosity. We will also justify this regime as being the most relevant in Hot Jupiters in Ch. 7.

In this section we explore further the regime where the energy injection scales as ϵ^2 that we have identified, and we will demonstrate that it results from convective turbulence damping the background tidal flow. First, we fit the convective velocities as a function of Rayleigh number in the left-hand panel of Fig. 4.3 to verify our predictions based on RMLT. The data is obtained from simulations with fixed $\mathrm{Ek} = 5 \cdot 10^{-5.5}$, and with such values of ϵ that only sustained energy injection is present without visible bursts of elliptical instability (which tend to produce larger vertical velocities when they occur). These values of ϵ that contain no visible bursts of the elliptical instability vary with Rayleigh number as stronger convective driving results in stronger suppression of the elliptical instability; for example at $\mathrm{Ra} = 4\mathrm{Ra}_c \approx 0.9 \cdot 10^8$ values up to $\epsilon = 0.04$ are used, while at $\mathrm{Ra} = 10\mathrm{Ra}_c \approx 2.2 \cdot 10^8$ we use up to $\epsilon = 0.075$, and at $\mathrm{Ra} = 20\mathrm{Ra}_c \approx 4.4 \cdot 10^8$ we use up to $\epsilon = 0.1$. The same values of ϵ are used for all subsequent figures as a function of Ra in this chapter.

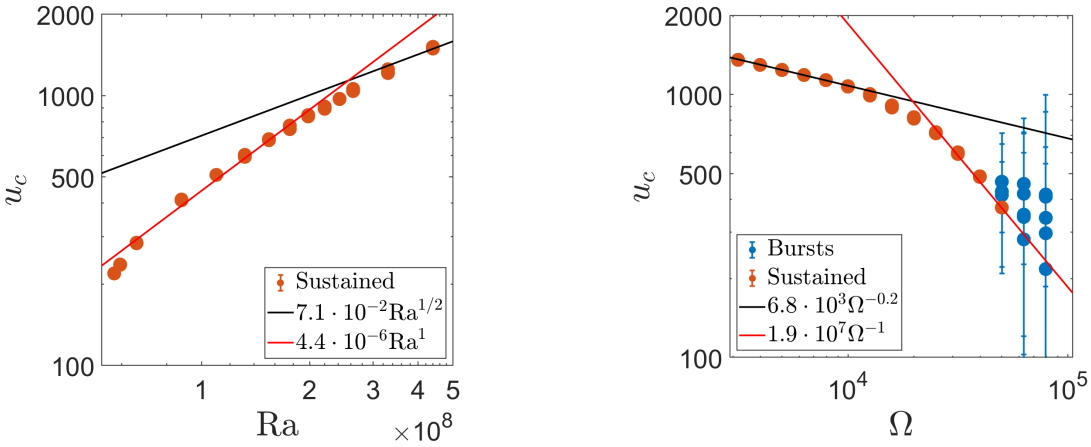

Figure 4.3: Scaling of the vertical convective velocity compared with the predictions of MLT and RMLT. Left: Scaling of the vertical convective velocity with fixed $\mathrm{Ek} = 5 \cdot 10^{-5.5}$. Only those simulations with sufficiently small ellipticities are used such that no bursts of the elliptical instability are present, as indicated by the orange data points. At these ellipticities the vertical velocity is negligibly impacted by the ellipticity. We observe the RMLT scaling with Ra in solid-red, and a hint for the non-rotating MLT scaling for larger Ra with $\mathrm{Ra}^{1/2}$ in solid-black. Right: Scaling of the vertical convective velocity with fixed $\mathrm{Ra} = 1.3 \cdot 10^8$ and $\epsilon \in [0.02, 0.05]$ as a function of $\Omega = (1/2)\mathrm{Ek}^{-1}$. The blue data points correspond to simulations with bursts of the elliptical instability. We retrieve the RMLT scaling in solid-red at large Ω, and find that the scaling tends to the MLT prediction, i.e. to become independent of rotation rate, as Ω becomes small, here illustrated by the solid-black line, which follows $\Omega^{-0.2}$. At smaller rotation rates we expect the convective velocity to become fully independent of the rotation rate, as MLT predicts.

In this and subsequent figures, orange circles represent simulations without bursts of the elliptical instability and blue circles represent those in which there are visible bursts. We plot the best fit RMLT scaling in solid-red and for stronger convection (i.e. relatively weaker rotation), we fit the non-rotating MLT scaling in solid-black. The RMLT scaling is in very good agreement with our data for $\mathrm{Ra} \lesssim 3 \cdot 10^8$, indicating that RMLT is the appropriate description of strongly rotationally-constrained convection in our simulations.

We separately fit the convective velocities as a function of the rotation rate Ω in the right-hand panel of Fig. 4.3 at constant $\mathrm{Ra} = 1.3 \cdot 10^8$ at $\epsilon \in [0.02, 0.05]$. These values of ϵ are used in all subsequent figures with fixed Ra. We have elected to plot the results in Fig. 4.3 and in the rest of this chapter as a function of Ω, measured in inverse viscous times, instead of the Ekman number because Ω has a more direct relation to the tidal frequency ω than the Ekman number, particularly in real bodies where $\nu, d \neq 1$. In these simulations we have set $\nu = d = 1$, however, so $\Omega = (1/2)\mathrm{Ek}^{-1}$. The simulations at high rotation rate do feature bursts of the elliptical instability, because the associated high tidal frequency strengthens the elliptical instability whilst weakening the convective driving because the Rayleigh number is fixed. The data points at strong rotation, $\Omega \geq 10^{4.4}$, fit the RMLT prediction of Ω^{-1} well. The data points at weaker rotation rates become more weakly dependent on Ω as they begin to approach the non-rotating MLT prediction. The black-

solid line fitted to the left-most data points scales only weakly as $\Omega^{-0.2}$. It is expected that at even smaller rotation rates, or larger Rayleigh numbers, this scaling would become fully independent of rotation. This figure indicates that the transition from MLT to RMLT is indeed gradual, instead of abrupt. From both figures we find – according to RMLT – that the convective velocity is well-described by

$$u_c = 0.28\mathrm{RaEk}\frac{\kappa}{d}, \tag{4.16}$$

for rapid rotation, and for weaker rotation it approaches the non-rotating MLT scaling

$$u_c = 7.1 \cdot 10^{-2}\mathrm{Ra}^{1/2}\mathrm{Pr}^{1/2}\frac{\kappa}{d}. \tag{4.17}$$

Next we obtain the horizontal lengthscale from simulations with fixed Rayleigh number $\mathrm{Ra} = 1.3 \cdot 10^8$ and with fixed supercriticality $R = 6$ as a function of Ω. We use two different methods to calculate a dominant l_c, illustrated here using the heat flux spectrum $F(k_\perp) = \mathrm{Re}(\hat{u}_z\hat{T}^*)$ as a function of horizontal wavenumber $k_\perp = \sqrt{k_x^2 + k_y^2}$. Hats indicate a 2D (k_x, k_y) Fourier transform. We have averaged over the inner vertical 1/3 of the box, i.e. between $z = 1/3$ and $z = 2/3$, and subsequently summed up the contribution from all modes within an integer bin of $k_\perp$. The first prescription was used by Barker et al. (2014) and Currie et al. (2020):

$$l_c = 2\pi\left(\frac{\int k_\perp F(k_\perp)\,\mathrm{d}k_\perp}{\int F(k_\perp)\,\mathrm{d}k_\perp}\right)^{-1}, \tag{4.18}$$

and the second was used by Parodi et al. (2004):

$$l_c = 2\pi\frac{\int (k_\perp)^{-1}F(k_\perp)\,\mathrm{d}k_\perp}{\int F(k_\perp)\,\mathrm{d}k_\perp}. \tag{4.19}$$

In our simulations both methods agree very well when based on the same quantity. However, vastly different results are obtained if the energy spectrum (as used by Parodi et al., 2004) is used instead of $F(k_\perp)$ (as used by Barker et al., 2014; Currie et al., 2020). In Fig. 4.4 the convective lengthscales calculated using the heat flux according to Eq. (4.18) are plotted in solid (and dashed) lines. The lengthscales according to Eq. (4.19), but for the vertical kinetic energy spectrum $E_z(k_\perp) = \frac{1}{2}|\hat{u}_z|^2$ instead of $F(k_\perp)$, are plotted in dotted lines. We have opted to calculate lengthscales based on the "vertical kinetic energy" spectrum $E_z(k_\perp)$ in the latter instead of the total kinetic energy spectrum because the total kinetic energy spectrum is strongly dominated by the large-scale horizontal motions of the LSV. This forces the power to be concentrated on the largest scales, while these horizontal motions are unlikely to contribute substantially to heat transport or provide the dominant contribution to the effective viscosity. The spectra from cases with the most extreme parameters we considered are displayed; those at the largest Ekman number, $\mathrm{Ek} = 5 \cdot 10^{-4.5}$, with fixed $\mathrm{Ra} = 1.3 \cdot 10^8$ are plotted in solid-blue and dotted-purple, those at the smallest Ekman number, $\mathrm{Ek} = 5 \cdot 10^{-6}$, with fixed $\mathrm{Ra} = 1.3 \cdot 10^8$ are plotted in solid-yellow and dotted-burgundy, and those at the smallest Ekman number with fixed

$R = 6$ are plotted in solid-green and dotted-orange. The heat flux spectra at small Ekman number contain dashed parts, indicating negative heat flux for these $k_\perp$.

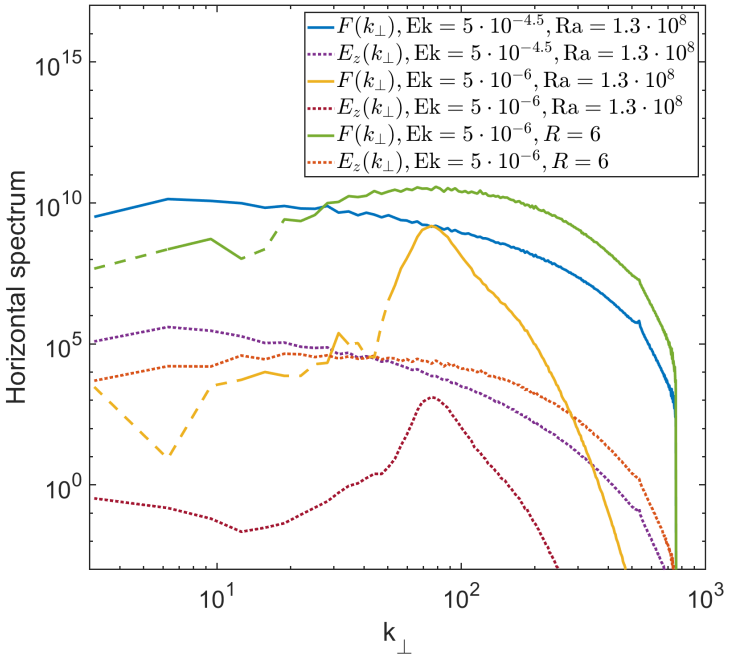

Figure 4.4: The heat flux $F(k_\perp)$ (solid and dashed lines) and the vertical kinetic energy $E_z(k_\perp)$ (dotted lines) spectra as a function of horizontal wavenumber $k_\perp$. The spectra are plotted at the most extreme values of the surveyed parameter space in Ekman number. The spectra at the largest Ekman number, Ek $= 5 \cdot 10^{-4.5}$, with fixed Ra $= 1.3 \cdot 10^8$ are plotted in solid-blue and dotted-purple. The spectra at the smallest Ekman number, Ek $= 5 \cdot 10^{-6}$, with fixed Ra $= 1.3 \cdot 10^8$ are plotted in solid-yellow and dotted-burgundy, and those at the smallest Ekman number with fixed $R = 6$ are plotted in solid-green and dotted-orange. Dashed parts of the heat flux spectra indicate negative heat flux for these scales.

At the largest Ekman number considered in solid-blue and dotted-purple the majority of the heat flux appears concentrated towards small horizontal wavenumbers, i.e. large scales. This is in agreement with the behaviour of the vertical velocity in the right-hand panel of Fig. 4.3, which indicates that this simulation is close to the MLT regime, in which the lengthscale of the heat flux should agree with that of vertical box size, i.e. $k = 2\pi$. The heat flux distribution is however broad, and we observe that the smaller scales also contribute to the heat transport. Turning our attention to the simulation with Ek $= 5 \cdot 10^{-6}$, Ra $= 1.3 \cdot 10^8$ in solid-yellow and dotted-burgundy, we see that a strong peak emerges. This simulation is executed at a Rayleigh number very close to the critical Rayleigh number, with corresponding $R \approx 1.3$, and therefore we expect the contributing wavenumbers to strongly follow the linear onset wavenumber. We do indeed observe that the peak is located exactly at the most linearly unstable wavenumber of $k_\perp \approx 76$, indicating that this simulation is dominated by onset dynamics, i.e. affected by viscosity. Finally, the simulation with Ek $= 5 \cdot 10^{-6}$, R $= 6$, which corresponds to Ra $= 6.1 \cdot 10^8$, in solid-green and dotted-orange shows that the heat flux in this simulation is the result of a

broad distribution at larger wavenumbers, corresponding to a smaller convective length-scale, as we expect from RMLT predictions. There is a slight discrepancy between the heat flux and the vertical kinetic energy spectrum; the heat flux appears peaked around $k_\perp \approx 100$, while the kinetic energy appears peaked around $k_\perp \approx 50$, with the dominant contributing modes concentrated towards lower wavenumbers. Furthermore, because the simulation is now no longer close to onset, more scales are involved in heat transport, and the linear onset scale is no longer the most dominant.

We conclude that the locations of the peaks of the heat flux spectra are indeed located at large scales when we expect the simulation to be in the MLT regime and small scales when we expect the simulation in the RMLT regime, as long as the simulations are far enough removed from onset such that viscous effects are weak on the relevant scales and the simulations are no longer dominated by the onset scale. Thus we will use the heat flux spectra to obtain the convective lengthscale. We can also draw a conclusion on the well-resolvedness of these results: the conventional rule of thumb that the power in the peak of the spectrum must be a factor of at least 10^3 larger than at the de-aliasing scale is maintained in the kinetic energy spectra as well as the heat flux spectra. This indicates that our simulations are therefore likely to be spatially converged in the horizontal plane.

We now show the obtained horizontal lengthscales in our simulations in Fig. 4.5 and Fig. 4.6. The lengthscales calculated using the heat flux according to Eq. (4.18) are plotted in orange diamonds. For completeness the lengthscales according to Eq. (4.19) for the vertical kinetic energy spectrum $E_z(k_\perp)$ are plotted in yellow diamonds and the lengthscale obtained from the temperature fluctuation spectrum, i.e. $|\hat{\theta}(k_\perp)|^2$, is also plotted in green diamonds. Furthermore, we have added the lengthscale corresponding to the highest peak of the heat flux spectrum as a proxy for the dominant lengthscale in blue squares. The lengthscales corresponding to the peaks in the vertical kinetic energy and temperature perturbation spectra are omitted, because they tend to be located at the box scale, likely due to influence of the LSV, and then rapidly decrease and eventually align with the linear onset scale for $\Omega \gtrsim 10^{4.6}$. Finally, fits to the data are included, with the RMLT prediction fit in solid-red and the linear onset lengthscale in dashed-purple.

In Fig. 4.5 we display l_c as a function of Ω with fixed $\mathrm{Ra} = 1.3 \cdot 10^8$, on the same interval of Ω as the right-hand panel of Fig. 4.3. We find that the blue squares, i.e. the peaks of the heat flux spectrum, follow a fit proportional to Ω^{-1} in solid-red. Note that the blue squares do not agree with this fit when $\Omega \gtrsim 10^{4.5}$, which is probably because the simulations are not turbulent enough to follow RMLT and instead lie more closely to the linear onset lengthscale. In terms of the lengthscales as obtained from the integrals there are substantial differences between those calculated based on different quantities. All three quantities match together close to linear onset for the three right-most data points, which have supercriticalities of $R = [2.4, 1.8, 1.3]$ from left to right, but they diverge for $\Omega \lesssim 10^{4.8}$, coinciding with the generation of the LSV as the supercriticality of the system increases. The lengthscale corresponding with squared temperature perturbations in green diamonds stays close to the linear onset scale, i.e. it scales as roughly $\Omega^{-1/3}$. The lengthscale based

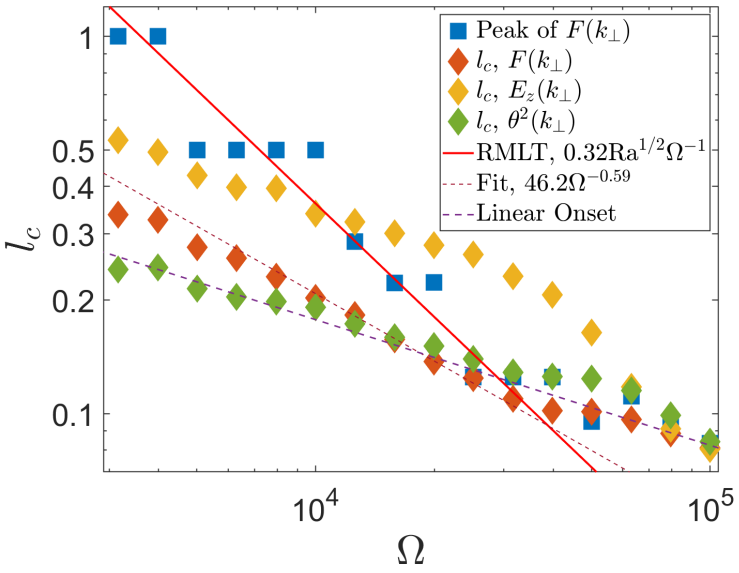

Figure 4.5: The horizontal convective lengthscale as a function of rotation rate with fixed $\mathrm{Ra} = 1.3 \cdot 10^8$, calculated using the integration methods in Eqs. (4.18) and (4.19), which agree well. Data points are calculated based on the heat flux (orange diamonds), vertical kinetic energy (yellow diamonds) and the squared temperature perturbations (green diamonds). The peaks of the heat flux spectrum are included in blue squares. The solid-red fit is the RMLT prediction of $\mathrm{Ra}^{1/2}\Omega^{-1}$ (Eq. (4.20)), and the dashed-purple line is the linear onset lengthscale. The peaks of the heat flux agree well with the RMLT prediction. The steepest fit to the heat flux lengthscale is plotted in dashed-burgundy, which probably differs from the RMLT prediction in solid-red because of the modest supercriticalities involved. The linear onset scaling is plotted in dashed-purple, which only agrees with our data for the three right-most points with the smallest supercriticalities.

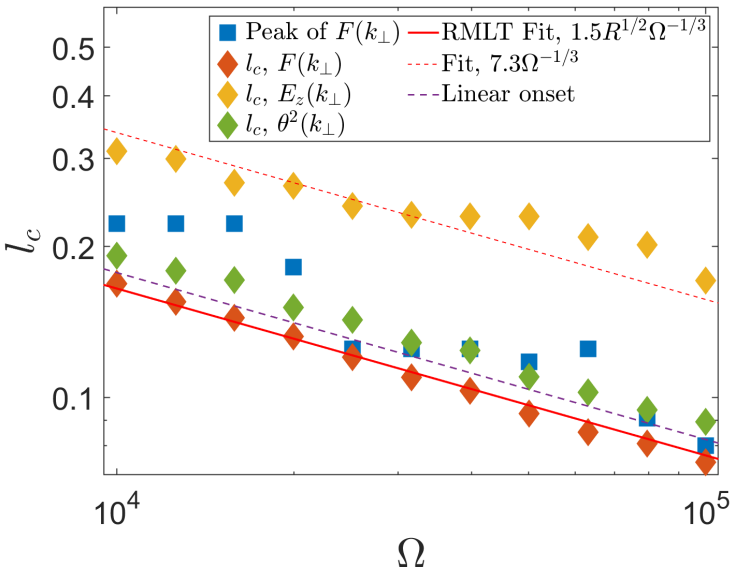

Figure 4.6: Same as Fig. 4.5, but with fixed supercriticality $R = 6$. The heat flux data agree well with the RMLT prediction in solid-red, which is the same fit as the solid-red line in Fig. 4.5. The linear onset scaling is plotted in dashed-purple, and differs from our simulation results.

on the kinetic energy is much larger than the other two, but also follows a scaling roughly similar to $\Omega^{-1/3}$ (fit not shown) in the interval $\Omega \in [10^{3.5}, 10^{4.6}]$. These two scalings do not match our predictions according to RMLT and also do not display a transition to become independent of rotation when $\Omega \lesssim 10^{4.4}$. The lengthscale calculated using the heat flux on the other hand is steeper than the other two in the range $\Omega \in [10^{4.3}, 10^{4.6}]$. RMLT is expected to apply in this range because the flow is turbulent and strongly rotationally-constrained. The slope fitted within this range in dashed-burgundy scales as $\Omega^{-0.6}$, which should be compared with the temperature-based RMLT scaling as Ω^{-1}. This disagreement is likely to arise from the narrow range of Ra considered and because these simulations are not turbulent enough to match the RMLT scaling fully. However, it is much steeper than the result obtained from the other two quantities, and the data points taper off at small Ω as expected.

In Fig. 4.6 we demonstrate that with fixed supercriticality R, our results are consistent with the RMLT prediction, based on the supercriticality, of $l_c \propto \Omega^{-1/3}$ regardless of which quantity or method is used to compute the lengthscale. The solid-red line, with the same parameters as the solid-red line in the left-hand panel matches the heat flux data well. The lengthscale obtained from the temperature fluctuations is slightly larger, and the lengthscale obtained from the vertical kinetic energy is much larger. Interestingly, the peaks in blue squares do not follow the solid-red RMLT prediction as closely as they do in Fig. 4.5. We attribute this difference to fluctuations in the spectrum causing the peak to shift around, particularly as the spectrum near the peak of the heat flux is quite broad as was observed in Fig. 4.4, so the lengthscale based on integrals may be better suited here. Furthermore, while these data superficially seem to follow the linear onset scaling, each of these follows a distinct scaling with a different prefactor than the onset scaling. Note that when the supercriticality is fixed (equivalent to plotting results as a function of $\mathrm{RaEk}^{4/3}$) instead of the Rayleigh number, the predictions of RMLT have the same dependence on Ω as the linear onset scaling, but this does not imply that the lengthscale is controlled by viscosity.

Based on these results, we use the lengthscale obtained from the integral heat flux method in Fig. 4.6 in the rest of this work, i.e. the dark orange diamonds, and use the solid-red RMLT fit whenever it is expected to apply. From the solid-red fit in both Fig. 4.5 and Fig. 4.6, if we reintroduce Ra using the definition $\mathrm{Ra}_c \approx 8.7\mathrm{Ek}^{-4/3}$, we obtain:

$$l_c = 0.63\mathrm{Ra}^{1/2}\mathrm{EkPr}^{-1/2}d. \tag{4.20}$$

Using this scaling together with Eq. (4.16) we also obtain a scaling law for the convective frequency

$$\omega_c \approx 0.44\mathrm{Ra}^{1/2}\mathrm{Pr}^{1/2}\frac{\kappa}{d^2}. \tag{4.21}$$

Thus we conclude that indeed the RMLT prescriptions agree well with our simulations, and show that the majority of our simulations are indeed in the rapidly-rotating regime as expected.

4.2.3 Effective viscosity verification using rotating mixing-length theory

Having verified the RMLT prescriptions in our simulations we now examine the scaling of the effective viscosity with convective driving (Ra) in Fig. 4.7 for simulations with $\mathrm{Ek} = 5 \cdot 10^{-5.5}$. Only results from simulations with sustained energy injection are plotted in this figure. There is a minimum value of $\mathrm{Ra} \approx 2.5\mathrm{Ra}_c$ for which using an effective viscosity according to RMLT reasonably approximates the data. This minimum also corresponds to the threshold value above which the convective LSV appears (Favier et al., 2014b; Guervilly et al., 2014).

We apply these theoretically-predicted and empirically-fitted scaling laws to determine an effective viscosity in Fig. 4.7. The effective viscosity portrayed in this figure is derived from the time-averaged values of I_{3D}, and as such it is given by $\nu_{\mathrm{eff},3D}$, but it is equal to ν_{eff} because the time-averaged values of I and I_{3D} are the same. The blue line corresponds to the low frequency regime in Eq. (4.7), the black line corresponds to the intermediate frequency regime, and the red line to the high frequency regime, with orange data points indicating the simulations. Varying Ra in this figure also means varying the ratio of tidal to convective frequencies, which can change which regime might be predicted in Eq. (4.7). The low and intermediate frequency predictions agree well with the simulations at high Ra, where ω_c is larger and thus the ratio of the tidal to convective frequencies is lower than at low Ra. At low Ra the simulations agree with the high frequency prediction, though there is a departure for the smallest Ra for which the simulations are no longer sufficiently turbulent, as noted previously.

The left-hand panel of Fig. 4.8 shows instead the effective viscosity as a function of the rotation rate Ω with fixed $\mathrm{Ra} = 1.3 \cdot 10^8$. Because Ra is fixed we expect the effective viscosity to rapidly decrease as the rotation rate increases. Since we set $\gamma = \Omega$ in these simulations the tidal frequency is $\omega = 2\gamma = 2\Omega$. The scalings of the effective viscosity obtained using RMLT according to Eq. (4.7) in terms of Ω are then respectively Ω^{-2}, $\Omega^{-2.5}$ and Ω^{-4} in the low, intermediate and high tidal frequency regime. In the left-hand panel of Fig. 4.8 we over-plot these low, intermediate and high frequency regime scalings, which are in good agreement with the simulation results. Based on our results for the convective lengthscale from the simulations there is some uncertainty around the solid-red fit of Ω^{-4}. According to the simulation data this should possibly scale as $\Omega^{-3.6}$ instead, as the scaling obtained for the convective lengthscale goes as $\Omega^{-0.6}$ instead of Ω^{-1}. The difference in the results is negligible however, and for consistency with the RMLT prediction for the effective viscosity we opted to keep instead the Ω^{-4} scaling in the plot.

In the right-hand panel of Fig. 4.8 we fixed $R = 6$ at $\epsilon \in [0.02, 0.05]$, which are the values of ϵ used for all subsequent results with fixed R. We examined the variation of the effective viscosity with Ω. Again, we observe a decrease as the rotation rate is increased, though this is a weaker trend than we found when fixing Ra. We also observe two possible scaling regimes. When we compare with those expected by RMLT we again find good agreement with our simulation results. We find that even when fixing the convective supercriticality, we obtain bursts of elliptical instability for sufficiently large Ω. This may

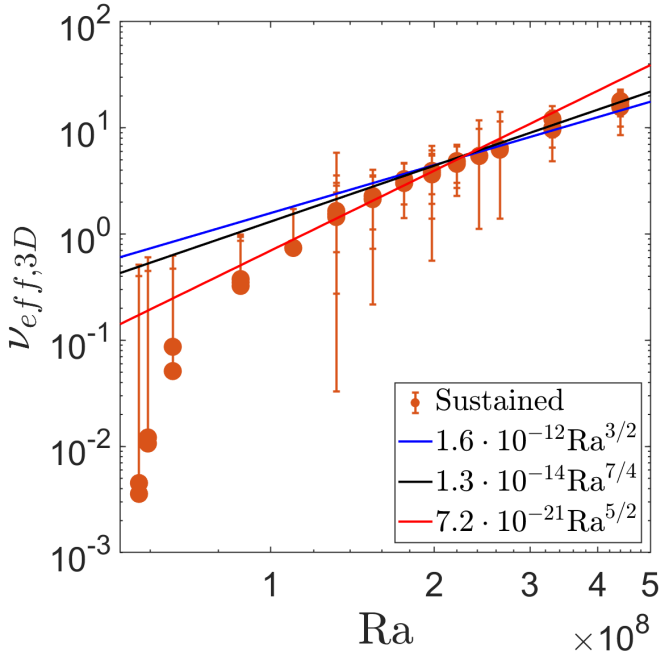

Figure 4.7: Effective viscosity as a function of Ra with fixed $\mathrm{Ek} = 5 \cdot 10^{-5.5}$. Only simulations featuring sustained energy injection are plotted. In addition, all three scaling law regimes predicted using RMLT are plotted. All three scaling laws agree well with the data in the appropriate regimes, the intermediate and low frequency scaling laws agree at high Ra. The high frequency regime agrees at low Ra, except for the smallest values of Ra.

be caused by a diminished suppressive effect of convection on the elliptical instability for larger Ω because the effective viscosity is lowered, while the increased rotation rate enhances the growth rate of the elliptical instability (relative to the viscous damping rate).

In this section we have generally found good agreement with both the predictions of RMLT for convective velocities and lengthscales, and with their application to the scaling laws for the effective viscosity acting on (tidal) oscillatory shear flows in Duguid et al. (2020). Based on our fits of RMLT scaling laws to the data in Figs. 4.7 and 4.8, we find the following effective viscosity regimes:

$$\nu_{\mathrm{eff}} = \begin{cases} 6.4 \cdot 10^{-3}\mathrm{Ra}^{3/2}\mathrm{Ek}^2\mathrm{Pr}^{-1/2}\kappa & \text{low frequency,} \\ 0.012\mathrm{Ra}^{7/4}\mathrm{Ek}^2\mathrm{Pr}^{-1/4}\kappa^{3/2}d^{-1}\omega^{-1/2} & \text{intermediate frequency,} \\ 0.11\mathrm{Ra}^{5/2}\mathrm{Ek}^2\mathrm{Pr}^{1/2}\kappa^3 d^{-4}\omega^{-2} & \text{high frequency.} \end{cases} \tag{4.22}$$

4.2.4 Analysis of regime transitions

The previous section tentatively suggests we can use MLT and RMLT and the tidal frequency regimes observed in simulations to interpret (and make predictions for) the effective viscosity. However, to understand the full picture, one would need to understand when

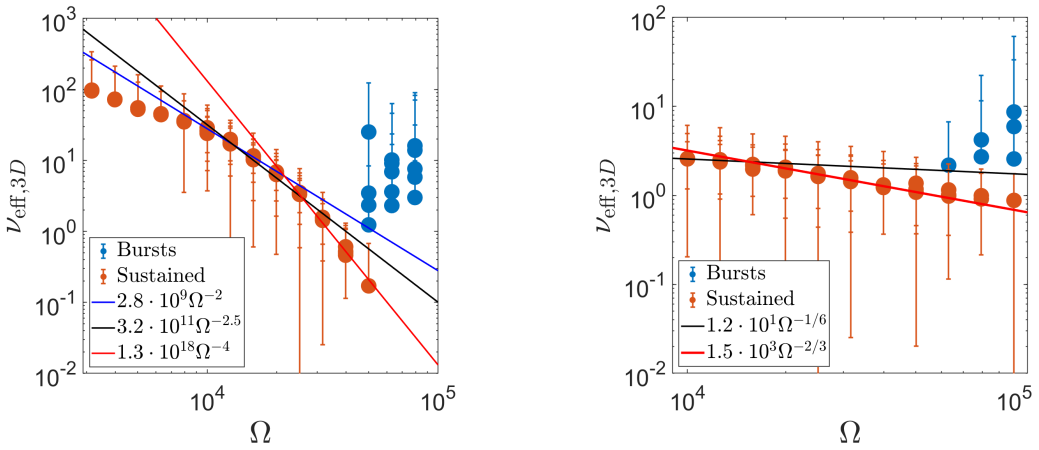

(a) Fixed Ra

(b) Fixed R (supercriticality)

Figure 4.8: Effective viscosity as a function of the rotation rate with fixed Rayleigh number and supercriticality. Left: Effective viscosity with fixed Rayleigh number $\mathrm{Ra} = 1.3 \cdot 10^8$ and $\epsilon \in [0.02, 0.05]$ as a function of rotation rate, together with all three predictions based on RMLT and the scalings obtained in Duguid et al. (2020). Right: Same as above but at constant supercriticality $R = 6$ and $\epsilon \in [0.02.0.05]$.

transitions between different regimes occur. As described in Sec. 4.2.1, by virtue of setting $\Omega = \gamma$ in our simulations, the values of the Rossby number at which these transitions are likely to occur are similar to each other. Therefore, the occurrence of these combined transitions (MLT/RMLT and the different tidal frequency regimes) makes it unclear which regimes of the effective viscosity are observed in Fig. 4.7 and Fig. 4.8. One way to separate these two transitions is to first consider the quantity ω/ω_c, which is important because it controls the regime transitions of the effective viscosity. However, it is also controlled by the transition from MLT to RMLT, because ω_c depends on u_c and l_c.

In Fig. 4.9 the ratio ω/ω_c is plotted as a function of the Rayleigh number at constant $\mathrm{Ek} = 5 \cdot 10^{-5.5}$. We calculate ω_c using the convective velocities obtained from simulations, whilst basing the convective lengthscale on Eq. (4.5). In addition, the prediction of ω/ω_c according to RMLT simulation results, with ω_c given by Eq. (4.21), is plotted in solid-red. By forcing the convective lengthscale to follow the RMLT prediction, i.e. $l_c \sim \mathrm{Ra}^{1/2}$, ω_c will no longer scale as $\mathrm{Ra}^{1/2}$ when u_c deviates from the RMLT prediction, i.e. when its scaling changes from $u_c \sim \mathrm{Ra}$ to $u_c \sim \mathrm{Ra}^{1/2}$. This in turn forces the scaling of ω_c to go from $\omega_c \sim \mathrm{Ra}^{1/2}$ to $\omega_c \sim \mathrm{Ra}^0$. Examining where this transition occurs allows us to identify at what value of ω/ω_c the change from MLT to RMLT occurs. In the figure, the change of scaling laws is manifested by the data points deviating from the solid-red prediction as their slope decreases when $\mathrm{Ra} \gtrsim 2 \cdot 10^8$, in accordance with what is observed in Fig. 4.7. Thus, by using the RMLT scaling to obtain the convective lengthscale, but using the simulation data for the convective velocity, we can easily identify at what values of ω/ω_c this transition from RMLT to MLT occurs. We find the transition at $\omega/\omega_c \approx 10$, or a convective Rossby number $\mathrm{Ro}_c \approx 0.1$.

In Fig. 4.10 we show the ratio ω/ω_c as a function of Ω at constant $\mathrm{Ra} = 1.3 \cdot 10^8$

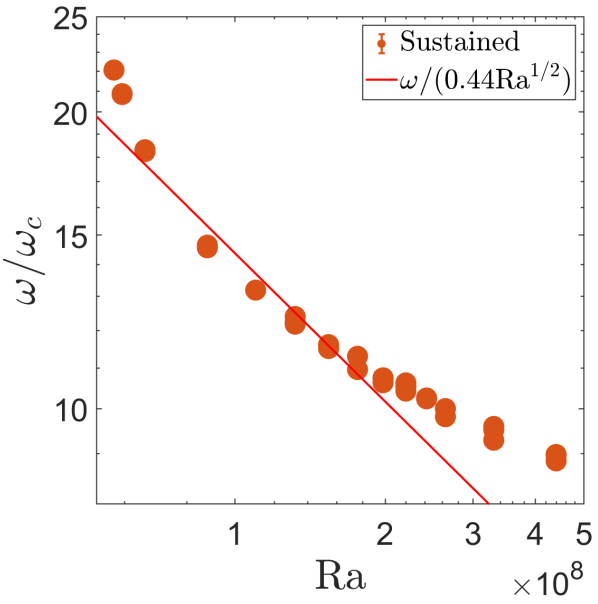

Figure 4.9: Ratio of the tidal to convective frequencies as a function of Ra compared with the RMLT prediction with fixed $\mathrm{Ek} = 5 \cdot 10^{-5.5}$. The data for u_c is obtained from simulations, while l_c is calculated using Eq. (4.5). The predicted result based on Eq. (4.21) is plotted in solid-red. The change from the RMLT to MLT scaling occurs around $\mathrm{Ra} \approx 2 \cdot 10^8$ in the left-hand panel of Fig. 4.3, which matches the departure observed here and occurs at $\omega/\omega_c \approx 10$, i.e. $\mathrm{Ro}_c \approx 0.1$.

using orange and blue (with elliptical instability bursts) circles, which is computed in the same way as in Fig. 4.9. In addition, ω/ω_c is calculated using the simulation data directly for both u_c and l_c in purple and burgundy squares. Purple squares indicate simulations without the elliptical instability, and burgundy squares indicate simulations with bursts of the elliptical instability. The prediction for ω/ω_c in the RMLT regime is again plotted in solid-red. The deviation of the orange data points from this solid-red line occurs for $\Omega \lesssim 10^{4.4}$ as in the left-hand panel of Fig. 4.8. Furthermore, this deviation coincides with $\omega/\omega_c \approx 10$, as was found in Fig. 4.9.

The convective frequency calculated directly using the simulation results for both u_c and l_c in the purple and burgundy squares illustrates how the transition from RMLT to MLT occurs in our simulations. First of all, the purple squares and some of the burgundy squares in the range $\Omega = [10^{4.5},\ 10^5]$ match the dashed-black fit of $\omega/\Omega^{-0.4} \sim \Omega^{1.4}$, illustrating that indeed according to simulations $\omega_c \sim u_c/l_c \sim \Omega^{-1}/\Omega^{-0.6} \sim \Omega^{-0.4}$. The purple squares in the interval $\Omega = [10^{3.5},\ 10^{4.4}]$ do not deviate as much from the solid-red prediction as the pure RMLT convective lengthscale results in orange on the same interval. The convective velocity and lengthscale therefore appear to become independent of Ω at roughly the same value of Ro_c. As a result ω_c is maintained to be almost independent of Ω, which is indicated by scaling as $\omega_c \sim \Omega^{0.2}$ according to the dashed-blue fit. Note also that the value of ω/ω_c using simulation results decreases to ≈ 1, suggesting that the effective viscosity in this range should transition from the high tidal frequency to the intermediate tidal frequency regime, but not to the low tidal frequency regime, according

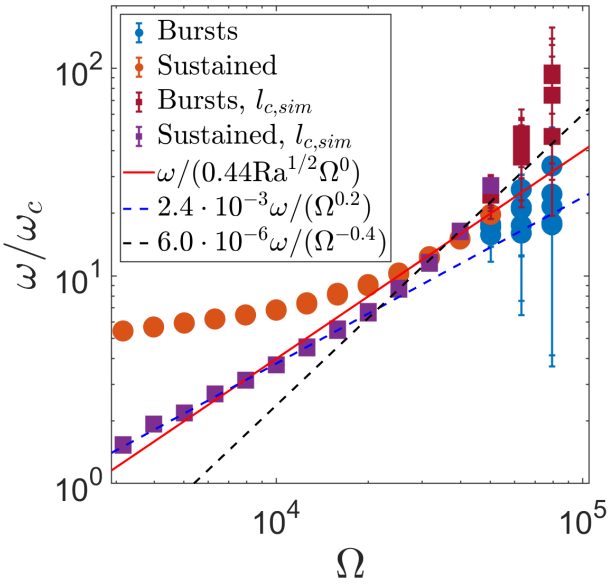

Figure 4.10: Ratio of the tidal to convective frequencies as a function of Ω with fixed $\mathrm{Ra} = 1.3 \cdot 10^8$, calculated in the same way as in Fig. 4.9 in orange and blue circles. Using this calculation the change from MLT to RMLT occurs around $\Omega \approx 10^{4.5}$, like in Fig. 4.8, corresponding to $\omega/\omega_c \approx 10$, and $\mathrm{Ro}_c \approx 0.1$. The purple and burgundy squares represent ω_c calculated using both u_c and l_c, which stays closer to the prediction of ω_c independent of the rotation rate, and therefore attains lower values than the RMLT prediction, crossing below the $\omega/\omega_c = 5$ threshold.

to the transition found in the non-rotating simulations of Duguid et al. (2020), if these hold here.

Both Fig. 4.9 and Fig. 4.10 indicate that care must be taken to first identify the regime of rotational influence on the convection (i.e. MLT vs RMLT) to predict the value of ω_c before calculating the ratio ω/ω_c, and thus determining which frequency regime is relevant for the effective viscosity. The deviation from the RMLT prediction for these quantities in both figures occurs roughly when $\mathrm{Ro}_c^{-1} \approx 10$, so we conclude that when $\mathrm{Ro}_c < 0.1$, RMLT is the correct prescription for the rotating convection, and that $\mathrm{Ro}_c \approx 0.1$ is where the transition from RMLT to MLT begins and the rotational influence diminishes for increasing Ro_c.

To fully disentangle and interpret the effective viscosity and its dependence on Ω and ω separately, we should also calculate the effective viscosity as a function of the ratio ω/ω_c. To this end we use values of ω_c obtained from the simulations, i.e. corresponding to the square markers in Fig. 4.10. The results for $\nu_{\mathrm{eff},3D}$ are plotted in Fig. 4.11. These figures are closely related to Fig. 4.8, but are specifically designed to explore the ω/ω_c dependence. In the left-hand panel of Fig. 4.11, we show results with fixed $\mathrm{Ra} = 1.3 \cdot 10^8$, while in the right-hand panel simulations with fixed $R = 6$ are plotted. The effective viscosity is divided by the factor of $u_c l_c$ which is present in all expressions for this quantity. By eliminating this factor the dependence of the effective viscosity on the ratio of ω/ω_c is therefore directly measured. It is important to note that due to the transition from MLT to RMLT in the

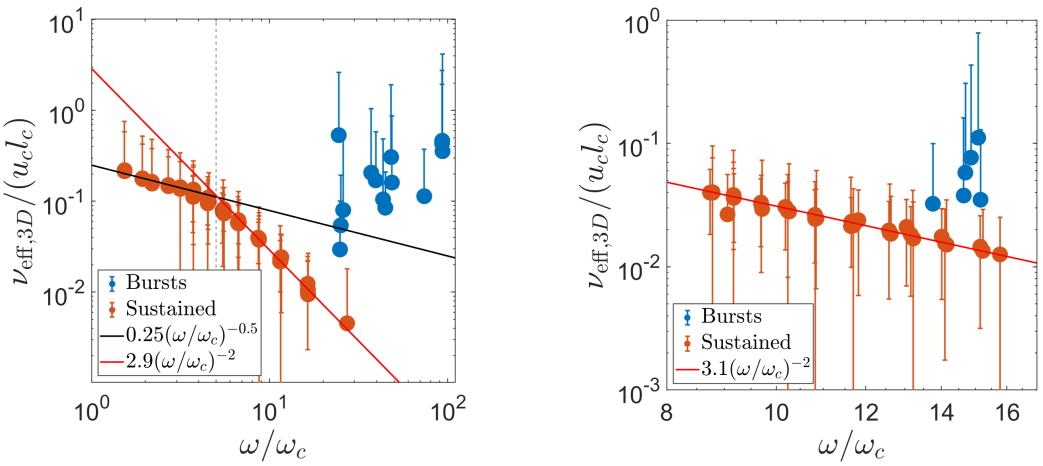

(a) Fixed Ra (b) Fixed R (supercriticality)

Figure 4.11: The effective viscosity divided by $u_c l_c$ as a function of ω/ω_c. Left: Effective viscosity with fixed Rayleigh number $\mathrm{Ra} = 1.3 \cdot 10^8$. The high frequency prediction is plotted in solid-red, and the intermediate frequency prediction is plotted in black. The vertical dashed-black line indicates the transition between these regimes at $\omega/\omega_c = 5$ found previously (without rotation by Duguid et al., 2020), which matches the transition in our data well. Right: The same with fixed supercriticality $R = 6$; only the high frequency regime is present in the data.

left-hand panel and the choice of fixed supercriticality in the right-hand panel, ω/ω_c in general depends on the Ekman number. In the left-hand panel both the intermediate and high frequency regimes are observed. The high frequency regime is plotted in solid-red line, while the intermediate frequency regime is plotted in solid-black. Both scalings agree well with simulation data. The transition from the high frequency to the intermediate frequency regime found previously at $\omega/\omega_c \approx 5$ (without rotation in Duguid et al., 2020) is plotted using a vertical dashed line in the left-hand panel. The location of this transition agrees remarkably well with our data. In the right-hand panel, only the high frequency regime is observed. We thus conclude that we have not observed the low tidal frequency regime in our simulations. Moreover, we find that the intermediate regime in Duguid et al. (2020) is reproduced and the transition to this from the high frequency regime seems to occur at the same value of ω/ω_c, even when the convective velocity and lengthscale are influenced by rotation. The prefactors of the intermediate and high frequency regime are however different from those found in Duguid et al. (2020), both lower by approximately a factor of two. Reproducing Eq. (4.1) with these altered prefactors:

$$\nu_{\mathrm{eff}} = \begin{cases} 5 u_c l_c & \frac{|\omega|}{\omega_c} \lesssim 10^{-2}, \\ 0.25 u_c l_c \left(\frac{\omega_c}{\omega}\right)^{\frac{1}{2}} & \frac{|\omega|}{\omega_c} \in [10^{-2}, 5], \\ 3 u_c l_c \left(\frac{\omega_c}{\omega}\right)^{2} & \frac{|\omega|}{\omega_c} \gtrsim 5. \end{cases} \tag{4.23}$$

In summary, to correctly interpret and make predictions for the effective viscosity, one must first determine whether or not the convection is strongly influenced by rotation

(i.e. whether RMLT or MLT is an appropriate description) using the convective Rossby number. Then the ratio of ω/ω_c, i.e. the "tidal Rossby number", can be used to determine which of the low, intermediate or high tidal frequency regimes are appropriate. Upon substituting the results for u_c and l_c from Eq. (4.16) and Eq. (4.20) into Eq. (4.23) we finally arrive at:

$$\nu_{\text{eff}} = \begin{cases} 0.88\text{Ra}^{3/2}\text{Ek}^2\text{Pr}^{-1/2}\kappa & \frac{|\omega|}{\omega_c} \lesssim 10^{-2}, \\ 0.029\text{Ra}^{7/4}\text{Ek}^2\text{Pr}^{-1/4}\kappa^{3/2}d^{-1}\omega^{-1/2} & \frac{|\omega|}{\omega_c} \in [10^{-2}, 5], \\ 0.10\text{Ra}^{5/2}\text{Ek}^2\text{Pr}^{1/2}\kappa^3 d^{-4}\omega^{-2} & \frac{|\omega|}{\omega_c} \gtrsim 5. \end{cases} \tag{4.24}$$

These scalings are likely to be more robust than the scalings in Eq. (4.22), because the numerical coefficient of the scaling for the low frequency regime is based on a measured result in Duguid et al. (2020) and the scaling for the intermediate frequency regime is no longer unclear because the two transitions are occurring at the same time.

4.3 Conclusions

We have found the elliptical instability to provide time-averaged tidal dissipation rates consistent with an ϵ^3 scaling when it operates (consistently with Barker & Lithwick, 2013, 2014; Barker, 2016a). We have defined an efficiency factor χ, such that $D \equiv \chi\epsilon^3\gamma^3$, to represent the intermittent and imperfect operation of the elliptical instability. We observed this efficiency to be $\chi \approx 0.05$, with an upper bound of $\chi \lesssim 0.18$. Furthermore, the efficiency factor seems to be independent of the convective driving (Rayleigh number) as long as the elliptical instability operates. Some of our results are also consistent with a steeper ϵ^6 scaling, which, if robust, would significantly weaken tidal dissipation for realistic values of ϵ, restricting the effectiveness of this mechanism except for the very shortest orbital periods.

We have also found a sustained energy injection rate scaling as ϵ^2 in our simulations for smaller values of ϵ than those for which the elliptical instability is observed. This can be interpreted as an effective viscosity arising from the interaction between rotating convection and the equilibrium tidal flow that is independent of ϵ (as would be predicted by a linear tidal mechanism). On the other hand, this effective viscosity is observed to depend on the convective velocity, lengthscale and tidal frequency. We have obtained scaling laws for convective velocities and lengthscales, which are used to find predictions for the convective frequency and the effective viscosity, using both (temperature-based) MLT and RMLT prescriptions. We find very good agreement between the predictions of RMLT and our simulation data. Our simulations confirm the applicability of the diffusion-free scalings of RMLT (e.g. Stevenson, 1979; Barker et al., 2014; Aurnou et al., 2020; Currie et al., 2020) to describe sufficiently turbulent rapidly rotating convection. We observe the transition from RMLT to MLT to begin around $\text{Ro}_c \approx 0.1$ as in Barker et al. (2014), and find RMLT is the appropriate description of (sufficiently turbulent) convection for $\text{Ro}_c \lesssim 0.1$. Furthermore, these scaling laws, which we have confirmed using temperature-based RMLT,

match those obtained from Coriolis-Inertial-Archimedean (CIA) triple balance arguments (e.g. Ingersoll & Pollard, 1982; Aubert et al., 2001; Jones, 2015; Gastine et al., 2016; Guervilly et al., 2019; Aurnou et al., 2020; Bouillaut et al., 2021, and many others) and the applicability of these temperature-based scalings reinforce the applicability of the diffusion-free flux-based scalings.

Finally, we find that the scaling laws for the effective viscosity as a function of convective velocity, lengthscale and frequency – when the rotational modification of these quantities is accounted for – previously found in non-rotating simulations (Duguid et al., 2020) largely hold true in our rotating simulations. Our results support the frequency-reduction of the effective viscosity for fast tides $(\omega_c/\omega)^2$ when $\omega \gg \omega_c$. We also confirm the presence of the intermediate frequency regime of $(\omega_c/\omega)^{-1/2}$, as found in Duguid et al. (2020) and Vidal and Barker (2020b), in our simulations, and that the transition to this regime from the high frequency regime occurs at a similar ratio of $\omega/\omega_c \approx 5$.

We will discuss the astrophysical applications of our results in Ch. 7. To this end we will generate models of the interiors of giant planets, to which we will apply the scaling laws we have obtained for the elliptical instability, as well as the predictions for the effective viscosity.

Chapter 5

Theoretical background of the precessional instability and convection

In the next two chapters we will turn our attention to the precessional instability and its interaction with convection. The precessional instability is similar in mechanism to the elliptical instability and therefore most of the concepts introduced in Ch. 2 are applicable here. Indeed we will again start by discussing the form of the background precessing flow and summarising the findings of the previously performed linear stability analysis of the precessional instability in isolation. We will once again derive the quantities of interest in this system. From here we will detail the DEDALUS (Burns et al., 2020) and NEK5000 (Fischer et al., 2008) codes we employ to study these interactions. We verify that we accurately captured both the precessional and convective instabilities in isolation in both codes. After confirming the instabilities in isolation are properly captured, we will perform a new linear stability analysis of the precessional instability in the presence of stratification and attempt to verify this using both codes. Finally, we will once again detail the parameters we will vary in this study as well as the resolutions we will employ in our simulations.

5.1 The precessional instability

5.1.1 The background precessional flow

The precessional instability is an instability of axially precessing flows. Tidal forces from the secondary can induce axial precession in the primary if the spin axis of the primary is not aligned with the orbital angular momentum vector of the system, such that the obliquity of the body is non-zero. Such a process is important for example for the Earth, whose spin axis gradually precesses in space due to tidal forcing from the Moon and Sun. The relevant tidal component that results in the axial precession is part of the "obliquity

tide", namely the $l = 2,\ m = 1,\ n = 0$ component of the tide. The rotation rate of this flow is tied to the tidal frequency of this component, which is $\omega_{2,1,0} = -\Omega_s$. This component gives rise to the Poincaré solution in a full homogeneous fluid body (Poincaré, 1910) in the absence of viscosity. We consider the full Poincaré solution in the precessing frame, as depicted in the schematic in Fig. 1.10. In the precessing frame the body spins around its own axis, while this whole system rotates around a secondary axis called the precession axis, i.e. it precesses, according to an observer that is located in space. We choose the direction of the spin-axis to be the $\tilde{z}$-axis. Tildes denote quantities defined in the precessing frame. In this frame the spin of the body is generally much faster than the precession, and the precession forces the whole body to rotate. The component of the precessional vector that is parallel to the body's rotation is unimportant to the precessional instability, so we choose to set it to zero. The precession vector can therefore be assumed to take the form $\tilde{\boldsymbol{\Omega}}_p = \mathrm{Po}\,\Omega\hat{\boldsymbol{x}}$ (Kerswell, 1993), with $\mathrm{Po} = \Omega_p/\Omega$ the Poincaré number. This setup is shown on the left-hand side of Fig. 5.1. The Poincaré number fulfils the same role in the precessional instability as the ellipticity ϵ does in the elliptical instability, and one can see numerous parallels between these two quantities in the rest of this chapter. The Poincaré number is, like the ellipticity, a small parameter in most astrophysical systems. On Earth, for example, the precessional period is ≈ 26000 yrs, such that $\mathrm{Po} \approx 10^{-7}$. Even so, Kerswell (1996) estimated that the maximum possible energy injected by the precessional instability could be sufficient to power the geodynamo. In Hot Jupiters, with both larger oblateness and closer proximity to the tide raising body and therefore stronger torques, these values are more likely to be on the order of $\mathrm{Po} = \mathcal{O}(10^{-4} - 10^{-3})$. Thus these values are small, but still of such a size that the precessional instability is thought to be relevant for aligning the spins and orbits of such Hot Jupiters (Barker, 2016b). Note that the frequency of the precessional flow and the frequency of the precession differ. In the precessing frame, ignoring the effects of viscosity and stratification, the precessing flow that satisfies the incompressible equations of motion is (Kerswell, 1993):

$$\tilde{\boldsymbol{V}}_0 = \Omega \begin{pmatrix} 0 & -1 & 0 \\ 1 & 0 & -(1+\eta)\mu \\ 0 & \mu & 0 \end{pmatrix} \tilde{\boldsymbol{x}}, \tag{5.1}$$

where $\tilde{\boldsymbol{x}}$ represents the position vector from the centre of the body, η is the oblateness of the body and μ is the ratio of the ellipticity of the streamlines to the shearing of the streamlines in Fig. 1.10. In this geometry this ratio is given by $\mu = 2\mathrm{Po}/\eta$. We are interested in just the shearing effects, as these are thought to be more important than the ellipticity of the streamlines. In this case one can start from Eq. (1.1) in Kerswell (1993) instead, ignoring any term involving μ^2. The precessing flow then reduces to (Kerswell, 1993):

$$\tilde{\boldsymbol{U}}_0 = \Omega \begin{pmatrix} 0 & -1 & 0 \\ 1 & 0 & -2\mathrm{Po} \\ 0 & 0 & 0 \end{pmatrix} \tilde{\boldsymbol{x}}. \tag{5.2}$$

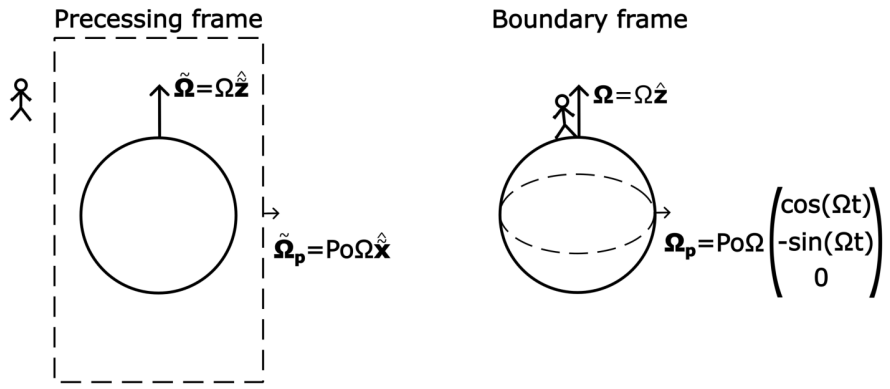

Figure 5.1: Schematic of the frames employed when studying the precessional instability. On the left we show the precessing frame. In this frame the observer is located in space and watches the body spin around its axis with spin vector $\tilde{\boldsymbol{\Omega}}$, pointing in the $\tilde{z}$-direction, while the whole body precesses due to the precession vector $\tilde{\boldsymbol{\Omega}}_p$, pointing in the $\tilde{x}$-direction. On the right we show the boundary frame or mantle frame, where the observer is located on the body. The body spins around its axis with spin vector $\boldsymbol{\Omega}$, pointing in the z-direction. Because the observer is located on the body and is therefore spinning around, the precession vector lies in the equatorial plane and rotates around – indicated by the dashed lines – with precession vector $\boldsymbol{\Omega}_p$, such that the direction of the precession vector is time-dependent.

This background flow takes the form of a uniform rotation about $\hat{\tilde{\boldsymbol{z}}}$ with a vertical shear given by $-2\mathrm{Po}\Omega z\hat{\tilde{\boldsymbol{y}}}$. It is this shear which allows for the excitation of inertial waves and thus the operation of what is referred to as the precessional instability, although it is also referred to as the inertial instability by e.g. Tilgner and Busse (2001).

The above two prescriptions for the precessing flow are given in the precessing frame, however, it is often preferred to work in the boundary frame. In this frame the flow inside the body appears to precess according to an observer located on the boundary of the body, i.e. in the case of Earth the observer is located on the mantle and is observing the precessing flow within the Earth's liquid core. This frame is therefore sometimes also referred to as the "mantle frame". In this frame the spin axis points in the z-direction, rotating at rate Ω, while the precession vector is given by $\boldsymbol{\Omega}_p = \mathrm{Po}\,\Omega(\cos(\Omega t), -\sin(\Omega t), 0)^T$. The precession vector thus rotates around the body in the equatorial plane in this frame. A schematic of this frame is shown on the right-hand side of Fig. 5.1. It is generally preferred to work in the boundary frame, as the background flow $\boldsymbol{U}_0$ reduces to an easier form, becoming translationally invariant in x and y:

$$\boldsymbol{U}_0 = \mathrm{A}\boldsymbol{x} = -2\mathrm{Po}\Omega\begin{pmatrix}0 & 0 & \sin(\Omega t)\\ 0 & 0 & \cos(\Omega t)\\ 0 & 0 & 0\end{pmatrix}\boldsymbol{x}, \tag{5.3}$$

where $\boldsymbol{x}$ now represents the position vector from the centre of the body which is rotating with the body. The precessing flow in this frame takes the form of a shear in z, whose

direction is rotating in the x, y-plane. Alternatively, this can be interpreted as a rotation which is sheared in z, as we expect from the schematic in Fig. 1.10.

5.1.2 Governing equations and setup of the problem

We once again choose to work in a local Cartesian model, building on the previous works of Kerswell (1993), R. Mason and Kerswell (2002), Wu and Roberts (2008), Barker (2016b), and Pizzi et al. (2022), to study the interaction of the precessional instability with convection, with a focus on studying the resulting tidal dissipation. We use stress-free impermeable walls in the z-direction, such that we build upon the setup in which R. Mason and Kerswell (2002) studied the precessional instability, a setup that was also employed by Wu and Roberts (2008) to study the precessionally-driven dynamo. This setup allows us to again study convection using the Rayleigh-Bénard prescription. We adopt a box with dimensions $[d, d, d]$, i.e. a box where $L_x = L_y = L_z$. We choose to work in a box with aspect ratio one because the introduction of walls modifies the way the precessional instability operates, and therefore the results in the absence of convection – as obtained in Barker (2016b) – should first be explored with these new boundary conditions as well. We will defer studying different aspect ratios to later work. In this setup gravity points in the vertical direction, $\boldsymbol{g} = g\hat{\boldsymbol{z}}$, and as a result it is (anti-)aligned with the rotation axis, which implies that we are examining flow near the poles. The boundary conditions are the same as those in Sec. 2.1.2, but for completeness we repeat them here. The boundary conditions in the horizontal directions are periodic, while in the vertical direction the walls are impermeable, $u_z(z = 0) = u_z(z = d) = 0$, stress-free, $\partial_z u_x(z = 0) = \partial_z u_x(z = d) = \partial_z u_y(z = 0) = \partial_z u_y(z = d) = 0$, and perfectly conducting, $\theta(z = 0) = \theta(z = d) = 0$.

Convection is again modelled using Rotating Rayleigh-Bénard Convection, hence the choice of impermeable walls to avoid "homogeneous convection". In the literature the precession vector is often rewritten as $\boldsymbol{\epsilon}(t) = \mathrm{Po}(\cos(\Omega t), -\sin(\Omega t), 0)^T$. This precession vector adds a second Coriolis-like term to the momentum equation, as well as an additional term that is sometimes referred to as the Poincaré force. The governing equations for the total velocity $\boldsymbol{U}$, temperature T_{tot} and pressure P_{tot} are as given in Kerswell (1993), R. Mason and Kerswell (2002), with the addition of the temperature terms and heat equation using the Boussinesq approximation:

$$\frac{\mathrm{D}\boldsymbol{U}}{\mathrm{D}t} + 2\Omega\left(\hat{\boldsymbol{z}} + \boldsymbol{\epsilon}(t)\right) \times \boldsymbol{U} = -\frac{1}{\rho_0}\nabla P_{\mathrm{tot}} + \alpha g T_{\mathrm{tot}}\hat{\boldsymbol{z}} + 2z\Omega^2\boldsymbol{\epsilon}(t) + \nu\nabla^2\boldsymbol{U}, \tag{5.4}$$

$$\frac{\mathrm{D}T_{\mathrm{tot}}}{\mathrm{D}t} = \kappa\nabla^2 T_{\mathrm{tot}}, \tag{5.5}$$

$$\nabla \cdot \boldsymbol{U} = 0, \tag{5.6}$$

where

$$\frac{\mathrm{D}}{\mathrm{D}t} \equiv \frac{\partial}{\partial t} + \boldsymbol{U} \cdot \nabla. \tag{5.7}$$

The background temperature profile is the same as in the previous three chapters; the conduction state profile that depends only on z:

$$T(z) = T_0 - \frac{\Delta T}{d} z. \tag{5.8}$$

We decompose the velocity, temperature and pressure profile into a background state and a perturbation as before: $\boldsymbol{U} = \boldsymbol{U}_0 + \boldsymbol{u}$, $T_{\text{tot}} = T(z) + \theta$ and $P_{\text{tot}} = P(z) + p$. Applying these decompositions and non-dimensionalising the governing equations by scaling lengths with the vertical domain size d, times with d^2/κ, velocities with κ/d, temperatures with ΔT and pressures with $\rho_0 \kappa^2/d^2$ we obtain:

$$\frac{\mathrm{D}\boldsymbol{u}}{\mathrm{D}t} + \boldsymbol{u} \cdot \nabla \boldsymbol{U}_0 + \frac{\mathrm{Pr}}{\mathrm{Ek}}(\hat{\boldsymbol{z}} + \boldsymbol{\epsilon}(t)) \times \boldsymbol{u} = -\nabla p + \mathrm{RaPr}\theta \hat{\boldsymbol{z}} + \mathrm{Pr}\nabla^2 \boldsymbol{u}, \tag{5.9}$$

$$\nabla \cdot \boldsymbol{u} = 0, \tag{5.10}$$

$$\frac{\mathrm{D}\theta}{\mathrm{D}t} - u_z = \nabla^2 \theta, \tag{5.11}$$

where

$$\frac{\mathrm{D}}{\mathrm{D}t} \equiv \frac{\partial}{\partial t} + \boldsymbol{U}_0 \cdot \nabla + \boldsymbol{u} \cdot \nabla. \tag{5.12}$$

The Ekman number, Prandtl number and Rayleigh number are defined as before. We will fix $\mathrm{Pr} = 1$ in this and the following chapter.

5.1.3 Known properties of the precessional instability

Using the above governing equations one can perform a linear stability analysis of the precessional instability. This has already been done in the absence of convection, with walls in the vertical direction, in R. Mason and Kerswell (2002). We summarise their most important results here.

As in Sec. 2.1.3 the inertial modes considered are those derived in the ordinary case between two stress-free impermeable walls given in Eq. (2.28) (Greenspan, 1968). Like the elliptical instability, these two modes denoted by A and B, need to satisfy a number of resonance conditions to be able to grow. The origins of these resonance conditions will be explained in more detail in Sec. 5.3. For now, the most important of these resonance conditions, and one that is changed with respect to the elliptical instability, is the condition on the frequencies of the two waves λ_B and λ_A, which satisfy the inertial wave dispersion relation in Eq. (1.45), reproduced here:

$$\lambda = \pm \frac{2\Omega k_z}{k}. \tag{5.13}$$

In the case of the precessional instability the two waves must satisfy $\lambda_B = \lambda_A \pm \Omega$ since the precessing flow has frequency magnitude Ω; without loss of generality we choose $\lambda_B = \lambda_A + \Omega$. A second resonance condition on the vertical wavenumbers, given by

$k_z = n\pi$ with integer n, arises from the boundary conditions. This resonance condition states that $(n_B - n_A)$ mod $2 = 1$, i.e. the difference between n_A and n_B must be odd. This contrasts with the elliptical instability, where the resonance condition required that $n_B = |n_A|$. This, in combination with the requirement that $k_{\perp,B} = k_{\perp,A}$, where $k_\perp$ is again the horizontal wavenumber, leads to very different conditions on the perpendicular wavenumber. Instead of one $k_\perp$ per value of n as in the case of the elliptical instability, there is a value of $k_\perp$ that satisfies the resonance conditions on the frequency for every combination of n_A and n_B. The precessional instability, with stress-free walls, therefore has a characteristic size for each mode pair. We refer to this as the "mode selection constraint". The particular value of $k_\perp$ for every mode pair is however a function of Po as well, as is illustrated in Fig. 3 of R. Mason and Kerswell (2002).

The resonance condition that the two modes have odd parity in the vertical wavenumber appears because of the impermeable boundary conditions in z, and is therefore not present in the triply periodic calculations and simulations of Kerswell (1993), Naing and Fukumoto (2011), and Barker (2016b). It however appears to some extent in simulations of precessing spheroidal cavities (see Fig. 9 and Fig. 10 of Lorenzani & Tilgner, 2001), where the unstable modes come in pairs, one symmetric and one anti-symmetric with respect to the equator of the spheroid. This provides an indication that this mode selection constraint has some physical basis in the geometries that we are trying to model using the local approximation, as opposed to being a purely mathematical constraint introduced by our specific choice of boundary conditions.

The inviscid growth rate σ of two modes n_A and n_B is determined by first calculating the $k_\perp$ that satisfies the resonance condition and then calculating the growth rate (see Eq. (4.11)-(4.15) of R. Mason & Kerswell, 2002). Some example inviscid growth rates and associated values of $k_\perp$ are found in Table 1 of R. Mason and Kerswell (2002). The largest inviscid growth rates are found when considering modes where $|n_B - n_A| = 1$ and n_A, n_B are large. However, in our simulations, these modes with large n_A and n_B do not produce the largest growth rates due to the damping effects of viscosity. As n_A and n_B increase, so do the $k_\perp$ that satisfy the frequency resonance condition, and thus these modes are more strongly damped by viscosity. As a result, those modes with the largest growth rate in our simulations are often those with $n_A = 1$, $n_B = 2$. Finally, the growth rate vanishes identically when either n_A or n_B is equal to zero, such that these modes should be unable to grow in purely precessional simulations.

In the case of $n_A = 1$, $n_B = 2$, the velocity field – in the absence of stratification and viscosity – grows according to (R. Mason & Kerswell, 2002):

$$\boldsymbol{u} = (A_0 \boldsymbol{u}_A \mathrm{e}^{-\mathrm{i}\lambda_A t} + B_0 \boldsymbol{u}_B \mathrm{e}^{-\mathrm{i}\lambda_B t}) \mathrm{e}^{0.3547 \mathrm{Po}\Omega t}. \tag{5.14}$$

The growth rate of the instability is thus proportional to Po, with a proportionality constant that is smaller than 1. More specifically, the maximum theoretically attained

value for this proportionality constant is ≈ 0.385, which is a factor of $2/\pi$ smaller than in the triply periodic case (R. Mason & Kerswell, 2002). The introduction of walls therefore decreases the growth rate of the precessional stability, unlike for the elliptical instability as shown in Ch. 2.

5.1.4 Energetic analysis of simulations

To analyse the flow we will again derive a kinetic energy equation by taking the scalar product with $\boldsymbol{u}$ of Eq. (5.9) and then averaging over the box. We define the averaging operation on a quantity X as $\langle X \rangle = \frac{1}{L^2 d} \int_V X \, \mathrm{d}V$, which is the same as the one defined in Sec. 2.1.5. We then obtain:

$$\frac{\mathrm{d}}{\mathrm{d}t} K = -\langle \boldsymbol{u} \cdot (\boldsymbol{u} \cdot \nabla \boldsymbol{U}_0) \rangle - \langle \boldsymbol{u} \cdot (\boldsymbol{U}_0 \cdot \nabla \boldsymbol{u}) \rangle + W_B - D_\nu. \tag{5.15}$$

The term associated with the Coriolis-like force due to the precessional rotation has vanished for the same reason as the Coriolis term: both terms do no work. Using the same arguments as in Sec. 2.1.5 we recover the same kinetic energy equation as before:

$$\frac{\mathrm{d}}{\mathrm{d}t} K = I + W_B - D_\nu, \tag{5.16}$$

with the definitions as before in Eqs. (2.62)-(2.65). Note that the evaluation of I is changed compared to the one in Sec. 2.1.5 however, because the form of the background flow is different.

The heat equation is unaltered, and therefore the equation for the thermal (potential) energy is the same. When the stratification is convectively unstable, i.e. $\mathrm{Ra} > 0$:

$$\frac{\mathrm{d}}{\mathrm{d}t} P = W_B - D_\kappa, \tag{5.17}$$

with definitions as before in Eq. (2.70). The total energy is again $E = K + P$, which thus obeys:

$$\frac{\mathrm{d}}{\mathrm{d}t} E = I + 2W_B - D_\nu - D_\kappa = I + 2W_B - D, \tag{5.18}$$

where again $D = D_\nu + D_\kappa$ is the total dissipation rate. When stably stratified, we obtain $I = D$ instead in steady state, because the W_B terms cancel, like in Ch. 2. We will therefore consider the tidal energy dissipation rate by examining the tidal energy injection rate I based on the same arguments as before.

To obtain a scaling argument for the precessional instability we will use the same heuristic approach based on a single dominant mode as before, by considering the growth rate as the inverse of a growth timescale:

$$\frac{1}{t_{\mathrm{grow}}} \sim \sigma \mathrm{Po}\Omega \sim \mathrm{Po}\Omega. \tag{5.19}$$

We also define a non-linear damping timescale according to:

$$\frac{1}{t_{\text{damp}}} \sim ku, \tag{5.20}$$

where k is the wavenumber magnitude and u is the velocity amplitude. The instability is expected to saturate when the growth and damping timescale are equal, giving:

$$u \sim \text{Po}\Omega/k. \tag{5.21}$$

The total dissipation rates therefore scales as:

$$D \sim u^2/t_{\text{damp}} \sim \text{Po}^3\Omega^3 k^{-2}. \tag{5.22}$$

We retrieve the now familiar scaling for the energy injection rate, which can be compared with Eq. (2.79) for the elliptical instability:

$$D = I \propto \text{Po}^3. \tag{5.23}$$

This scaling is consistent with some local simulations (Barker, 2016b; Pizzi et al., 2022) at sufficiently (but still $\text{Po} < 1$) high values of the Poincaré number. An energy injection rate that is consistent with a scaling closer to Po^2 at low values of the Poincaré number is also retrieved by Barker (2016b). A theoretical basis for such a scaling was not identified, but we will still examine if it also arises in our simulations.

Based on our studies in Ch. 3 of the elliptical instability and rotating convection, we expect to observe the non-linear creation of large-scale geostrophic flows from both the convective instability as well as the precessional instability. We again define a decomposition into a 2D z-invariant flow and 3D z-dependent flow. We will, however, use different definitions for these compared to the definitions in Sec. 2.1.5 for reasons that will become clear later. In this case, we define the energy of the z-invariant flow K_{2D} as:

$$K_{2D} = \frac{1}{2V}\iint\left(\int u_x \,\mathrm{d}z\right)^2 \mathrm{d}y\,\mathrm{d}x + \frac{1}{2V}\iint\left(\int u_y \,\mathrm{d}z\right)^2 \mathrm{d}y\,\mathrm{d}x. \tag{5.24}$$

We have chosen not to include u_z in the definition of K_{2D} because the z-invariant vertical velocity must be zero due to the impermeability boundary condition. This choice is made so that the decomposition is similar to that in Sec. 2.1.5, in that the $k_z = 0$ mode cannot contribute to K_{2D}. The definition of K_{3D} then follows as:

$$K_{3D} = K - K_{2D}. \tag{5.25}$$

Furthermore, we can expand the energy injection using the definition of the background flow:

$$I = 2\text{Po}\Omega\left(\langle u_x u_z\rangle \sin(\Omega t) + \langle u_y u_z\rangle \cos(\Omega t)\right). \tag{5.26}$$

We can see that, by definition, I_{2D} must be zero, because every term in Eq. (5.26) contains the vertical velocity. Thus, the decomposition of I into I_{2D} and I_{3D} is unfortunately no longer available to us as a useful diagnostic tool.

Finally, we can use the same technique as in Sec. 2.1.5 to obtain an estimate of the turbulent effective viscosity due to the convection acting on the precessional flow, which we have strong reason to believe will arise in these simulations as well. In this case the strain rate tensor $e^0_{ij} \equiv \frac{1}{2}(\partial_i U_{0,j} + \partial_j U_{0,i})$ is given by:

$$e^0 = -\mathrm{Po}\Omega \begin{pmatrix} 0 & 0 & \sin(\Omega t) \\ 0 & 0 & \cos(\Omega t) \\ \sin(\Omega t) & \cos(\Omega t) & 0 \end{pmatrix}, \tag{5.27}$$

such that the rate at which energy is dissipated is given by:

$$\frac{2\nu_{\mathrm{eff}}}{V} \int_V e^0_{ij} e^0_{ij} \, \mathrm{d}V = 4\nu_{\mathrm{eff}} \mathrm{Po}^2 \Omega^2. \tag{5.28}$$

Upon equating this expression to I we can define the effective viscosity according to:

$$\nu_{\mathrm{eff}} = I/(4\mathrm{Po}^2\Omega^2). \tag{5.29}$$

The effective viscosity might be expected to be independent of Po; this implies that, if the interaction of turbulence acting on the precessional flow can be parametrised as a turbulent effective viscosity, it should scale as:

$$D = I \propto \mathrm{Po}^2. \tag{5.30}$$

Finally, we will also study the heat transport in these simulations, to see if we observe the same kind of modification as we found with the elliptical instability. The definition of the Nusselt number is unaltered from the one presented in Eq. (2.86).

5.2 Numerical setup

We will use two codes in tandem to study the precessional instability interacting with convection, namely the DEDALUS and NEK5000 codes. We are forced to step away from the normally well-suited SNOOPY code because the employed sine-cosine decomposition is incompatible with the precessional vertical background shear flow. We choose to use these two codes together to ensure that we are capturing the dynamics in the system accurately, as they are based on different numerical methods.

5.2.1 The DEDALUS code

Firstly, we will discuss the DEDALUS code (Burns et al., 2020). DEDALUS implements a pseudo-spectral method like the SNOOPY code, but is more versatile than SNOOPY because

it allows to easily switch between different geometries – for example: plane layer, box, disk, spherical shell and full sphere – and different basis functions. Of particular relevance is the possibility to utilise Chebyshev polynomials instead of a Fourier series as a basis.

Chebyshev polynomials can be used to construct an orthogonal basis like Fourier series. This however consists of polynomials instead of sines and cosines and is therefore not inherently periodic. This inherent aperiodicity is ideally suited when considering impermeable walls in one or multiple directions of the system. Chebsyhev polynomials in z are what allows us to avoid using the sine-cosine decomposition in the DEDALUS code, and thus to simulate this problem. Additionally, we employ a so-called "real" Fourier basis, like the sine-cosine decomposition in Ch. 2, which means we use sines and cosines instead of exponentials in the x and y directions. An arbitrarily chosen single mode in this basis is given by:

$$\begin{aligned} u_x &= \mathrm{Re}[\hat{u}_x(t)\, T_n(z)\, \sin(k_x x)\cos(k_y y)], \\ u_y &= \mathrm{Re}[\hat{u}_y(t)\, T_n(z)\, \cos(k_x x)\sin(k_y y)], \\ u_z &= \mathrm{Re}[\hat{u}_z(t)\, U_{n-1}(z)\, \cos(k_x x)\cos(k_y y)], \\ p &= \mathrm{Re}[\hat{p}(t)\, T_n(z)\, \cos(k_x x)\cos(k_y y)], \\ \theta &= \mathrm{Re}[\hat{\theta}(t)\, U_{n-1}(z)\, \cos(k_x x)\cos(k_y y)], \end{aligned} \tag{5.31}$$

with k_x and k_y the wavenumbers in the x and y-directions respectively, which satisfy $k_\perp^2 = k_x^2 + k_y^2$, and $T_n(z) = \cos\left[n \arccos\left[(z+1)/2\right]\right]$, $U_n(z) = \frac{\sin\left[(n+1)\arccos\left[(z+1/2)\right]\right]}{\sin\left[\arccos\left[(z+1/2)\right]\right]}$ the n-th Chebyshev polynomials of the first kind and second kind respectively, both defined on the interval $z = [0, 1]$ with $n \in [0, n_z - 1]$. The other modes that exist in the real Fourier basis are obtained by exchanging one or both of the cosines in these expressions for sines and vice versa. There are therefore four different modes in this basis per given k_x and k_y such that the maximum achieved horizontal wavenumbers are $k_{x,max},\ k_{y,max} = \frac{\pi n_x}{L_x},\ \frac{\pi n_y}{L_y}$, with $n_x,\ n_y$ the resolution in the x and y-direction. Note also the absence of k_z in the Chebyshev polynomials. Multiple Chebyshev polynomials are needed to construct a single sine or cosine with a given k_z, and thus multiple polynomials together are needed to satisfy the boundary conditions. This is also the reason for the alternative definition of K_{2D} in Eq. (5.24). As mentioned, DEDALUS employs a pseudo-spectral method such that it converges exponentially with resolution for smooth solutions (Boyd, 2001). Another advantage of Chebyshev polynomials is that the associated grid points in real space are non-uniformly distributed in space, being clustered towards the boundaries, which avoids the Runge phenomenon. This is also useful to more easily resolve boundary layers.

Another important point to note is the absence of time-dependence in the perpendicular wavenumbers compared to Eq. (2.87). Shearing waves have previously been applied to the precessional instability in a periodic domain, like with the elliptical instability. The introduction of walls has made these shearing waves redundant. The background flow only violates periodicity in the vertical direction, and with walls this periodicity is

automatically removed. This does however imply that the term:

$$\boldsymbol{U}_0 \cdot \nabla \boldsymbol{u} = -2\mathrm{Po}\Omega z(\sin(\Omega t)\partial_x + \cos(\Omega t)\partial_y)\boldsymbol{u}, \tag{5.32}$$

needs to be implemented explicitly by the code instead of evolving the wavenumbers in time, which adds computational time, mainly by ensuring this term is resolved accurately in time.

We employ a two-stage second order Runge-Kutta timestepping scheme, identified in DEDALUS as RK222 (described in Sec. 2.6 of Ascher et al., 1997). In this scheme the non-linear terms, advection terms between the background flow and the velocity perturbations and the Coriolis-like term that arises due to the precession are explicitly calculated, while the other terms – including the usual Coriolis term – are calculated implicitly. We employ a CFL safety factor set to 0.5 to ensure that the timesteps are small enough to accurately capture the dynamics. For de-aliasing purposes the resolution is expanded with a factor 3/2 when calculating the non-linear terms, so as to satisfy the standard 3/2 rule (Boyd, 2001).

5.2.2 The NEK5000 code

In addition to the pseudo-spectral method of DEDALUS we also employ the NEK5000 code (Fischer et al., 2008), which utilises a spectral element method instead of pseudo-spectral method. In spectral element methods (and also in finite element methods) the domain is first split up into a number of elements $\mathcal{E}$. Inside each element the velocity, temperature and pressure fields are then expanded using a chosen basis. The basis functions in a spectral element method are comprised of orthogonal polynomials. In NEK5000 Legendre polynomials are used, which fulfil a similar role as the Chebyshev polynomials in DEDALUS. The polynomials in each element of NEK5000 are of much lower order $\mathcal{N}$ than those in DEDALUS, as they only need to provide sufficient resolution inside each element, instead of the entire domain. The associated grid points to these polynomials are calculated using the Gauss-Legendre-Lobatto quadrature points, such that the edges of the elements are included in the grid points. The number of grid points inside each element is given by $(\mathcal{N}+1)^3$. Due to overlapping grid points on the boundaries of the elements the total number of grid points in a simulation is given by $\mathcal{E}\mathcal{N}^3$.

Using a finite element or spectral element method generally has two advantages. First, the elements allow for constructing arbitrary meshes, and thus allow for geometries that are impossible to use with pseudo-spectral methods. In our setup we are considering a Cartesian box and as such this advantage does not provide any assistance currently, but can be useful when one would want to consider for example the precessional instability in a spheroidal model, taking into account the oblateness of the body. Second, because the calculations are split up into elements, the code can be very efficiently parallelised, which is the case with NEK5000. A spectral element method furthermore combines the versatility of the element method with the speed and accuracy of spectral methods by

making the calculations inside of each element fast, in particular, no matrix inversions are required when calculating the time derivatives due to the orthogonal property of the Legendre polynomials. It follows that, like in DEDALUS, there is no possibility to implement shearing waves and thus we are forced to calculate the term in Eq. (5.32) in NEK5000 as well.

We work in a Cartesian box with sides of equal length, such that the obvious choice for the number of elements in every direction is $\mathcal{E}^{1/3}$, and we typically use $\mathcal{E} = 1000$ elements. In addition, NEK5000 is most efficient with polynomials of order $\mathcal{N} \in [5, 10]$ in every direction inside each element, such that it is often preferable to increase the number of elements instead of the order of the polynomials to increase resolution. We set $\mathcal{N} = 9$ unless otherwise specified. Due to the element method in NEK5000 the grid is irregular in all three directions. We have therefore opted to interpolate to a regular grid to calculate K_{2D}, and so this quantity is susceptible to interpolation errors. We will interpolate to a 100^3 regular grid for such integrations unless specified otherwise.

Finally, we timestep using an implicit second order backwards difference scheme for the pressure and diffusion terms, and a second order characteristics-based method to evolve the non-linear, buoyancy and Coriolis terms, as well as the Coriolis-like term due to the precession and the advection terms of the background flow and the velocity perturbation. We employ a CFL safety factor set to 0.3 to ensure small enough timesteps, although note that characteristics-based timesteppers are allowed to exceed this value while still guaranteeing accuracy when integrating the advective non-linear terms. De-aliasing is dealt with by increasing the order of the polynomials inside the elements when calculating the non-linear terms, with a factor that approximately satisfies the 3/2 rule (Boyd, 2001).

We choose to use NEK5000 in addition to DEDALUS precisely because the utilised methods are different. Any results that are produced by both codes are then code independent and are therefore more robust, because the methods of obtaining said results are different. This allows for an additional check on the results we obtain.

5.2.3 Benchmarking

We once again perform benchmarking tests to ensure that the precessional and convective instabilities in isolation are both properly computed in the simulations. To this end we performed numerous simulations with the perturbation non-linearities switched off in both DEDALUS and NEK5000. We have fitted the kinetic energy in the simulations $K = \frac{1}{2}\langle|\boldsymbol{u}|^2\rangle$, where the brackets represent a volume-average. The growth rate of the velocity can then be found by taking half of the growth rate of the kinetic energy. We compare the growth rates from the simulations to those from the theoretical predictions given in Eq. (5.14) and obtained by numerically solving the cubic dispersion relation in Eq. (2.54) for the precessional and convective instabilities respectively.

The results of the benchmarking simulations of both instabilities in isolation, along with the theoretical predictions, are plotted in Fig. 5.2. The DEDALUS simulations por-

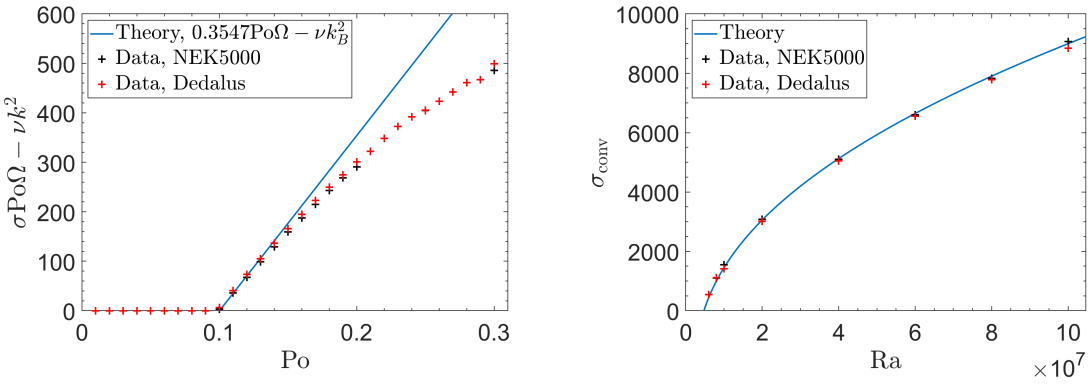

Figure 5.2: Benchmark simulations of the linear growth rate of the precessional instability and convective instability, each in isolation at $\mathrm{Ek} = 5 \cdot 10^{-5}$ in a 1-by-1-by-1 box using both NEK5000 (black) and DEDALUS (red). Left: The growth rate of the precessional instability. The most unstable mode pair, after taking the viscous reduction into account, is $n_A = 1,\ n_B = 2$. The theoretical prediction for small Po for this mode is given in blue. The simulation data obtained using both codes match each other and the theoretical prediction well in the interval $\mathrm{Po} \in [0.1, 0.15]$ and accurately predict the critical value of Po for inhibition of the instability by viscosity. Deviation from the predicted maximum growth at higher Po partly arises from higher order Po effects. In addition, the most unstable horizontal wavenumber changes as Po is increased, see Fig. 3a in R. Mason and Kerswell (2002), and therefore the mode becomes increasingly more de-tuned. Right: Benchmark simulations of the linear growth rate of convection in isolation at $\mathrm{Ek} = 5 \cdot 10^{-5}$ in a 1-by-1-by-1 box. The growth rates in the simulations match each other and the theoretical growth rate of convection well.

trayed in this figure are executed in a 1-by-1-by-1 box, with a resolution of 32^3. The NEK5000 simulations are executed in a 1-by-1-by-1 box with a resolution of 10^3 elements, each with a polynomial of order 4. Thus the total number of grid points is 40^3.

The predicted most unstable modes of the precessional instability with the smallest horizontal wavenumber according to R. Mason and Kerswell (2002) are the modes with $n_A = 1,\ n_B = 2$ and $k_\perp = \sqrt{k_x^2 + k_y^2} \approx 18.059$. In the 1-by-1-by-1 box the modes with $n_x = n_y = 2 \Rightarrow k_x = k_y = 4\pi$ have $k_\perp \approx 17.77$, so the modes with these horizontal wavenumbers almost satisfy the perpendicular wavenumber requirement of the most unstable modes. Thus we expect these modes to match the theoretically predicted growth rate well, except for a small discrepancy which can be attributed to de-tuning. The unstable horizontal wavenumber changes with the chosen value of Po however, and for this particular mode decreases as Po increases (see Fig. 3a in R. Mason & Kerswell, 2002). According to this figure, the unstable horizontal wavenumber of these modes satisfies $k_\perp = 17.77$ around $\mathrm{Po} \approx 0.1$.

As detailed in Sec. 5.1.3, this particular mode is only the most unstable mode when viscosity is taken into account. Modes with larger wavenumbers have larger growth rates, but they are more strongly inhibited by viscosity, reducing the growth rate by approximately $-\nu k^2$. Note that we ignore the secondary effects of viscosity in shifting the resonances, which is expected to be much weaker than the damping we consider. The growth

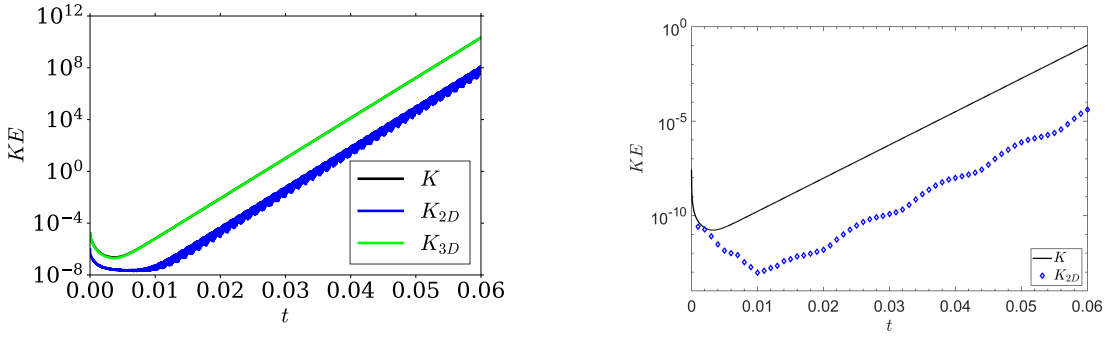

Figure 5.3: Comparison of simulations executed using DEDALUS (left) and NEK5000 (right) at the same parameters of Ek $= 5 \cdot 10^{-6}$, Po $= 0.02$. The K_{3D} component dominates the growth, but clearly a growing K_{2D} is produced by both simulations, while this is not possible according to the linear inviscid analysis. Because this is reproduced by two different codes with different numerical schemes we conclude this effect is real.

rate of this particular mode is given by: $0.3547\text{Po}\Omega - \nu k^2$. This theoretically predicted growth rate, where we have chosen $k^2 = k_\perp^2 + n_B^2\pi^2$, is plotted in solid-blue in the left-hand panel of Fig. 5.2 along with the simulation data plotted in black (NEK5000) and red (DEDALUS) markers. The growth rates obtained from both simulations executed with both DEDALUS and NEK5000 match each other very well. They match the theoretically predicted growth rate very well on the interval $\text{Po} \in [0.1, 0.15]$, where the most unstable wavenumber very strongly matches the one available within the box, and additionally predicts the range of Poincaré numbers at which the instability is inhibited by viscosity very well. The simulation data starts deviating again from the theoretically predicted growth rate at higher values of Po as the most unstable mode changes away from what is possible in the box. The discrepancy here can thus, at least partially, be attributed to de-tuning. Higher order effects at large Po may also play a role in this discrepancy; see for example the higher order correction to the precessional instability growth rate in Naing and Fukumoto (2011), albeit in a triply periodic box. Therefore we conclude that we capture the growth of the precessional instability in isolation in both codes, and that we have reproduced the previously obtained results of simulations with stress-free impermeable walls at the top and bottom of the local box.

We have also run multiple simulations to ensure the convective instability is captured accurately in the simulations. The theoretical prediction as well as the simulation data at the same Ek $= 5 \cdot 10^{-5}$ in a 1-by-1-by-1 box are plotted in the right-hand panel of Fig. 5.2. To calculate the theoretical maximum growth rate we solved the dispersion relation for rotating convection with stress-free impenetrable walls. The simulation data from both codes agree well with each other and the theoretically predicted growth rates.

Thus we conclude that both the precessional instability and the convective instability in isolation are both captured well by the two codes, and the codes produce the same results.

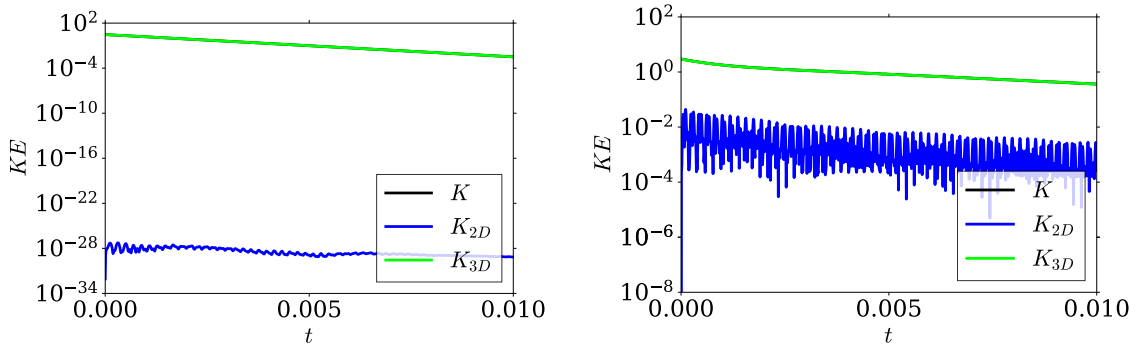

Figure 5.4: Two linear simulations of the precessional instability, both initialised with the most unstable modes $n_A = 1$ and $n_B = 2$ satisfying the incompressibility condition. These initial conditions have zero K_{2D}. In the left-hand panel Po was set to 0, so that there is no instability and indeed the energy is decaying while the energy in the K_{2D} component is maintained at a value corresponding to zero (within machine precision). The right-hand panel is the exact same simulation with Po = 0.015, which does not allow growth according to the linear stability analysis. The total energy is decaying at a slower rate compared to the simulation on the left. The K_{2D} component initially jumps up and then starts oscillating with a decaying trend, indicating that the origin of this signal is separate from the precessional instability.

5.2.4 The K_{2D} signal as obtained from simulations

According to the derivation in R. Mason and Kerswell (2002) the "exceptional inertial wave" with $n_z = \lambda = 0$ is explicitly forbidden from growing. This exceptional inertial wave is by definition part of K_{2D}, and thus we examine if this mode does indeed not grow in linear simulations by calculating the growth of K_{2D}, which we would then expect to decay due to viscosity. In DEDALUS K_{2D} is calculated directly according to the method given in Eq. (5.24). The same method is utilised in NEK5000, but u_x and u_y are first interpolated to a regular grid for ease of analysis before this integration is performed. The value of K_{2D} in NEK5000 is thus sensitive to this interpolation. The resolution in these simulations is 40^3; we have interpolated to a regular grid of 50^3. In Fig. 5.3 the simulations of the precessional instability alone (i.e. without the convective instability) with parameters Ek $= 5 \cdot 10^{-6}$, Po $= 0.02$ executed in DEDALUS (left-hand panel) and NEK5000 (right-hand panel) are shown. The value of K_{2D} is growing in these simulations, implying growth of kinetic energy in vertically-invariant geostrophic flows, in contrast to the linear inviscid analysis of R. Mason and Kerswell (2002) that predicts $n_z = 0$ to be unable to grow. This result is present in all test simulations that were run to explore this effect. The value of K_{2D} grows as the unstable modes grow, and the ratio K_{2D}/K depends on the value of Po, increasing with increasing Po. This result is robust to changes in timestep, timestepping scheme and spatial resolution. Finally, this effect is reproduced by two separate codes utilising different numerical methods, effectively ruling out the possibility of a numerical error as the cause of this effect.

To determine whether this results from the precessional instability or some other

source we tested the behaviour of K_{2D} when the precessional instability is unable to grow. We have executed a pair of test simulations in DEDALUS with parameters such that the suppressive effects of viscosity on the modes are stronger than the destabilising effects from the instability itself. When initialising simulations without power in the modes contributing to K_{2D}, the K_{2D} signal should not be able to grow and thus should remain at zero, instead of being present alongside the K_{3D} signal. The simulation presented in the left-hand panel of Fig. 5.4 at $\mathrm{Ek} = 10^{-5}$, $\mathrm{Po} = 0.0$ is initialised with the two most unstable modes, i.e., those with $n_z = 1$ and $n_z = 2$, as initial conditions, satisfying the incompressibility condition. No meaningful K_{2D} is present in this simulation initially, and when executing the simulation K_{2D} indeed does not grow. In the panel on the right the same simulation is shown, except we have set $\mathrm{Po} = 0.015$. In this simulation power is transferred to the flow components with $n_z = 0$ as indicated by the sudden increase in K_{2D} after one timestep. This then starts to oscillate, but never grows beyond this initial increase, and in fact decays alongside the decay of the two input modes. This leads us to the conclusion that this behaviour is not part of an instability.

Instead we hypothesise that the origin of non-zero K_{2D}, i.e. the 2D modes obtaining power, most likely resides in a boundary layer effect. We suspect that all three terms introduced by the precessional background flow in the momentum equation violate the stress-free conditions because they all contain some z-dependence which does not satisfy $\partial_z(\text{of those terms}) = 0$. This would therefore require a boundary layer to ensure that the solutions in the bulk can match the boundary conditions at the boundaries. Such a boundary layer effect would be consistent with the power being transferred into the $n_z = 0$ modes instead of it being part of the precessional instability, and thus allowing power to arise in simulations where the precessional instability does not grow. Indeed it is also consistent with the Po-dependence of the ratio K/K_{2D}: if Po is smaller, than these terms are smaller, and therefore less energy will be transferred to the K_{2D} modes. We suspect that this effect was present in the simulations of R. Mason and Kerswell (2002) but not identified by them, perhaps because they were interested in measuring different quantities.

Nevertheless, after identifying this effect we will not study it further because it is not our primary focus, and because it is generally a weak effect for the parameters we will explore with simulations.

5.3 The precessional instability modified by stratification

Following on from the benchmarking of the precessional and convective instabilities in isolation, we now wish to derive growth rates of the precessional instability taking into account the stable or unstable stratification. The growth rate for this problem was previously derived in a different setup in Benkacem et al. (2022). Although they considered an infinite cylinder instead of a Cartesian box, we might expect some similarities to the current problem. In their model, they found that stable stratification inhibits the linear growth of the precessional instability, while unstable stratification, i.e. in convectively unstable systems, enhances the linear growth of the precessional instability at weak con-

vective driving, but again inhibits it at strong convective driving. We will attempt to see if this general behaviour is reproduced in our geometry.

5.3.1 Analytical derivation for the linear growth rate

To derive the growth rate in our setup we will perform a new linear stability analysis building upon the one in R. Mason and Kerswell (2002). We start from the governing equations for linear perturbations prior to non-dimensionalising. In essence, we start from the same governing equations as in R. Mason and Kerswell (2002), but add a buoyancy term to the momentum equation, and add the heat equation:

$$\frac{\partial \boldsymbol{u}}{\partial t} + 2\Omega\hat{\boldsymbol{z}} \times \boldsymbol{u} + \nabla p - \theta\hat{\boldsymbol{z}} - \nu\nabla^2\boldsymbol{u} = \mathrm{Po}[\mathrm{e}^{\mathrm{i}\Omega t}\mathcal{L} + \mathrm{e}^{-\mathrm{i}\Omega t}\mathcal{L}^*]\boldsymbol{u}, \tag{5.33}$$

$$\frac{\partial \theta}{\partial t} + u_z N^2 - \kappa\nabla^2\theta = \mathrm{Po}[\mathrm{e}^{\mathrm{i}\Omega t}\mathcal{F} + \mathrm{e}^{-\mathrm{i}\Omega t}\mathcal{F}^*]\theta, \tag{5.34}$$

$$\nabla \cdot \boldsymbol{u} = 0. \tag{5.35}$$

We have defined:

$$\mathcal{L} \equiv \Omega \begin{bmatrix} z(\partial_y - \mathrm{i}\partial_x) & 0 & -2\mathrm{i} \\ 0 & z(\partial_y - \mathrm{i}\partial_x) & 2 \\ \mathrm{i} & -1 & z(\partial_y - \mathrm{i}\partial_x) \end{bmatrix}, \tag{5.36}$$

and

$$\mathcal{F} \equiv z\Omega(\partial_y - \mathrm{i}\partial_x). \tag{5.37}$$

We have set α, g and d to 1, such that: $N^2 = -\Delta T$. The terms on the left-hand side of Eq. (5.33) and Eq. (5.34) are the same as in the ordinary rotating Rayleigh-Bénard problem, and would result in a dispersion relation corresponding to the convective instability, for negative N^2. The terms on the right-hand side of these equations however, are the terms that originate from precession, as is clearly indicated by the presence of the Poincaré number in these terms. Like in R. Mason and Kerswell (2002), these terms couple the inertial waves – in the absence of buoyancy – together and allow the precessional instability to operate. In the presence of buoyancy, these terms instead couple inertia-gravity waves when these exist. The dispersion relation and normal mode prescriptions of these inertia-gravity waves can be obtained by considering the inviscid rotating Rayleigh-Bénard problem, which in these equations can also be denoted as the inviscid equations at $\mathcal{O}(1)$. The inertia-gravity wave dispersion relation in this formulation is given by:

$$\lambda^2 = \frac{4\Omega^2 k_z^2 + N^2 k_\perp^2}{k^2}, \tag{5.38}$$

with corresponding normal modes of the form:

$$\begin{bmatrix} u_x \\ u_y \\ u_z \\ \theta \\ p \end{bmatrix} = \begin{pmatrix} k^2(k_x\lambda - 2\Omega \mathrm{i} k_y)\cos(k_z z)/4\Omega^2 k_\perp^2 \\ k^2(k_y\lambda + 2\Omega \mathrm{i} k_x)\cos(k_z z)/4\Omega^2 k_\perp^2 \\ -\frac{\mathrm{i}k_z\lambda}{-N^2+\lambda^2}\sin(k_z z) \\ \frac{k_z N^2}{-N^2+\lambda^2}\sin(k_z z) \\ \cos(k_z z) \end{pmatrix} \mathrm{e}^{\mathrm{i}(k_x x + k_y y + \lambda t)}. \tag{5.39}$$

Following R. Mason and Kerswell (2002), we write down a linear combination of inertia-gravity waves with $\lambda_A \neq \lambda_B$ for both the velocity fields and temperature perturbation. We introduce a slow timescale $\tau = \mathrm{Po}\, t$, where we consider Po as the small parameter, and a fast timescale t_0. As in Ch. 2 the time derivative then becomes:

$$\frac{\partial}{\partial t} = \frac{\partial}{\partial t_0} + \mathrm{Po}\frac{\partial}{\partial \tau}. \tag{5.40}$$

We can then write for the velocity and temperature:

$$\boldsymbol{u} = A(\tau)\boldsymbol{u}_A(\boldsymbol{x})\mathrm{e}^{\mathrm{i}\lambda_A t} + B(\tau)\boldsymbol{u}_B(\boldsymbol{x})\mathrm{e}^{\mathrm{i}\lambda_B t} + \mathrm{Po}\,\boldsymbol{u}_1(\boldsymbol{x},t) + \mathcal{O}(\mathrm{Po}^2), \tag{5.41}$$

$$\theta = A(\tau)\theta_A(\boldsymbol{x})\mathrm{e}^{\mathrm{i}\lambda_A t} + B(\tau)\theta_B(\boldsymbol{x})\mathrm{e}^{\mathrm{i}\lambda_B t} + \mathrm{Po}\,\theta_1(\boldsymbol{x},t) + \mathcal{O}(\mathrm{Po}^2). \tag{5.42}$$

We must combine the heat equation and the momentum equation into a single equation such that we take into account all of the background flow forcing terms in these equations. Next we take a similar approach as we did when deriving the dispersion relation of inertia-gravity waves, and take the z-component of the curl of the momentum equation to eliminate the pressure gradient. This results in the vorticity equation:

$$\frac{\partial \omega_z}{\partial t} - 2\Omega\frac{\partial u_z}{\partial z} = \mathrm{Po}\,\hat{\boldsymbol{z}}\cdot(\nabla\times\mathcal{G}\boldsymbol{u}), \tag{5.43}$$

where we have defined the operator:

$$\mathcal{G} \equiv [\mathrm{e}^{\mathrm{i}\Omega t}\mathcal{L} + \mathrm{e}^{-\mathrm{i}\Omega t}\mathcal{L}^*]. \tag{5.44}$$

Writing the vorticity equation at $\mathcal{O}(1)$ and order $\mathcal{O}(\mathrm{Po})$:

$$\frac{\partial \omega_{z,0}}{\partial t_0} - 2\Omega\frac{\partial u_{z,0}}{\partial z} = 0, \tag{5.45}$$

$$\mathrm{Po}\,\frac{\partial \omega_{z,1}}{\partial t_0} + \mathrm{Po}\,\frac{\partial \omega_{z,0}}{\partial \tau} - 2\mathrm{Po}\,\Omega\frac{\partial u_{z,1}}{\partial z} = \mathrm{Po}\,\hat{\boldsymbol{z}}\cdot(\nabla\times\mathcal{G}\boldsymbol{u}_0). \tag{5.46}$$

We perform the same decomposition into an equation at $\mathcal{O}(1)$ and one at $\mathcal{O}(\mathrm{Po})$ for the heat equation:

$$\frac{\partial \theta_0}{\partial t_0} = -u_{z,0}N^2, \tag{5.47}$$

$$\mathrm{Po}\,\frac{\partial \theta_1}{\partial t_0} + \mathrm{Po}\,\frac{\partial \theta_0}{\partial \tau} = -\mathrm{Po}\,u_{z,1}N^2 + \mathrm{Po}\,\mathcal{H}\theta_0, \tag{5.48}$$

where we have defined the operator:

$$\mathcal{H} \equiv [\mathrm{e}^{\mathrm{i}\Omega t}\mathcal{F} + \mathrm{e}^{-\mathrm{i}\Omega t}\mathcal{F}^*]. \tag{5.49}$$

Then, we take the z-component of the curl of the curl of the momentum equation:

$$-\frac{\partial \nabla^2 u_z}{\partial t} - 2\Omega\frac{\partial \omega_z}{\partial z} + \nabla_\perp^2\theta = \mathrm{Po}\,\hat{\boldsymbol{z}}\cdot(\nabla\times\nabla\times\mathcal{G}\boldsymbol{u}), \tag{5.50}$$

with $\nabla_\perp^2 = \nabla^2 - \partial_z^2$ the horizontal Laplacian. Again, we decompose this into order $\mathcal{O}(1)$ and order $\mathcal{O}(\mathrm{Po})$:

$$-\frac{\partial \nabla^2 u_{z,0}}{\partial t_0} - 2\Omega\frac{\partial \omega_{z,0}}{\partial z} + \nabla_\perp^2\theta_0 = 0, \tag{5.51}$$

$$-\mathrm{Po}\,\frac{\partial \nabla^2 u_{z,1}}{\partial t_0} - \mathrm{Po}\,\frac{\partial \nabla^2 u_{z,0}}{\partial \tau} - 2\mathrm{Po}\,\Omega\frac{\partial \omega_{z,1}}{\partial z} + \mathrm{Po}\,\nabla_\perp^2\theta_1 = \mathrm{Po}\,\hat{\boldsymbol{z}}\cdot(\nabla\times\nabla\times\mathcal{G}\boldsymbol{u}_0). \tag{5.52}$$

The first of these equations leads to the dispersion relation of inertia-gravity waves when we seek normal mode solutions. The equation at $\mathcal{O}(\mathrm{Po})$ is what we will use to derive the growth rate of the precessional instability. We drop all mentions of Po and take the derivative only with respect to t_0 so as to maintain the equation at $\mathcal{O}(\mathrm{Po})$:

$$-\frac{\partial^2 \nabla^2 u_{z,1}}{\partial t_0^2} - \frac{\partial^2 \nabla^2 u_{z,0}}{\partial t_0 \partial \tau} - 2\Omega\frac{\partial^2 \omega_{z,1}}{\partial t_0 \partial z} + \nabla_\perp^2\frac{\partial \theta_1}{\partial t_0} = \hat{\boldsymbol{z}}\cdot\frac{\partial(\nabla\times\nabla\times\mathcal{G}\boldsymbol{u}_0)}{\partial t_0}. \tag{5.53}$$

Substituting in the heat equation Eq. (5.48) and vorticity equation Eq. (5.46) at $\mathcal{O}(\mathrm{Po})$, after some algebra, results in:

$$\begin{aligned}-\frac{\partial^2 \nabla^2 u_{z,1}}{\partial t_0^2} - 4\Omega^2\partial_z^2 u_{z,1} - \nabla_\perp^2 u_{z,1}N^2 = \frac{\partial^2 \nabla^2 u_{z,0}}{\partial t_0 \partial \tau} \\ - 2\Omega\frac{\partial^2 \omega_{z,0}}{\partial z \partial \tau} + \nabla_\perp^2\frac{\partial \theta_0}{\partial \tau} + 2\Omega\hat{\boldsymbol{z}}\cdot\frac{\partial(\nabla\times\mathcal{G}\boldsymbol{u}_0)}{\partial z} \\ -\nabla_\perp^2\mathcal{H}\theta_0 + \hat{\boldsymbol{z}}\cdot\frac{(\nabla\times\nabla\times\mathcal{G}\boldsymbol{u}_0)}{\partial t_0}.\end{aligned} \tag{5.54}$$

Following the same reasoning as MK02, we can define the inner product under which the inertia-gravity waves are orthogonal:

$$\langle \boldsymbol{u}, \boldsymbol{v}\rangle \equiv \lim_{L\to\infty}\frac{1}{4L^2}\int_{-L}^{L}\int_{-L}^{L}\int_0^1 \boldsymbol{u}^*\cdot\boldsymbol{v}\;\mathrm{d}z\,\mathrm{d}y\,\mathrm{d}x. \tag{5.55}$$

We use this definition to obtain amplitude equations as in R. Mason and Kerswell (2002) by considering $\langle \boldsymbol{u}_{A_z}\mathrm{e}^{\mathrm{i}\lambda_A t}, (5.54)\rangle$. This produces the same requirements as in the derivation with the precessional instability in isolation, and we obtain: $\lambda_B = \lambda_A \pm \Omega$. Without loss of generality we choose $\lambda_B = \lambda_A + \Omega$. Equally, we consider $\langle \boldsymbol{u}_{B_z}\mathrm{e}^{\mathrm{i}\lambda_B t}, (5.54)\rangle$. After satisfying the resonance condition on the frequencies we obtain two equations for $A_\tau = \frac{\mathrm{d}A}{\mathrm{d}\tau}$

and $B_\tau = \frac{\mathrm{d}B}{\mathrm{d}\tau}$:

$$B\langle u_{A_z}, -2\Omega\hat{\boldsymbol{z}}\cdot\frac{\partial(\nabla\times\mathcal{L}^*\boldsymbol{u}_B)}{\partial z}+\nabla_\perp^2\mathcal{F}^*\theta_B-\hat{\boldsymbol{z}}\cdot\frac{\partial(\nabla\times\nabla\times\mathcal{L}^*\boldsymbol{u}_B)}{\partial t_0}\rangle = A_\tau\langle u_{A_z}, \frac{\partial\nabla^2 u_{A_z}}{\partial t_0}-2\Omega\frac{\partial\omega_{A_z}}{\partial z}+\nabla_\perp^2\theta_A\rangle, \quad (5.56)$$

$$A\langle u_{B_z}, -2\Omega\hat{\boldsymbol{z}}\cdot\frac{\partial(\nabla\times\mathcal{L}\boldsymbol{u}_A)}{\partial z}+\nabla_\perp^2\mathcal{F}\theta_A-\hat{\boldsymbol{z}}\cdot\frac{\partial(\nabla\times\nabla\times\mathcal{L}\boldsymbol{u}_A)}{\partial t_0}\rangle = B_\tau\langle u_{B_z}, \frac{\partial\nabla^2 u_{B_z}}{\partial t_0}-2\Omega\frac{\partial\omega_{B_z}}{\partial z}+\nabla_\perp^2\theta_B\rangle. \quad (5.57)$$

Assuming there exist growing solutions of the form $(A,B)=(A_0,B_0)\mathrm{e}^{\sigma\mathrm{Po}\Omega t}$ with growth rates $\sigma\Omega$ we can combine the above equations to obtain:

$$\sigma^2\Omega^2=\frac{\mathcal{AB}}{\mathcal{CD}}, \quad (5.58)$$

with

$$\mathcal{A}=\left\langle u_{A_z}, -2\Omega\hat{\boldsymbol{z}}\cdot\frac{\partial(\nabla\times\mathcal{L}^*\boldsymbol{u}_B)}{\partial z}+\nabla_\perp^2\mathcal{F}^*\theta_B-\hat{\boldsymbol{z}}\cdot\frac{\partial(\nabla\times\nabla\times\mathcal{L}^*\boldsymbol{u}_B)}{\partial t_0}\right\rangle, \quad (5.59)$$

$$\mathcal{B}=\left\langle u_{B_z}, -2\Omega\hat{\boldsymbol{z}}\cdot\frac{\partial(\nabla\times\mathcal{L}\boldsymbol{u}_A)}{\partial z}+\nabla_\perp^2\mathcal{F}\theta_A-\hat{\boldsymbol{z}}\cdot\frac{\partial(\nabla\times\nabla\times\mathcal{L}\boldsymbol{u}_A)}{\partial t_0}\right\rangle, \quad (5.60)$$

$$\mathcal{C}=\left\langle u_{A_z}, \frac{\partial\nabla^2 u_{A_z}}{\partial t_0}-2\Omega\frac{\partial\omega_{A_z}}{\partial z}+\nabla_\perp^2\theta_A\right\rangle, \quad (5.61)$$

$$\mathcal{D}=\left\langle u_{B_z}, \frac{\partial\nabla^2 u_{B_z}}{\partial t_0}-2\Omega\frac{\partial\omega_{B_z}}{\partial z}+\nabla_\perp^2\theta_B\right\rangle. \quad (5.62)$$

This derivation does not take into account the finite Poincaré number effects on either the horizontal wavenumber or the value of σ, since we have assumed Po is small and only considered leading order effects. We expect that the derivation is valid at small values of Po and becomes progressively more inaccurate as Po becomes larger.

5.3.2 Results of the linear stability analysis

We utilise MATHEMATICA to calculate the growth rate of a given pair of n_A and n_B. Prior to calculating σ we must first find the solution for $k_\perp$ as a function of the buoyancy frequency using the resonance condition on the frequencies:

$$\sqrt{\frac{4\Omega^2k_{B_z}^2+N^2k_\perp^2}{k_B^2}}=-\sqrt{\frac{4\Omega^2k_{A_z}^2+N^2k_\perp^2}{k_A^2}}+\Omega. \quad (5.63)$$

The most general solution is the one portrayed above, where $\lambda_B>0$, $\lambda_A<0$, but the other solutions with $\lambda_B>0$, $\lambda_A>0$ or $\lambda_B<0$, $\lambda_A<0$ can also satisfy the resonance conditions for the right combinations of n_B, n_A or the right values of N^2 and Ω. In general, we first find $k_\perp$ for a given Ω and N^2, and then calculate the associated growth rate. The script to obtain both $k_\perp$ and σ is provided in Appendix A.

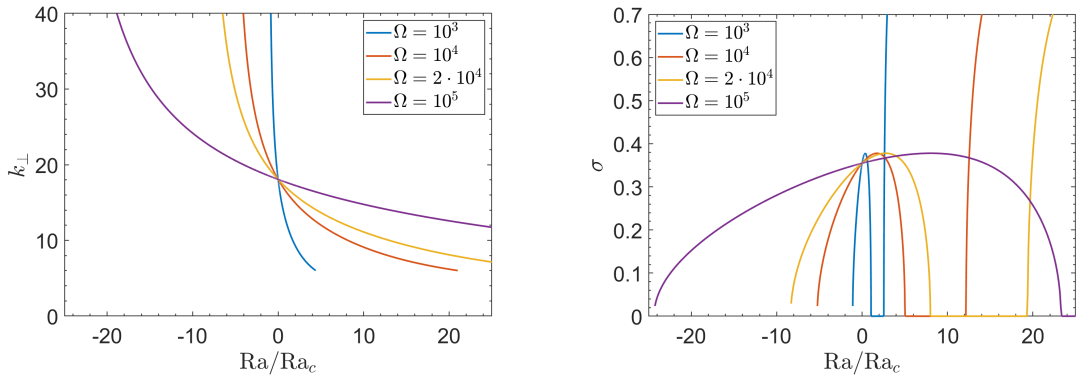

Figure 5.5: The horizontal wavenumber $k_\perp$ of the unstable mode and growth rate σ as a function of the Rayleigh number with various values of Ω with fixed $n_A = 1$, $n_B = 2$. Left: The horizontal wavenumber. Stable stratification increases the unstable horizontal wavenumber, while unstable stratification decreases it. Larger values of Ω decrease the slope. Right: σ without viscous reduction. Stable stratification reduces the growth rate, unstable stratification first increases the growth rate and then rapidly decreases it. A secondary lobe of instability exists at larger $\mathrm{Ra}/\mathrm{Ra}_c$, corresponding to the $\lambda_B > 0$, $\lambda_A > 0$ alternative solution.

In the left-hand panel of Fig. 5.5 we display the values of $k_\perp$ that satisfy the frequency resonance condition in Eq. (5.63) with $n_A = 1$, $n_B = 2$ with fixed $\Omega = [10^3,\ 10^4,\ 2 \cdot 10^4,\ 10^5]$, where $\mathrm{Ek} = \frac{1}{2\Omega d^2}$. The viscous reduction of the growth rate, with $\mathrm{Pr} = 1$, is expected to be $-\nu k^2$ (R. Mason & Kerswell, 2002). Therefore, we can apply this reduction after calculating the inviscid linear growth rate to obtain the linear growth rate as if the linear stability analysis in Sec. 5.3.1 included viscosity. For this reason, and for consistency with later simulation results, we also plot the values of $k_\perp$ and σ as a function of $\mathrm{Ra}/\mathrm{Ra}_c = -\alpha g N^2 \nu\kappa/\mathrm{Ra}_c$. In this figure we set all parameters $\alpha = g = \nu = \kappa = 1$. We calculate Ra_c by numerically solving the convective dispersion relation in Eq. (2.58). First we note that when $\mathrm{Ra} = 0$, i.e. in the absence of stratification, we retrieve the same value as R. Mason and Kerswell (2002) for $k_\perp$. This value of $k_\perp$ is independent of Ω in the absence of stratification, and is in this figure easily identified by the intersection of all four curves. In the convectively unstable regime, i.e. at $\mathrm{Ra} > 0$, the horizontal wavenumber is smaller than in the absence of buoyancy. Larger values of Ω reduce the slope of this reduction. Equivalently, with stable stratification the wavenumber is increased until it hits the asymptotic value where the resonance condition can no longer be satisfied. The further modification of the most unstable horizontal wavenumber due to larger values of Po has not been taken into account in this calculation, so these results are only accurate at small values of Po.

We can use the obtained values of $k_\perp$ to calculate the values of σ as given in Eq. (5.58), noting that these values do not yet include a viscosity correction. We plot these inviscid values of σ in the right-hand panel of Fig. 5.5. Once again, at $\mathrm{Ra} = 0$ we retrieve the growth rate as found in R. Mason and Kerswell (2002). This growth rate is again independent of Ω in the absence of stratification and is thus easily identified as the intersection of all four curves. The introduction of unstable stratification results in

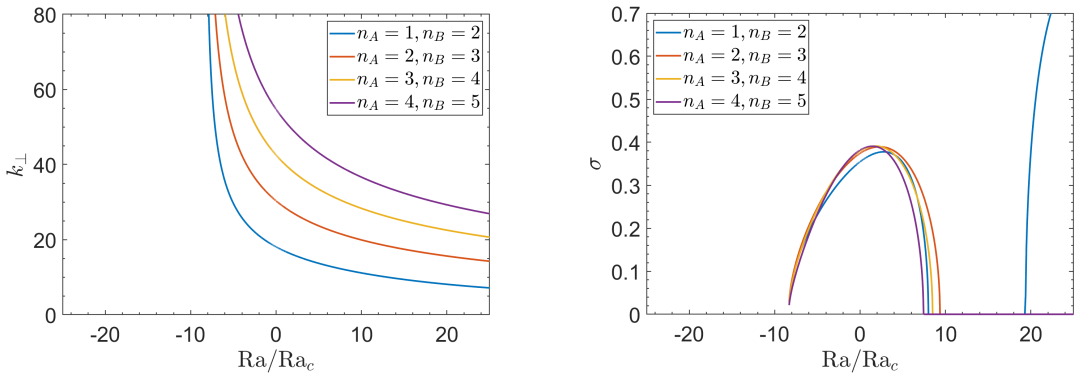

Figure 5.6: Same as Fig. 5.5, but varying the vertical wavenumbers n_A, n_B with fixed $\Omega = 2 \cdot 10^4$. Left: The horizontal wavenumber. Larger values of n_A and n_B result in larger values of the unstable horizontal wavenumber, the overall behaviour is the same at all values, but the curves are steeper at larger values of n_A and n_B. Right: σ without viscous reduction. Larger values of n_A and n_B result in slightly larger maximum values of σ and steeper curves. The secondary lobe also moves to larger values of Ra/Ra$_c$ at larger n_A and n_B.

a small increase of the growth rate followed by a rapid decrease as the Rayleigh number is increased, until the precessional instability is stabilised. This occurs at all values of Ω but again the slopes are reduced at larger values of Ω. The curves indicate a secondary lobe of instability with much larger growth rate at even larger values of the Rayleigh number, which is the result of the resonance condition on the frequencies being satisfied with $\lambda_B > 0$, $\lambda_A > 0$ instead of $\lambda_B > 0$, $\lambda_A < 0$. Finally, stable stratification inhibits the instability, until the resonance condition can no longer be satisfied, as indicated by $k_\perp$ going to infinity in the left-hand panel of Fig. 5.5.

We have also examined the horizontal wavenumber of the most unstable mode and the growth rate at different values of n_A, n_B with fixed $\Omega = 2 \cdot 10^4$ in Fig. 5.6. As was found previously in Table 1 of R. Mason and Kerswell (2002) larger values of n_A, n_B result in larger horizontal wavenumbers and larger values of σ in the absence of stratification. Our script exactly reproduces the values of both $k_\perp$ and σ found in their Table 1 in the absence of stratification for each pair considered. We have opted to only examine those combinations where $|n_A - n_B| = 1$ as these have the largest growth rates in the absence of stratification. We find the same qualitative behaviour for all combinations of n_A and n_B; larger values of n_A and n_B appear to result in steeper curves for both the horizontal wavenumber and growth rate. Furthermore, the growth rates go to zero at lower Ra/Ra$_c$ for the initial lobe in the regime of unstable stratification when considering large wavenumbers. Perhaps more interestingly, the secondary lobe with $\lambda_A > 0$, $\lambda_B > 0$ moves to larger and larger values of the Rayleigh number at larger values of n_A and n_B.

5.3.3 Comparison to simulations

To test our results we performed several linear simulations using the DEDALUS code. We start by examining the case with Po $= 0.06$, $\Omega = 2 \cdot 10^4$, and thus Ek $= 2.5 \cdot 10^{-5}$.

We set the box size of these simulations such that the largest modes that fit into the box exactly satisfy the predicted $k_\perp$ for $n_A = 1$, $n_B = 2$, as portrayed in the solid-blue line in Fig. 5.6. These simulations were initialised with random noise. Furthermore, for the simulations we have set the resolution to $n_x = n_y = 4$, $n_z = 32$. By using this very low horizontal resolution we avoid the appearance of the convective instability. The horizontal wavenumbers of the modes that are convectively unstable, obtained by solving the cubic dispersion relation, are not available in the simulation domain. Other mode combinations of the precessional instability are also not available in the simulation for the same reason. The linear growth rates obtained using these simulations are portrayed using purple circles in Fig. 5.7. We compare this with the theoretical prediction of σ, with the viscous reduction of the growth rate, given by $-\nu k^2$, applied. The viscous reduction changes the overall shape of the curve, as the suppressive effects are stronger in the regime of stable stratification where $k_\perp$ is large, whereas its suppressive effect is weaker in the regime of unstable stratification because $k_\perp$ is small. We have plotted two theoretical curves, one with $k^2 = k_A^2 = k_\perp^2 + \pi^2$ in solid-blue, and the other with $k^2 = k_B^2 = k_\perp^2 + 4\pi^2$ in solid-orange. We plot both as we expect the true value of the growth rate after the reduction due to viscosity to lie in between both of these, since the two modes involved have $n_A = 1$ and $n_B = 2$.

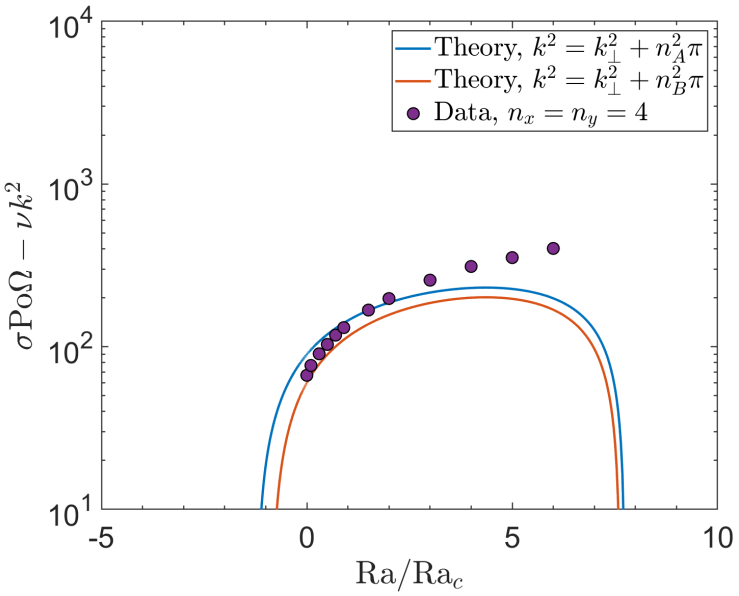

Figure 5.7: The growth rate of the precessional instability in the presence of buoyancy with $\Omega = 2 \cdot 10^4$, $\mathrm{Po} = 0.06$ and $\mathrm{Ek} = 2.5 \cdot 10^{-5}$. The theoretical predictions for the precessional instability with $n_A = 1$, $n_B = 2$ in solid-blue and solid-orange correspond to the growth rate after viscous reduction with $-\nu k_A^2 = -\nu(k_\perp^2 + n_A^2\pi^2)$ and $-\nu k_B^2 = -\nu(k_\perp^2 + n_B^2\pi^2)$. We compare these predictions to simulations executed using DEDALUS. These simulations are executed with a horizontal resolution of $n_x = n_y = 4$, such that the convective instability cannot operate even when $\mathrm{Ra} > \mathrm{Ra}_c$. The growth rates of these simulations is plotted in purple circles. The data and theoretical predictions agree well when $\mathrm{Ra} < 2\mathrm{Ra}_c$; for larger Rayleigh numbers the growth rate in the simulations is larger than the theoretical prediction.

We find good agreement between our theoretical prediction and the data in the range $\mathrm{Ra} \in [0, 2\mathrm{Ra}_c]$, but the data deviates from the theoretical prediction at larger values of the Rayleigh number. The growth rates are larger than what is theoretically predicted for larger Ra, and does not appear to decrease sharply when the theory predicts that it should. To examine this deviation more closely we have lowered the viscosity and thermal diffusivity to $\nu = \kappa = 0.1$, still maintaining $\mathrm{Pr} = 1$ and $\Omega = 2{\cdot}10^4$, and thus $\mathrm{Ek} = 2.5{\cdot}10^{-6}$, in thermal timescales. To achieve this, we have executed our simulations using rotational timescales, i.e. $\Omega = 1$, and so $\nu = 5 \cdot 10^{-6}$, instead of thermal timescales, and converted the obtained growth rates to thermal timescales for consistency with Fig. 5.7. Lowering the viscosity has a number of consequences; firstly, the difference between the two viscous reductions is much smaller. Thus the two linear prediction curves will be much closer together. Secondly, we can employ smaller values of Po, such that any effects of finite Po should be reduced. Finally, because the viscosity and thermal diffusivity are lowered, if this departure results from a boundary layer effect, for instance, it will also be weakened. As a result of lowering the viscosity we have increased the value of the Rayleigh number at a given value of N^2 by a factor of ν^{-2}. Furthermore, because we have lowered the Ekman number, we have increased the value of $\mathrm{Ra_c}$ by a factor of $\approx \nu^{-4/3}$. Thus we have widened the theoretically predicted curves by a factor $\nu^{-2/3}$ as can be seen in Fig. 5.8, where we set $\mathrm{Po} = 0.02$. Moreover, the two theoretically predicted curves have almost collapsed onto each other due to the reduced viscosity, as desired.

The growth rates obtained from the simulations – following the same procedure as for the data in Fig. 5.7 – executed using DEDALUS are plotted in purple circles. Again we notice good agreement when $\mathrm{Ra} \lesssim 6\mathrm{Ra}_c$, and also find good agreement in the regime of stable stratification. We still observe departure when the Rayleigh number is large and positive, but the departure appears much less significant. We suspect that this discrepancy may arise from a modification of the linear stability analysis due to viscosity or thermal diffusivity or perhaps be because the convective instability itself is modified by precession, which is not included in our analysis. Preliminary work using a Floquet method indicates that the discrepancy might arise because one should consider more than two daughter waves in this linear stability analysis; it appears a number of waves might be excited and growing together instead of just two, resulting in a larger growth rate.

We have also performed a number of simulations at $n_x = n_y = 16$ such that the convective instability can operate in the simulations; the growth rates of these simulations is plotted using yellow circles in Fig. 5.8. We retrieve the same growth rates when $\mathrm{Ra} < \mathrm{Ra}_c$, as expected. However, when $\mathrm{Ra} > \mathrm{Ra}_c$ we find growth rates that are much larger than those of the precessional instability. In the non-linear simulations this instability will thus dominate over the precessional instability, and as such the theoretical growth rate of the precessional instability when $\mathrm{Ra} > \mathrm{Ra}_c$ does not matter as much. When Po becomes sufficiently large such that the growth rate of the precessional instability does equal that of the convective instability, the horizontal wavenumber will be significantly modified due to finite Po effects and as such this derivation is no longer valid. Furthermore, this violates

the starting assumption of the derivation that Po is small.

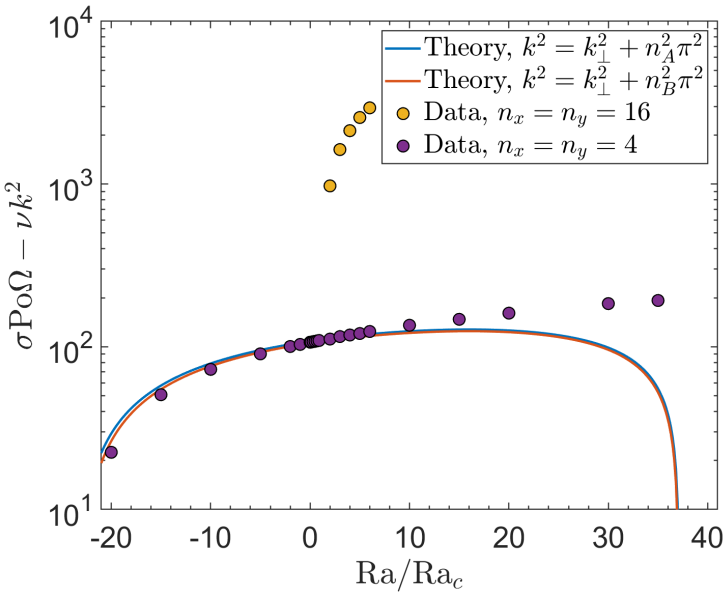

Figure 5.8: Same as Fig. 5.7, but with $\nu = \kappa = 0.1$, $\mathrm{Po} = 0.02$ and $\mathrm{Ek} = 2.5 \cdot 10^{-6}$. The lowered viscosity reduces the difference between the two theoretical curves. In this figure we also compare the theoretical predictions to simulations executed using the DEDALUS code. The purple circles once again correspond to simulations that are executed with a horizontal resolution of $n_x = n_y = 4$, such that the convective instability cannot operate even when $\mathrm{Ra} > \mathrm{Ra}_c$. The data and theoretical predictions agree well when $\mathrm{Ra} \lesssim 6\mathrm{Ra}_c$ and also agree well for the simulations in the stably stratified regime. For larger Rayleigh numbers however the growth rate in the simulations is again larger than the theoretical prediction. We have also executed the same simulations with a horizontal resolution of $n_x = n_y = 16$. The growth rates in these simulations are plotted using yellow circles. They produce the same growth rate when $\mathrm{Ra} < \mathrm{Ra}_c$, but the convective instability has a much larger growth rate than the precessional instability when it does operate.

In summary, we have performed a new derivation for the growth rate of the precessional instability in the presence of stratification that can be applied to every mode combination of the precessional instability using the MATHEMATICA script provided in Appendix A. This derived expression is valid when the Poincaré number is small and it matches the growth rates from simulations well in the regime where the precessional instability is important, i.e. when $\mathrm{Ra}/\mathrm{Ra}_c \lesssim \mathcal{O}(1)$.

5.4 Parameter variations

To examine the quantities of interest, namely the kinetic energy, energy injection and heat transport, the latter of which is represented by the Nusselt number, we will execute a large parameter sweep. We will vary the Rayleigh number, Ekman number and Poincaré number to be able to independently vary the convective driving, rotational constraint and driving of the precessional instability.

The values of the Rayleigh number are typically reported as $R = \mathrm{Ra}/\mathrm{Ra}_c$ for clar-

ity, where Ra_c is the onset critical Rayleigh number (determined numerically by solving Eq. (2.54)) and R is the supercriticality. The range of this ratio studied at $\mathrm{Ek} = 2.5 \cdot 10^{-5}$ is from $R \in [0, 15]$. We examine the interval of $\mathrm{Po} \in [0.01, 1.10]$, allowing the likely astrophysically irrelevant but fluid dynamically interesting case that the precession is faster than the regular rotation. Finally, we performed simulations with three different values of the Ekman number: $\mathrm{Ek} = [5 \cdot 10^{-5}, 2.5 \cdot 10^{-5}, 10^{-5}]$. When varying the Ekman number we fix the Rayleigh number to 0, i.e. there is no convective instability in this set of these simulations.

We have opted to use the faster NEK5000 code to perform most of the parameter sweeps, while executing selected simulations for interesting cases in DEDALUS. DEDALUS provides more accurate values of K_{2D} and allows for accurate creation of horizontal power spectra without any need for interpolation, but was found to run these simulations much more slowly than NEK5000, hence this division of labour between the two codes. We have checked that the two codes also produce the same results in select non-linear simulations with the same parameters. This will be shown in the figures in Ch. 6.

A table of the parameters in the simulations performed in DEDALUS, as well as the associated resolution of those simulations, is given in Table 5.1. We have verified that the quantities computed here are independent of the resolution chosen, such that for the reported quantities the simulations are all well resolved. The reported resolutions show the number of grid points in the simulations. Because we utilise a real Fourier basis, however, we only have wavenumber modes up to $n_x/2, n_y/2$ in the x and y directions. The grid is expanded by a factor of 3/2 for de-aliasing purposes. Likewise, a table of the parameters in the simulations performed in NEK5000, as well as the associated resolutions of those simulations, is given in Table 5.2. We utilise polynomials of order $\mathcal{N} = 9$ in all directions, inside 10 elements in all directions, thus resulting in a resolution of 90^3. For de-aliasing purposes we increase the polynomial order to 14 when calculating the non-linear terms, satisfying the 3/2 rule.

Table 5.1: Table of resolutions used in the DEDALUS simulations to study the precessional instability with different Rayleigh numbers, Ekman numbers, and box size $L_x = L_y = L_z = 1$. The resolutions we report are the resolutions prior to expanding the grid with a factor 3/2 for de-aliasing.

DEDALUS	
$\mathrm{Ek} = 2.5 \cdot 10^{-5}$, $R = 0$	n_x, n_y, n_z
$\mathrm{Po} = 0.15, 0.17, 0.18, 0.20, 0.25$	$96, 96, 96$
$\mathrm{Ek} = 2.5 \cdot 10^{-5}$, $R = 2$	n_x, n_y, n_z
$\mathrm{Po} = 0.25$	$96, 96, 96$
$\mathrm{Ek} = 2.5 \cdot 10^{-5}$, $R = 0$	n_x, n_y, n_z
$\mathrm{Po} = 0.0, 0.10, 0.15, 0.25, 0.40$	$96, 96, 96$
$\mathrm{Ek} = 2.5 \cdot 10^{-5}$, $R = 6$	n_x, n_y, n_z
$\mathrm{Po} = 0.25$	$96, 96, 96$

Table 5.2: Same as Table 5.1 for the NEK5000 simulations. The given resolutions are obtained by using polynomials of order 9 in all directions in a cube of 10 elements in all directions. We expand the polynomials to order 14 for de-aliasing purposes.

NEK5000	
$\mathrm{Ek} = 2.5 \cdot 10^{-5}$, $\mathrm{Po} = 0.04$	n_x, n_y, n_z
$R = 0, 1.5, 2, 3, 4, 5, 6, 8, 10, 15$	$90, 90, 90$
$\mathrm{Ek} = 2.5 \cdot 10^{-5}$, $\mathrm{Po} = 0.10$	n_x, n_y, n_z
$R = 0, 1.5, 2, 3, 4, 5, 6, 8, 10, 15$	$90, 90, 90$
$\mathrm{Ek} = 2.5 \cdot 10^{-5}$, $\mathrm{Po} = 0.25$	n_x, n_y, n_z
$R = 0, 1.5, 2, 3, 4, 5, 6, 8, 10, 15$	$90, 90, 90$
$\mathrm{Ek} = 5 \cdot 10^{-5}$, $R = 0$	n_x, n_y, n_z
$\mathrm{Po} = 0.12, 0.14, 0.15, 0.16, 0.18, 0.20, 0.22, 0.24, 0.25, 0.26, 0.28, 0.30$	$90, 90, 90$
$\mathrm{Ek} = 2.5 \cdot 10^{-5}$, $R = 0$	n_x, n_y, n_z
$\mathrm{Po} = 0.06, 0.08, 0.10, 0.12, 0.14, 0.15, 0.16, 0.17, 0.18, 0.20, 0.25, 0.30, 0.35, 0.40, 0.45, 0.50, 0.60, 0.80, 1.00, 1.10$	$90, 90, 90$
$\mathrm{Ek} = 10^{-5}$, $R = 0$	n_x, n_y, n_z
$\mathrm{Po} = 0.03, 0.04, 0.05, 0.06, 0.08, 0.10, 0.11, 0.12, 0.13, 0.14, 0.15, 0.16, 0.18, 0.20, 0.25, 0.30$	$90, 90, 90$
$\mathrm{Ek} = 2.5 \cdot 10^{-5}$, $R = 2$	n_x, n_y, n_z
$\mathrm{Po} = 0.01, 0.02, 0.03, 0.04, 0.06, 0.08, 0.10, 0.12, 0.14, 0.15, 0.16, 0.18, 0.20, 0.25, 0.30, 0.35, 0.40, 0.45, 0.50$	$90, 90, 90$
$\mathrm{Ek} = 2.5 \cdot 10^{-5}$, $R = 4$	n_x, n_y, n_z
$\mathrm{Po} = 0.01, 0.02, 0.03, 0.04, 0.06, 0.08, 0.10, 0.15, 0.20, 0.25, 0.30, 0.35, 0.40, 0.45, 0.50$	$90, 90, 90$
$\mathrm{Ek} = 2.5 \cdot 10^{-5}$, $R = 6$	n_x, n_y, n_z
$\mathrm{Po} = 0.01, 0.02, 0.03, 0.04, 0.06, 0.08, 0.10, 0.15, 0.20, 0.25, 0.30, 0.35, 0.40, 0.45, 0.50$	$90, 90, 90$

5.5 Summary

In this chapter we have discussed the precessional instability and convective instability in rotating systems with impermeable walls in the vertical direction. From the non-dimensionalised governing equations, with $\mathrm{Pr} = 1$, we have found the parameters that we can vary within our simulations, namely the Poincaré number, Ekman number, and Rayleigh number. We have detailed the known properties of the precessional instability without convection in our setup, as previously found in R. Mason and Kerswell (2002). We have also derived expressions for the quantities which we wish to analyse in simulations, namely the kinetic energy, K, Nusselt number, Nu, and energy injection rate from the precessional flow, I. These expressions turn out to be the same as in Ch. 2, except for the evaluation of I.

We have also decomposed the kinetic energy into its geostrophic (or vortex) modes represented by the z-invariant part of the kinetic energy K, referred to as K_{2D}, and waves and eddies represented by the z-dependent part of K, referred to as K_{3D}. This choice together with the boundary conditions implies that u_z is not part of K_{2D}. As a result, the energy injection I cannot be split into 2D and 3D components, as it contains u_z. Unlike

the elliptical instability case, the energy injection rate due to the precessional instability is by definition solely part of the 3D component.

We have found – using a crude argument which considers the saturation of a single mode – that this energy injection term might be expected to scale as $I \propto \mathrm{Po}^3$ if the precessional instability operates in a sufficiently turbulent regime. If however the energy injection or tidal dissipation of the flow is by action of the convective turbulence on the precessional flow like an effective viscosity, independent of Po, it was found that the energy injection should scale as $I \propto \mathrm{Po}^2$, while still depending on the Rayleigh number as we observed previously.

We have detailed the DEDALUS and NEK5000 codes used to execute our simulations. We have verified that each code captures both instabilities accurately by examining the growth rates of the kinetic energy in linear test simulations, comparing these growth rates with the theoretical predictions for both instabilities and finding good agreement. We have also found that modes with $n_z = 0$, i.e. modes that contribute to K_{2D}, arise in the linear simulations of the precessional instability. These modes are not able to grow according to the inviscid linear stability analysis. Despite this, they appear in simulations executed using both the DEDALUS and NEK5000 codes. Therefore we conclude that the signal of these modes is real as it is produced by both codes. We hypothesise that it might arise from boundary layer effects, and does not arise from the linear instability.

Finally, we have also derived an expression for the growth rate of the precessional instability in the presence of stratification. The theory matches the simulations well in the regime of stable stratification and weak unstable stratification, but deviates significantly when the unstable stratification is sufficiently strong. We suspect that this discrepancy arises due to the influence of the viscosity and thermal diffusivity or modification of convection by precession. In our simulations with 1-by-1-by-1 boxes the discrepancy however does not matter as the growth rate of the convective instability, possibly affected by the precession, is much larger at these values of the Rayleigh number and Ekman number.

Now that we have demonstrated that both codes accurately reproduce both instabilities we can be confident to move on to analyse non-linear simulations of the precessional instability and Rayleigh-Bénard convection and to study their interactions.

Chapter 6

Interactions of the precessional instability and convection

In this chapter we will explore the interactions of the precessional instability and convection. We start with the behaviour of individual simulations, examining snapshots of the flow as well as time series of the quantities that we wish to study. We will try to explain the behaviours we observe in simulations using analysis of the horizontal energy spectra. Afterwards, we will take time-averages of the quantities that we are interested in and attempt to verify the scalings postulated in Sec. 5.1.4. We examine whether the interactions of convection with the precessional instability impact the operation and efficiency of the precessional instability. In particular, we want to study whether this impact is the same as the one convection has on the operation of the elliptical instability in Ch. 3. All simulations in this chapter are executed with $\mathrm{Pr} = 1$ and in a 1-by-1-by-1 box since these are less computationally demanding at our chosen Ra and Ek. As a result of the smaller box size we expect that the LSV is not as energetically dominant as in Ch. 3 and Ch. 4 because it is forced to stop growing at the smaller box scale, and thus lower energies. Because the LSV is not as dominant, we also expect the suppressive effects of the LSV to be lessened compared to those in Ch. 3 and Ch. 4.

6.1 Analysis of illustrative simulations

6.1.1 Snapshots of the vertical vorticity

We will begin our discussion by presenting snapshots of the vertical vorticity ω_z as obtained from the simulations using NEK5000 with $\mathrm{Ek} = 2.5 \cdot 10^{-5}$ in Fig. 6.1. This is the same Ekman number as utilised in R. Mason and Kerswell (2002) in the strongly precessing case, after correcting for the factor of two which is present in our definition of the Ekman number and absent in theirs. The top two snapshots are taken from a simulation studying the precessional instability, in the absence of convection, with $\mathrm{Po} = 0.1$, $\mathrm{Ra} = 0$. Based on the previous results in R. Mason and Kerswell (2002), Barker (2016b), and Pizzi et al. (2022) we expect the flow in these simulations to be bursty in nature, similar to the elliptical

instability. More specifically, R. Mason and Kerswell (2002) identified three branches of non-linear behaviour in their three-dimensional simulations. The simulation at this value of Po is situated in the region of parameter space where their branch B emerges, displaying bursty behaviour. R. Mason and Kerswell (2002) have found that branch B contains primarily the most unstable linear modes and modes with frequencies $\lambda = 0.5\Omega$ and $\lambda = 1.5\Omega$, as well as featuring small amounts of energy in many other modes with different frequencies, which most likely results from secondary wave-wave interactions.

We do indeed observe the bursty behaviour of this branch in the snapshots of the flow at these parameters plotted in the top panels of Fig. 6.1. In Fig. 6.1a we plot the vorticity at time $t = 0.344$, given in thermal time units. This coincides with a burst in energy injection and kinetic energy of the precessional instability. These bursts are associated with the most unstable linear modes, with a horizontal planform consisting of two full sinusoids in both horizontal directions and a combination of the modes with $n_z = 1$ and $n_z = 2$ in the vertical direction. After the burst in energy injection has occurred the most unstable linear modes break down and instead a large-scale flow emerges. This large-scale flow is portrayed in a snapshot taken at $t = 0.37$ in Fig. 6.1b. It does not look like the vortices we normally expect from inertial wave breakdown; instead it appears a large-scale sheared flow has formed, the direction of which oscillates in time, likely related to the rotating shear introduced by the background flow. This large-scale flow inhibits growth of the most unstable linear modes of the precessional instability all the same however, and continues to do so until it has been slowly viscously dissipated. The most unstable linear modes will then arise again in the flow and the cycle starts anew; the flow is maintained in this fashion throughout the entirety of the simulation.

If instead we consider the flow with Po $= 0.2$, Ra $= 0$ in the middle panels of Fig. 6.1 we observe much stronger vorticities than in the more laminar simulation with Po $= 0.1$, Ra $= 0$. Note the changed colour scale in the middle and bottom panels compared to the one in the top panels. In Fig. 6.1c we plot a snapshot taken at $t = 0.06$, after the initial instability has saturated. We observe the formation of vortices in this simulation as opposed to the more layer-like large-scale flow in Fig. 6.1b. The main vortex, however, appears to dominate the flow less than in similar cases of the elliptical instability we examined in Ch. 3. In these simulations a "secondary transition" occurs as the values of the vorticity, and associated with it the kinetic energy and energy injection, suddenly increase. This is visible in the massively increased values of the vorticity in the snapshot in Fig. 6.1d, taken at $t = 0.072$. The vortex in this snapshot appears to dominate the flow more than in Fig. 6.1c. When examining the vertical vorticity as a function of depth it might appear that the vortex does not extend all the way down to the bottom of the box. As it turns out, the vortex does extend to the bottom, but it is sheared, as we might expect from the precessional shear, and the bottom of the vortex is located towards the middle of the horizontal plane in this particular snapshot. The direction of this shear, which we might consider to be the vortex axis, is precessing in time, on a timescale slightly longer than the precession period in this simulation. As a result, the strong vortex is not

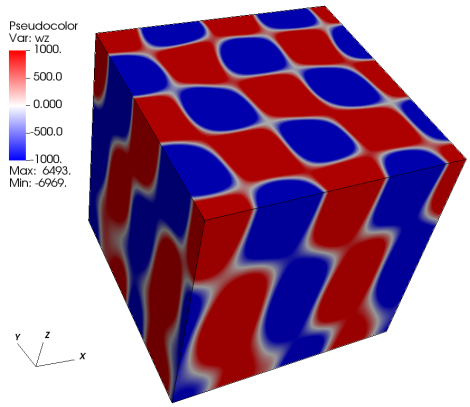

(a) $t = 0.344$, $\mathrm{Po} = 0.1$, $\mathrm{Ra} = 0$.

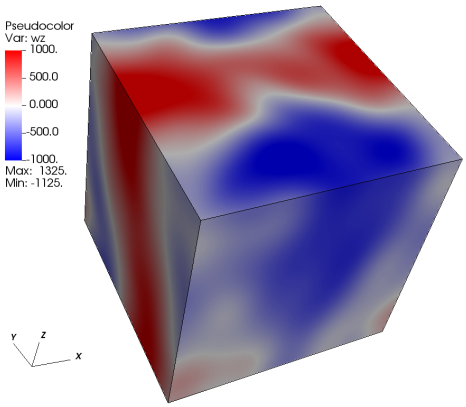

(b) $t = 0.37$, $\mathrm{Po} = 0.1$, $\mathrm{Ra} = 0$.

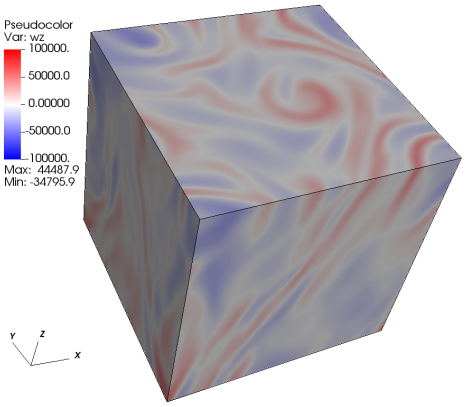

(c) $t = 0.062$, $\mathrm{Po} = 0.2$, $\mathrm{Ra} = 0$.

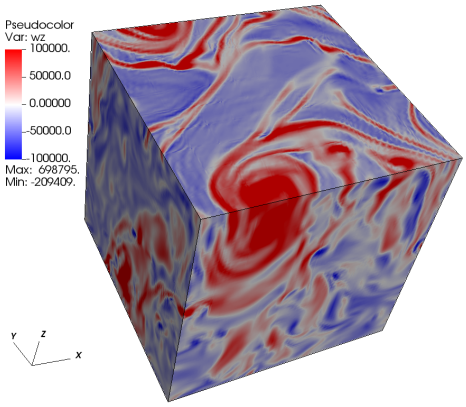

(d) $t = 0.07$, $\mathrm{Po} = 0.2$, $\mathrm{Ra} = 0$.

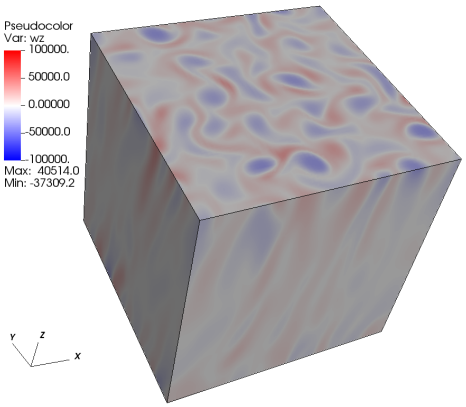

(e) $t = 0.05$, $\mathrm{Po} = 0.1$, $\mathrm{Ra} = 2\mathrm{Ra}_c$.

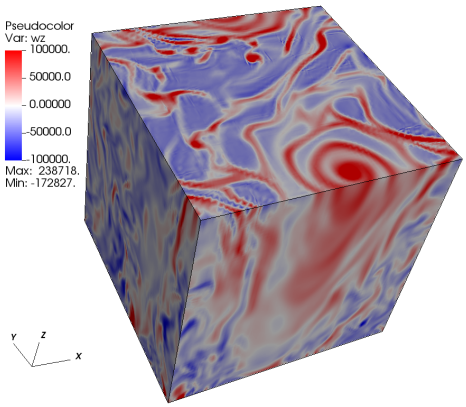

(f) $t = 0.05$, $\mathrm{Po} = 0.1$, $\mathrm{Ra} = 6\mathrm{Ra}_c$.

Figure 6.1: Snapshots of the vertical vorticity ω_z of the flow in simulations executed using NEK5000 with $\mathrm{Ek} = 2.5 \cdot 10^{-5}$. The top left and top right panels, both obtained from the same simulation, show snapshots taken during a burst of the energy injection and during the period of large-scale flow after the burst, respectively. The middle panels, both taken from a simulation with stronger precessional driving than the top panels, show vortices in the flow instead. A rapid "secondary transition" appears to occur in this simulation, indicated by a large increase in vorticity and kinetic energy from the panel on the left to the one on the right. The bottom left panel shows a simulation with weak convective driving; the bursty behaviour of the precessional instability appears absent and instead the convection appears to dominate this flow. In the bottom right panel a snapshot of the simulation with stronger convective driving is shown. This flow strongly resembles that of the middle right panel, but it is unclear whether the vortex is driven by convection or precession.

completely z-invariant, such that the 2D energy according to our definition does not fully capture the energies in these vortices. We expect that the observed secondary transition may be associated with branch C reported in R. Mason and Kerswell (2002). This branch appears in their simulations after a transition from the initial state at branch B. Branch C is associated with the emergence of modes with frequencies λ which are multiples of 0.5Ω, in addition to the absence of the most unstable linear modes and much larger energies compared to branch B.

We will now use these snapshots to get an idea how convection modifies the behaviour of the flow. We start by examining a snapshot of the simulation with $\mathrm{Po} = 0.1,\ \mathrm{Ra} = 2\mathrm{Ra}_c$ in Fig. 6.1e. This snapshot was taken at $t = 0.05$, after saturation of the initial instability and transients have died down. The flow in this snapshot is representative of the flow at all times. The flow in this simulation is very different from all previously observed behaviours, showing large-scale up and down flows, which appear somewhat sheared in the horizontal directions, and very small-scale but not vortex-like behaviour in the horizontal plane. These small-scale features appear, by eye, to be consistent with the size of the convectively unstable linear modes. We attribute this behaviour to the convective motions, but note that this close to onset the convection is unable to form a convective large-scale vortex both with and in the absence of precession, as observed in Ch. 3 and previously observed in Guervilly et al. (2014). The precessional instability appears to be weak or absent compared to these convective motions, as there is no clear evidence of its operation in the flow.

Finally, we turn to even stronger convective driving in Fig. 6.1f, with $\mathrm{Po} = 0.1,\ \mathrm{Ra} = 6\mathrm{Ra}_c$ taken at $t = 0.05$. Again the initial transients have died down at this point in the simulation. The flow has saturated in a way that is very similar to the one in Fig. 6.1d. We observe again a vortex in the flow, but the areas around the vortex appear to be more noisy as we have come to expect from convective simulations. This noisiness is presumably associated with the convective eddies present in the simulation. It is unclear whether the vortex is of a convective nature or generated by the precessional instability or both. We will examine the time series of the energy injection, as in the case of the elliptical instability, to examine whether the precessional instability is operating in these simulations with strong convection present.

We wish to briefly discuss what appears to be signatures of the grid scale present in both Fig. 6.1d and Fig. 6.1f. These are prominent here, but are much less pronounced and usually absent in the velocity snapshots that we have used to compute these vorticity snapshots. The prominence of the features here is likely an artefact of how we have computed the vorticity on this grid, and the colour scale we have used to plot these snapshots. To ensure that these simulations executed in NEK5000 are well-resolved however, without resorting to interpolating the data to generate energy spectra, we will check if the following criterion:

$$k_{\max} l_d > 1, \tag{6.1}$$

with

$$l_d = (\nu^3/D_\nu)^{1/4}, \tag{6.2}$$

is satisfied. The quantity l_d represents the Kolmogorov lengthscale, the scale at which viscosity dominates the flow, while $k_{\max} = 2\pi/L_x n_x$ is the maximum wavenumber in one direction available in the simulation. This is likely to be a conservative estimate because the spectrum is steeper than the Kolmogorov spectrum, as we will show in Fig. 6.5 and Fig. 6.6, with less power in smaller-scale modes near the dissipation scale. Wavevectors are not employed in NEK5000, and as such we will pretend it is a regular grid for the purposes of this calculation, with $n_x = 90$. We find for the simulations in Fig. 6.1d and Fig. 6.1f that the ratios are 1.8 and 1.6 respectively. We have ensured that this condition is also satisfied for all other simulations. Thus we conclude that these simulations are indeed well-resolved, even though artefacts of the grid scale appear in the figures.

We will conduct a few further tests to ensure the well-resolvedness and validity of our results. We will study the energy spectra obtained from the simulations executed in DEDALUS, to confirm that they are well-resolved, such that the agreement between the simulations in NEK5000 and DEDALUS further demonstrates the validity of our time series results.

6.1.2 Time series of quantities of interest

We clearly observe quite diverse flow behaviours when looking at the flow snapshots, even when considering just the non-linear evolution of the precessional instability in isolation. To better understand the differences between these flows, we now turn to the time series of our quantities of interest, K, K_{2D}, I and u_z. The latter of these is obtained by calculating the rms vertical velocity. These time series, obtained using NEK5000, are portrayed in Fig. 6.2. The snapshots in Fig. 6.1 taken from these simulations have been marked with vertical dotted-black lines at the times that they were taken. All these simulations have been executed with $\mathrm{Ek} = 2.5 \cdot 10^{-5}$. In Fig. 6.2a the simulation with $\mathrm{Po} = 0.1,\ \mathrm{Ra} = 0$ is presented. This simulation corresponds to the snapshots in the top two panels of Fig. 6.1, showing the bursty behaviour. The peaks of the kinetic energy and energy injection correspond to flows that look similar to Fig. 6.1a, while those flows found in Fig. 6.1b occur during the troughs. The linearly unstable modes are associated with bursts in both total energy followed by bursts in the 2D energy with a slight delay. Furthermore, we observe that the energy injection is also bursty, and primarily associated with the 3D energy as one would expect. The vertical velocity appears to follow the kinetic energy quite closely in all panels of this figure.

In Fig. 6.2b we plot the time series of the simulation executed with $\mathrm{Po} = 0.2,\ \mathrm{Ra} = 0$. As we expect from the middle panels in Fig. 6.1, the bursty behaviour is absent. Instead, the simulation goes through a regime of lower kinetic energy and energy injection from $t = 0.03 - 0.06$ and then the flow goes through a rapid secondary transition into a regime with the kinetic energy, energy injection and vertical velocity maintained at strongly elevated levels. We will denote this regime as the "continuously turbulent" regime, in contrast to

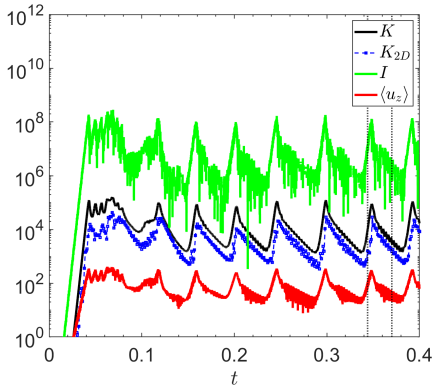

(a) Po = 0.1, Ra = 0.

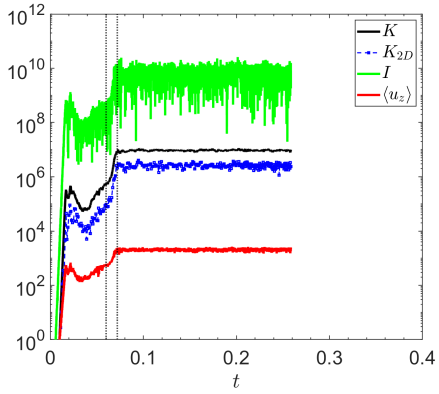

(b) Po = 0.2, Ra = 0.

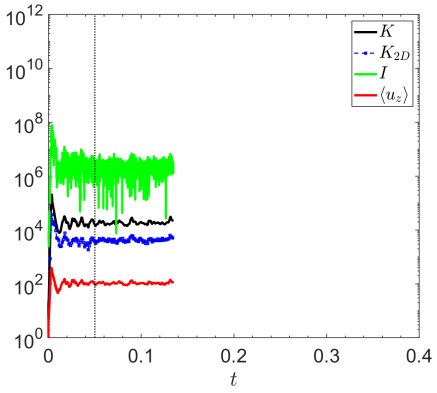

(c) Po = 0.1, Ra = $2\mathrm{Ra}_c$.

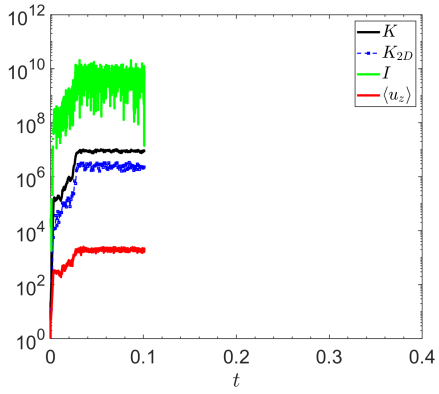

(d) Po = 0.2, Ra = $2\mathrm{Ra}_c$.

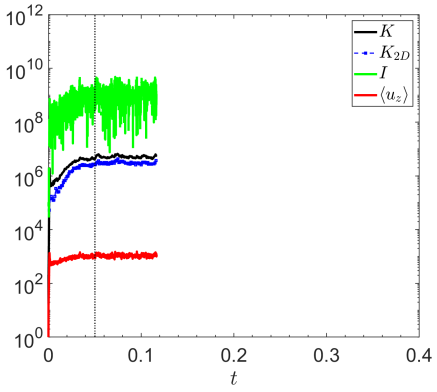

(e) Po = 0.1, Ra = $6\mathrm{Ra}_c$.

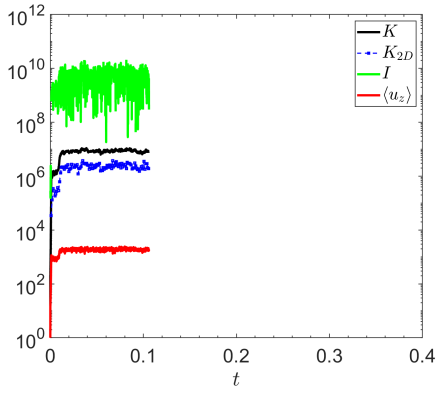

(f) Po = 0.2, Ra = $6\mathrm{Ra}_c$.

Figure 6.2: Time series of the precessional instability and convection with $\mathrm{Ek} = 2.5 \cdot 10^{-5}$, executed using NEK5000. Vertical dotted-black lines correspond to the times at which the snapshots in Fig. 6.1 are taken. The top left and right panels show the precessional instability in isolation. The simulation in the top left panel produces the expected bursty behaviour, while the top right panel with stronger precessional driving features a secondary transition to a continuously turbulent state. The introduction of convection inhibits the bursty behaviour in the figure on the middle left, displaying a continuous energy injection instead. The simulation on the middle right with stronger precessional driving than the one on the middle left shows similar behaviour to the panel on the top right. The simulation on the bottom left with strong convective driving shows evidence for a secondary transition that is more gradual than in the top right panel, so convection might allow the precessional instability to become continuously turbulent at lower values of the Poincaré number. Finally, the simulation on the bottom right also shows the secondary transition, but stronger convective driving appears to allow the transition to occur sooner.

the bursty regime at lower values of the Poincaré number. As stated before, we suspect this corresponds to the transition from branch B to branch C as reported in R. Mason and Kerswell (2002). We do not however observe a transition from branch C back down to branch B, like they do, in any of our simulations. This continued presence of branch C might be because of the increased resolution in our simulations, as the length of time we run the simulations for is similar to or exceeding those in R. Mason and Kerswell (2002).

We now turn to examine the modification of these flows and corresponding time series due to the introduction of convection. In Fig. 6.2c the time series of the simulation with $\mathrm{Po} = 0.1,\ \mathrm{Ra} = 2\mathrm{Ra}_c$ is shown. This simulation indeed shows the absence of the bursty behaviour, but has a kinetic energy roughly on the same order of magnitude as the one above. The precessional instability appears to not be operating in this figure, as we concluded from the snapshot. Comparing this simulation to those where the elliptical instability was absent in Ch. 3, and the energy injection was instead due to the convection acting on the background flow like an effective viscosity, we see very similar behaviour. We therefore attribute this behaviour to the convection acting like an effective viscosity in damping the precessional flow as well. In Fig. 6.2d we show the simulation with parameters $\mathrm{Po} = 0.2,\ \mathrm{Ra} = 2\mathrm{Ra}_c$. Even though the convection is present we again observe the secondary transition, likely indicating the operation of the precessional instability in this simulation. The kinetic energy and energy injection appear to saturate at slightly lower values compared to Fig. 6.2b.

The time series corresponding to the simulation with $\mathrm{Po} = 0.1,\ \mathrm{Ra} = 6\mathrm{Ra}_c$ is shown in Fig. 6.2e. We observe a mixture of the convective energy injection behaviour and the precessional instability secondary transition. A transition akin to the precessional secondary transition does arise, but it is much more gradual. So neither from the snapshot of the flow nor from the time series can we properly conclude whether this is due to the precessional instability or a property of convection modified by precession. If it is indeed the precessional instability then the convection allows for the secondary transition to appear at smaller values of the Poincaré number. This can potentially enhance the energy injection and thus dissipation significantly, and is therefore important to examine further. Finally, we examine the time series of the simulation with $\mathrm{Po} = 0.2,\ \mathrm{Ra} = 6\mathrm{Ra}_c$ in Fig. 6.2f. We again notice a secondary transition, which occurs much faster than in the case of the top right and middle right panels, even though the Poincaré number of all three simulations is the same. The energy and energy injections prior to this transition are larger due to the convective driving. We thus conclude that the convective driving does not disrupt the operation of the precessional instability; instead it appears that convection allows the precessional instability to attain its continuously turbulent regime at lower values of the Poincaré number. This is possibly caused by the increased value of the energy or 2D energy – and thus presence of a vortex in the flow – due to convection.

6.1.3 Examination of the 2D energy using DEDALUS

If we do indeed wish to attribute the secondary transition to the large-scale vortices, then one way to probe them is by studying the values of K_{2D}. To this end we will turn to the K_{2D} obtained using DEDALUS simulations. Of particular interest would be to see if and how the convective instability allows the precessional instability to attain the continuously turbulent regime at lower values of the Poincaré number. We again note that the vortices in the snapshots in Fig. 6.1 appear to not be z-invariant, and thus K_{2D} does not fully capture the energy in these vortices. To be able to better compare and study the values of K_{2D} and its importance in these simulations relative to K we plot normalised values of the total kinetic energy K, the 2D energy K_{2D} as well as their ratio in Fig. 6.3. We have normalised all these simulations by the same value, namely the largest value of the total kinetic energy reached in this set of six simulations, which is found in the simulation with $\mathrm{Po} = 0.2,\ \mathrm{Ra} = 0$.

In Fig. 6.3a the simulation with $\mathrm{Po} = 0.1,\ \mathrm{Ra} = 0$ is plotted. The expected bursty behaviour is again evident in the values of K, and the behaviour closely resembles that of the simulation executed using NEK5000 in Fig. 6.2a. The 2D energy follows closely behind the burst in total kinetic energy, and is maintained more strongly after the burst than the 3D energy, such that after the burst the ratio of the total to the 2D energy attains the largest values, while during the bursts this ratio dips. The 2D energy appears to peak at normalised values of order $\mathcal{O}(10^{-3})$ in this simulation. In Fig. 6.3b the simulation with $\mathrm{Po} = 0.17,\ \mathrm{Ra} = 0$ is plotted; this simulation was found, when examining the NEK5000 simulations (not shown), to transition into the continuously turbulent regime after many rotation times in the lower energy turbulent state and we observe the same here. Prior to the secondary transition the bursty behaviour has clearly disappeared. It has been replaced by the flow containing a vortex, like the one in Fig. 6.1c. K_{2D} keeps growing in this simulation, and we observe the secondary transition to start once K_{2D} has attained a normalised value of $\approx 10^{-2}$. The final state appears to have a ratio of K_{2D} to K that is somewhat larger than this pre-turbulent state, but unlike the $\mathrm{Po} = 0.1,\ \mathrm{Ra} = 0$ case with bursty behaviour the K_{2D} does not achieve a dominant state in these simulations. In Fig. 6.3c we plot the simulation with $\mathrm{Po} = 0.18,\ \mathrm{Ra} = 0$. This simulation goes through the secondary transition faster, because the K_{2D} energy increases faster and more steadily than in the $\mathrm{Po} = 0.17,\ \mathrm{Ra} = 0$ case. The transition again appears to happen roughly when the normalised value of K_{2D} exceeds 10^{-2}. Next, in Fig. 6.3d we plot the simulation with $\mathrm{Po} = 0.2,\ \mathrm{Ra} = 0$; the K_{2D} energies attain large values more rapidly then the simulations at lower values of the Poincaré number, and again the transition happens faster than at lower values of Po. We also note that the final saturation energies increase with increasing Poincaré number, because the energy injection increases with Po.

Thus we conclude that it is likely that the secondary transition into the continuously turbulent regime for the precessional instability in isolation is mediated by the presence of vortices and their energy K_{2D}. A sufficiently large amount of energy in these vortices is needed, which is paired to sufficiently large values of the Poincaré number and suppression

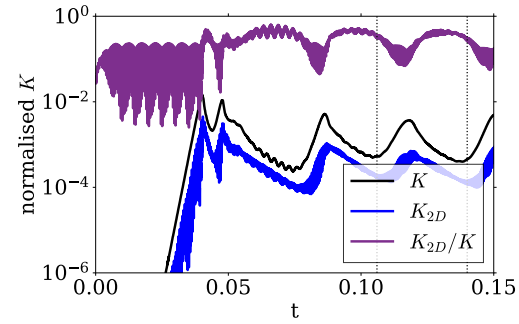

(a) Po = 0.1, Ra = 0.

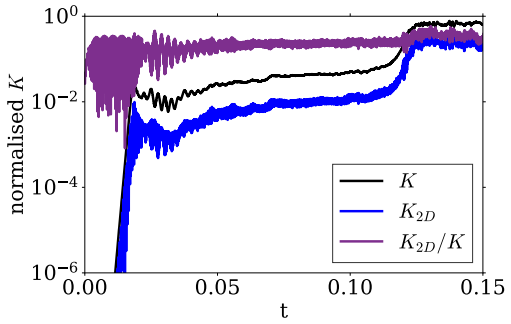

(b) Po = 0.17, Ra = 0.

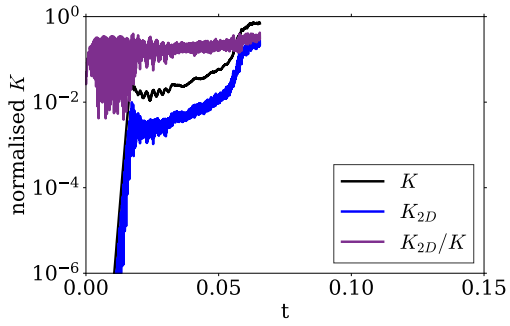

(c) Po = 0.18, Ra = 0.

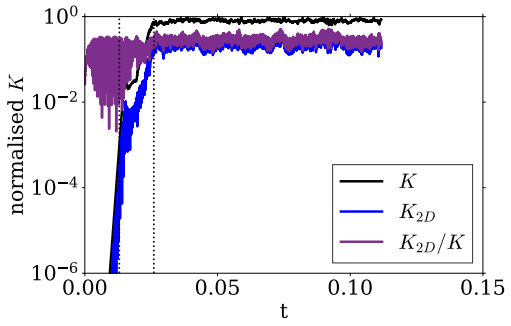

(d) Po = 0.2, Ra = 0.

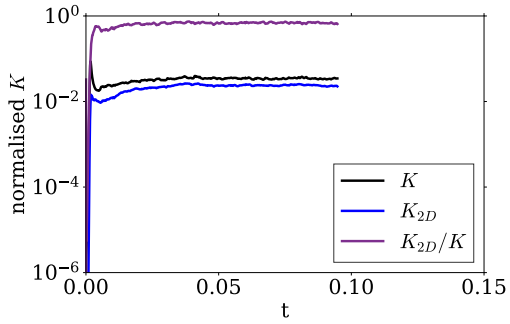

(e) Po = 0, Ra = $4\mathrm{Ra}_c$.

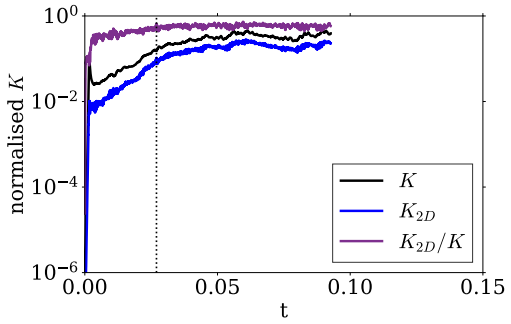

(f) Po = 0.1, Ra = $4\mathrm{Ra}_c$.

Figure 6.3: Normalised energy time series of the precessional instability and convection with $\mathrm{Ek} = 2.5 \cdot 10^{-5}$, executed using DEDALUS. Vertical dotted lines correspond to the ends of the intervals of the spectra shown in Figs. 6.4, 6.5 and 6.6. The energies are normalised by the largest energy attained in this group of six simulations, which occurs in the simulation in the middle right panel. The expected bursty behaviour is observed in the top left panel, as well as dominance of K_{2D} in the absence of the bursts of the precessional instability. The top right panel features an absence of bursty behaviour and a very gradual increase in energy until the secondary transition is reached. The middle left panel, with stronger precessional driving than the top right panel, attains the secondary transition faster, and the deciding factor when the secondary transition occurs appears to be the value of K_{2D}. The precessional driving in the simulation in the middle right panel is even stronger, such that the secondary transition is achieved very rapidly. In the bottom left panel a purely convective simulation is shown, which achieves rapid saturation with much fewer fluctuations compared to the precessional cases, and a clear dominance of the K_{2D} energy. In the convective and precessional simulation in the bottom right panel the energy far exceeds that of the convective simulation and the precessional instability in isolation with Po = 0.1; thus the combination indeed allows for larger energies to be achieved.

of the bursty behaviour. This is in stark contrast to the elliptical instability case, where the vortices instead suppressed the instability.

Next we examine these same quantities in the presence of convection in the bottom panels of Fig. 6.3. In Fig. 6.3e the simulation with Po = 0, Ra = $4\mathrm{Ra}_c$ is plotted; we can see that the energies saturate rapidly at values around the required transition value, with K_{2D} dominating the flow from the start as we would expect. The flow saturates and attains its final statistically steady state very rapidly. Furthermore, it displays much fewer high frequency fluctuations than the cases where the precession is present. Finally, we examine Fig. 6.3f in which we have plotted the simulation with Po = 0.1, Ra = $4\mathrm{Ra}_c$. A much higher energy state is achieved in this simulation compared to both simulations with precession and convection in isolation for these same parameters. The transition to the high energy state again appears more gradual than the secondary transitions of the precessional instability in isolation. This gradual transition arises roughly when the normalised value of K_{2D} exceeds 10^{-2}. The ratio of K_{2D} to K is maintained at a larger value compared to the purely precessional simulations that have gone through a turbulent transition, although the value is smaller than the one of the purely convective case. Thus we conclude that if the convection reaches a certain energy, and the precessional instability is able to operate, then the convection assists the precessional instability in achieving the continuously turbulent regime.

This cannot, however, be the full picture, as this would imply that once a certain K_{2D} energy is reached the precessional instability will always be able to achieve the continuously turbulent state. As a result even the smallest values of Po would reach this state in convective simulations that are sufficiently strongly driven. When examining these simulations we still observe the dominance of convection acting as an effective viscosity for a majority of the lower values of Po. Thus there must be a secondary part to explain this phenomenon. To this end, we will examine the spectra of these flows, both before and after the transition, as well as in the presence of convection. In addition, and for completeness, we examine the spectra of a simulation displaying bursty behaviour.

6.1.4 Horizontal energy spectra of the flow

We start by examining the horizontal energy spectra of the bursty simulation with Po = 0.1, Ra = 0 in Fig. 6.4, corresponding to Fig. 6.3a. These horizontal energy spectra are obtained at the mid-plane of the simulation, i.e. $z = 0.5$. They are captured over one burst and decay period, in Fig. 6.3a denoted by the interval between the vertical dotted lines from $t = 0.106$ to $t = 0.140$. We have averaged these spectra every five output steps, with a time between outputs of $t = 0.001$. The times corresponding to each spectrum are shown in the legend. Energy is preferentially injected by the precessional instability into the modes near $k_\perp = 18.059$, which in these energy spectra is contained within the bin centred at $k_\perp = 6\pi \approx 18.85$. In all the averaged energy spectra in this figure this injection is represented by the large spike in energy. The period under study starts with a significant fraction of the kinetic energy in the K_{2D} modes compared to the total energies,

which is represented in the energy spectrum in blue by the bin with the lowest horizontal wavenumber containing comparable energy to the wavenumbers where energy is injected. As the simulation evolves the energy increases due to a burst in energy injection. This is represented by a large increase in the energy located in the primary energy injection spike in both the orange and green spectra, also adding energy in the smallest wavenumber bin corresponding to the large-scale flow. Towards the end of the burst energy is being transferred to smaller and smaller scales as indicated by the wider green spectrum. After the burst finishes the energy starts decreasing again in the red, purple, brown and pink spectra. It should be noted that the energy in the smallest wavenumber bins has increased in the red spectrum compared to the green spectrum. Once these energies have decayed sufficiently another burst can occur again and the cycle starts anew. Finally, we have plotted the turbulent Kolmogorov scaling of $k_\perp^{-5/3}$ in a dashed-black line in the figure, but we note that no parts of the spectra agree with this line, as we expect, since the flow does not appear turbulent at any stage from the snapshots.

Next we turn our attention to the spectra of the simulation with $\mathrm{Po} = 0.2,\ \mathrm{Ra} = 0$ in Fig. 6.5, corresponding to the interval between the vertical dotted lines in Fig. 6.3d from $t = 0.013$ to $t = 0.026$, in which we capture the final stages of the initial instability followed by the secondary transition. We have averaged the spectra in this figure over two output steps, again with a time between outputs of $t = 0.001$. During the linear instability we again retrieve the primary peak of the most unstable linear modes at $k_\perp = 6\pi$, as well as a secondary peak at $k_\perp = 12\pi$. As the instability saturates in the orange spectrum, energy is moved to smaller and smaller scales, as well as into the largest-scale modes. The energy starts aligning to a more traditional turbulent shape while the energy in the lowest wavenumber bin keeps growing in the green spectrum; the clear peak in the linear modes vanishes from the green to the red spectrum, and the K_{2D} starts to dominate the flow in all subsequent spectra. This seems to allow the secondary transition to occur, with energy subsequently being distributed across the scales. We have again plotted the Kolgomorov scaling as $k_\perp^{-5/3}$ in dashed-black. It appears that the intermediate scales in this simulation agree well with this prediction. Thus we can be reasonably justified in calling this regime the continuously turbulent regime. We can use these energy spectra to examine the well-resolvedness of the flow, using the rule of thumb that the largest energy in one bin must be at least a factor of 10^3 larger than the energy at the de-aliasing scale, which is clearly satisfied in these spectra. As the simulation continues evolving it eventually achieves a statistically steady state, with spectra resembling the pink spectrum in Fig. 6.5. The energy in the smallest wavenumber bin in these spectra is of order $\mathcal{O}(10^7)$ and the one in the largest wavenumber bin of order $\mathcal{O}(10^2)$. Therefore, we conclude that this simulation is well-resolved.

Finally, we turn to the effect convection has on these flows by examining the energy spectra of the simulation with $\mathrm{Po} = 0.1$, $\mathrm{Ra} = 4\mathrm{Ra}_c$ in Fig. 6.6. The time we examine is denoted by the interval between the start of the simulation and the vertical dotted-black line in Fig. 6.3f, from $t = 0$ to $t = 0.027$. We average the spectra over four output steps,

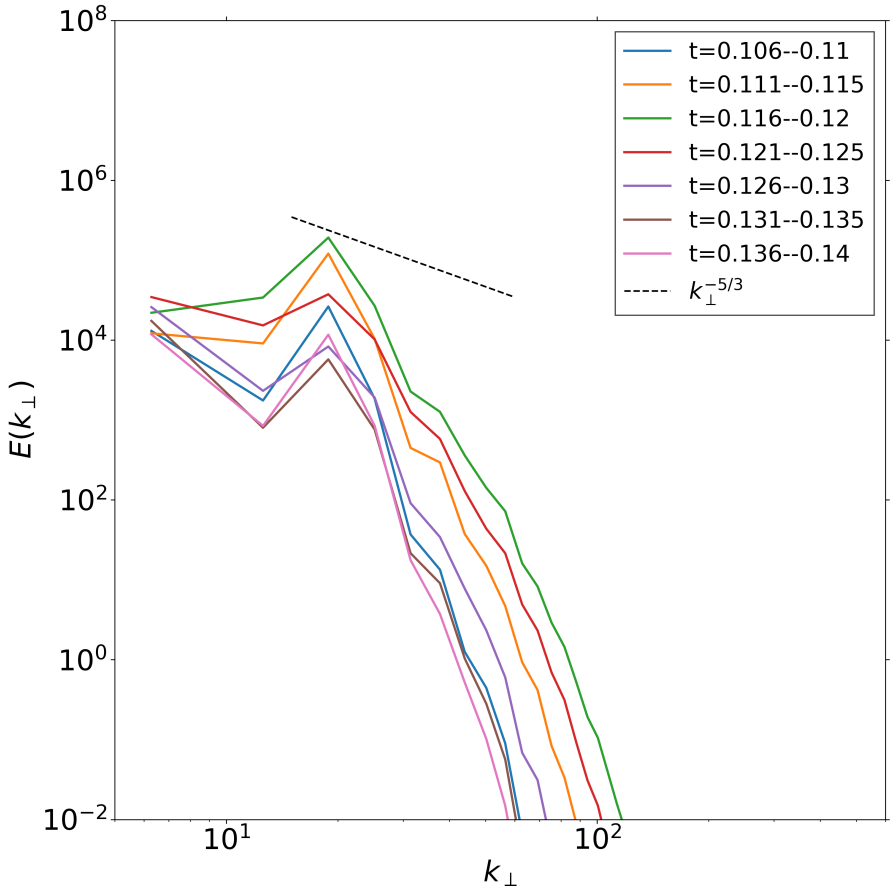

Figure 6.4: Horizontal energy spectra taken at $z = 0.5$ of the simulation with Po $= 0.1$, Ra $= 0$ from $t = 0.106$ to $t = 0.140$, corresponding to the interval between the vertical dotted lines in Fig. 6.3a. The simulation goes through a burst and decay period in this interval. In the spectra this is indicated by the increase and subsequent decrease in the main energy injection spike in the wavenumber bin with $k_\perp = 6\pi$, while the 2D energy, here located in the smallest wavenumber bin, lags slightly behind this spike. The spectra clearly do not match the Kolmogorov scaling as $k_\perp^{-5/3}$ in dashed-black, implying it is not turbulent, as we would expect from the snapshots of this simulation.

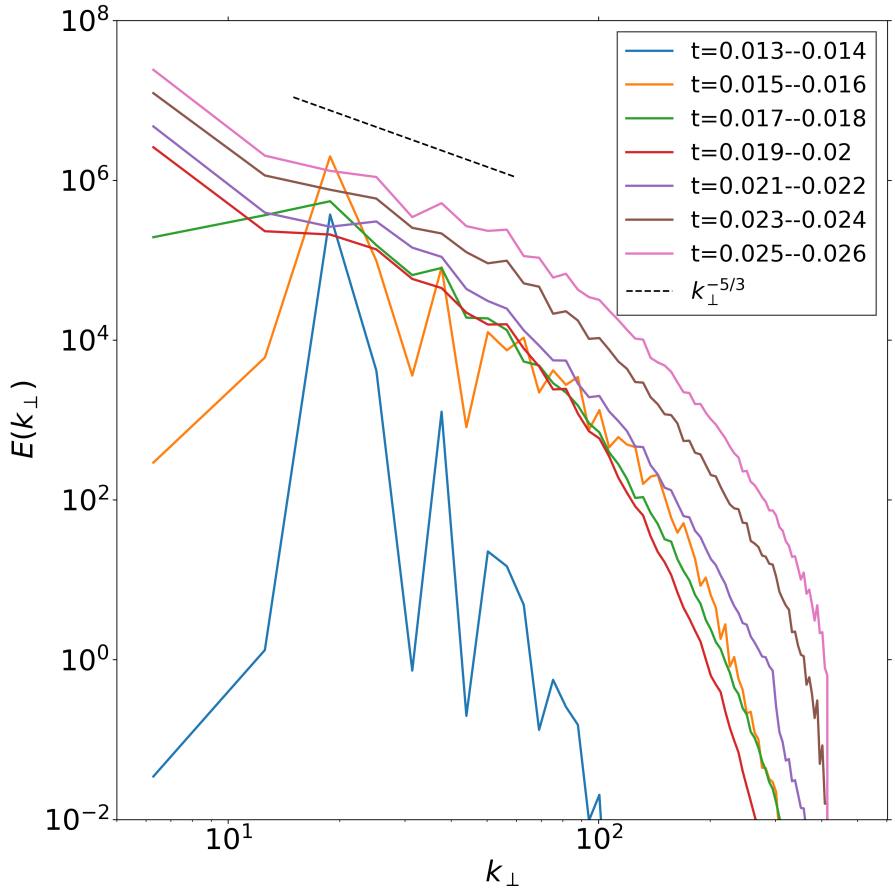

Figure 6.5: Horizontal energy spectra taken at $z = 0.5$ of the simulation with Po $= 0.2$, Ra $= 0$ from $t = 0.013$ to $t = 0.026$, corresponding to the interval between the vertical dotted lines in Fig. 6.3d. The simulation goes through the end of the linear growth phase and the short low-energy turbulent phase followed by the secondary transition. The energy at the end of the linear growth phase, in the blue and orange spectra, is predominantly located in the bin with the linearly most unstable wavenumbers as well as integer multiples of this bin, possibly pointing to triadic resonances. K_{2D} increases just before the secondary transition in the green spectrum, and then the secondary transition makes the simulation continuously turbulent, agreeing well with the Kolmogorov scaling as $k_\perp^{-5/3}$ in dashed-black at intermediate wavenumbers for the times indicated by the red, purple, brown and pink spectra.

with an output step every $t = 0.001$. The spectra appear turbulent from the start of the simulation, as we would expect from sufficiently strongly driven convection. There is a hint of energy injection by the precessional instability into the bin containing the precessionally unstable wavenumbers in the blue spectrum, because it is the bin with the most energy in this particular spectrum. As the simulation evolves the energy goes up predominantly in the smallest wavenumber bin and maintains roughly the same shape. Interestingly, it appears that the spectrum has actually become more concentrated towards larger scales in the orange spectrum compared to the initial blue spectrum, possibly due to the decay of the initial transient "burst" before non-linear saturation, and has subsequently started widening again over time. We again plot the Kolmogorov scaling in dashed-black, to which the intermediate scales of the spectra again agree reasonably well.

The spectrum shows that this simulation is also well-resolved. As the simulation evolves and achieves a statistically steady state, the spectra resemble the pink spectrum in Fig. 6.6, with the energy in the smallest wavenumber bin saturating at $\mathcal{O}(10^7)$, but with lower energies than the simulation in Fig. 6.5, while the energy in largest wavenumber bin saturates at $\mathcal{O}(10^0)$. We have also compared the energy spectra of this simulation with the ones of the purely convective simulation with $\mathrm{Po} = 0$, $\mathrm{Ra} = 4\mathrm{Ra}_c$. These spectra look very similar to the ones in Fig. 6.6, such that we have decided not to plot them. There is however one crucial difference, the energy in the purely convective spectra stops growing. Most notably, the energy in the smallest wavenumber bin does not grow like in Fig. 6.6, instead stagnating at an energy of $\approx 10^6$, i.e. this bin saturates at lower energies.

We conclude that the energy spectra support the hypothesis that the 2D energy is at the very least related to the secondary transition to the continuously turbulent regime. We also find that convection assists in achieving this energy in a rapid manner in originally bursty simulations in the absence of convection, such that even simulations with small values of the Poincaré number can achieve the continuously turbulent regime. However, the precessional instability must also be sufficiently strong to achieve this growth, as otherwise the precessional instability appears erased in favour of the turbulent effective viscosity regime. The increase in precessional growth rate by the convective driving as seen in the linear simulations in Fig. 5.7 and Fig. 5.8 could be an explanation as to why the precessional instability is still sufficiently strong to achieve the continuously turbulent regime in these simulations. This implies that, as the convective driving is increased, the continuously turbulent regime is attainable at lower and lower values of the Poincaré number in these simulations.

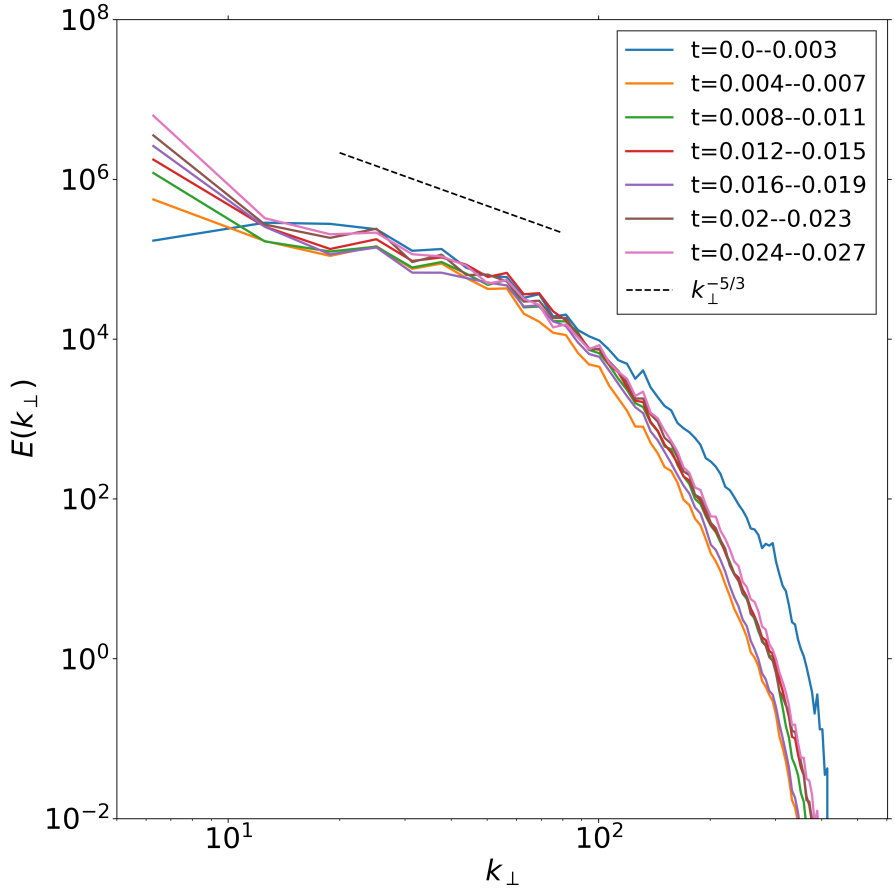

Figure 6.6: Horizontal energy spectra taken at $z = 0.5$ of the simulation with $\mathrm{Po} = 0.1$, $\mathrm{Ra} = 4\mathrm{Ra}_c$ from $t = 0.0$ to $t = 0.027$, corresponding to the interval between the start of the simulation and the vertical dotted line in the Fig. 6.3f. The simulation goes through the linear growth phase and the gradual transition to a higher energy state. No clear evidence of the precessional instability is present. Note the decrease of energy at smallest scales from the start of the simulation in the blue spectrum to the latter parts of the simulation, possibly due to the decay of the initial transient "burst" before non-linear saturation. Again we find good agreement with the Kolmogorov scaling as $k_\perp^{-5/3}$ in dashed-black for the intermediate wavenumbers.

6.2 Scaling laws of the quantities of interest

We now turn to obtain scalings laws for the quantities of interest. We will attempt to constrain the scaling of the time-averaged value of the energy injection, I, rms vertical velocity, u_z, and Nusselt number, Nu, as a function of the Rayleigh number, Ekman number and Poincaré number. We time-average these quantities starting from a suitable time in the simulations after a steady state has been reached. Because the continuously turbulent regime appears to be the final steady state in all simulations which feature it, we have taken time-averages only over this part of such simulations, neglecting any part of these simulations prior to the secondary transition.

6.2.1 Scaling laws as a function of the Poincaré number

We have identified three different qualitative regimes as a function of Po and Ra, and examined the transitions and reasons for them. In the absence of convection and at low Poincaré numbers the flow is laminar, alternating between the most unstable mode and the z-invariant large-scale flow. The results in Barker (2016b) indicate that the energy injection associated with this behaviour might be consistent with a scaling as Po^2, as they appear to scale similarly to the laminar dissipation of the background flow $\boldsymbol{U}_0$; see the bottom left panel of Fig. 7 in Barker (2016b). Note that their measured dissipation, and the energy injection in our setup, does not include the laminar dissipation however, such that this only gives a tentative indication how the energy injection in our simulations might scale with the Poincaré number in the laminar regime, without explaining the mechanism behind it. If however convection is present at low Poincaré number the flow appears much more turbulent due to convective action. The bursty behaviour has disappeared, reminiscent of the suppression of the elliptical instability by convection. Instead a continuous energy injection is present because of the action of turbulent convection on the precessional flow. We would expect to see this behaviour scale as Po^2 also and, more importantly, also depend on the Rayleigh number based on the results in Ch. 4. Finally, regardless of the presence of convection these simulations indicate a continuously turbulent regime at high Poincaré number. We would expect the energy injection in this regime to scale as Po^3. Even stronger convection might also suppress this regime or result in an effective viscosity, whose energy injection overshadows that of the precessional instability.

The time-averaged values of the energy injection rate I as a function of Po with fixed $\mathrm{Ek} = 2.5 \cdot 10^{-5}$ are plotted in Fig. 6.7. In this figure numerous parameter sweeps at different values of the Rayleigh number are plotted; the runs executed using NEK5000 are plotted using circles, while the runs executed using DEDALUS are plotted using diamonds. As stated previously, the majority of these simulations have been executed using NEK5000. But the simulations we have executed using DEDALUS always show very good agreement with their NEK5000 counterparts, thus validating the results obtained using both codes. The simulations executed at $\mathrm{Ra} = 0$ in blue circles start at $\mathrm{Po} = 0.06$ because the precessional instability is not unstable below this value of the Poincaré number with this value of the Ekman number. Out of interest for the results we have also run this

parameter sweep out to the likely astrophysically irrelevant value of $\mathrm{Po} = 1.1$.

For clarity and to highlight the different regimes we have split the figure into two panels in Fig. 6.7. The top panel of Fig. 6.7 shows the data on the interval of $\mathrm{Po} = [0.01, 0.12]$, thus capturing the effective viscosity as well as the laminar regime of the precessional instability in detail. The bottom panel on the other hand shows the data on the interval $\mathrm{Po} = [0.1, 1.1]$, highlighting the transition between the two regimes and the continuously turbulent regime. The influence of convection on the occurrence of the secondary transition, as well as the action of convection on the energy injection in the continuously turbulent regime are also visible. Note the overlap between these two figures, which was chosen deliberately so that the departure from certain behaviours and associated scaling laws are more clearly illustrated. Note also the different vertical axes between the two panels. The legend for both panels of the figure is the same, and as such has only been included in the bottom panel. We will fit the data points where applicable using either of the obtained Po^2 or Po^3 scalings. As in the case of the elliptical instability, we will define $D \equiv \zeta\Omega^3\mathrm{Po}^3$ and $D_{\mathrm{lam}} \equiv \Upsilon\Omega^2\mathrm{Po}^2$, with ζ and Υ the proportionality or efficiency "factors" of both scaling laws respectively. We have defined D_{lam} for the dissipation scaling as Po^2 reported in Barker (2016b) and Pizzi et al. (2022). Note that we reserve the proportionality factor Υ for the precessional laminar scaling laws exclusively, and will not use this factor when fitting the effective viscosity. Furthermore, we have chosen an arbitrary scaling of this laminar energy injection as Ω^2 for ease of comparison with the energy injection due to the effective viscosity, but, since there is no theoretical basis for this scaling, we will allow Υ to depend on Ω. Lastly, ζ can also depend on the Rayleigh number.

In the top panel of Fig. 6.7 the data points obtained with different values of the Rayleigh number agree well with the Po^2 scaling. Indeed, even the dataset obtained at $\mathrm{Ra} = 0$ agrees with this crude scaling with $\Upsilon = 3.5$, which we have plotted in dashed-black. Although it should be stressed that this parameter sweep primarily agrees with this scaling law for a different reason than those parameter sweeps where convection is present. The energy injection rate at $\mathrm{Ra} = 2\mathrm{Ra}_c$, represented with yellow circles and fitted in solid-red, is lower than at $\mathrm{Ra} = 0$; the convection has prevented the precessional instability from operating, even though the energy injection from the convection acting on the background flow is actually lower than that of the precessional instability in isolation with $\mathrm{Ra} = 0$. We also observe that the energy injection in this regime increases with convective driving, as fully expected from our previous results for the effective viscosity. A final point of note is that both the purple circles with $\mathrm{Ra} = 4\mathrm{Ra}_c$, with fit in solid-grey, and the light blue circles with $\mathrm{Ra} = 6\mathrm{Ra}_c$, with solid-blue fit, deviate from their respective fits as Po^2 for $\mathrm{Po} \geq 0.10$ and $\mathrm{Po} \geq 0.06$ respectively. Instead, they then seem to agree with a fit as Po^3 in solid-black, providing a tentative hint for the continuously turbulent scaling we have predicted previously. Finally, the two burgundy circles with $\mathrm{Ra} = 15\mathrm{Ra}_c$ with associated solid-pink fit, do not agree with the solid-black fit. This is possibly because the energy injection due to the convection interacting with the background flow is larger than the solid-black fit on this interval of Po, because the convective driving for these parameters

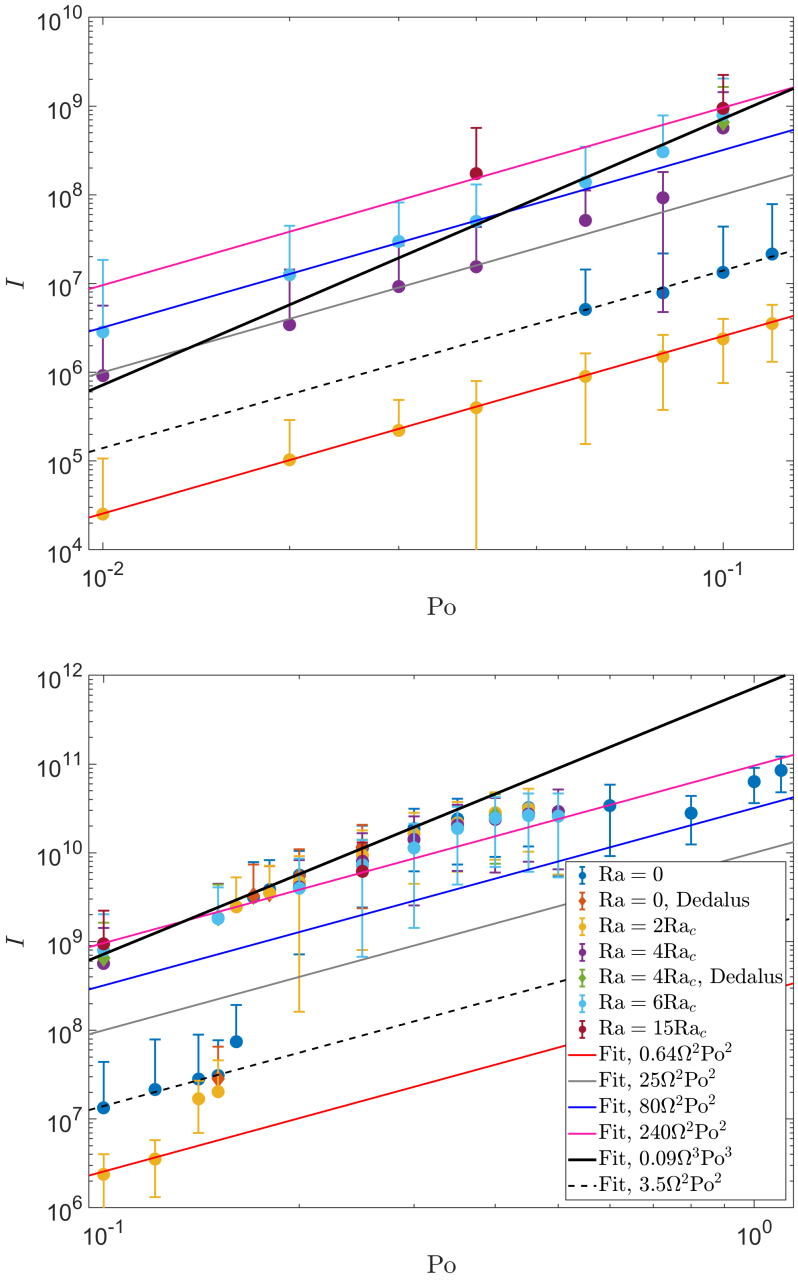

Figure 6.7: Time-averaged energy injection I with fixed $\mathrm{Ek} = 2.5 \cdot 10^{-5}$. The figure has been split into two panels, with a slight overlap to highlight the different regimes. Note the different vertical axes. The legend for both figures is placed in the lower panel. The simulations executed using NEK5000 are presented with circles, the ones executed using DEDALUS with diamonds. The top panel shows the low Poincaré number regimes, i.e. the laminar dissipation regime scaling as Po^2 in the absence of convection and the effective viscosity regime also scaling as Po^2 for simulations with convection present. The bottom panel instead shows the transition regime of the purely precessional case around $\mathrm{Po} = 0.16$. The continuously turbulent regime that all simulations agree with at large values of Po has been fitted with a solid-black line scaling as Po^3. Note that as the Poincaré number is increased beyond $\mathrm{Po} \approx 0.35$ the energy injection plateaus and eventually appears to decrease.

is quite strong.

Moving on to the second half of the figure in the bottom panel of Fig. 6.7, we have retained all the fits of the top panel of the figure for continuity purposes, although it is clear that the majority of the simulations with Po $\gtrsim 0.15$ do not agree with these fits anymore. Indeed we observe a strong jump in energy injection in both the purely precessional simulations with Ra $= 0$ and the simulation with the weakest convective driving considered with Ra $= 2\mathrm{Ra}_c$. Both of these scalings first deviate weakly from their Po^2 fits, associated with the turbulent state without a secondary transition. Then, when the secondary transition does present itself in the simulations, the energy injection jumps up abruptly as a function of Po and instead aligns with the solid-black fit scaling as Po^3. This abrupt jump again occurs at different values of the Poincaré number, as previously observed in the Ra $= 4\mathrm{Ra}_c$ and Ra $= 6\mathrm{Ra}_c$ parameter sweeps. The abrupt jump occurs at Po $= 0.16$ for the Ra $= 2\mathrm{Ra}_c$ parameter sweep and at Po $= 0.17$ for the Ra $= 0$ parameter sweep. Thus we also observe in this figure that the secondary transition to the turbulent state is facilitated by the convection such that it occurs at lower Po for larger Ra.

Once the turbulent scaling has been reached all simulations are, within the error bars, consistent with the solid black fit scaling as Po^3 with $\zeta = 0.09$ up to and including Po ≈ 0.35. At larger values of the Poincaré number higher order effects seem to arise, and the energy injection seems to plateau or possibly decrease slightly as a function of Po, deviating from the solid-black fit. At even larger values of Po > 0.5 the energy injection does again increase a little bit, but the specific reason for this is unclear. It could be due to, for example, further higher-order effects, boundary layer effects, or possibly even the horizontal wavenumber decreasing sufficiently, as Po is increased, such that it is now no longer de-tuned as it selects a different mode available in the simulation. Finally, although all data points are consistent with the solid-black fit within error bars a trend does appear to arise as a function of the Rayleigh number. The energy injection rate decreases as the Rayleigh number is increased, which we will show in more detail in Fig. 6.12. This decrease is expected to continue with increasing values of the Rayleigh number until the turbulent energy injection of the precessional instability is overshadowed by the energy injection due to the effective viscosity. This has already happened to the burgundy circle with Ra $= 15\mathrm{Ra}_c$ at Po $= 0.25$ where the energy injection agrees with the Po^2 fit in solid-pink, even though it is in the continuously turbulent regime and visual inspection of the time series of this simulation (not shown) reveals the secondary transition.

Having examined the time-averaged energy injection we can also examine the vertical velocity and the Nusselt number, although the latter only in the simulations with Ra $\neq 0$. We examine the time-averaged vertical velocity u_z in Fig. 6.8. The velocities largely follow the same patterns as the energy injection; since we have examined these patterns thoroughly already we opt not to split the figure here. At low Poincaré numbers the convection dominates and the vertical velocity is therefore independent of Po. The vertical velocities instead scale with the Rayleigh number as we observed for the convective velocity in Ch. 4. As the precessional driving is increased these values start deviating from the

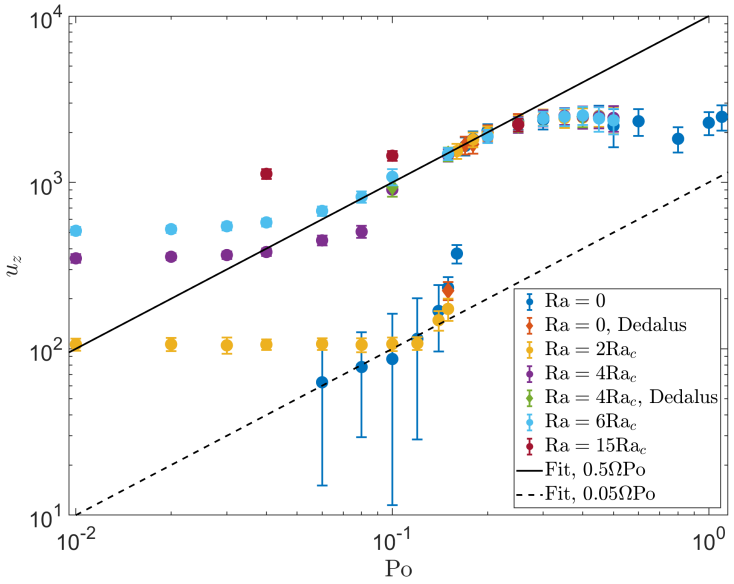

Figure 6.8: Same as Fig. 6.7, instead showing the time-averaged rms vertical velocity u_z. The vertical velocity in the absence of convection agree with two different fits in the laminar, plotted in dashed-black, and continuously turbulent regimes, plotted in solid-black. Both fits are consistent with a scaling as Po. The velocities in the presence of convection agree with the convective velocity, until the continuously turbulent precessional regime arises in the simulation, at which point they align with the continuously turbulent scaling. The vertical velocity plateaus around Po ≈ 0.30.

purely convective result, with clearly noticeable departure from Po $\gtrsim 0.06$ for Ra $= 4\text{Ra}_c$ and Ra $= 6\text{Ra}_c$. At even larger values of Po these data points instead start aligning with what appears to be a scaling with Po in solid-black. This scaling was predicted in our theoretical arguments to derive the energy injection rate in Sec. 5.1.4. The solid-black fit again tends to agree with the results in the continuously turbulent regime after the abrupt jump at all values, up until Po ≈ 0.30 after which it appears to plateau again. Note that the burgundy data points corresponding to the parameter sweep with Ra $= 15\text{Ra}_c$ only agree in the continuously turbulent regime; in the convectively dominated regime the velocities of this sweep are much larger than predicted by our Po scaling in solid-black. The purely precessional results in blue data points at Ra $= 0$ do however present one additional interesting characteristic: the velocities are consistent with a different fit, still scaling as Po, prior to the jump. We have plotted this fit in dashed-black. It should be noted that vertical velocities associated with this fit are about one order of magnitude smaller than those in the continuously turbulent regime.

Finally, we can examine the value of the Nusselt number in the convective, Ra $\neq 0$, simulations we have executed. For these convective parameter sweeps the Nusselt number follows the same general behaviour as the vertical velocity. The Nusselt number starts at the convective value, and then remains almost constant until it starts to transition into the continuously turbulent precessional regime. In the continuously turbulent precessional regime the Nusselt number is higher than in the absence of precession for most of the

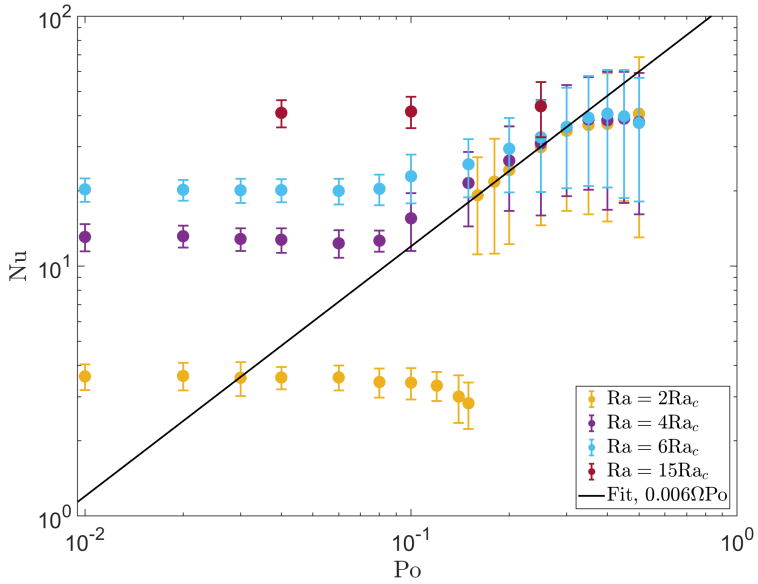

Figure 6.9: Same as Fig. 6.7, instead showing the time-averaged Nusselt number Nu. The parameter sweep with Ra = 0 has not been plotted as the Nusselt number is one by definition. The Nusselt number appears to decrease slightly in the effective viscosity regime as the 2D energy gets stronger with stronger precessional driving for the Ra = 2Ra$_c$ case. Then it jumps or increases to meet the continuously turbulent regime, where the Nusselt number appears to collapse onto a scaling consistent with Po like the vertical velocity. The Nusselt number plateaus around Po $\approx$ 0.35.

Rayleigh numbers we have probed, as also found in Wei and Tilgner (2013). In the case of Ra = 4Ra$_c$ and particularly in the case of Ra = 6Ra$_c$ this transition is very gradual. The parameter sweep with Ra = 2Ra$_c$ prior to the transition does however show an interesting effect. As the simulations become more turbulent at larger precessional driving, but have not yet attained sufficiently large values of the Poincaré number to attain the secondary transition to the continuously turbulent regime, the Nusselt number exhibits a downward trend. This is likely a result of the large-scale flow forming a vortex and becoming more energetic in these simulations as the Poincaré number is increased. After the abrupt jump the results seem to agree roughly with a scaling as Po in the solid-black fit, just like the convective velocity. The Nusselt number once again deviates from this scaling from Po $\approx$ 0.35 onwards. Note that the results obtained at Ra = 15Ra$_c$ do not agree with the solid-black fit, as the inherent Nusselt number due to convection is larger than any effects of the precessional instability in this parameter sweep. It is likely that the inherent heat transport of the convection forces the Ra = 6Ra$_c$ data points to agree with the solid-black fit only from Po = 0.25 until Po = 0.35. We suspect that the convective velocity, and as a result the convective heat transport, is increased because the convection is inhibited less by rotation due to the introduction of precession. The reasoning is as follows: in our setup, the introduction of precession adds a secondary rotation – with rotation axis perpendicular to the spin axis of the body – to the system, which results in the precessional Coriolis-like term in the momentum equation. This additional rotation and its resultant Coriolis-like term result in an effective rotation axis that is no longer parallel to the direction of gravity.

The direction of the effective rotation axis deviating from the one of gravity in this setup possibly results in a decreased inhibition of convection as the Taylor-Proudman theorem becomes less and less relevant with increased precessional driving.

We thus clearly observe several scaling regimes with Po for the energy injection and rms vertical velocity, including those we predicted in Sec. 5.1.4, and also fitted a scaling law for the Nusselt number. Therefore, we will now turn to the scalings as a function of the rotation rate Ω and the Rayleigh number for the energy injection, as that is the main quantity of interest in this work.

6.2.2 Scaling laws as a function of the rotation rate

To start our examination of the effects of the rotation rate on the precessional instability, in the absence of convection, we have performed parameter sweeps as a function of the Poincaré number with three different values of the Ekman number, $\mathrm{Ek} = [5\cdot10^{-5}, 2.5\cdot10^{-5}, 10^{-5}]$, which we have achieved by varying the rotation rate. The results are plotted in the top panel of Fig. 6.10. In addition to these three parameter sweeps indicated in blue, orange and purple triangles we have also added the DEDALUS simulations we have performed in yellow diamonds. The energy injection increases as the Ekman number decreases, but the same general behaviour is maintained across all three parameter sweeps. All three parameter sweeps feature a laminar energy injection that appears to be consistent with a fit scaling as Po^2. We have reproduced the dashed-black laminar fit from Fig. 6.7. The energy injection of all three parameter sweeps starts deviating slightly from the laminar scaling and then abruptly jumps to an energy injection that appears to be consistent with a fit scaling as Po^3. We also reproduce the solid-black fit from Fig. 6.7. The value of the Poincaré number at which this abrupt jump occurs decreases with decreasing Ekman number.

In the bottom panel of Fig. 6.10 we have attempted to rescale the x-axis of the top panel in such a way that the jump occurs at roughly the same value for all three parameter sweeps at different values of the Ekman number. We have found the best agreement (by eye) by rescaling the x-axis as $\mathrm{Ek}^{-4/10}\mathrm{Po}$. This rescaling seems to indicate that the continuously turbulent regime of the precessional instability appears to emerge when $\mathrm{Ek}^{-4/10}\mathrm{Po} \gtrsim 9$. We have tested both changing the viscosity and Ω to alter the Ekman number in these simulations, and have found that indeed it is the Ekman number that governs this transition, finding the same location of the transition independently of varying the viscosity or rotation rate. The energy injection rate itself is however affected solely by the rotation rate and not by the Ekman number, because it is the rotation rate that represents the tidal frequency. In astrophysical systems, with values of the Poincaré number that are not too small and very small values of the Ekman number, we might thus expect to be in the continuously turbulent regime for the precessional instability in isolation.

Next we wish to test our scaling of the energy injection as a function of both the Poincaré number and rotation rate Ω in Fig. 6.11. In this figure we have not rescaled the

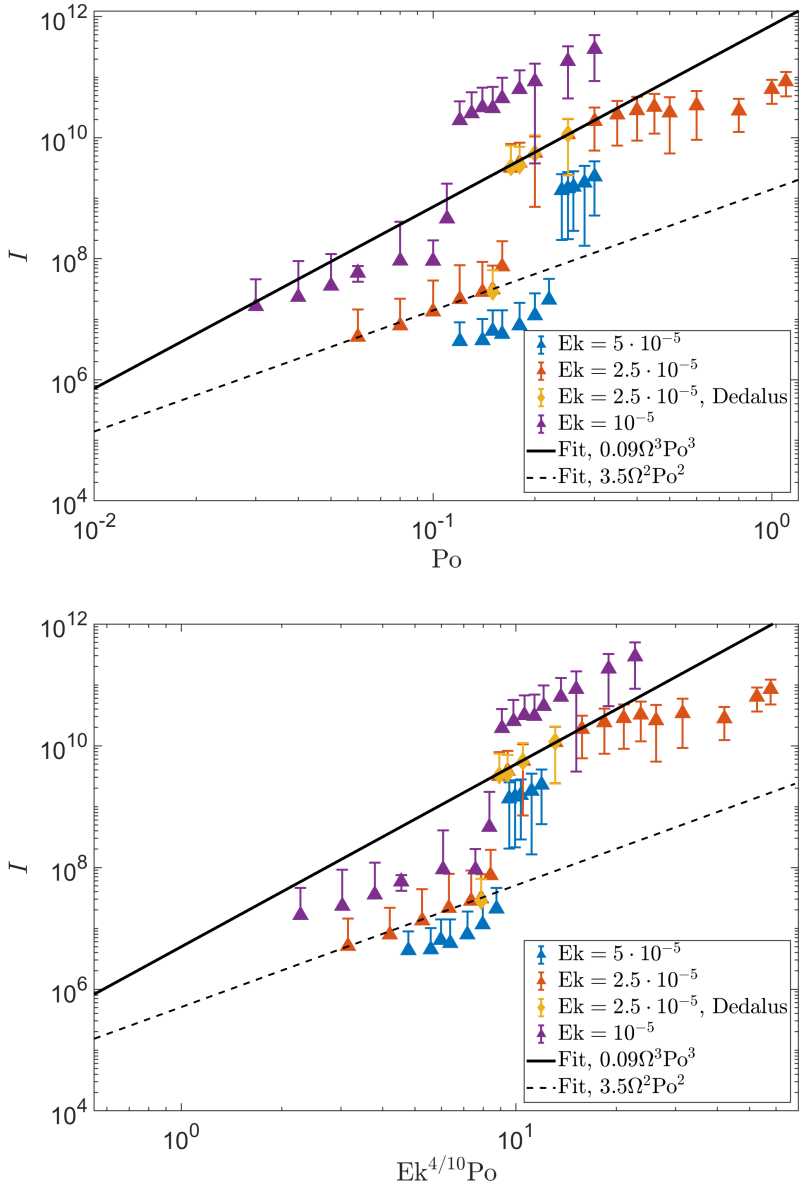

Figure 6.10: The time-averaged energy injection I as a function of the Poincaré number at different values of the Ekman number, in the absence of convection. The chosen values of the Ekman number are $\mathrm{Ek} = [5 \cdot 10^{-5}, 2.5 \cdot 10^{-5}, 10^{-5}]$ in blue, orange and purple triangles respectively. The DEDALUS results are plotted in yellow diamonds. We have reproduced the continuously turbulent scaling in solid-black and the laminar scaling in dashed-black from Fig. 6.7. The top panel shows that the transition to the continuously turbulent regime decreases with increasing Po, while the energy injection itself increases with increasing Ω. In an attempt to find how the Ekman number affects the transition we have rescaled the x-axis with $\mathrm{Ek}^{-4/10}$ in the bottom panel and find good agreement of the location of the transition in all three cases.

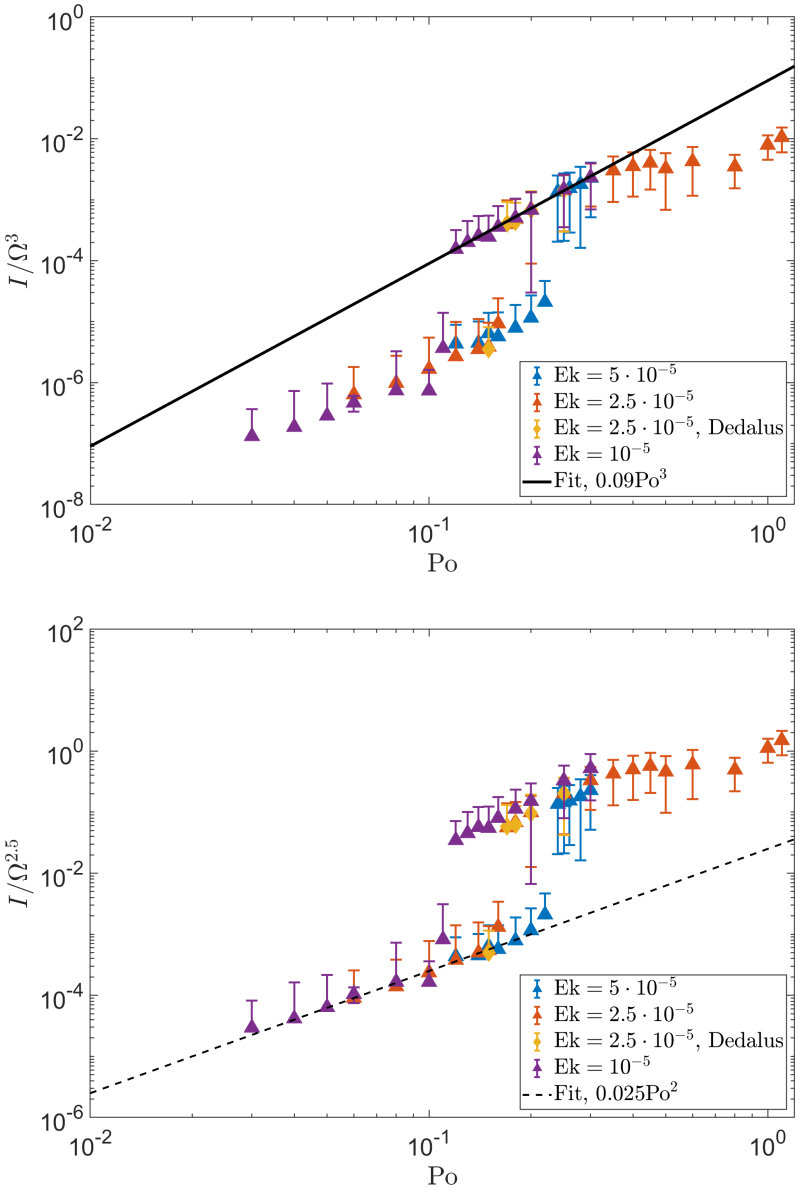

Figure 6.11: Same as Fig. 6.10, after rescaling the energy injection with the rotation rate. As in Fig. 6.10 the chosen values of the Ekman number are $\text{Ek} = [5 \cdot 10^{-5}, 2.5 \cdot 10^{-5}, 10^{-5}]$ in blue, orange and purple triangles respectively. The DEDALUS results are plotted in yellow diamonds. In the top panel we have rescaled the y-axis with Ω^3 instead, and find that all three parameter sweeps collapse to the solid-black fit of the continuously turbulent regime. In the bottom panel we rescale with $\Omega^{5/2}$ instead and find that now the parameter sweeps collapse to the laminar scaling in dashed-black.

x-axis. In the top panel we have scaled the energy injection rate of all three parameter sweeps by dividing each by their respective rotation rate cubed, which is the predicted scaling of the energy injection in the continuously turbulent regime. We find that the data points which are located in the continuously turbulent region do indeed collapse and agree remarkably well with the fit of the energy injection rate in the continuously turbulent regime in solid-black as given in Fig. 6.7, with $\zeta = 0.09$. The data points located in the laminar regime in this panel do not collapse under this rescaling, and as such we have omitted the dashed-black fit corresponding to the laminar regime. Finally, in the bottom panel of Fig. 6.11 we have rescaled the energy injection by dividing by $\Omega^{5/2}$ for each parameter sweep. This differs from our arbitrary choice in which the energy injection in the laminar regime scales as Ω^2. However, we find that the data points collapse more uniformly and better agreement with the fit in dashed-black is possible when we rescale by $\Omega^{5/2}$ instead, and thus we choose to plot this. We choose to maintain our original definition in which the energy injection scales as Ω^2 in the laminar regime and thus find the proportionality factor to be $\Upsilon = 0.025\Omega^{1/2}$. Indeed all three parameter sweeps in the laminar regime agree very well with the Po^2 fit in dashed-black. We conclude that the energy injection rate associated with the precessional instability in isolation, in this setup, scales as:

$$I = \begin{cases} 0.025\Omega^{5/2}\mathrm{Po}^2 & \text{for} \quad \mathrm{Ek}^{-4/10}\mathrm{Po} \lesssim 9, \\ 0.09\Omega^{3}\mathrm{Po}^3 & \text{for} \quad \mathrm{Ek}^{-4/10}\mathrm{Po} \gtrsim 9. \end{cases} \tag{6.3}$$

6.2.3 Scaling laws as a function of the Rayleigh number

Our final aim is to constrain the impact the convective driving has in decreasing the turbulent energy injection as well as constraining the energy injection due to the turbulent effective viscosity of convection acting on the precessional flow. To this end we have plotted the results we have obtained in three large parameter sweeps as a function of the Rayleigh number with $\mathrm{Po} = [0.04, 0.10, 0.25]$. The fitting of the precessional instability is complicated by the convection acting on the tidal flow like an effective viscosity and extracting energy from the precessional flow in our simulations, such that at high values of the Rayleigh number we expect the energy injection of the effective viscosity to overshadow that of the precessional instability.

We start by examining the behaviour of the three parameter sweeps presented as a function of the Rayleigh number in Fig. 6.12. We immediately notice the clear difference between the parameter sweeps at $\mathrm{Po} = 0.04, 0.10$ and the one at $\mathrm{Po} = 0.25$. The energy injection in the former two increases as the Rayleigh number is increased, while the energy injection in the latter appears to decrease as the Rayleigh number is increased. This behaviour is expected from Fig. 6.7; in the effective viscosity regime we see that larger Rayleigh numbers increase the energy injection, whereas in the continuously turbulent regime larger Rayleigh numbers decrease the energy injection. We expect that the parameter sweep with $\mathrm{Po} = 0.04$ in blue squares portrays only the effective viscosity as the

precessional instability is expected to be unable to operate at this value of the Poincaré number, unless the convective driving is very strong, in which case the precessional instability is likely to be overshadowed by the effective viscosity regardless. Therefore we have fitted this parameter sweep using the now familiar scalings of the effective viscosity in Eq. (4.7). In particular we have used the scalings of the high and intermediate frequency regime in solid-red and solid-black respectively, continuing the colour scheme from Ch. 4. We once again observe that the energy injection agrees well with the high frequency prediction when $\mathrm{Ra} \gtrsim 3\mathrm{Ra}_c$, until the convective driving becomes too strong, such that the simulations enter the intermediate frequency regime, agreeing well with the solid-black fit instead of the solid-red fit. From the fits we have obtained the following scalings for the intermediate and high frequency regimes:

$$\nu_{\mathrm{eff}} = \begin{cases} 0.091\mathrm{Ra}^{7/4}\mathrm{Ek}^2\mathrm{Pr}^{-1/4}\kappa^{3/2}d^{-1}\omega^{-1/2} & \text{intermediate frequency,} \\ 0.380\mathrm{Ra}^{5/2}\mathrm{Ek}^2\mathrm{Pr}^{1/2}\kappa^{3}d^{-4}\omega^{-2} & \text{high frequency,} \end{cases} \tag{6.4}$$

with $\omega = \omega_{2,1,0} = \Omega$. We will assume that the fits for u_c and l_c as obtained in Ch. 4 still apply. This is a valid assumption in the absence of precession, but as seen in Fig. 6.8, the convective velocities do increase as Po is increased. Upon reproducing both the low frequency regime scalings from Eq. (4.1) for completeness, since we do not observe it here, and reproducing the frequencies at which these regimes apply, we find that the effective viscosity in these simulations is described by:

$$\nu_{\mathrm{eff}} = \begin{cases} 5u_c l_c & \frac{|\omega|}{\omega_c} \lesssim 10^{-2}, \\ 0.78u_c l_c \left(\frac{\omega_c}{\omega}\right)^{\frac{1}{2}} & \frac{|\omega|}{\omega_c} \in [10^{-2}, 5], \\ 11.5u_c l_c \left(\frac{\omega_c}{\omega}\right)^{2} & \frac{|\omega|}{\omega_c} \gtrsim 5. \end{cases} \tag{6.5}$$

It appears that the scalings are fairly consistent between the elliptical and precessional background flows, but the specific flow appears to introduce different prefactors, even when its form is already taken into account in the definition of the effective viscosity in Eq. (5.29).

Next we turn our attention to the parameter sweep with $\mathrm{Po} = 0.10$ in orange squares. It is much more complicated to determine the behaviour in this parameter sweep and as such we have not performed any fits to this set. Instead we have plotted two vertical dotted lines to indicate the boundaries between the three regimes that appear to be present in this sweep. In the leftmost third of the figure the sweep follows the effective viscosity, when the convection is unstable, following the exact same pattern as the sweep in blue squares. In the middle third the energy injection no longer follows the same behaviour as the blue squares and instead appears to be decreasing with increasing Rayleigh number. This agrees with the observations in Fig. 6.7; the convective driving has allowed the precessional instability to achieve the continuously turbulent regime. The orange squares in this middle third between the two dashed lines follow the same behaviour as that of the

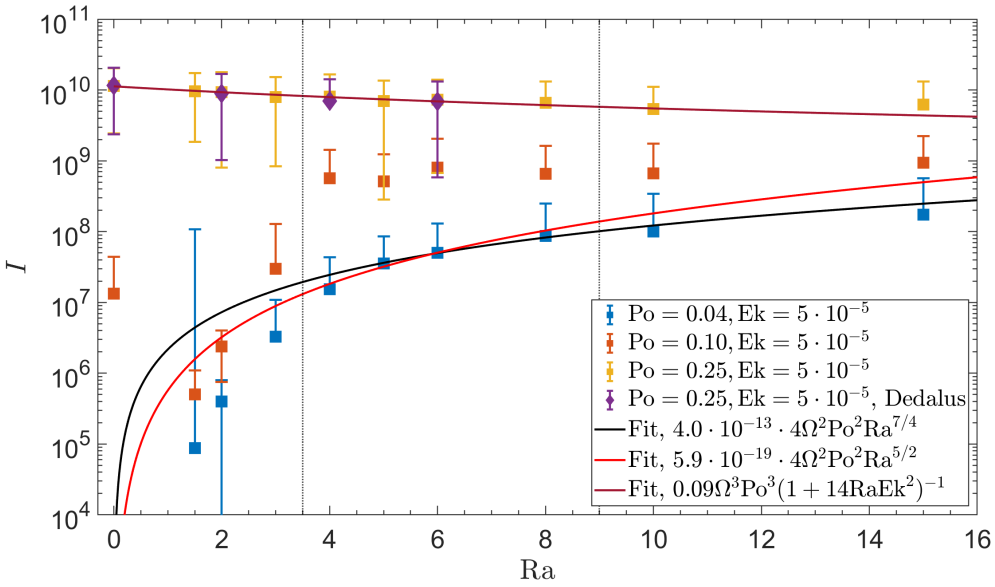

Figure 6.12: The time-averaged energy injection I as a function of the Rayleigh number at different values of the Poincaré number. The parameter sweeps executed using NEK5000 with Po $= [0.04, 0.10, 0.025]$ are plotted in blue, orange and yellow squares respectively. The DEDALUS results at Po $= 0.25$ are plotted in purple diamonds. The agreement between the results obtained using both codes is very good. The results at Po $= 0.04$ portray the effective viscosity for all simulation values plotted, and we have therefore fitted them using the prescriptions of the effective viscosity given in Eq. (4.7) in the high and intermediate frequency regimes in solid-red and solid-black respectively. We again observe good agreement for Ra $> 3\text{Ra}_c$. The parameter sweep with Po $= 0.10$ is split into three parts by the vertical dotted-black lines. In the left third, when Ra $\neq 0$ the results follow the same pattern as the blue squares, and thus portray the effective viscosity. In the middle third the results instead follow the same pattern as the yellow squares and thus portray the convectively enabled continuously turbulent regime. Finally in the right third the energy injection due to the effective viscosity is larger than that of the continuously turbulent precessional instability and thus the results portray the effective viscosity again. The results with Po $= 0.25$ show that the convection does indeed decrease the energy injection due to the continuously turbulent precessional instability, which is fitted in the solid-burgundy line.

parameter sweep with Po = 0.25 in yellow squares. Finally, the energy injection due to the convection acting as an effective viscosity on the background flow overtakes the energy injection of the continuously turbulent precessional instability in the right-most part of the figure, and the two orange squares again follow the same trend as the blue squares.

Finally, we examine the energy injection in the parameter sweep with Po = 0.25 plotted in the yellow squares, as well as purple diamonds from the same simulations executed using DEDALUS. We again find good agreement between the DEDALUS and NEK5000 results. In this continuously turbulent regime we notice a continuous downward trend until $\mathrm{Ra} = 15\mathrm{Ra_c}$, where the energy injection of the turbulence acting like an effective viscosity again overtakes the precessional turbulence. We have fitted all yellow squares bar this last datapoint, by modifying the fit obtained for the continuously turbulent regime in Eq. (6.3). The easiest way to modify this fit is according to:

$$I = 0.09\Omega^3\mathrm{Po}^3(1 + \Xi\mathrm{RaPr}^{-1}\mathrm{Ek}^2)^{-1}, \tag{6.6}$$

with Ξ the fit parameter to be determined. We have opted for $\mathrm{RaPr}^{-1}\mathrm{Ek}^2$ instead of Ra to maintain the essence of N^2/Ω^2 in this fit, which is the ratio that most often arises in the linear stability analysis. The proportionality factor $\zeta = I/\Omega^3\mathrm{Po}^3$ thus depends on the convective driving, here represented by the Rayleigh number. Upon fitting this to the data we find:

$$I = 0.09\Omega^3\mathrm{Po}^3(1 + 14\mathrm{RaPr}^{-1}\mathrm{Ek}^2)^{-1}. \tag{6.7}$$

This fit is plotted in solid-burgundy in Fig. 6.12. No clear theoretical basis for this prescription has been identified yet, but it agrees very well to the data. Moreover, the parameter sweep is narrow, and hindered by the presence of the effective viscosity in the simulation. We therefore caution the reader that this prescription may not be the correct one outside of the explored parameter regime. It, however, clearly demonstrates the qualitative result that the energy injection due to the continuously turbulent precessional instability decreases as the convective driving is increased.

6.3 Conclusions

We have simulated the precessional instability in a local Cartesian model and its interaction with rotating Rayleigh-Bénard convection in this chapter. The precessional instability in isolation in our setup displays two main types of behaviour. We observe the expected bursty behaviour in simulations with small values of the Poincaré number, consisting of alternating periods of energy injection into the most unstable linear modes and periods where oscillating large-scale flows dominate. No formation of large-scale vortices is observed in these flows. Meanwhile, at larger values of Po we observe a slightly more turbulent state with a large-scale vortex forming, which, when sufficiently powerful, allows a rapid secondary transition to a continuously turbulent state in which the flow itself is characterised

by (sheared) vortices. We expect that this transition has been seen before in the works of R. Mason and Kerswell (2002) using the same setup, who describe a strongly energetic branch C arising from 3D simulations at large enough values of Po. This phenomenon therefore appears to be important in this local model of the precessional instability.

We have furthermore identified that the introduction of convection replaces these two regimes. At small values of Po a predominantly convective regime is found, where the energy injection rate resembles that associated with the effective viscosity in Ch. 4. For sufficiently large Poincaré numbers, an abrupt secondary transition to the continuously turbulent regime of the precessional instability is again observed. However, the presence of convection lowers the Poincaré number that is required to achieve the continuously turbulent regime, in which case the secondary transition is much more gradual. On the other hand, the convection also reduces the energy injection in the continuously turbulent regime, resulting in lower energy injection with increasing Ra. It thus allows for a slightly weakened version of the continuously turbulent regime to be reached at lower values of Po.

We have examined the 2D energy of various simulations as well as the horizontal energy spectra of some of these simulations. To achieve the continuously turbulent regime of the precessional instability it appears that a certain value of K_{2D} needs to be reached. This may explain why convection allows the precessional instability to become continuously turbulent faster, as convection is likely to generate sufficiently large values of K_{2D}. However, this cannot be the full explanation, as it would imply that simulations with precession surpassing a certain convective driving strength always enter the continuously turbulent regime, which is not the case. Instead, we suspect that modification of the growth rate of the precessional instability due to the stronger convective driving also plays a role, requiring a sufficiently large growth rate to achieve the continuously turbulent regime, as well as a sufficiently large value of K_{2D}.

We fit the energy injection scalings of the precessional instability in isolation as functions of Po. We have found the energy injection rate in the laminar regime scales as the arbitrarily chosen $\Upsilon\Omega^2\mathrm{Po}^2$, with proportionality factor $\Upsilon = 0.025\Omega^{1/2}$. In the continuously turbulent regime we find that the energy injection rate scales as $\zeta\Omega^3\mathrm{Po}^3$, with $\zeta = 0.09$. Note that these scalings for the energy injection rate depend on the rotation rate Ω, as it represents the tidal frequency, and not the Ekman number, i.e. not on viscosity. The scaling law as $\Omega^3\mathrm{Po}^3$ was also identified for the precessional instability in the triply periodic box (Barker, 2016b; Pizzi et al., 2022). We find that in simulations with the precessional instability in isolation, the condition to achieve the continuously turbulent regime can be described by $\mathrm{Ek}^{-4/10}\mathrm{Po} \gtrsim 9$. This condition does depend on the Ekman number, rather than solely on Ω. Based on this condition we might expect that the continuously turbulent regime is the correct one in Hot Jupiters, with very small values of the microscopic Ekman number and not too small values of the Poincaré number. When considering the presence of convection the laminar regime is replaced by the energy injection rate of the convection acting like an effective viscosity scaling as $4\Omega^2\mathrm{Po}^2$, which

also depends on the Rayleigh number.

We find that in the continuously turbulent regime as well as in the laminar regime the vertical velocity scales linearly with Po, although with different proportionality factors, and the velocities are enhanced over the convective velocities in the absence of precession. We have also found that the Nusselt number is enhanced by the precession (this was previously observed in a different model by Wei & Tilgner, 2013), except at very small Rayleigh number. We find that the Nusselt number scales linearly with Po in the continuously turbulent regime, as long as the inherent heat transport of the convection is not too large to overshadow this scaling. A possible explanation for the enhancement of the convective velocity and heat transport in our simulations, before the continuously turbulent regime of precession is achieved, is the secondary Coriolis-like term introduced by precession. In our setup, this term together with the Coriolis-term itself results in an effective rotation axis that is no longer parallel to the direction of gravity, and thus acts to inhibit the convective motions less.

Finally, we have fitted the sustained energy injection in the laminar regime in convective simulations as a function of the Rayleigh number and retrieved good agreement with the intermediate and high frequency regimes of the effective viscosity damping the background precessional flow. The prefactors of these regimes are very close to those found previously for the background elliptical flow in Ch. 4. Furthermore, we have attempted to fit the modification of the energy injection due to the presence of convection in the continuously turbulent regime. We find that a proportionality factor that depends on the convective driving as $\zeta = 0.09(1 + 14\mathrm{RaPr}^{-1}\mathrm{Ek}^2)^{-1}$ is consistent with the data, but caution that no theoretical basis for this modification has yet been shown. However, we do conclude that the convective driving slightly reduces the energy injected by the precessional instability. We will attempt to quantify how much this modification impacts the efficiency of the precessional instability as a tidal dissipation mechanism using interior models in Ch. 7.

Chapter 7

Astrophysical applications

In this final chapter we will use the scaling laws that we have obtained in Ch. 4 and Ch. 6 for the elliptical instability, precessional instability, as well as the turbulent convection acting on their respective background flows like an effective viscosity, to derive estimates of the resulting tidal dissipation. We will apply our scaling laws to obtain simple estimates for Q' due to the elliptical instability, which contributes to $Q'_{2,2,2}$, and the precessional instability, contributing to $Q'_{2,1,0}$. Using these tidal quality factors we will obtain timescales for spin-orbit synchronisation, orbital circularisation and spin-orbit alignment. We will also obtain simple estimates for the effective viscosity in all three regimes based on estimates of the interior parameters for Jupiter.

Next, we will generate interior models of a Jupiter-like planet and a Hot Jupiter-like planet, using the MESA code, to obtain estimates whether such planets would be in the fast tides regime or not. We subsequently compute the effective viscosity as a function of radius inside these planets. Finally, we will compare the values of Q' computed for all three dissipation mechanisms as a function of tidal period so that we can determine their astrophysical significance. We will also compare these dissipation mechanisms to the tidal dissipation due to linearly-excited inertial waves. Thus, using the simulations performed in the previous chapters combined with the interior models we will determine which of these tidal dissipation mechanisms results in the lowest tidal quality factor, and can therefore be thought of as resulting in the fastest tidal evolution, in giant planets.

7.1 Simple estimates of the tidal dissipation

We start by reporting parameter estimates from the literature for Jupiter in Table 7.1. These parameters were obtained using models before (Guillot et al., 2004, hereafter GSHS04) and after (Gastine & Wicht, 2021, hereafter GW21) the Juno mission (e.g. Bolton et al., 2017). We will use these parameters later when computing our simple estimates.

Now we will attempt to obtain simple estimates for the tidal quality factors due to

Table 7.1: Table of dimensional and non-dimensional parameters in Jupiter. Parameters reproduced from Guillot et al. (2004) (GSHS04), Gastine and Wicht (2021) (GW21).

	GSHS04	GW21 $R = 0.196R_J$	GW21 $R = 0.98R_J$
u_c (m s^{-1})	0.1	$0.01 - 0.1$	1
Ω (s^{-1})	$1.75 \cdot 10^{-4}$	$1.75 \cdot 10^{-4}$	$1.75 \cdot 10^{-4}$
d (m)	$3 \cdot 10^6$	$5.5 \cdot 10^7$	$5.5 \cdot 10^7$
ν (m^2 s^{-1})	10^{-6}	$2.66 \cdot 10^{-7}$	$3.92 \cdot 10^{-7}$
κ (m^2 s^{-1})	10^{-5}	$2.7 \cdot 10^{-5}$	$1.32 \cdot 10^{-6}$
Pr	0.1	0.01	0.3
Ek	10^{-15}	10^{-18}	10^{-18}
Ra	10^{25}	10^{28}	10^{31}

the elliptical instability and the precessional instability using the scaling laws obtained from Ch. 4 and Ch. 6. We will use the scaling as $\chi\epsilon^3$ for the elliptical instability for an upper bound on the dissipation, instead of the one scaling as $\chi_2\epsilon^6$, because the latter results in lower dissipation than the former. Furthermore, we choose the upper bound value of $\chi = 0.18$ that we have obtained, such that this scaling law truly represents the upper bound on tidal dissipation due to the elliptical instability consistent with the bulk of our simulations. We will use the scaling as $\zeta \mathrm{Po}^3$ for the precessional instability, as the Ekman number in Table 7.1 indicates that the condition in Eq. (6.3) is likely satisfied if we assume that the Poincaré number is indeed $\mathcal{O}(10^{-4})$ in Hot Jupiters. We first examine the tidal dissipation due to the elliptical instability, for which we, after re-introducing dimensional units, find:

$$D = \chi M_1 R_1^2 \gamma^3 \epsilon^3. \tag{7.1}$$

We have made the rather crude choice to equate the size of our Cartesian box with the planetary radius in this expression. This choice is tentatively supported by the results in Barker (2016a), who studied the elliptical instability in isolation in global ellipsoidal simulations, and found the tidal dissipation to be consistent with Eq. (7.1), with a proportionality factor χ of $\mathcal{O}(10^{-2})$. It is unclear if it is valid to equate the planetary radius with the size of our Cartesian box upon introducing convection, or when considering the precessional instability. In the absence of global (ellipsoidal/spheroidal shell) simulations with convection, however, we choose to equate them because it provides us with a first estimate of tidal dissipation that is broadly consistent with the behaviour we observed in our simulations. To continue our derivation of the tidal quality factor, we now define the energy stored in the tidal response E_0:

$$E_0 \sim \frac{GM_1^2}{R_1}\epsilon^2, \tag{7.2}$$

with G the gravitational constant. The stored energy is the same for both the elliptical and precessional instabilities, and therefore we opt not to include subscripts. Note that this results in the introduction of ϵ for the precessional instability. We remind the reader that ϵ is a measure of the ellipticity in the context of the elliptical instability, but has broader

application as the tidal amplitude, hence why it is introduced even for the precessional instability. We apply Kepler's third law to substitute the semi-major axis in the definition of ϵ and find:

$$\epsilon = \frac{M_2}{M_1}\left(\frac{R_1}{a}\right)^3 = \left(\frac{M_2}{M_1+M_2}\right)\left(\frac{P_{\rm dyn}}{P_{\rm orb}}\right)^2, \tag{7.3}$$

with $P_{\rm orb}$ the orbital period and $P_{\rm dyn} = 2\pi\sqrt{\frac{R_1^3}{GM_1}}$ the dynamical or free-fall period of the body. We can then use the definition of $Q_{l,m,n}$ given in Eq. (1.13) to write for $Q'_{2,2,2}$ due to the elliptical instability (Barker & Lithwick, 2013):

$$Q'_{2,2,2} \sim \frac{3}{2k_2}\frac{\gamma E_0}{D} \approx \frac{1}{\chi}\frac{3}{2k_2}\left(\frac{M_1+M_2}{M_2}\right)\frac{P_{\rm orb}^2 P_{\rm tide}^2}{P_{\rm dyn}^4}, \tag{7.4}$$

with $P_{\rm tide}$ the tidal period. We substitute in some characteristic values for the orbital parameters as well as the dynamical period. For the Love number k_2 we use the value for Jupiter, $k_2 \approx 0.56$, obtained through observations of the Juno mission (e.g. Durante et al., 2020) and theoretical calculations (Lai, 2021; Dewberry & Lai, 2022). The Love number is further modified due to dynamical effects, the size of which depends on the tidal frequency (Dewberry & Lai, 2022). We choose not to take this modification into account, as the uncertainty introduced by the possibly different interior compositions of Hot Jupiters compared to Jupiter is likely to already significantly alter the Love number, although it is unclear by how much. We calculate the dynamical period for Jupiter and find ≈ 2.8 hours and choose a 1 day orbit. We will assume that the tidal period is equal to the orbital period. This is appropriate for circularisation of weakly eccentric orbits in spin-synchronised planets, whilst still providing a representative value for estimates of synchronisation tides with a circular orbit. Therefore we set the tidal period to be 1 day in this estimate, and substitute all of this into Eq. (7.4) and obtain:

$$Q'_{2,2,2} \approx 8\cdot 10^4 \frac{0.18}{\chi}\left(\frac{M_1+M_2}{M_2}\right)\left(\frac{P_{\rm orb}}{1\ {\rm d}}\right)^2\left(\frac{P_{\rm tide}}{1\ {\rm d}}\right)^2\left(\frac{2.8\ {\rm h}}{P_{\rm dyn}}\right)^4. \tag{7.5}$$

We once again remind the reader that this is an upper bound on the tidal dissipation, and thus lower bound on the value of $Q'_{2,2,2}$. To put the obtained value of the tidal quality factor into context we can compute tidal spin-orbit synchronisation and tidal circularisation timescales using Eq. (1.17) and Eq. (1.18) respectively. These equations depend on the other orbital parameters, such that the Eqs. (1.16)-(1.19) should ideally be solved in tandem throughout the evolution of the system. To keep our estimates simple, we will instead treat all parameters on the right-hand side of these equations as fixed. We then define a tidal timescale as an e-folding timescale, i.e. the time in which the quantity under consideration decreases (or increases, depending on the sign of $Q'_{2,2,2}$, which depends on the sign of the tidal frequency, and the sign in the relevant equation) by a factor of e. For

the synchronisation timescale, τ_{Ω_s}, we find:

$$\tau_{\Omega_s} = \frac{4}{9}\frac{Q'_{2,2,2}}{2\pi}\frac{M_1}{M_2}\left(\frac{M_1+M_2}{M_1}\right)^{5/3}\frac{L_s}{L_o}\frac{P_{\rm orb}^{13/3}}{P_{\rm dyn}^{10/3}}, \tag{7.6}$$

with

$$\frac{L_s}{L_o} = \frac{r_g^2 M_1^{2/3}(M_1+M_2)^{1/3}}{M_2}\frac{P_{\rm dyn}^{4/3}}{P_{\rm orb}^{1/3}P_{\rm rot}}(1-e^2)^{-1/2}; \tag{7.7}$$

the latter expression represents the ratio of the spin angular momentum L_s to the orbital angular momentum L_o, with r_g the dimensionless radius of gyration, e the eccentricity and $P_{\rm rot}$ the rotation period of the primary. Combining these expressions we find:

$$\tau_{\Omega_s} = \frac{4}{9}\frac{Q'_{2,2,2}r_g^2}{2\pi}\left(\frac{M_1+M_2}{M_2}\right)^2\frac{P_{\rm orb}^4}{P_{\rm rot}P_{\rm dyn}^2}(1-e^2)^{-1/2}. \tag{7.8}$$

One could express Eq. (7.8) in terms of just orbital parameters and the parameters of the two bodies by substituting in Eq. (7.5). We are however interested in showing the effect of different values of the tidal quality factor on the obtained timescales, as it is the tidal quality factor that is often quoted in observational (and theoretical) studies. We will therefore substitute in the values of the orbital parameters used to compute Eq. (7.5) and set $r_g^2 \approx 0.26$, which is the value for Jupiter. Moreover, we set the eccentricity to zero, set $M_1 = 0.001M_2$ (with M_1 the Hot Jupiter's mass, and the ratio of the masses approximately equalling the mass ratio of Jupiter and the Sun) and a tidal quality factor of $Q'_{2,2,2} = 10^5$, to find for the tidal spin-orbit synchronisation timescale:

$$\tau_{\Omega_s} \approx 9\cdot 10^2 \text{ yrs}\left(\frac{Q'_{2,2,2}}{10^5}\right)\left(\frac{P_{\rm orb}}{1\text{ d}}\right)^4\left(\frac{10\text{ h}}{P_{\rm rot}}\right)\left(\frac{2.8\text{ h}}{P_{\rm dyn}}\right)^2. \tag{7.9}$$

We thus find extremely rapid – compared to, for example, the main sequence lifetime of Sun-like stars and their planets – synchronisation for this value of $Q'_{2,2,2}$ and small orbital periods. We note that, in order to extrapolate to different orbital periods, when considering the elliptical instability as the tidal dissipation mechanism, the strong dependence on orbital and tidal period of $Q'_{2,2,2}$ should still be taken into account, such that the timescale depends more strongly on the orbital and tidal period than Eq. (7.9) would suggest. We will provide estimates of orbital periods at which the spin-orbit synchronisation timescale is 1 Gyr based on the results obtained from MESA models in Table 7.2.

We can also define a circularisation timescale τ_e, for which we can obtain an expression starting from Eq. (1.18) using the same methods as before:

$$\tau_e = \frac{8}{9}\frac{Q'_{2,2,2}}{2\pi}\frac{M_1}{M_2}\left(\frac{M_1+M_2}{M_1}\right)^{5/3}\frac{P_{\rm orb}^{13/3}}{P_{\rm dyn}^{10/3}}. \tag{7.10}$$

Again, upon substituting characteristic values we find:

$$\tau_e \approx 5 \cdot 10^6 \text{ yrs} \left(\frac{Q'_{2,2,2}}{10^5}\right)\left(\frac{P_{\text{orb}}}{1 \text{ d}}\right)^{13/3}\left(\frac{2.8 \text{ h}}{P_{\text{dyn}}}\right)^{10/3}. \tag{7.11}$$

The circularisation timescale is much longer than that of spin-orbit synchronisation, but circularisation can still be achieved while the host star is on the main sequence for these short orbital periods. We will also provide estimates of orbital periods at which the circularisation timescale is 1 Gyr in Table 7.2.

We will now perform a similar computation to obtain the tidal quality factor due to the precessional instability. To this end we exchange γ for Ω, ϵ for Po and χ for ζ in the definition of D in Eq. (7.1), and find for $Q'_{2,1,0}$:

$$Q'_{2,1,0} \sim \frac{3}{2k_2}\frac{\Omega E_0}{D} \approx \frac{1}{\zeta \text{Po}^3}\frac{3}{2k_2}\left(\frac{M_2}{M_1+M_2}\right)^2 \frac{P_{\text{dyn}}^2 P_{\text{rot}}^2}{P_{\text{orb}}^4}. \tag{7.12}$$

The rotation period P_{rot} is equal to the tidal period for this component of the tide. We can find the Poincaré number using $\text{Po} = P_{\text{rot}}/P_{\text{p}}$, where P_{p} is the precessional period given by (e.g. Kopal, 1959; Eggleton & Kiseleva-Eggleton, 2001; Barker, 2016b):

$$P_{\text{p}} = \frac{2r_g^2}{k_2}\frac{P_{\text{rot}} P_{\text{orb}}^2}{P_{\text{dyn}}^2}\left(\frac{M_1+M_2}{M_2}\right)\frac{(1-e^2)^{3/2}}{\cos i}, \tag{7.13}$$

with i the inclination or obliquity of the body's spin axis to its orbital rotation axis. We can use this expression to obtain an estimate for the precessional period, and thus Poincaré number, in Hot Jupiters. We again substitute characteristic values for Jupiter: $r_g^2 \approx 0.26$, the same Love number and dynamical period and an orbital and rotational period which are both 1 day, to mimic spin-orbit synchronisation already having occurred. We find for the precessional period:

$$P_{\text{p}} \approx 0.2 \text{ yrs} \left(\frac{P_{\text{rot}}}{1 \text{ d}}\right)\left(\frac{P_{\text{orb}}}{1 \text{ d}}\right)^2\left(\frac{2.8 \text{ h}}{P_{\text{dyn}}}\right)^2\left(\frac{M_1+M_2}{M_2}\right)\frac{(1-e^2)^{3/2}}{\cos i}. \tag{7.14}$$

We have chosen not to evaluate values of the eccentricity and inclination, but instead include them in the expression for completeness. The precessional period is several orders of magnitude smaller than Earth's precessional period, which suggests the precessional instability could be relevant in misaligned Hot Jupiters. We can constrain the importance of the precessional instability further by examining the Poincaré number:

$$\text{Po} \approx 0.01\left(\frac{1 \text{ d}}{P_{\text{orb}}}\right)^2\left(\frac{P_{\text{dyn}}}{2.8 \text{ h}}\right)^2\left(\frac{M_2}{M_1+M_2}\right)\frac{\cos i}{(1-e^2)^{3/2}}, \tag{7.15}$$

which is much larger than Earth's Poincaré number, and of the same order of magnitude as the tidal amplitude. For these values of the Poincaré number and the Ekman numbers in Table 7.1 we indeed find that the continuously turbulent regime of the precessional

instability is likely to be the appropriate one. Next we rewrite Eq. (7.12) by substituting $\mathrm{Po} = P_{\mathrm{rot}}/P_{\mathrm{p}}$, using Eq. (7.13), to find:

$$Q'_{2,1,0} \approx \frac{1}{\zeta}\frac{3}{2k_2}\left(\frac{2{r_g}^2}{k_2}\right)^3\left(\frac{M_1+M_2}{M_2}\right)\frac{P_{\mathrm{rot}}^2\,P_{\mathrm{orb}}^2}{P_{\mathrm{dyn}}^4}\left(\frac{(1-e^2)^{3/2}}{\cos i}\right)^3. \tag{7.16}$$

Using any of the three parameter estimates in Table 7.1 we find that the convective modification of the precessional dissipation according to Eq. (6.7) is negligible. We substitute the same characteristic values for Jupiter as before. The estimate for $Q'_{2,1,0}$ using these parameters is:

$$Q'_{2,1,0} \approx 1\cdot 10^5\,\frac{0.09}{\zeta}\left(\frac{M_1+M_2}{M_2}\right)\left(\frac{P_{\mathrm{rot}}}{1\ \mathrm{d}}\right)^2\left(\frac{P_{\mathrm{orb}}}{1\ \mathrm{d}}\right)^2\left(\frac{2.8\ \mathrm{h}}{P_{\mathrm{dyn}}}\right)^4\left(\frac{(1-e^2)^{3/2}}{\cos i}\right)^3. \tag{7.17}$$

The tidal quality factor of the precessional instability is slightly larger than that of the elliptical instability for similar parameters. The primary difference between these two tidal quality factors therefore resides in their application. According to Eqs. (1.16)-(1.19), the tidal dissipation due to the precessional instability solely contributes to the evolution of the inclination, for which so we will define a spin-orbit alignment timescale τ_i. We can use Eq. (1.19) to find an expression for this timescale:

$$\tau_i = \frac{8}{9}\frac{Q'_{2,1,0}}{2\pi}\frac{M_1}{M_2}\left(\frac{M_1+M_2}{M_1}\right)^{5/3}\left(1+\frac{L_o}{L_s}\right)^{-1}\frac{P_{\mathrm{orb}}^{13/3}}{P_{\mathrm{dyn}}^{10/3}}. \tag{7.18}$$

The orbital angular momentum of the planet is much higher than that of its spin, such that the ratio $L_o/L_s \gg 1$. We can therefore represent this timescale as approximately:

$$\tau_i \approx \frac{8}{9}\frac{Q'_{2,1,0}r_g^2}{2\pi}\left(\frac{M_1+M_2}{M_2}\right)^2\frac{P_{\mathrm{orb}}^4}{P_{\mathrm{rot}}P_{\mathrm{dyn}}^2}(1-e^2)^{-1/2}. \tag{7.19}$$

We substitute in characteristic values for Jupiter, the Sun, orbital parameters as we have discussed, set the eccentricity to zero and $Q'_{2,1,0} = 10^5$ to obtain:

$$\tau_i \approx 2\cdot 10^3\ \mathrm{yrs}\left(\frac{Q'_{2,1,0}}{10^5}\right)\left(\frac{P_{\mathrm{orb}}}{1\ \mathrm{d}}\right)^4\left(\frac{10\ \mathrm{h}}{P_{\mathrm{rot}}}\right)\left(\frac{2.8\ \mathrm{h}}{P_{\mathrm{dyn}}}\right)^2. \tag{7.20}$$

The timescales for spin-orbit alignment of a Hot Jupiter thus appear very short, like those for spin-orbit synchronisation. In reality, we expect them to be longer, because we have not taken into account the starting misalignment i in the expression for $Q'_{2,1,0}$; planets with $i \approx 90°$ will result in much larger values of $Q'_{2,1,0}$ and thus much longer alignment timescales. Estimates of orbital periods at which the spin-orbit alignment timescale is 1 Gyr can also be found in Table 7.2.

Both the elliptical and the precessional instabilities are non-linear tidal dissipation mechanisms, such that their tidal dissipation strongly depends on the tidal amplitude, and therefore the resultant values of Q' depend on the tidal amplitude. Both Q' have a strong dependence on the orbital period $P_{\rm orb}$, and therefore increase rapidly with increasing orbital period, increasing the associated tidal timescales. These timescales also increase with increasing orbital period, further compounding the orbital period dependencies. Our estimates therefore indicate that these mechanisms are only likely to be important in short-period planets experiencing strong tidal effects.

Next, we can make estimates for the effective viscosity of convection acting on tidal (or precessional) flows in a Jupiter-like body using the parameters in Table 7.1. First we calculate the ratio of tidal to convective frequencies (ω/ω_c). This ratio is found to be, in the case of the background elliptical flow, upon again setting $P_{\rm tide} = P_{\rm orb}$:

$$\omega/\omega_c = \begin{cases} 9.4 \cdot 10^1 \left(\frac{P_{\rm orb}}{1\ \rm d}\right)^{-1} & \text{GSHS04,} \\ 3.7 \cdot 10^2 \left(\frac{P_{\rm orb}}{1\ \rm d}\right)^{-1} & \text{GW21 at } R = 0.196 R_J, \\ 2.4 \cdot 10^2 \left(\frac{P_{\rm orb}}{1\ \rm d}\right)^{-1} & \text{GW21 at } R = 0.98 R_J. \end{cases} \tag{7.21}$$

For the precessional instability we also set $P_{\rm tide} = P_{\rm rot} = P_{\rm orb}$, again choosing a situation in which the spin and orbit are synchronised. As a consequence, the estimates in Eq. (7.21) are also obtained when considering the precessional background flow. Therefore, we conclude that we are firmly in the high-frequency tidal regime ($\omega/\omega_c \gg 1$) for the orbital periods associated with Hot Jupiters, which is the regime explored in most of our simulations. This is also likely to be the case in Jupiter due to tidal forcing from its moons (e.g. Goldreich & Nicholson, 1977).

The effective viscosity can also be calculated using the parameters from Table 7.1. To evaluate the different regimes, we assume the transitions from the low to intermediate frequency regimes obtained by Duguid et al. (2020). Using data from the GSHS04 column of Table 7.1 for the purposes of illustration, we find in the case of the elliptical flow:

$$\nu_{\rm eff} = \begin{cases} 8.8 \cdot 10^2 \quad \text{m}^2\ \text{s}^{-1}, & \frac{|\omega|}{\omega_c} < 10^{-2}, \\ 3.6 \left(\frac{P_{\rm orb}}{1\ \rm d}\right)^{1/2} \quad \text{m}^2\ \text{s}^{-1}, & \frac{|\omega|}{\omega_c} \in [10^{-2}, 5], \\ 2.5 \cdot 10^{-2} \left(\frac{P_{\rm orb}}{1\ \rm d}\right)^{2} \quad \text{m}^2\ \text{s}^{-1}, & \frac{|\omega|}{\omega_c} > 5. \end{cases} \tag{7.22}$$

We have included the low frequency regime for completeness even though this has not

been clearly probed with our simulations. Likewise, for the precessional flow we find:

$$\nu_{\text{eff}} = \begin{cases} 8.8 \cdot 10^{2} \quad \text{m}^2\ \text{s}^{-1}, & \frac{|\omega|}{\omega_c} < 10^{-2}, \\ 1.1 \cdot 10^{1} \left(\frac{P_{\text{orb}}}{1\ \text{d}} \right)^{1/2} \quad \text{m}^2\ \text{s}^{-1}, & \frac{|\omega|}{\omega_c} \in [10^{-2}, 5], \\ 8.8 \cdot 10^{-2} \left(\frac{P_{\text{orb}}}{1\ \text{d}} \right)^{2} \quad \text{m}^2\ \text{s}^{-1}, & \frac{|\omega|}{\omega_c} > 5. \end{cases} \tag{7.23}$$

The effective viscosities for the precessional flow are close to those in Eq. (7.22) for the elliptical flow, such that we conclude that the difference introduced by the background flows is indeed small. We therefore opt to use the prefactors of the effective viscosities found in Duguid et al. (2020), which we have reproduced in Eq. (4.1), instead of the ones we have found in Ch. 4 and Ch. 6, for both background flows as their prefactors represent a good middle ground between our results. These are therefore also the prefactors we will use for the computation of both $Q'_{2,2,2}$ and $Q'_{2,1,0}$ due to the effective viscosity.

7.2 Detailed computations of the tidal dissipation

To provide a more detailed estimate of the tidal dissipation due to the elliptical and precessional instabilities as well as the effective viscosity in a (Hot) Jupiter-like planet we require models for its internal structure, i.e. profiles of pressure and density (and other quantities) as a function of radius. To do so, we use a modified version of the test suite case *make_planets* of the Modules for Experiments in Stellar Astrophysics (MESA) code (Paxton et al., 2011, 2013, 2015, 2018; Paxton et al., 2019; Jermyn et al., 2023) with the MESASDK (Townsend, 2022) to generate 1D interior profiles. Such 1D interior models essentially assume a spherically symmetric object, in which the quantities of interest only vary as a function of spherical radius. These 1D interior profiles have a long history of being used to model stars and stellar evolution, but can also be applied to giant planets, because it is thought that much of giant planets' interior physics should be relatively similar to that of stars.

7.2.1 Planetary interior models using MESA

The MESA code has been previously used to generate a range of planetary models (e.g. Müller et al., 2020; Müller & Helled, 2023). However, some caveats reside in the applicability of this code to planets: since it is designed to model stars it uses equations of state (EOS) based on H and He without heavy elements – unless the EOS are modified (Müller et al., 2020) – necessary to generate for example a dilute core which is expected based on Juno's gravity field measurements of Jupiter (Stevenson, 2020; Helled et al., 2022). Furthermore, it treats the core itself as rigid and omits the possibility of stable layers produced by helium rain as detailed in Sec. 1.3. These may be important for tidal dissipation (e.g. Pontin et al., 2023; Dhouib et al., 2024; Pontin et al., 2024) but are outside the scope of our study. The MESA code by default treats the convection using mixing-length theory (MLT), for which we use the Cox prescription (Cox & Giuli, 1968), instead of rotating

mixing-length theory (RMLT). We have chosen to maintain the mixing-length parameter at the standard value of two, and intend to convert the obtained MLT values of these models to RMLT values.

Our initial Jupiter model has a radius of $2R_J$ and a mass of $1M_J$, of which 10 Earth-masses are located in an inert core with density 10 g cm^{-3}. We have evolved the model for 4.5 Gyr to mimic the age of Jupiter and we use a constant surface irradiation of $5 \cdot 10^4$ erg cm^{-2} s^{-1}, similar to what Jupiter receives from the Sun, which is deposited at a column depth of 300 g cm^{-2} (about 0.7 bar). We also create a Hot Jupiter model with the same parameters except that we increase the surface heating to represent the irradiation of a one-day planet around a Sun-like star of 10^9 erg cm^{-2} s^{-1}. Furthermore, we incorporate additional interior heating with uniform rate 0.05 erg cm^{-3} s^{-1} throughout the fluid envelope, which can be thought to represent the impact of tidal heating or Ohmic dissipation (or other mechanisms) that could possibly inflate a number of Hot Jupiters. In this way, whilst keeping all other parameters equal, we can determine the effects of the increased radius (and stronger convection) of a puffy Hot Jupiter on the effective viscosity and tidal dissipation rates. A summary of changes to the default inlists used to generate these models is provided in Appendix B.

The convective velocities and lengthscales (mixing-lengths) obtained using MESA are calculated using non-rotating MLT. Although the rotation rate – and thus the introduction of RMLT – is expected to affect convective lengthscales and velocities, the effect on the heat flux is likely to be negligible (Stevenson, 1979; Ireland & Browning, 2018). Therefore, we assume that the heat flux is independent of rotation, and thus the same in both MLT and RMLT. The temperature difference and the resulting buoyancy frequency, on the other hand, are both expected to change under the influence of rotation, in order to carry the same flux. Therefore we opt to use the flux-based scalings of MLT and RMLT instead of the temperature-based scalings used in Ch. 4. In these flux-based scalings the conversion from MLT to RMLT is defined differently to the temperature-based scalings; in the temperature-based scalings the corrections introduced for both u_c and l_c involve Ro_c linearly, while in the flux-based scalings the corrections are respectively:

$$u_c = \tilde{\mathrm{Ro}}_c^{1/5} \tilde{u}_c, \quad \text{and} \quad l_c = \tilde{\mathrm{Ro}}_c^{3/5} \tilde{l}_c, \tag{7.24}$$

where the quantities with a tilde are those calculated using non-rotating MLT. We have also denoted the Rossby number in the above equations with a tilde ($\tilde{\mathrm{Ro}}_c = \tilde{u}_c/(2\Omega\tilde{l}_c)$) because flux-based scalings imply Rossby numbers calculated using MLT and RMLT are different, unlike for the temperature-based scalings where they are the same. In the low frequency regime the effective viscosity must therefore be scaled by

$$\nu_{\mathrm{eff}} \sim u_c l_c \sim \tilde{u}_c \tilde{l}_c \tilde{\mathrm{Ro}}_c^{4/5}. \tag{7.25}$$

This correction factor of $\tilde{\mathrm{Ro}}_c^{4/5}$ was also employed by Mathis et al. (2016). In the high

tidal frequency regime the effective viscosity is instead scaled by

$$\nu_{\text{eff}} \sim u_c l_c \left(\frac{u_c}{l_c}\right)^2 \sim \tilde{u}_c \tilde{l}_c \tilde{\text{Ro}}_c^{4/5} \left(\frac{\tilde{u}_c}{\tilde{l}_c}\right)^2 \tilde{\text{Ro}}_c^{-4/5} \sim \tilde{u}_c \tilde{l}_c \left(\frac{\tilde{u}_c}{\tilde{l}_c}\right)^2. \tag{7.26}$$

Combining these, we find according to RMLT:

$$\nu_{\text{eff}} \propto \begin{cases} 5\tilde{u}_c \tilde{l}_c \tilde{\text{Ro}}_c^{4/5} & \frac{|\omega|}{\omega_c} \lesssim 10^{-2}, \\ 0.5\tilde{u}_c \tilde{l}_c \tilde{\text{Ro}}_c^{3/5} \left(\frac{\tilde{u}_c/\tilde{l}_c}{\omega}\right)^{\frac{1}{2}} & \frac{|\omega|}{\omega_c} \in [10^{-2}, 5], \\ \frac{25}{\sqrt{20}} \tilde{u}_c \tilde{l}_c \left(\frac{\tilde{u}_c/\tilde{l}_c}{\omega}\right)^2 & \frac{|\omega|}{\omega_c} \gtrsim 5. \end{cases} \tag{7.27}$$

Hence, while the effective viscosity in the low tidal frequency regime is strongly affected by rotation, it is entirely unaffected by rotation in the high tidal frequency regime according to RMLT (assuming a fixed flux independent of rotation). This follows when considering the scaling laws in Eq. (4.7) in terms of flux-based RMLT:

$$\nu_{\text{eff}} \propto \begin{cases} F^{3/5}\Omega^{-4/5} d^{4/5} & \text{low frequency}, \\ F^{7/10} d^{3/5} \Omega^{-3/5} \omega^{-1/2} & \text{intermediate frequency}, \\ F\omega^{-2} & \text{high frequency}. \end{cases} \tag{7.28}$$

The equivalent relations written using flux-based MLT would be:

$$\tilde{\nu}_{\text{eff}} \propto \begin{cases} F^{1/3} d^{4/3} & \text{low frequency}, \\ F^{1/2} d \omega^{-1/2} & \text{intermediate frequency}, \\ F\omega^{-2} & \text{high frequency}. \end{cases} \tag{7.29}$$

The scaling laws in the high tidal frequency regime with and without rapid rotation (i.e. according to MLT or RMLT) are therefore identical when written using flux-based scalings. However, the regime transitions may not be the same in both cases because the flux-based scalings for ω_c differ between MLT and RMLT. Convective frequencies are typically smaller in MLT, and as such the high tidal frequency regime is generally entered for lower tidal frequencies than in RMLT. This difference is however unlikely to be important for our purposes.

We now present our results for Rossby numbers and the corresponding effective viscosities – in both the fast tide and slow tide regimes, using both MLT and RMLT – as a function of radius in our two planetary models. For these illustrative calculations we set $P_{\text{orb}} = 1$ day and $P_{\text{rot}} = 10$ hrs for the Jupiter model, mimicking a planet similar to Jupiter but orbiting its star with a period of 1 day. For the Hot Jupiter model we instead set $P_{\text{orb}} = P_{\text{rot}} = 1$ day, representing spin-orbit synchronisation, and a tidal period of $P_{\text{tide}} = 1$ day. Note that the Jupiter model is only depicting the ratio of ω_c/ω when considering the background elliptical flow; when considering the background precessional

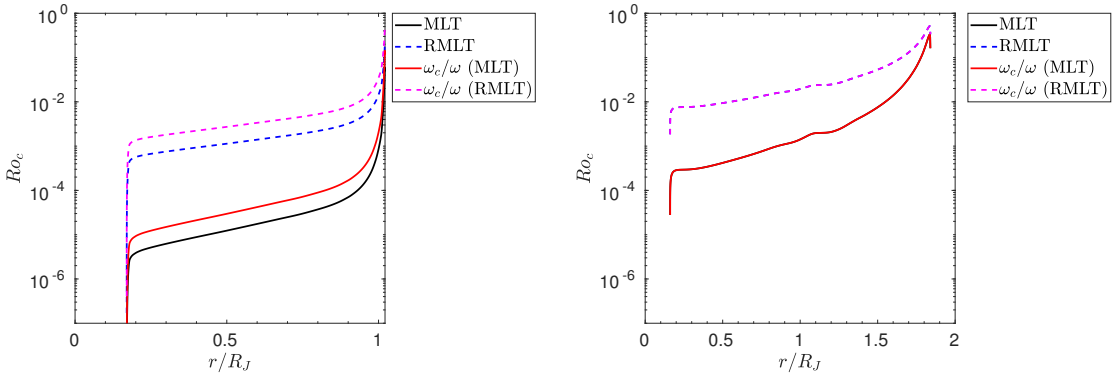

Figure 7.1: Flux-based MLT and RMLT Rossby numbers as a function of radius for a Jupiter-like and Hot Jupiter-like planet. Left: The Jupiter-like planet with $P_{\rm rot} = 10$ hrs, $P_{\rm orb} = P_{\rm tide} = 1$ day after evolving the model for 4.5 Gyr. This is much smaller than one in the whole of the interior according to both prescriptions, i.e. the interior is strongly rotationally constrained. The ratio of convective to tidal frequencies ("tidal Rossby number"), is also much smaller than one for these parameters, indicating that the planet is in the fast tides regime. Right: Same but for the inflated Hot Jupiter with $P_{\rm rot} = P_{\rm orb} = P_{\rm tide} = 1$ day. Convection is stronger in this model but the same regimes (rapid rotation and fast tides) hold as in the left-hand panel. The ratio of ω_c/ω is equal to the convective Rossby number here, hence the lines overlap.

flow, the tidal period is 10 hrs instead of 1 day. The correct ratio of frequencies for this background flow is however easily computed by multiplying the result obtained using the Jupiter model by $P_{\rm rot}/P_{\rm tide}$, which only serves to move the results further into the high tidal frequency regime, and thus leaves the results qualitatively unmodified.

In Fig. 7.1 the Rossby numbers are plotted in the Jupiter model in the panel on the left and the Hot Jupiter model in the panel on the right. The MLT Rossby number as calculated from the data is plotted in solid-black; the one calculated from RMLT is plotted in dashed-blue. The MLT Rossby numbers are clearly smaller, but even in RMLT they are much smaller than one, indicating that the convection is strongly rotationally-constrained. Note that the lower densities and stronger convection in the inflated Hot Jupiter model produce larger Rossby numbers, but they are still much smaller than one. This justifies the use of RMLT (over MLT) in giant planets.

The ratio of convective to tidal frequencies (ω_c/ω) is also plotted as a function of radius in Fig. 7.1. The MLT prediction for this "tidal Rossby number" is plotted in solid-red and the RMLT prediction is plotted in dashed-magenta. Due to our choice of rotation rate and tidal frequency in the Hot Jupiter model this tidal Rossby number is equal to the Rossby number, i.e. $\omega_c/\omega = {\rm Ro}_c$. For both models ${\rm Ro}_c \ll 1$, such that RMLT is the appropriate description for convection, and hence for the convective frequency. This figure indicates that the fast tides regime is relevant inside both models (except for perhaps the final percent or so of the radius where we approach the surface stable layer).

The effective viscosity as a function of radius is shown in Fig. 7.2 in both planetary models. Note that this is again a crude application, because we have equated the vertical

box size in our Boussinesq simulations with the mixing-length and assume that this process acts like an isotropic kinematic viscosity in damping the tidal flow. In the left-hand panel, we show the effective viscosity in the Jupiter model for our chosen rotational and tidal periods. Again these are computed with $P_{\rm rot} = 10$ hrs, $P_{\rm orb} = P_{\rm tide} = 1$ day, i.e. the orbital and spin frequencies associated with the background elliptical flow. The effective viscosities acting on the precessional flow, in the fast tides regime, would be further reduced due to the increased tidal frequency of $P_{\rm rot} = P_{\rm tide} = 10$ hrs. Regardless of the choice of background flow, the effective viscosities obtained this way are much larger than the microscopic viscosity (solid-black) for all predictions. To compute the kinematic viscosity in Jupiter requires sophisticated calculations outside the scope of our models (and not calculated within MESA), so we use the typical value obtained by French et al. (2012), of $\nu = 3 \cdot 10^{-7}$ m^2 s^{-1}, for reference in both panels of Fig. 7.2.

There are large differences between the various predictions for $\nu_{\rm eff}$ in the left-hand panel of Fig. 7.2. The MLT prediction in the slow tides regime in solid-blue predicts $\nu_{\rm eff} \approx 10^6$ m^2 s^{-1}, while the RMLT prediction in the same slow tides regime in dashed-cyan only attains values of $\approx 10^2$ m^2 s^{-1}. The MLT prediction for this regime decreases slightly from the interior to the surface, because the convective lengthscale decreases faster than the convective velocity increases from the core to the surface. On the other hand, the RMLT prediction increases towards the surface, because the Rossby number rapidly increases there. The fast tides regime prediction according to both RMLT and MLT (strictly obtained using all three regimes in Eq. (7.27) and the uncorrected version respectively, but the fast tides one is most relevant) are plotted in solid-green and dotted-red respectively. The two lines overlap because the effective viscosity is independent of rotation according to both theories, as we have demonstrated in Eq. (7.28) and Eq. (7.29). The effective viscosity in the fast tides regime is however several orders of magnitude smaller still than both predictions in the slow tides regime, with a value of only $\approx 10^{-2}$ m^2 s^{-1} except for close to the surface. This value is much larger than the microscopic viscosity, but is probably negligibly small for damping tidal flows.

The right-hand panel of Fig. 7.2 shows the effective viscosity as a function of radius for our inflated Hot Jupiter model. We observe that all values for $\nu_{\rm eff}$ have shifted upwards compared to our Jupiter model. However, even in this model we expect to be in the fast tides regime throughout (almost) the entire planet, which would predict $\nu_{\rm eff} \approx 10^2$ m^2 s^{-1}. Thus the increased irradiation and internal heating introduced here results in significantly larger effective viscosities, and will therefore result in smaller values of Q'.

7.2.2 Tidal dissipation rates in Jupiter and Hot Jupiters

Now that we have obtained radial profiles of $\nu_{\rm eff}$ we can use these to compute the resulting damping of the equilibrium tide and the associated tidal quality factors Q' in our planetary models. To this end we follow the approach described in Barker (2020), which follows many other works (e.g. Ogilvie & Lin, 2004; Ogilvie, 2013, 2014). First we must compute the perturbed gravitational potential of the planet Φ' after the tidal potential has been imposed

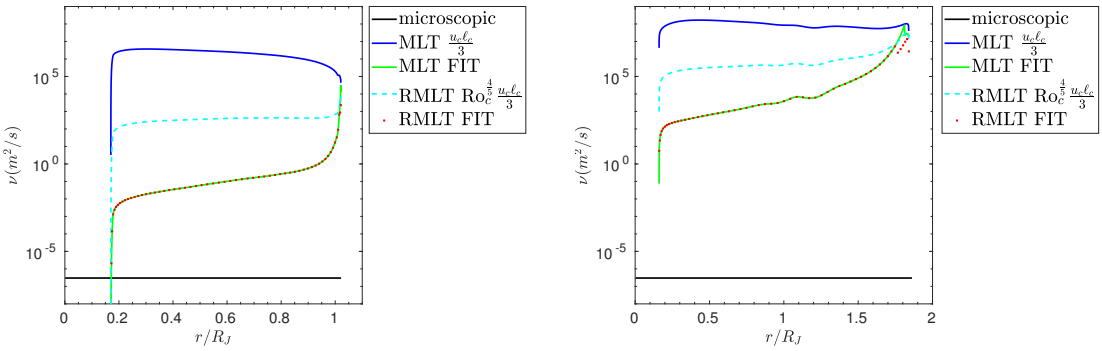

Figure 7.2: Effective viscosity as a function of radius for the Jupiter-like planet and Hot Jupiter-like planet. We show the microscopic viscosity $3 \cdot 10^{-7}$ m^2 s^{-1} reproduced from French et al. (2012) (solid-black) for reference, the MLT prediction in the low frequency regime (solid-blue), the MLT prediction in the fast tides regime (solid-green), the RMLT prediction in the slow tides regime (dashed-cyan) and the RMLT prediction in the fast tides regime (dotted-red). The fast tides predictions overlap regardless of regime whereas applying RMLT in the slow tides regime drastically reduces the effective viscosity. Left: The Jupiter-like planet with $P_{\rm rot} = 10$ hrs, $P_{\rm orb} = P_{\rm tide} = 1$ day after evolving the model for 4.5 Gyr. Right: Same but for the inflated Hot Jupiter with $P_{\rm rot} = P_{\rm orb} = P_{\rm tide} = 1$ day. The Hot Jupiter model has more efficient convection and larger effective viscosity in all regimes.

by solving Eq. (1.30) using a Chebyshev collocation method based on interpolating the obtained values of the pressure and density in the interior models. Once the perturbed gravitational potential has been found this can be used to find the tidal displacement $\boldsymbol{\xi}$. This work applies to the convective regions of the planet, so we will use the non-wavelike equilibrium tide $\boldsymbol{\xi}_{\rm nw}$ in Eq. (1.43). We define this tidal displacement for a single tidal component as:

$$\boldsymbol{\xi}_{\rm nw} = \left(\xi_r(r)\hat{\boldsymbol{r}} + r\xi_h(r)\nabla\right) Y_l^m(\theta,\phi)\mathrm{e}^{-\mathrm{i}\omega_{l,m,n}t}, \tag{7.30}$$

with ξ_r and ξ_h the radial and horizontal tidal displacement of the non-wavelike tide and $\hat{\boldsymbol{r}}$ is the radial unit vector.

The dissipation of this tidal flow is computed assuming an effective viscosity that acts like an isotropic microscopic kinematic viscosity but with a local value $\nu_{\rm eff}(r)$ to damp the equilibrium tide. To find the total dissipation in the convective regions of the planet originating from this tidal dissipation mechanism we must thus integrate over the entire radial extent of the convection zones of the body:

$$D_\nu = \frac{1}{2}\omega^2 \int r^2 \rho(r)\nu_{\rm eff}(r) D_l(r)\,\mathrm{d}r, \tag{7.31}$$

with

$$D_l(r) = 3\left|\frac{\mathrm{d}\xi_r}{\mathrm{d}r} - \frac{\Delta_l}{3}\right|^2 + l(l+1)\left|\frac{\xi_r}{r} + r\frac{\mathrm{d}}{\mathrm{d}r}\left(\frac{\xi_h}{r}\right)\right|^2 + (l-1)l(l+1)(l+2)\left|\frac{\xi_h}{r}\right|^2, \tag{7.32}$$

which represents the contribution to the dissipation from a single spherical harmonic

component with a given l, m, with

$$\Delta_l = \frac{1}{r^2}\frac{\mathrm{d}}{\mathrm{d}r}(r^2\xi_r) - l(l+1)\frac{\xi_h}{r}. \tag{7.33}$$

This procedure was followed previously in Sec. 2.1 of Barker (2020), which follows e.g. Ogilvie and Lin (2004). Note that only the degree l matters for this calculation, such that, because we have chosen to use the same expressions for the effective viscosity regardless of background flow, the tidal quality factor associated with the effective viscosity is the same regardless of the value of the order m. We therefore only compute this quantity using an imposed tidal potential given by $\Psi_{2,2,2}$ and crudely apply this to find both $Q'_{2,2,2}$ and $Q'_{2,1,0}$. The only modification compared to Barker (2020) here is that we account for the rotational dependence of ν_{eff} and ω_c as described above, otherwise we employ their Eq. 27 to obtain $\nu_{\mathrm{eff}}(r)$ in the various different frequency regimes. The resulting tidal quality factor is (Ogilvie, 2014):

$$Q'_{l,m,n} = \frac{3(2l+1)R_1^{2l+1}}{16\pi G}\frac{|\omega||A|^2}{D_\nu}, \tag{7.34}$$

where $A \propto \epsilon$ is the amplitude of the tidal perturbation (so that the ratio $D_\nu/|A|^2$ and hence $Q'_{l,m,n}$ is independent of tidal amplitude).

We have already determined expressions for $Q'_{2,2,2}$ and $Q'_{2,1,0}$ from the elliptical and precessional instability respectively in Eq. (7.4) and Eq. (7.16). Once again, we wish to stress that these expressions are crude, in the sense that we have extrapolated our Cartesian box to a full planet, and therefore do not take into account any sort of core or other interior structure. It does however account for non-linear evolution of the flow in convective regions, which – in the case of the elliptical and precessional instabilities – are of high importance.

To put our results in context, we also compute the tidal quality factor resulting from the dissipation of linearly-excited inertial waves in convective regions in this planetary model by applying the frequency-averaged formalism of Ogilvie (2013) to our planetary models. The tidal dissipation due to the linearly-excited inertial wave response is very strongly frequency-dependent, possibly differing by many orders of magnitude depending on the tidal frequency; see for example Fig. 1 of Ogilvie (2013). As a result, it might appear counter-intuitive to use a frequency-average, as it does not accurately represent the tidal dissipation of one specific planet with a given tidal frequency at a given point in its tidal evolution. On the other hand, we do not wish to make statements for a specific planet, but rather provide a general measure of tidal dissipation in Hot Jupiters due to linearly-excited inertial waves, and a frequency-average is well-suited to such a "population study", and this is how the frequency-average of tidal dissipation is generally employed (e.g. Mathis, 2015; Bolmont & Mathis, 2016; Barker, 2020; Barker, 2022, and many others). We follow the approach outlined in Section 3.1 of Barker (2020), fully accounting for the planetary structure. To this end we define the quantity $W_w = \mathrm{Re}[W_l(r)Y_l^m(\theta,\phi)]H(t)$,

as the wavelike part of the quantity W defined in Eq. (1.25), with $H(t)$ the Heaviside step function, corresponding to an impulsive tidal forcing. The W_l component of this quantity must then satisfy (Ogilvie, 2013):

$$\frac{1}{r^2}\frac{\mathrm{d}}{\mathrm{d}r}\left(r^2\rho\frac{\mathrm{d}W_l}{\mathrm{d}r}\right)-\frac{l(l+1)}{r^2}\rho W_l=\frac{2im\Omega}{r}\frac{\mathrm{d}\rho}{\mathrm{d}r}V_l, \tag{7.35}$$

subject to the boundary condition

$$\frac{\mathrm{d}W_l}{\mathrm{d}r}=\frac{2\mathrm{i}m\Omega V_l}{r}, \tag{7.36}$$

with V_l the radial dependence of the l component of the potential V that satisfies $\boldsymbol{\xi}_{nw}=\nabla V$. The boundary condition is nothing more than the requirement that the radial velocity of the wavelike tide vanishes at the edges of the convection zone. The tidal quality factor corresponding to the frequency-average of the tidal dissipation, $\langle Q'_{l,m,\mathrm{IW}}\rangle$, for a given tidal component with l,m is then given by (Ogilvie, 2013):

$$\frac{1}{\langle Q'_{l,m,\mathrm{IW}}\rangle}=\frac{32\pi^2 G}{3(2l+1)R^{2l+1}|A|^2}(E_{l,m}+E_{l-1,m}+E_{l+1,m}), \tag{7.37}$$

where

$$E_{l,m}=\frac{1}{4}\int\rho r^2(|a_{l,m}|^2+l(l+1)r^2|b_{l,m}|^2)\,\mathrm{d}r, \tag{7.38}$$

$$E_{l-1,m}=\frac{1}{4}\int\rho r^2 l(l-1)r^2|c_{l-1,m}|^2)\,\mathrm{d}r, \tag{7.39}$$

$$E_{l+1,m}=\frac{1}{4}\int\rho r^2(l+1)(l+2)r^2|c_{l+1,m}|^2)\,\mathrm{d}r, \tag{7.40}$$

and

$$a_{l,m}=\frac{2\mathrm{i}m\Omega}{r}V_l-\frac{\mathrm{d}W_l}{\mathrm{d}r}, \tag{7.41}$$

$$b_{l,m}=\frac{2\mathrm{i}m\Omega}{l(l+1)r^2}\left(r\frac{\mathrm{d}V_l}{\mathrm{d}r}+V_l\right)-\frac{W_l}{r^2}, \tag{7.42}$$

$$c_{l-1,m}=\frac{2\Omega q_{l,m}}{r^2}\left(r\frac{\mathrm{d}V_l}{\mathrm{d}r}+(l+1)V_l\right), \tag{7.43}$$

$$c_{l+1,m}=-\frac{2\Omega q_{l+1,m}}{r^2}\left(r\frac{\mathrm{d}V_l}{\mathrm{d}r}-lV_l\right), \tag{7.44}$$

$$q_{l,m}=\frac{1}{l}\left(\frac{l^2-m^2}{4l^2-1}\right)^{1/2}. \tag{7.45}$$

This prediction for $\langle Q'_{l,m,\mathrm{IW}}\rangle$ provides a tidal frequency-independent "typical level of dissipation" due to inertial waves according to linear theory. This is thought to be representative of the dissipation of inertial waves excited by linear tidal forcing, i.e. not via elliptical instability (because that also excites inertial waves through what we have called a non-linear tidal dissipation mechanism). This method necessarily ignores not only the complicated frequency-dependence of the dissipation in linear theory, but also any possible modifications by non-linear effects, convection, magnetic fields or differential rotation (e.g. Ogilvie & Lin, 2004; Favier et al., 2014a; Lin & Ogilvie, 2017a; Astoul & Barker, 2022,

2023). However, non-linear effects appear to not influence the found values of the tidal quality factor corresponding to the frequency-averaged dissipation of the $l = 2$, $m = 2$ component, $\langle Q'_{2,2,\mathrm{IW}} \rangle$, which is the most often studied component for modelling tidal evolution, to a great extent (Astoul & Barker, 2023).

One could also produce a frequency-averaged estimate of the tidal dissipation and associated tidal quality factor $Q'_{2,1,0}$ due to linearly-excited inertial waves for the obliquity tides using the same method. There are however a number of considerations preventing us from directly using this approach. Firstly, when considering purely the $l = 2$, $m = 1$, $n = 0$ component, a frequency-average is unnecessary, as there is only one possible tidal frequency. Still, a frequency-average could be useful, as for a given l, m these frequency-averages apply to all values of n, so the same frequency-average would also be applicable to $Q'_{2,1,2}$ as part of the obliquity tide. However, the tidal frequency of $-\Omega$ also resonates with what is known as the spin-over mode (Ogilvie, 2013). This is a mode that consists of a uniform rotation perpendicular to the spin axis of the body, and thus introduces an effective tilt in the rotation axis of the fluid by an amount that depends on its amplitude. This mode should not be dissipated viscously in a spherical body, even though the frequency-averaged formalism predicts a large dissipation associated with the spin-over mode resonance. The frequency-average of the tidal dissipation consequently massively overestimates the resulting dissipation (Ogilvie, 2014); the corresponding value of $\langle Q'_{2,1,\mathrm{IW}} \rangle$ is several orders of magnitude smaller than $\langle Q'_{2,2,\mathrm{IW}} \rangle$ calculated this way, unless very thin shells are considered, see Fig. 6 of Ogilvie (2013). Indeed, when shifting into the precessing frame where this resonance vanishes, as in Lin and Ogilvie (2017b), the associated viscous dissipation purely due to this mode also disappears. The tidal dissipation associated with the $l = 2$, $m = 1$, $n = 0$ component calculated this way depends on the size of the convective region, but generally turns out to be close to the same order of magnitude as the frequency-averaged dissipation of the $l = 2$, $m = 2$, $n = 2$ component (Lin & Ogilvie, 2017b). Therefore we opt not to plot $\langle Q'_{2,1,\mathrm{IW}} \rangle$, as it is unreliable. Instead we point to $\langle Q'_{2,2,\mathrm{IW}} \rangle$, which we will denote as $\langle Q'_{\mathrm{IW}} \rangle$ going forwards, to give an idea of the magnitude of the frequency-averaged dissipation due to linearly-excited inertial waves for the obliquity tide as well as for eccentricity and synchronisation tides.

We show Q' in Fig. 7.3 as a function of tidal period for each of these mechanisms. The spin frequency is fixed by setting $P_{\mathrm{rot}} = 10$ hr for the Jupiter model in the left-hand panel and $P_{\mathrm{rot}} = 1$ day for the Hot Jupiter model in the right-hand panel. The only exception to this is the precessional instability, where the tidal frequency is related to the spin frequency, and as such the spin frequency is not fixed for this mechanism. Moreover, we set $e = 0$, such that we consider a circular orbit, and $\cos i = 1$ when considering the precessional instability only. The latter implies that the spin and orbit are aligned, in which case the precessional instability does not operate. In this scenario Q' is infinite. We still choose this value for two reasons. Firstly, at small inclinations $\cos i \approx 1$, such that this computation is approximately representative of a small obliquity. Secondly, using this approach the computation provides a lower bound on $Q'_{2,1,0}$ due to the precessional

instability. For both the elliptical and precessional instabilities we provide two predictions, one with $P_{\rm orb} = 1$ day and the other with $P_{\rm orb} = 3$ days. When considering the tidal dissipation due to the effective viscosity acting on the precessional background flow in the RMLT regime, i.e. when considering the $Q'_{2,1,0}$ for $\nu_{\rm RMLT}$, the tidal frequency is again set by the spin frequency, and thus only one tidal frequency in this entire curve should be considered for this background flow. We expect the various dissipation mechanisms to scale differently as a function of the tidal frequency. When $\nu_{\rm eff}$ is independent of tidal frequency (in the low frequency regime), $D_\nu \propto \omega^2 \propto P_{\rm tide}^{-2}$ and $Q' \propto \omega^{-1} \propto P_{\rm tide}$, while in the high frequency regime where $\nu_{\rm eff} \propto \omega^{-2} \propto P_{\rm tide}^2$, D_ν is independent of ω and $Q' \propto \omega \propto P_{\rm tide}^{-1}$. In addition, we expect Q' due to elliptical and precessional instabilities to scale as $\omega^{-2} \propto P_{\rm tide}^2$ and the frequency-averaged inertial wave prediction to be independent of ω by definition.

The top panel of Fig. 7.3 demonstrates that convective damping of equilibrium tides by an effective viscosity is indeed an inefficient tidal dissipation mechanism in giant planets and leads to large Q' and thus large tidal timescales. The low tidal frequency regime in dashed-blue and dashed-magenta for MLT and RMLT, respectively, indicate their strongest dissipation when the tidal frequency is large. Note that these predictions are calculated using the classical prefactor of 1/3 for the effective viscosity for illustration. These lines indicate that if RMLT applies, as is expected, Q' is still $\mathcal{O}(10^9)$ if we neglect the frequency-reduction of $\nu_{\rm eff}$, thus the dissipation (and resulting tidal evolution) is weak. The combination of low, intermediate and high tidal frequency regimes for $\nu_{\rm eff}$ with the fitted prefactors in Eq. (4.1) dubbed $\nu_{\rm FIT}$ in solid-blue and solid-red indicates that the high tidal frequency regime impacts the effective viscosity significantly, particularly when $P_{\rm tide}$ is small. These predictions approximately connect to the frequency-independent MLT and RMLT predictions for large $P_{\rm tide}$ where there is a transition to the intermediate and low frequency regimes. The prefactors obtained using fits to simulations are larger than the dashed-magenta prediction, thus resulting in a slightly lower Q' when transitioning into the low tidal frequency regime. This is because the factor 1/3 often utilised, as plotted here for the MLT and RMLT lines, is essentially arbitrary, unlike our numerical fits.

The elliptical and precessional instabilities on a 1 day orbit (solid-green and solid-black) on the other hand are both efficient dissipation mechanisms, particularly when the tidal frequency, and thus for the precessional instability the rotation rate of the planet, is high. Note that according to our calculations both instabilities result in roughly the same value of Q'. They are both significantly more effective than convective damping of equilibrium tides according to each prediction for the entire range of tidal periods considered. The elliptical and precessional instabilities on a 3 day orbit (dashed-green and dashed-black) are weaker than the 1 day orbit prediction, but would still predict more effective dissipation than the (irrelevant) slow tides MLT effective viscosity for almost all of the parameter range considered. The most efficient mechanism in this model, except for the very highest tidal frequencies, is the frequency-averaged dissipation due to inertial waves shown in solid-cyan, which produces a $Q' = \mathcal{O}(10^3)$ for our chosen rotation period.

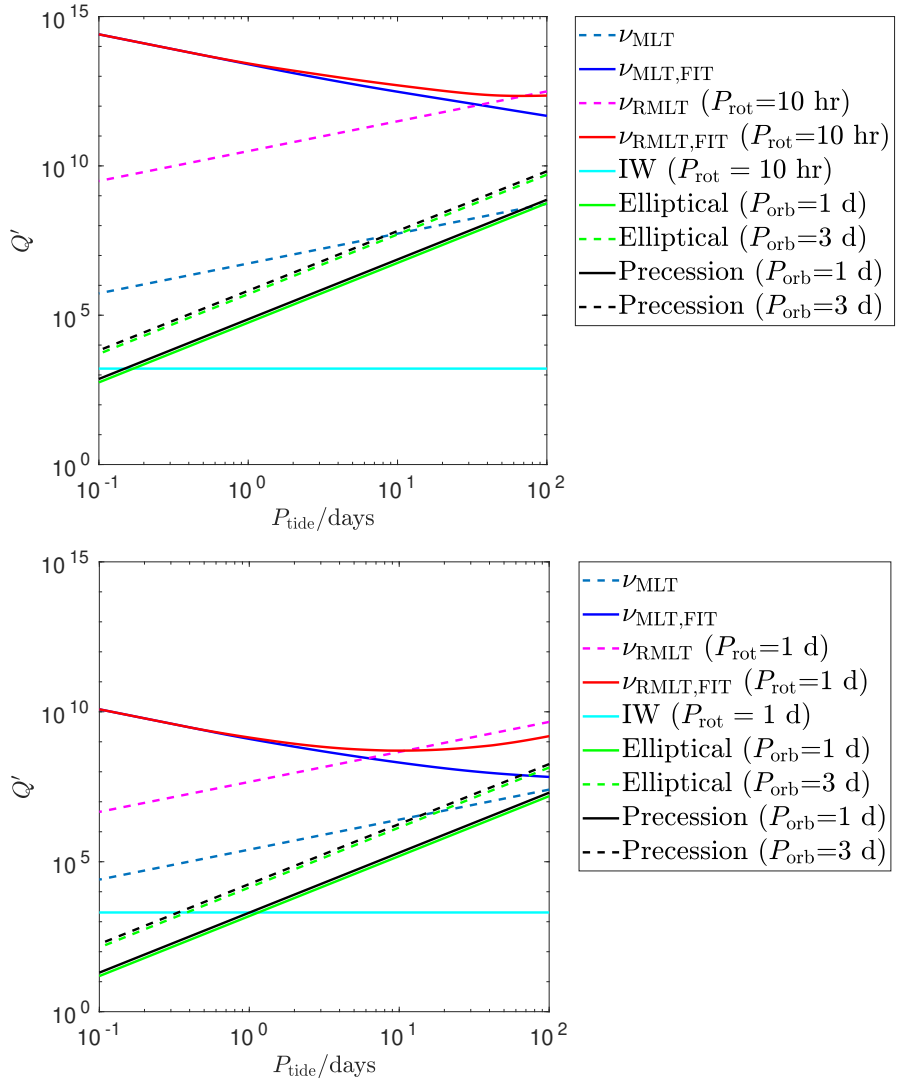

Figure 7.3: Tidal quality factor Q' as a function of tidal period for a myriad of mechanisms. Top: Jupiter model. Bottom: Inflated Hot Jupiter model. In both panels MLT and RMLT predictions for Q' due to convective damping of equilibrium tides using an effective viscosity with no tidal frequency reduction (low frequency regime) are shown in dashed-blue and -magenta respectively. The frequency-reduced effective viscosities in solid-blue and -red for MLT and RMLT respectively indicate that the frequency reduction significantly reduces the effectiveness of the dissipation. The elliptical instability in solid-green and dashed-green lines and the precessional instability in solid-black and dashed-black for two different orbital periods, and the (linear) frequency-averaged inertial wave dissipation in solid-cyan, are also plotted. Note that the inertial wave mechanism only applies when $|\omega| \leq |\Omega|$, such that this mechanism is only valid when $P_{\rm tide} \geq \frac{P_{\rm rot}}{2}$. Inertial waves are considerably more dissipative than equilibrium tide damping by turbulent viscosity, whether they are linearly or non-linearly (i.e. via elliptical or precessional instabilities) excited. The elliptical and precessional instabilities are predicted to be dominant for the shortest tidal periods, and linear excitation of inertial waves is dominant for longer periods. The Hot Jupiter model has smaller Q' (hence more efficient dissipation) for all dissipation mechanisms due to the larger radius and slower rotation.

Since the rotation period is known, we would thus predict a typical value

$$Q' \approx 2 \cdot 10^3 \left(\frac{P_{\rm rot}}{10{\rm hr}} \right)^2 , \tag{7.46}$$

for tidal dissipation due to inertial waves. Note that the inertial wave mechanism only applies when $|\omega| \leq |\Omega|$, such that this mechanism is only valid when $P_{\rm tide} \geq \frac{P_{\rm rot}}{2}$. Indeed, this is sufficiently dissipative to explain tidal dissipation rates in Jupiter and Saturn (Lainey et al., 2009; Lainey et al., 2012, 2017), without requiring any resonance-locking scenario (e.g. Fuller et al., 2016).

The Hot Jupiter model in the bottom panel of Fig. 7.3 on the other hand has a larger radius, stronger convection, and is rotating somewhat more slowly, so it has much higher effective viscosities and is impacted to a lesser extent by rotation. As a result, all mechanisms except the dissipation of (linear) inertial waves are more efficient. The elliptical and precessional instabilities are predicted to be particularly efficient for short orbital periods, e.g. 1 day orbit prediction for $Q' = \mathcal{O}(10^3)$ when the tidal period – and thus rotation period for the precessional instability – is 1 day. The increase in dissipation here due to the elliptical and precessional instabilities stems from the large radius of the Hot Jupiter, resulting in $\epsilon \approx 0.095$. Radius inflation and internal heating, as well as the marginally decreased rotation rate, allows the convective damping of equilibrium tides to operate more efficiently than in the Jupiter-like model in the top panel. However, once again the inertial wave mechanisms are predicted to be substantially more dissipative than effective viscosity acting on equilibrium tides. Linear dissipation of inertial waves occurs with a similar order of magnitude to the Jupiter-like model, and is predicted to be dominant for $P_{\rm tide} \gtrsim 2$ days.

To further illustrate what these obtained values of the tidal quality factors for the various tidal dissipation mechanisms represent we have made estimates of the orbital periods at which the synchronisation, circularisation and alignment timescales in Eq. (7.9), Eq. (7.11) and Eq. (7.20) respectively are 1 Gyr in Table 7.2. A 1 Gyr timescale is chosen because it allows sufficient time for spin-orbit synchronisation, circularisation and spin-orbit alignment of the Hot Jupiter to occur, and thus potentially be observable, while its (Sun-like) host star is on the main sequence. We have obtained estimates for all four tidal dissipation mechanisms we have considered previously: the elliptical instability (EI), precessional instability (PI), effective viscosity of convection (eff. viscosity) and frequency-averaged linearly-excited inertial waves (IW). When a tidal dissipation mechanism is not applicable to a tidal timescale we have left the entry in the table blank.

We have produced these estimates for both the Jupiter-like and Hot Jupiter-like model. For the computations for the former we have set $P_{\rm rot} = 10$ hrs, $P_{\rm tide} = 1$ d, except for the alignment timescale, where we have set $P_{\rm tide} = P_{\rm rot} = 10$ hrs, and used Jupiter's dynamical period. For the Hot Jupiter-like model we have used $P_{\rm rot} = P_{\rm tide} = 1$ d. The dynamical period for the Hot Jupiter model is increased by a factor of $\approx 1.8^{3/2}$ due to

Table 7.2: Table of orbital periods in days at which the estimates of the synchronisation, circularisation and alignment timescales in Eq. (7.9), Eq. (7.11) and Eq. (7.20) respectively, in Jupiter-like or Hot Jupiter-like planets, are 1 Gyr. The tidal dissipation mechanisms are the elliptical instability (EI), precessional instability (PI), effective viscosity of convection (eff. viscosity) and frequency-averaged inertial waves (IW). When a tidal dissipation mechanism does not contribute to a timescale we have left the entry blank. In the Jupiter-like estimates we have used $P_{\rm rot} = 10$ hrs, $P_{\rm tide} = 1$ d, except for the alignment timescale, where we have to use $P_{\rm tide} = P_{\rm rot} = 10$ hrs. For the Hot Jupiter-like model we have used $P_{\rm rot} = P_{\rm tide} = 1$ d. We have taken values of Q' from Fig. 7.3 at the specified tidal periods. For the computation of the alignment timescale we have set an initial inclination $i = 30°$, and we have set the eccentricity to zero in the computation of the synchronisation and alignment timescales.

	EI	PI	eff. viscosity	IW
Jupiter synchronisation	10 d		0.32 d	86 d
Jupiter circularisation	2.3 d		0.05 d	8.3 d
Jupiter alignment		12 d	0.24 d	63 d
Hot Jupiter synchronisation	30 d		6.3 d	167 d
Hot Jupiter circularisation	6.8 d		0.80 d	17 d
Hot Jupiter alignment		24 d	4.6 d	123 d

the larger radius of the Hot Jupiter-like planet. We have taken values of Q' from both panels of Fig. 7.3 at the specified tidal periods for each of the four mechanisms. For the computation of the alignment timescale we have set the inclination to be $i = 30°$, and we have set to eccentricity to zero in the computation of the synchronisation and alignment timescales.

We stress that these estimates are obtained in a rather crude way by fixing rotational and tidal periods, and are only for illustrative purposes. They do however indicate what we expect from the tidal quality factors in Fig. 7.3. The orbital periods at which the effective viscosity can achieve significant tidal evolution are extremely small, particularly for the Jupiter-like planets. They are also much smaller than the estimates for the elliptical and precessional instabilities, which can, for these tidal periods, potentially explain the observations of circularisation of Hot Jupiters in Fig. 1.3. Finally, the frequency-averaged inertial wave dissipation is the most effective mechanism. We caution that this mechanism is most efficient when the rotation of the body is fast, such that the tidal dissipation decreases as its spin and orbit synchronise for planets at larger orbital periods, and thus complete tidal evolution, i.e. total spin-orbit synchronisation, circularisation or spin-orbit alignment, due to the linearly-excited inertial waves mechanism at these large orbital periods (compared to Hot Jupiter orbital periods) is less likely to be achieved than these estimates indicate.

7.3 Conclusions

In this chapter we have used the scaling laws obtained in Ch. 4 and Ch. 6 to estimate the tidal quality factors of the three considered tidal dissipation mechanisms, the elliptical

and precessional instabilities and effective viscosity of convection in giant planets. We have derived simple (but necessarily crude) predictions for the tidal quality factors $Q'_{2,2,2}$ and $Q'_{2,1,0}$ due to the elliptical and precessional instabilities respectively and have used these to obtain estimates of tidal evolution timescales. Furthermore, we have used relevant parameters in Jupiter to obtain estimates for the effective viscosity in Jupiter, and find that it is practically the same irrespective of the considered (elliptical or precessional) background flow.

Next we employed the MESA code to construct illustrative interior models of a Jupiter-like and an inflated Hot Jupiter-like planet, subject to Jupiter-like irradiation and Hot Jupiter-like irradiation plus artificial interior heating, respectively. We have computed the rotational modifications of convective velocities and lengthscales in these models, as well as the modifications of the effective viscosity to allow us to compute tidal dissipation resulting from convective damping of equilibrium tides according to the scaling laws we have derived and verified with simulations. In both models (even in inflated short-period Hot Jupiters), we find the convective Rossby numbers to be much smaller than one, indicating that the convection is strongly affected by rotation, thus further motivating studying this regime. Furthermore, we find that, for almost all applications to giant planets, the fast tides regime, in which the tidal frequency is much larger than the convective frequency, is highly likely to be the relevant one. In this regime the effective viscosity scales as $\nu_{\rm eff} \propto (\omega_c/\omega)^2$. We also find that the origin of the background flow (whether elliptical or precessional) does not matter for this qualitative result. The resulting tidal quality factors $Q'_{2,2,2}$ and $Q'_{2,1,0}$ for equilibrium tide damping (computed following Barker, 2020) due to the convective turbulence acting on the background flow are estimated to be in excess of 10^9 for tidal periods of interest, and this mechanism is therefore predicted to be an ineffective one in giant planets.

On the other hand, we predict that the elliptical and precessional instabilities are efficient for very short orbital and tidal periods (with $Q' \sim 10^3$ in Hot Jupiters for periods of order one day), but that their efficiencies fall off rapidly with increasing (tidal and orbital) periods. We have also computed $\langle Q'_{\rm IW} \rangle$ arising from the frequency-averaged dissipation due to inertial waves in "realistic models" of giant planets (following Ogilvie, 2013; Barker, 2020). We compute the frequency-averaged dissipation and associated tidal quality factor of the $l = m = n = 2$ tidal component only, and argue that this is also a good indicator for the tidal quality factor due to the $l = 2,\ m = 1,\ n = 0$ tidal component, the latter of which cannot be accurately computed using a similar frequency-average (Ogilvie, 2013, 2014; Lin & Ogilvie, 2017b). This mechanism assumes these waves to be excited linearly by tidal forcing, as opposed to non-linearly (with respect to tidal amplitude) by the elliptical or precessional instabilities. Inertial waves are by far the most efficient mechanism studied here, either those excited by the elliptical or precessional instabilities for short orbital and tidal periods, or by the linear frequency-averaged dissipation. The latter leads to $Q' \approx 10^3 (P_{\rm rot}/10{\rm hr})^2$ for Jupiter-like rotation periods, which is consistent with the efficient tidal dissipation rates required to explain the observed orbital migration of

the moons of Jupiter and Saturn (e.g. Lainey et al., 2009; Lainey et al., 2012, where tidal amplitudes are likely to be too small for the elliptical instability to operate effectively), see also Dewberry (2023), Lin (2023), Dhouib et al. (2024), and Pontin et al. (2024).

All mechanisms except the frequency-averaged inertial wave mechanism are more efficient in the inflated Hot Jupiter model due to its larger radius, weaker rotation and stronger convective driving. This allows the elliptical and precessional instabilities to be on par with or even be more efficient than linearly-excited inertial waves in the shortest-period Hot Jupiters. We conclude that inertial wave mechanisms are probably the most efficient ones for dissipating tidal energy in giant planets, at least those without extended stable layers.

Chapter 8

Conclusion

Tidal dissipation of the equilibrium tide in giant planets and stars is often thought to explain certain aspects of their observed orbital evolution, among which are spin-orbit synchronisation, orbital circularisation and spin-orbit alignment. In this thesis we have examined the interaction of the equilibrium tide with convection and the resultant tidal dissipation. In particular we consider the elliptical flow associated with the asynchronous tide and the precessional flow associated with the obliquity tide. These give rise to two tidal dissipation mechanisms: the elliptical instability, associated with the elliptical flow, and the precessional (or inertial) instability associated with the precessional flow. These two mechanisms are both parametric instabilities which excite inertial waves due to the form of their respective background flows. Both require a finite amplitude tidal flow to operate, represented by the ellipticity ϵ and Poincaré number Po respectively, and as such we refer to these as non-linear tidal dissipation mechanisms. A third mechanism arises specifically due to the interaction of convection with the background flows: sufficiently turbulent convection can act on these flows like an effective viscosity, which can extract energy from these flows and result in tidal dissipation. We refer to this as a linear tidal mechanism instead, as there is no requirement on the amplitude of the tidal flow to allow this mechanism to occur. We analyse how the elliptical and precessional instabilities and their resultant tidal dissipation, in this thesis represented by the tidal energy injection into the local system we consider, are affected by their interactions with convection. We also analyse the tidal dissipation due to convection acting as an effective viscosity on these flows.

8.1 Summary

In Ch. 3 and Ch. 4 we presented our study of the interactions of the elliptical instability and rotating Rayleigh-Bénard convection in a Cartesian model using pseudo-spectral hydrodynamical numerical simulations involving horizontal shearing waves. In Ch. 3 we found that the introduction of convection leads to a suppression of the elliptical instability, which is primarily the result of the convectively-generated large-scale vortex (LSV). Con-

vection furthermore gives rise to a sustained energy injection into the flow (i.e. transfer from the elliptical flow). Furthermore, we have found that the inertial waves excited by the elliptical instability can transport heat in the presence of both stable and unstable stratification. If the elliptical instability is suppressed however, the sustained energy injection from the tidal flow into the system results in a more energetic LSV, which then acts to suppress the heat transport. In Ch. 3 we also found that a simulation initialised from a convective turbulent state including an LSV reduces the growth rate of the elliptical instability compared with the inviscid or viscous growth rate prediction. Using a detailed analysis of the frequency and wavenumber Fourier spectra of the energy in our simulations – which allows us to clearly identify inertial modes and convective flows – we observed that the elliptical instability (and energy injection into inertial modes more generally) is indeed inhibited by convective flows. We also found that the most unstable linear mode of the elliptical instability, when it does operate, is unchanged due to the convective vortex, and therefore this indicates that perturbation of the phases of the inertial waves by the convective vortex may be the explanation for the reduced growth rate and inhibition of the elliptical instability by the large-scale vortex.

In Ch. 4 we found that the elliptical instability provides time-averaged tidal dissipation rates approximately consistent with an ϵ^3 scaling when it operates. We have defined an efficiency or proportionality factor χ, such that the tidal dissipation is given by $D \equiv \chi\epsilon^3\gamma^3$, to represent the imperfect and probably intermittent operation of the elliptical instability. We observed the upper bound on this efficiency factor to be $\chi \approx 0.18$. Furthermore, this efficiency factor seems to be independent of the convective driving. We have found that the sustained energy injection rate observed in Ch. 3 scales as ϵ^2 in our simulations when the elliptical instability is suppressed. This sustained energy injection can therefore be interpreted as an effective viscosity that is independent of ϵ. On the other hand, this effective viscosity is observed to depend on the convective velocity, lengthscale and tidal frequency. We have obtained scaling laws for convective velocities and lengthscales, which we use to find predictions for the convective frequency and the effective viscosity, using both (temperature-based) mixing-length theory (MLT) and rotating mixing-length theory (RMLT) prescriptions. The agreement between the predictions of RMLT and our simulation data is very good, hence our simulations confirm the applicability of the diffusion-free scalings of RMLT to describe sufficiently turbulent rapidly rotating convection. Moreover, they allow us to use RMLT to find predictions for the effective viscosity. Our simulation data as a function of the tidal frequency ω and the convective frequency ω_c support the frequency-reduction of the effective viscosity for fast tides $(\omega_c/\omega)^2$ when $\omega \gg \omega_c$. We also confirm the presence of the intermediate frequency regime of $(\omega_c/\omega)^{-1/2}$ in our simulations (found by Duguid et al., 2020), and that the transition to this regime occurs at a ratio of $\omega/\omega_c \approx 5$, consistently with Duguid et al. (2020).

In Ch. 5 and Ch. 6 we have simulated the precessional instability in a local Cartesian model and its interaction with rotating Rayleigh-Bénard convection. In Ch. 5 we have derived growth rates of the precessional instability in the presence of stable and unstable

stratification by extending R. Mason and Kerswell (2002), and found, together with linear simulations, that the growth rate is typically reduced by stable stratification while the growth rate is increased by unstable stratification. In Ch. 6 we observe the expected bursty behaviour of the precessional instability in simulations with small values of the Poincaré number. Meanwhile, at larger values of Po we observe a vortex forming, which, when sufficiently powerful, seems to allow a rapid secondary transition to a continuously turbulent state instead of a bursty state. When convection is introduced at low Po the precessional instability disappears and instead a continuous energy injection resembling that in Ch. 3 arises. At larger values of Po in the presence of convection we again retrieve the continuously turbulent state. The energy injection rate is lowered due to the presence of convection, but the secondary transition occurs at lower and lower values of Po as the convective driving is increased. Again we find that the inertial waves generated by the precessional instability can transport heat, and heat transport is enhanced by precession regardless of Rayleigh number in the continuously turbulent regime, in strong contrast to the heat transport due to the elliptical instability interacting with convection.

We fit the tidal dissipation scalings of the precessional instability in isolation as functions of Po. In the continuously turbulent regime we find that the dissipation scales as $D \equiv \zeta \Omega^3 \mathrm{Po}^3$, with $\zeta = 0.09$ in the absence of convection, again representing an upper bound. The sustained energy injection we observed in these simulations at low values of the Poincaré number scales as Po^2, which means that this sustained energy injection can again be thought of as an effective viscosity, that is independent of Po, acting on the precessional flow. Again we observe this effective viscosity to depend on the Rayleigh number, and we find good agreement between the simulation data and the fitted RMLT predictions for intermediate and high frequency regimes of the effective viscosity damping the background precessional flow. The prefactors of these regimes are very close to those found previously for the background elliptical flow in Ch. 4, such that we conclude that the form of the background flow has little influence on the value of the effective viscosity.

Finally, in Ch. 7 we have obtained estimates for the tidal quality factors $Q'_{2,2,2}$ and $Q'_{2,1,0}$ due to the elliptical and precessional instabilities respectively, based on the scaling laws that we have derived and approximately validated in Ch. 4 and Ch. 6. Using these estimates we find that Hot Jupiters are expected to be in the continuously turbulent regime of the precessional instability, and that the reduction of the tidal dissipation due to the precessional instability interacting with convection for Hot Jupiter parameters is negligible. Next we employed the MESA code to construct illustrative interior models of a Jupiter-like and an inflated Hot Jupiter-like planet. We find that, for almost all applications to giant planets, the fast tides regime, in which the tidal frequency is much larger than the convective frequency, is highly likely to be the relevant one. We also find that the origin of the background flow (whether elliptical or precessional) does not matter for this qualitative result. The resulting tidal quality factors $Q'_{2,2,2}$ and $Q'_{2,1,0}$ for equilibrium tide damping due to the convective turbulence acting on the background flow are estimated to be in excess of 10^9 for tidal periods of interest, and this mechanism is therefore predicted

to be an ineffective one in giant planets. On the other hand, we predict that the elliptical and precessional instabilities are efficient for very short orbital and tidal periods (with $Q' \sim 10^3$ in Hot Jupiters for periods of order one day), but that they fall off rapidly with increasing (tidal and orbital) periods. We have also computed $\langle Q'_{\rm IW} \rangle$ arising from the frequency-averaged dissipation due to inertial waves in "realistic models" of giant planets. This mechanism assumes these waves to be excited linearly by tidal forcing, as opposed to non-linearly (with respect to tidal amplitude) by the elliptical instability. This mechanism leads to $Q' \approx 10^3 (P_{\rm rot}/10{\rm hr})^2$ for Jupiter-like rotation periods, which is consistent with the efficient tidal dissipation rates required to explain the observed orbital migration of the moons of Jupiter and Saturn where tidal amplitudes are likely to be too small for the elliptical instability to operate effectively. All mechanisms except the frequency-averaged inertial wave mechanism are more efficient in the inflated Hot Jupiter model due to its larger radius, weaker rotation and stronger convective driving. This allows the elliptical and precessional instabilities to be on par with or even be more efficient than linearly-excited inertial waves in the shortest-period Hot Jupiters. We conclude that inertial wave mechanisms are probably the most efficient ones for dissipating tidal energy in giant planets.

8.2 Future work

Numerous avenues of research can be pursued to follow on from the results in this thesis. A clear path is to study the interactions in this thesis in anelastic or even fully compressible simulations, which means these simulations could perhaps be considered valid for whole convective regions instead of single pressure scale heights. The results would then potentially be more valid for stars and giant planets with large convection zones, as well as lend more credibility to the extrapolation of the tidal dissipation to whole bodies. Finally, this would allow for verification of (rotating) mixing length theory in these different approximations, which would be very beneficial, not only for this work, but also for 1D stellar modelling.

Below we will consider more specific avenues of future work, which are either related to the tidal and precessional flows we have considered, or more generally to the setup we have considered, the rotating mixing length theory we have used to describe convection, the introduction of magnetic fields and finally how we have applied our scalings laws to the generated MESA models.

Elliptical flow

On the topic of the elliptical instability, it would be of interest to perform simulations varying γ and Ω, to fully disentangle the different dependencies on ${\rm Ro}_c$ and ${\rm Ro}_\omega$. Changing γ and Ω independently would allow the realistic scenario of a planet orbiting with a non-zero orbital frequency in the inertial frame to be studied. This would likely impact the strength of the elliptical instability as it changes its linear growth rate. This would be expected to cause suppression of the elliptical instability for different strengths of

convective driving (or for a different ϵ for fixed Ra). However, we do not expect any of our conclusions will be substantially modified in this case. Still, this would perhaps allow a clear quantification regarding what values of ϵ and convective driving suppress the elliptical instability. Furthermore, it might shed more light on the mechanism by which the large-scale vortices suppress the elliptical instability.

For both the elliptical tidal flow and the precessional flow it would be of interest to continue exploring different parameters of our simulations, particularly by varying the Prandtl number. In particular, low Prandtl number ($\mathrm{Pr} < 0.67$) rotating convection itself excites inertial waves (Chandrasekhar, 1961), which can subsequently interact through a triadic resonance (Lin, 2021). These convectively created inertial waves might also be unstable to the elliptical and precessional instabilities and could, due to their constant generation by the oscillatory convection, result in another source of potentially continuous tidal dissipation. Furthermore, if these convectively generated inertial waves instead result in another LSV, or zonal flows, this might instead suppress the elliptical instability at different values of the Rayleigh number, or modify the Poincaré number at which the precessional instability transitions to the continuously turbulent regime.

Precessional flow

On the topic of the precessional flow, one avenue of future work that is certainly of interest is a more complete study of the modification of convection by precession. A good place to start would be the linear stability analysis of convection in the presence of precession, as well as a continued investigation of the stability analysis of the precessional instability in the presence of stratification. At the time of writing, this analysis is being undertaken using a numerical Floquet method. Next, a more detailed analysis of convective quantities such as the Nusselt number and convective velocity in non-linear simulations would be interesting, to more clearly constrain the effect that precession has on convective motions, although it appears that precession acts primarily to enhance convection in this setup.

A further avenue of exploration is studying local boxes with different aspect ratios, which we have not used when studying the precessional instability due to finite computational time, but did explore when considering the elliptical instability. Boxes that are larger in the horizontal direction allow larger energies in the convectively generated vortices and possibly also in the precessional vortices. The continuously high energies in the vortices appear to have been important to the suppression of the elliptical instability, but their effects on the precessional instability is unclear. Furthermore, we have not probed the effects of stable stratification in non-linear simulations. Our linear stability analysis and linear simulations suggest that stable stratification stabilises the precessional instability. Nevertheless, for stable stratification – when the precessional instability can still operate – the heat transport and tidal dissipation produced would be worth exploring.

Finally, a larger parameter sweep at larger values of the rotation rate and thus smaller values of the Ekman number could prove useful. This would reduce the effective viscosities, both because the tidal frequency would increase and the convective velocities

and lengthscales would decrease. If the effective viscosity is less powerful, while the energy injection is larger due to larger rotation rates, the energy injection can be probed at larger Rayleigh numbers because it would no longer be overshadowed by the energy injection due to the effective viscosity. This would allow the effects of convection on the energy injection by the precessional instability to be constrained in a broader region of parameter space.

Transition to other latitudes

The Cartesian box in which we executed our simulations of both instabilities is situated at the poles of the planet, with the gravity and rotation axis both pointing in the z-direction. The latitudinal location of the box, and thus the relative directions of gravity and the rotation axis could affect the resulting tidal dissipation. If the box is moved to a lower latitude, the directions of gravity and the rotation axis will be misaligned, causing convective motions subjected to rapid rotation to change angle (Novi et al., 2019; Currie et al., 2020). At lower latitudes the vortices introduced by rotating convection turn into zonal flows, which could modify dissipation due to the elliptical and precessional instabilities as well as the effective viscosity of convection. In addition, Currie et al. (2020) demonstrated that the predictions of RMLT hold from the poles to mid-latitudes, but at low-latitudes deviations were observed due to the presence of both zonal flows and because boundary conditions constrain the flow in the latitudinal direction. Hence, future work should focus on obtaining a theoretical understanding of turbulent rotating convection and of the effective viscosity at mid and low latitudes, in the presence of strong zonal flows.

Furthermore, global simulations that are sufficiently turbulent and rapidly rotating to capture regimes similar to those we have explored would also be worthwhile, somewhat along the lines of the previous laminar simulations presented in e.g. Cébron et al. (2010). Following Barker (2016a), one could also study the interaction of the bursty non-linear dynamics of the elliptical instability with convection. Another possibility is to study the interactions of the precessional instability and convection like in Wei and Tilgner (2013), specifically examining the resulting tidal dissipation. One advantage of global simulations (in full ellipsoids or oblate spheroids) is that the inertial waves are no longer constrained by the (artificial) aspect ratio of the box. Furthermore, one might find that the inertial waves, excited by the precessional and elliptical instabilities, can lead to wave attractors if one studies them in spherical shells (e.g. Hollerbach & Kerswell, 1995; Noir et al., 2001), which can be thought of as mimicking a giant planet with a dilute core that is sufficiently stably stratified. Again, low Prandtl number ($\mathrm{Pr} < 0.67$) rotating convection itself excites inertial waves (Chandrasekhar, 1961), which could possibly also result in wave attractors (Lin, 2021), a possibility that would be interesting to study by itself. Finally, the convective zonal flows might affect the paths of these wave attractors, and thus the amount of dissipation they result in, in a similar manner to the non-linearly generated zonal flows due to tidally excited inertial waves (Astoul & Barker, 2022). The resultant effect of convection on tidal dissipation due to the inertial wave mechanisms should thus be studied in these global models.

Magnetic fields

There are strong magnetic fields present in Jupiter, and it is expected that Hot Jupiters would also have strong fields. This expectation is supported by observations tentatively inferring that a number of Hot Jupiters possess strong magnetic fields (Cauley et al., 2019). Therefore it is important to study the effects of magnetic fields in our simulations, as they could have significant effects on tidal dissipation. Magnetic fields may prevent LSV formation (Mak et al., 2017) by the elliptical instability, and therefore allow a continuous operation of the resulting energy transfers (Barker & Lithwick, 2014). It is likely that they also prevent the formation of the convective LSV (e.g. Maffei et al., 2019), and if so could allow continuous operation of the elliptical instability while convection is present in the system, potentially allowing for enhanced tidal dissipation. The precessional instability seems to achieve the continuously turbulent regime even at small values of Po when magnetic fields are introduced (Barker, 2016b), but it would be interesting to see if this is maintained if convection is also present. Furthermore, since our results point to a slight reduction of the energy injected by the precessional instability in the presence of convection, but Barker (2016b) points to enhanced energy injection in the presence of magnetic fields, it would be interesting to see if magnetic fields can act to remedy this weakening of the precessional instability as a tidal dissipation mechanism. Furthermore, it would be important to study the precessional instability as a dynamo mechanism (Malkus, 1968; Kerswell, 1996; Tilgner, 2005; Wu & Roberts, 2008; Le Bars et al., 2015) with convection present, to study if it is still efficient as a dynamo mechanism. On the other hand, our results, like those of Wei and Tilgner (2013), also point to more vigorous convection in the presence of precessional flow, and it would be useful to study if precession could possibly act to enhance rotating convection as a dynamo mechanism.

In addition, sufficiently strong magnetic fields will modify the properties of the convection and therefore the effective viscosity, and it remains to be seen how valid the predictions of Stevenson (1979) would be in this case. Also on the topic of magnetic fields, in a similar fashion to convection acting as an effective viscosity, an effective turbulent magnetic resistivity might arise (Cattaneo & Tobias, 2013; Tobias & Cattaneo, 2013). The turbulent magnetic resistivity has been explored previously in accretion discs (Lesur & Longaretti, 2009), but not in the context of tidal dissipation. It is entirely unknown whether an effective resistivity acting on a tidal flow features the same frequency-reduction as the effective viscosity (as assumed by Wei, 2022), and whether it might be an effective dissipation mechanism of the equilibrium tide for high tidal frequencies.

Applicability of the effective viscosity

Another question is whether effective turbulent diffusivities like the effective viscosity and effective resistivity are applicable to other flows than the ones studied. The effective viscosity as calculated here is purely representative of the interaction of rotating convection with the considered background flows. It is unclear if, for instance, the interaction between inertial waves generated by the elliptical and precessional instabilities (or more directly by

tidal forcing) and convection can be modelled in the same way. Studying the interaction of convection with inertial waves, and calculating whether (and if so how) this can be modelled using an effective viscosity is an important topic for future work. In addition, the possible role of alternative energy transfer routes for fast tides (Terquem, 2021), such terms involving correlations between tidal flow components and gradients of the convective flow (which identically vanish in our model), should be explored in global models to determine if they are ever important, although the first work in this direction by Barker and Astoul (2021) finds tidal dissipation that is much less relevant, by several orders of magnitude, than claimed by Terquem (2021).

Calculation of dissipation rates

A final avenue of future work is related to the analysis of tidal dissipation rates using planetary models. It would be worthwhile to modify the equation of state in a manner akin to Müller et al. (2020), which would allow us to obtain an extended dilute core and to measure the impact of such a core on tidal dissipation rates. Furthermore, a stably stratified dilute core might provide an important additional contribution to tidal dissipation by permitting the excitation of internal (inertia-)gravity waves (e.g. Fuller et al., 2016; André et al., 2019; Pontin et al., 2020; Pontin, 2022; Dewberry, 2023; Lin, 2023; Pontin et al., 2023; Dhouib et al., 2024; Pontin et al., 2024) as well as modifying the efficiency of inertial wave excitation in the overlying convective envelope (Pontin, 2022; Pontin et al., 2024). Finally, studying how Q' evolves with planetary evolution for each of these mechanisms would be worthwhile, research which has been started in the investigation of Lazovik et al. (2023). For self-consistency, one might then consider also evolving orbital parameters and irradiation fluxes in tandem with the structural evolution.

Appendix A

The MATHEMATICA script for Precessional instability

Below is the MATHEMATICA script used to compute the values of $k_\perp$ and σ in Ch. 5. The script computes σ according to Eq. (5.58) by first calculating the terms $\mathcal{A}$, $\mathcal{B}$, $\mathcal{C}$ and $\mathcal{D}$ from the normal mode solutions of the inertia-gravity waves. The relevant input parameters are n_A, n_B, ΔT and Ω, represented by `nA, nB, DT, Omega` in the script. Note that the script uses ΔT instead of N^2; the two quantities are related by $\Delta T = -N^2$ after setting $\alpha = g = d = 1$

To use the script one should set the desired n_A and n_B by modifying the definition of `kz` and `kzB` in the script respectively. One can then change the desired value of Ω and run the whole script. The script will calculate k_x, k_y and σ for all values of $\Delta T \in [-\Omega^2, \Omega^2]$. The script automatically saves the values of k_x, k_y, Ω, ΔT, σ – in that order – to a CSV text file, the name of which is set at the end of the script.

```
ClearAll["Global`*"]

(* Define the L matrices here, explicitly define them after derivative *)

L = {{z (I ky + kx), 0, - 2 I}, {0, z (I ky + kx), 2}, {I, - 1,
    z (I ky + kx)}};
Lconj  = {{z (I ky - kx), 0, 2 I}, {0, z (I ky - kx), 2}, {-I, - 1,
    z (I ky - kx)}};

(* Define the wavenumbers, change nA and nB here by changing kz and kzB *)
kz = 1*Pi; kzB = 2*Pi; kp =  Sqrt[kx^2 + ky^2]; kpB=kp;
k = Sqrt[kp^2 + kz^2]; kB =  Sqrt[kp^2 + (kzB)^2];

(* Define the frequencies *)
```

```
lambdaA = - Sqrt[ (4 Omega^2 kz^2 - DT kp^2)/k^2]; lambdaB = lambdaA + Omega;

(* Define the normal modes of inertia-gravity waves of both mode A and B *)
uAx = (k^2 (kx lambdaA - 2 I ky Omega)/(4 Omega^2 kp^2)) Cos[ kz (z)];
uAy = (k^2 (ky lambdaA + 2 I kx Omega)/(4 Omega^2 kp^2)) Cos[ kz (z)];
uAz = (- I  kz lambdaA/(DT+lambdaA^2) ) Sin[ kz (z)];
thA = (- kz DT/(DT + lambdaA^2)) Sin[ kz (z)];

uBx = (kB^2 (kx lambdaB - 2 I ky Omega)/(4 Omega^2 kpB^2)) Cos[kzB (z)];
uBy = (kB^2 (ky lambdaB + 2 I kx Omega)/(4 Omega^2 kpB^2)) Cos[kzB (z)];
uBz = (- I kzB lambdaB/(DT+lambdaB^2)) Sin[kzB (z)];
thB = (- kzB DT/(DT + lambdaB^2)) Sin[ kzB (z)];

uA = {uAx, uAy, uAz};
uB = {uBx, uBy, uBz};

(* Define the operators F and H acting on the modes A and B *)
FA = Omega (E ^ (I Omega t)  E ^ (I (kx x + ky y))
      E ^ (I lambdaA t) L.uA);

FB = Omega (E ^ (-I Omega t)  E ^ (I (kx x + ky y))
      E ^ (I lambdaB t) Lconj.uB);

HA = Omega (E ^ (I Omega t)  E ^ (I (kx x + ky y))
      E ^ (I lambdaA t) z (I ky + kx) thA);

HB = Omega (E ^ (-I Omega t)  E ^ (I (kx x + ky y))
      E ^ (I lambdaB t) z (I ky - kx) thB);

FA = Simplify[FA, {kx > 0, ky > 0, kz>0, z>0,Omega>0, DT>0}];

FB = Simplify[FB, {kx > 0, ky > 0, kz>0, z>0,Omega>0, DT>0}];

HA = Simplify[HA, {kx > 0, ky > 0, kz>0, z>0,Omega>0, DT>0}];

HB = Simplify[HB, {kx > 0, ky > 0, kz>0, z>0,Omega>0, DT>0}];


(* Calculate term A in Eq. 5.59, velocity part *)
termAu = Simplify[(-D[Curl[Curl[FB,{x,y,z}],{x,y,z}],t]
                   - 2 Omega D[Curl[FB,{x,y,z}],z]) /
                  (E ^ (I(kx x + ky y)) E ^ (I lambdaA t)),
```

```
                {kx > 0, ky > 0, kz>0, z>0, Omega>0, DT>0}];

(* Temperature part *)
termAth = Simplify[(D[D[HB,x],x] + D[D[HB,y],y]) /
                  (E ^ (I(kx x + ky y)) E ^ (I lambdaA t)),
                  {kx > 0, ky > 0, kz>0, z>0, Omega>0, DT>0}];

(* Put both parts together and perform integration over z *)
termA = Integrate[Simplify[Conjugate[uAz] (termAu[[3]] + termAth),
                {kx > 0, ky > 0, kz>0, z>0, Omega>0, DT>0}], {z,0,1}];


(* Calculate term B in Eq. 5.60 *)
termBu = Simplify[(-D[Curl[Curl[FA,{x,y,z}],{x,y,z}],t]
                  - 2 Omega D[Curl[FA,{x,y,z}],z])/
                 (E ^ (I (kx x + ky y)) E ^ (I lambdaB t)),
                 {kx > 0, ky > 0, kz>0, z>0, Omega>0, DT>0}];

termBth = Simplify[(D[D[HA,x],x] + D[D[HA,y],y]) /
                  (E ^ (I (kx x + ky y)) E ^ (I lambdaB t)),
                  {kx > 0, ky > 0, kz>0, z>0, Omega>0, DT>0}];

termB = Integrate[Simplify[Conjugate[uBz] * (termBu[[3]] + termBth),
                {kx > 0, ky > 0, kz>0, Omega>0, DT>0}], {z,0,1}];



(* Calculate term C in Eq. 5.61 *)
termCu = Simplify[(D[Laplacian[uA E ^ (I(kx x + ky y))
                     E ^ (I lambdaA t),{x,y,z}],t]
                  - 2 Omega D[Curl[uA E ^ (I(kx x + ky y))
                     E ^ (I lambdaA t),{x,y,z}],z]),
                 {kx > 0, ky > 0, kz>0, z>0, Omega>0, DT>0}];

termCth = Simplify[(D[D[thA E ^ (I(kx x + ky y))
                      E ^ (I lambdaA t),x],x]
                   + D[D[thA E ^ (I(kx x + ky y))
                      E ^ (I lambdaA t),y],y]),
                  {kx > 0, ky > 0, kz>0, z>0, Omega>0, DT>0}];

termC = Integrate[Simplify[Conjugate[uAz] (termCu[[3]]+termCth) /
                 (E ^ (I(kx x + ky y)) E ^ (I lambdaA t)),
```

```
        {kx > 0, ky > 0, kz>0, z>0, Omega>0, DT>0}], {z,0,1}];


(* Calculate term D in Eq. 5.62 *)
termDu = Simplify[(D[Laplacian[uB E ^ (I(kx x + ky y))
                    E ^ (I lambdaB t),{x,y,z}],t]
                  - 2 Omega D[Curl[uB E ^ (I(kx x + ky y))
                    E ^ (I lambdaB t),{x,y,z}],z]),
                 {kx > 0, ky > 0, kz>0, z>0, Omega>0, DT>0}];

termDth = Simplify[(D[D[thB E ^ (I(kx x + ky y))
                      E ^ (I lambdaB t),x],x]
                    + D[D[thB E ^ (I(kx x + ky y))
                      E ^ (I lambdaB t),y],y]),
                   {kx > 0, ky > 0, kz>0, z>0, Omega>0, DT>0}];

termD = Integrate[Simplify[Conjugate[uBz] (termDu[[3]]+termDth) /
                (E ^ (I(kx x + ky y)) E ^ (I lambdaB t)),
                {kx > 0, ky > 0, kz>0, z>0, Omega>0, DT>0}], {z,0,1}];

(* Code for generating text files of data depending on values of Omega *)

(* Set Omega here *)
Omega1=20000


(* Create list of DT to calculate with, ranges from -Omega^2 to Omega^2 *)
DTlist = Join[{-Omega1^2}, Reverse[PowerRange[Omega1,Omega1^2,10^(1/500)]],
             -Reverse[PowerRange[1,Omega1,10^(1/10)]], {0},
             PowerRange[1,Omega1,10^(1/10)],
             PowerRange[Omega1,Omega1^2,10^(1/500)],{Omega1^2}] // N

(* Solve for kperp here, we set kx=ky here. *)
(* The Nsolve provides eight solutions total, most are imaginary wavenumbers *)
(* For |nA-nB|=/=1 sometimes provides different solutions, with own sigma *)
Do[replaclist=Append[replaclist, Join[NSolve[1 - Sqrt[
                    (4 kz^2 - DT/Omega^2 kp^2)/k^2] ==
                    Sqrt[ (4 kzB^2 - DT/Omega^2 kp^2)/kB^2]
                    && kx==ky, {kx,ky}][[1]]
                        /. {Omega->Omega1, DT->i},{Omega->Omega1, DT->i}]],
                        {i,DTlist}]
```

```
(* Calculate values of sigma, remove square root for values of sigma^2 *)
Do[sigmalist=Append[sigmalist,Re[Sqrt[{Re[termA termB /
                    ( termC termD Omega^2)] /. i}]]],{i,replaclist}]

(* Create the output list, outputs kx, ky, Omega, DeltaT and sigma *)
finallistraw = {}
Do[finallistraw=Append[finallistraw, {kx,ky,Omega,DT}/. i],{i,replaclist}]
finallist = Join[finallistraw,sigmalist,2]

(* Save the calculated results as a CSV text file for post processing *)
Export["n1n2Omega2_10_4.txt", finallist, "CSV"]
```

Appendix B

Parameters used in the MESA inlists

The illustrative models in Ch. 7 are based on the MESA test suite case *make_planets*. We highlight here changes in the inlist files we used to obtain these models. Any parameters not mentioned here are unchanged from the test suite default values. The ***inlist_create*** and ***inlist_core*** are the same for both the Jupiter and Hot Jupiter model:

inlist_create
max_model_number = 1020
initial_Y=0.27

inlist_core
dlg_core_mass_per_step=0.002d0

The differences between these models lies in ***inlist_evolve***; for the Jupiter model:

max_model_number = 2500
irradiation_flux = 50000.d0
inject_uniform_extra_heat = 0.0d0
max_age=4.5d9

and for the Hot Jupiter model:

max_model_number = 2500
irradiation_flux = 1.d9
inject_uniform_extra_heat = 0.05d0
max_age=4.5d9.

References

André, Q., Mathis, S., & Barker, A. J. (2019). Layered semi-convection and tides in giant planet interiors. II. Tidal dissipation. *Astronomy & Astrophysics*, *626*, A82. https://doi.org/10.1051/0004-6361/201833674

Ascher, U. M., Ruuth, S. J., & Spiteri, R. J. (1997). Implicit-explicit Runge-Kutta methods for time-dependent partial differential equations. *Applied Numerical Mathematics*, *25*(2), 151–167. https://doi.org/10.1016/S0168-9274(97)00056-1

Astoul, A., & Barker, A. J. (2022). The effects of non-linearities on tidal flows in the convective envelopes of rotating stars and planets in exoplanetary systems. *Monthly Notices of the Royal Astronomical Society*, *516*(2), 2913–2935. https://doi.org/10.1093/mnras/stac2117

Astoul, A., & Barker, A. J. (2023). Tidally excited inertial waves in stars and planets: Exploring the frequency-dependent and averaged dissipation with nonlinear simulations. *The Astrophysical Journal Letters*, *955*(1), L23. https://doi.org/10.3847/2041-8213/acf49f

Aubert, J., Brito, D., Nataf, H.-C., Cardin, P., & Masson, J.-P. (2001). A systematic experimental study of rapidly rotating spherical convection in water and liquid gallium. *Physics of the Earth and Planetary Interiors*, *128*(1-4), 51–74. https://doi.org/10.1016/S0031-9201(01)00277-1

Aurnou, J. M., Horn, S., & Julien, K. (2020). Connections between nonrotating, slowly rotating, and rapidly rotating turbulent convection transport scalings. *Physical Review Research*, *2*, 043115. https://doi.org/10.1103/PhysRevResearch.2.043115

Barker, A. J. (2020). Tidal dissipation in evolving low-mass and solar-type stars with predictions for planetary orbital decay. *Monthly Notices of the Royal Astronomical Society*, *498*(2), 2270–2294. https://doi.org/10.1093/mnras/staa2405

Barker, A. J. (2016a). Non-linear tides in a homogeneous rotating planet or star: Global simulations of the elliptical instability. *Monthly Notices of the Royal Astronomical Society*, *459*(1), 939–956. https://doi.org/10.1093/mnras/stw702

Barker, A. J. (2016b). On turbulence driven by axial precession and tidal evolution of the spin–orbit angle of close-in giant planets. *Monthly Notices of the Royal Astronomical Society*, *460*(3), 2339–2350. https://doi.org/10.1093/mnras/stw1172

Barker, A. J. (2022). Tidal dissipation due to inertial waves can explain the circularization periods of solar-type binaries. *The Astrophysical Journal Letters*, *927*(2), L36. https://doi.org/10.3847/2041-8213/ac5b63

Barker, A. J., & Astoul, A. A. V. (2021). On the interaction between fast tides and convection. *Monthly Notices of the Royal Astronomical Society: Letters*, *506*(1), L69–L73. https://doi.org/10.1093/mnrasl/slab077

Barker, A. J., Braviner, H. J., & Ogilvie, G. I. (2016). Non-linear tides in a homogeneous rotating planet or star: Global modes and elliptical instability. *Monthly Notices of the Royal Astronomical Society*, *459*(1), 924–938. https://doi.org/10.1093/mnras/stw701

Barker, A. J., Dempsey, A. M., & Lithwick, Y. (2014). Theory and simulations of rotating convection. *The Astrophysical Journal*, *791*(1), 13. https://doi.org/10.1088/0004-637x/791/1/13

Barker, A. J., & Lithwick, Y. (2013). Non-linear evolution of the tidal elliptical instability in gaseous planets and stars. *Monthly Notices of the Royal Astronomical Society*, *435*(4), 3614–3626. https://doi.org/10.1093/mnras/stt1561

Barker, A. J., & Lithwick, Y. (2014). Non-linear evolution of the elliptical instability in the presence of weak magnetic fields. *Monthly Notices of the Royal Astronomical Society*, *437*(1), 305–315. https://doi.org/10.1093/mnras/stt1884

Baruteau, C., Crida, A., Paardekooper, S.-J., Masset, F., Guilet, J., Bitsch, B., Nelson, R., Kley, W., & Papaloizou, J. (2014). Planet-disk interactions and early evolution of planetary systems. In H. Beuther, R. S. Klessen, C. P. Dullemond, & T. Henning (Eds.), *Protostars and Planets VI* (pp. 667–689). University of Arizona Press. https://doi.org/10.2458/azu_uapress_9780816531240-ch029

Batygin, K., Bodenheimer, P. H., & Laughlin, G. P. (2016). In situ formation and dynamical evolution of hot Jupiter systems. *The Astrophysical Journal*, *829*(2), 114. https://doi.org/10.3847/0004-637X/829/2/114

Bayly, B. J. (1986). Three-dimensional instability of elliptical flow. *Physical Review Letters*, *57*, 2160–2163. https://doi.org/10.1103/PhysRevLett.57.2160

Bekki, Y., Cameron, R. H., & Gizon, L. (2022). Theory of solar oscillations in the inertial frequency range: Amplitudes of equatorial modes from a nonlinear rotating convection simulation. *Astronomy & Astrophysics*, *666*, A135. https://doi.org/10.1051/0004-6361/202244150

Benbakoura, M., Réville, V., Brun, A. S., Le Poncin-Lafitte, C., & Mathis, S. (2019). Evolution of star-planet systems under magnetic braking and tidal interaction. *Astronomy & Astrophysics*, *621*, A124. https://doi.org/10.1051/0004-6361/201833314

Benkacem, N., Salhi, A., Khlifi, A., Nasraoui, S., & Cambon, C. (2022). Destabilizing resonances of precessing inertia-gravity waves. *Physical Review E*, *105*, 035107. https://doi.org/10.1103/PhysRevE.105.035107

Böhm-Vitense, E. (1958). Über die Wasserstoffkonvektionszone in Sternen verschiedener Effektivtemperaturen und Leuchtkräfte. *Zeitschrift für Astrophysik*, *46*, 108.

Bolmont, E., & Mathis, S. (2016). Effect of the rotation and tidal dissipation history of stars on the evolution of close-in planets. *Celestial Mechanics and Dynamical Astronomy*, *126*(1-3), 275–296. https://doi.org/10.1007/s10569-016-9690-3

Bolton, S. J., Lunine, J., Stevenson, D., Connerney, J. E. P., Levin, S., Owen, T. C., Bagenal, F., Gautier, D., Ingersoll, A. P., Orton, G. S., Guillot, T., Hubbard, W., Bloxham, J., Coradini, A., Stephens, S. K., Mokashi, P., Thorne, R., & Thorpe, R. (2017). The Juno mission. *Space Science Reviews*, *213*(1-4), 5–37. https://doi.org/10.1007/s11214-017-0429-6

Bouillaut, V., Miquel, B., Julien, K., Aumaître, S., & Gallet, B. (2021). Experimental observation of the geostrophic turbulence regime of rapidly rotating convection. *Proceedings of the National Academy of Science*, *118*(44), e2105015118. https://doi.org/10.1073/pnas.2105015118

Boyd, J. P. (2001). *Chebyshev and Fourier spectral methods*. Dover Publications.

Braviner, H. J. (2015). *Stellar and planetary tides at small orbital radii* [Doctoral dissertation, University of Cambridge].
Apollo - University of Cambridge Repository.

Burns, K. J., Vasil, G. M., Oishi, J. S., Lecoanet, D., & Brown, B. P. (2020). Dedalus: A flexible framework for numerical simulations with spectral methods. *Physical Review Research*, *2*(2), 023068. https://doi.org/10.1103/PhysRevResearch.2.023068

Cattaneo, F., & Tobias, S. M. (2013). On the measurement of turbulent magnetic diffusivities: The three-dimensional case. *Journal of Fluid Mechanics*, *735*, 457–472. https://doi.org/10.1017/jfm.2013.506

Cattaneo, F., Emonet, T., & Weiss, N. (2003). On the interaction between convection and magnetic fields. *The Astrophysical Journal*, *588*(2), 1183. https://doi.org/10.1086/374313

Cauley, P. W., Shkolnik, E. L., Llama, J., & Lanza, A. F. (2019). Magnetic field strengths of hot Jupiters from signals of star-planet interactions. *Nature Astronomy*, *3*, 1128–1134. https://doi.org/10.1038/s41550-019-0840-x

Cébron, D., Le Bars, M., Moutou, C., & Le Gal, P. (2012). Elliptical instability in terrestrial planets and moons. *Astronomy & Astrophysics*, *539*, A78. https://doi.org/10.1051/0004-6361/201117741

Cébron, D., Maubert, P., & Le Bars, M. (2010). Tidal instability in a rotating and differentially heated ellipsoidal shell. *Geophysical Journal International*, *182*(3), 1311–1318. https://doi.org/10.1111/j.1365-246X.2010.04712.x

Cébron, D., Le Bars, M., Le Gal, P., Moutou, C., Leconte, J., & Sauret, A. (2013). Elliptical instability in hot Jupiter systems. *Icarus*, *226*(2), 1642–1653. https://doi.org/10.1016/j.icarus.2012.12.017

Chandrasekhar, S. (1967). Ellipsoidal figures of equilibrium—an historical account. *Communications on Pure and Applied Mathematics*, *20*(2), 251–265. https://doi.org/10.1002/cpa.3160200203

Chandrasekhar, S. (1961). *Hydrodynamic and hydromagnetic stability*. Oxford University Press.

Cox, J. P., & Giuli, R. T. (1968). *Principles of stellar structure*. Gordon and Breach.

Craik, A. D. D. (1989). The stability of unbounded two- and three-dimensional flows subject to body forces: Some exact solutions. *Journal of Fluid Mechanics*, *198*, 275–292. https://doi.org/10.1017/S0022112089000133

Crow, S. C. (1970). Stability theory for a pair of trailing vortices. *AIAA Journal*, *8*(12), 2172–2179. https://doi.org/10.2514/3.6083

Currie, L. K., Barker, A. J., Lithwick, Y., & Browning, M. K. (2020). Convection with misaligned gravity and rotation: Simulations and rotating mixing length theory. *Monthly Notices of the Royal Astronomical Society*, *493*(4), 5233–5256. https://doi.org/10.1093/mnras/staa372

Dawson, R. I., & Johnson, J. A. (2018). Origins of hot Jupiters. *Annual Review of Astronomy and Astrophysics*, *56*(1), 175–221. https://doi.org/10.1146/annurev-astro-081817-051853

Dewberry, J. W. (2023). Dynamical tides in Jupiter and other rotationally flattened planets and stars with stable stratification. *Monthly Notices of the Royal Astronomical Society*, *521*(4), 5991–6004. https://doi.org/10.1093/mnras/stad546

Dewberry, J. W., & Lai, D. (2022). Dynamical tidal Love numbers of rapidly rotating planets and stars. *The Astrophysical Journal*, *925*(2), 124. https://doi.org/10.3847/1538-4357/ac3ede

Dhouib, H., Baruteau, C., Mathis, S., Debras, F., Astoul, A., & Rieutord, M. (2024). Hydrodynamic modelling of dynamical tide dissipation in Jupiter's interior as revealed by Juno. *Astronomy & Astrophysics*, *682*, A85. https://doi.org/10.1051/0004-6361/202347703

Dintrans, B., Rieutord, M., & Valdettaro, L. (1999). Gravito-inertial waves in a rotating stratified sphere or spherical shell. *Journal of Fluid Mechanics*, *398*, 271–297. https://doi.org/10.1017/S0022112099006308

Duguid, C. D., Barker, A. J., & Jones, C. A. (2019). Tidal flows with convection: Frequency dependence of the effective viscosity and evidence for antidissipation. *Monthly Notices of the Royal Astronomical Society*, *491*(1), 923–943. https://doi.org/10.1093/mnras/stz2899

Duguid, C. D., Barker, A. J., & Jones, C. A. (2020). Convective turbulent viscosity acting on equilibrium tidal flows: New frequency scaling of the effective viscosity. *Monthly Notices of the Royal Astronomical Society*, *497*(3), 3400–3417. https://doi.org/10.1093/mnras/staa2216

Duguid, C. D. (2020). *The influence of convection on tidal flows* [Doctoral dissertation, University of Leeds].
White Rose eTheses Online. https://etheses.whiterose.ac.uk/28578/.

Durante, D., Parisi, M., Serra, D., Zannoni, M., Notaro, V., Racioppa, P., Buccino, D. R., Lari, G., Gomez Casajus, L., Iess, L., Folkner, W. M., Tommei, G., Tortora, P., & Bolton, S. J. (2020). Jupiter's gravity field halfway through the Juno mission. *Geophysical Research Letters*, *47*(4), e2019GL086572. https://doi.org/10.1029/2019GL086572

Eggleton, P. P., & Kiseleva-Eggleton, L. (2001). Orbital evolution in binary and triple stars, with an application to SS Lacertae. *The Astrophysical Journal*, *562*(2), 1012. https://doi.org/10.1086/323843

Favier, B., Barker, A. J., Baruteau, C., & Ogilvie, G. I. (2014a). Non-linear evolution of tidally forced inertial waves in rotating fluid bodies. *Monthly Notices of the Royal Astronomical Society*, *439*(1), 845–860. https://doi.org/10.1093/mnras/stu003

Favier, B., Grannan, A. M., Le Bars, M., & Aurnou, J. M. (2015). Generation and maintenance of bulk turbulence by libration-driven elliptical instability. *Physics of Fluids*, *27*(6), 066601. https://doi.org/10.1063/1.4922085

Favier, B., Silvers, L. J., & Proctor, M. R. E. (2014b). Inverse cascade and symmetry breaking in rapidly rotating Boussinesq convection. *Physics of Fluids*, *26*(9), 096605. https://doi.org/10.1063/1.4895131

Favier, B., Guervilly, C., & Knobloch, E. (2019). Subcritical turbulent condensate in rapidly rotating Rayleigh–Bénard convection. *Journal of Fluid Mechanics*, *864*, R1. https://doi.org/10.1017/jfm.2019.58

Fischer, P. F., Lottes, J. W., & Kerkemeier, S. G. (2008). Nek5000 web page. http://nek5000.mcs.anl.gov

French, M., Becker, A., Lorenzen, W., Nettelmann, N., Bethkenhagen, M., Wicht, J., & Redmer, R. (2012). Ab initio simulations for material properties along the Jupiter adiabat. *The Astrophysical Journal Supplement Series*, *202*(1), 5. https://doi.org/10.1088/0067-0049/202/1/5

Fuller, J., Luan, J., & Quataert, E. (2016). Resonance locking as the source of rapid tidal migration in the Jupiter and Saturn moon systems. *Monthly Notices of the Royal Astronomical Society*, *458*(4), 3867–3879. https://doi.org/10.1093/mnras/stw609

Galanti, E., Kaspi, Y., Miguel, Y., Guillot, T., Durante, D., Racioppa, P., & Iess, L. (2019). Saturn's deep atmospheric flows revealed by the Cassini Grand Finale gravity measurements. *Geophysical Research Letters*, *46*(2), 616–624. https://doi.org/10.1029/2018GL078087

Gastine, T., & Wicht, J. (2021). Stable stratification promotes multiple zonal jets in a turbulent jovian dynamo model. *Icarus*, *368*, 114514. https://doi.org/10.1016/j.icarus.2021.114514

Gastine, T., Wicht, J., & Aubert, J. (2016). Scaling regimes in spherical shell rotating convection. *Journal of Fluid Mechanics*, *808*, 690–732. https://doi.org/10.1017/jfm.2016.659

Gledzer, E. B., Dolzhanskii, F. V., Obukhov, A. M., & Ponomarev, V. M. (1976). An experimental and theoretical study of the stability of motion of a liquid in an elliptical cylinder. *Akademiia Nauk SSSR Fizika Atmosfery i Okeana*, *11*, 981–992.

Goldreich, P., & Nicholson, P. D. (1977). Turbulent viscosity and Jupiter's tidal Q. *Icarus*, *30*(2), 301–304. https://doi.org/10.1016/0019-1035(77)90163-4

Goodman, J., & Dickson, E. S. (1998). Dynamical tide in solar-type binaries. *The Astrophysical Journal*, *507*(2), 938. https://doi.org/10.1086/306348

Goodman, J., & Oh, S. P. (1997). Fast tides in slow stars: The efficiency of eddy viscosity. *The Astrophysical Journal*, *486*(1), 403–412. https://doi.org/10.1086/304505

Grannan, A. M., Favier, B., Le Bars, M., & Aurnou, J. M. (2017). Tidally forced turbulence in planetary interiors. *Geophysical Journal International*, *208*(3), 1690–1703. https://doi.org/10.1093/gji/ggw479

Greenspan, H. P. (1968). *The Theory of Rotating Fluids*. Cambridge University Press.

Guervilly, C., Cardin, P., & Schaeffer, N. (2019). Turbulent convective length scale in planetary cores. *Nature*, *570*(7761), 368–371. https://doi.org/10.1038/s41586-019-1301-5

Guervilly, C., Hughes, D. W., & Jones, C. A. (2014). Large-scale vortices in rapidly rotating Rayleigh-Bénard convection. *Journal of Fluid Mechanics*, *758*, 407–435. https://doi.org/10.1017/jfm.2014.542

Guillot, T. (1999). A comparison of the interiors of Jupiter and Saturn. *Planetary and Space Science*, *47*(10), 1183–1200. https://doi.org/10.1016/S0032-0633(99)00043-4

Guillot, T., Stevenson, D. J., Hubbard, W. B., & Saumon, D. (2004). The interior of Jupiter. In F. Bagenal, T. E. Dowling, & W. B. McKinnon (Eds.), *Jupiter. The Planet, Satellites and Magnetosphere* (pp. 35–57). Cambridge University Press.

Hagey, S. R., Edwards, B., & Boley, A. C. (2022). Evidence of long-term period variations in the Exoplanet Transit Database (ETD). *The Astronomical Journal*, *164*(5), 220. https://doi.org/10.3847/1538-3881/ac959a

Hamer, J. H., & Schlaufman, K. C. (2019). Hot Jupiters are destroyed by tides while their host stars are on the main sequence. *The Astronomical Journal*, *158*(5), 190. https://doi.org/10.3847/1538-3881/ab3c56

Helled, R., Stevenson, D. J., Lunine, J. I., Bolton, S. J., Nettelmann, N., Atreya, S., Guillot, T., Militzer, B., Miguel, Y., & Hubbard, W. B. (2022). Revelations on Jupiter's formation, evolution and interior: Challenges from Juno results. *Icarus*, *378*, 114937. https://doi.org/10.1016/j.icarus.2022.114937

Hollerbach, R., & Kerswell, R. R. (1995). Oscillatory internal shear layers in rotating and precessing flows. *Journal of Fluid Mechanics*, *298*, 327–339. https://doi.org/10.1017/S0022112095003338

Ingersoll, A. P., & Pollard, D. (1982). Motion in the interiors and atmospheres of Jupiter and Saturn: Scale analysis, anelastic equations, barotropic stability criterion. *Icarus*, *52*(1), 62–80. https://doi.org/10.1016/0019-1035(82)90169-5

Ireland, L. G., & Browning, M. K. (2018). The radius and entropy of a magnetized, rotating, fully convective star: Analysis with depth-dependent mixing length theories. *The Astrophysical Journal*, *856*(2), 132. https://doi.org/10.3847/1538-4357/aab3da

Jermyn, A. S., Bauer, E. B., Schwab, J., Farmer, R., Ball, W. H., Bellinger, E. P., Dotter, A., Joyce, M., Marchant, P., Mombarg, J. S. G., Wolf, W. M., Wong, T. L. S., Cinquegrana, G. C., Farrell, E., Smolec, R., Thoul, A., Cantiello, M., Herwig, F., Toloza, O., … Timmes, F. X. (2023). Modules for Experiments in Stellar As-

trophysics (MESA): Time-dependent convection, energy conservation, automatic differentiation, and infrastructure. *The Astrophysical Journal Supplement Series*, *265*(1), 15. https://doi.org/10.3847/1538-4365/acae8d

Jones, C. (2015). 8.05 - Thermal and Compositional Convection in the Outer Core. In G. Schubert (Ed.), *Treatise on Geophysics* (Second Edition, pp. 115–159). Elsevier. https://doi.org/10.1016/B978-0-444-53802-4.00141-X

Kerswell, R. R. (1993). The instability of precessing flow. *Geophysical & Astrophysical Fluid Dynamics*, *72*(1-4), 107–144. https://doi.org/10.1080/03091929308203609

Kerswell, R. R. (1996). Upper bounds on the energy dissipation in turbulent precession. *Journal of Fluid Mechanics*, *321*, 335–370. https://doi.org/10.1017/S0022112096007756

Kerswell, R. R. (2002). Elliptical instability. *Annual Review of Fluid Mechanics*, *34*(1), 83–113. https://doi.org/10.1146/annurev.fluid.34.081701.171829

Kopal, Z. (1959). *Close binary systems*. Wiley.

Kumar, V., Pizzi, F., Mamatsashvili, G., Giesecke, A., Stefani, F., & Barker, A. J. (2024). Dynamo action driven by precessional turbulence. *Physical Review E*, *109*, 065101. https://doi.org/10.1103/PhysRevE.109.065101

Lai, D. (2021). Jupiter's dynamical Love number. *The Planetary Science Journal*, *2*(4), 122. https://doi.org/10.3847/PSJ/ac013b

Lainey, V., Arlot, J.-E., Karatekin, O., & Van Hoolst, T. (2009). Strong tidal dissipation in Io and Jupiter from astrometric observations. *Nature*, *459*, 957–9. https://doi.org/10.1038/nature08108

Lainey, V., Jacobson, R. A., Tajeddine, R., Cooper, N. J., Murray, C., Robert, V., Tobie, G., Guillot, T., Mathis, S., Remus, F., Desmars, J., Arlot, J.-E., De Cuyper, J.-P., Dehant, V., Pascu, D., Thuillot, W., Le Poncin-Lafitte, C., & Zahn, J.-P. (2017). New constraints on Saturn's interior from Cassini astrometric data. *Icarus*, *281*, 286–296. https://doi.org/10.1016/j.icarus.2016.07.014

Lainey, V., Karatekin, Ö., Desmars, J., Charnoz, S., Arlot, J.-E., Emelyanov, N., Poncin-Lafitte, C. L., Mathis, S., Remus, F., Tobie, G., & Zahn, J.-P. (2012). Strong tidal dissipation in Saturn and constraints on Enceladus' thermal state from astrometry. *The Astrophysical Journal*, *752*(1), 14. https://doi.org/10.1088/0004-637x/752/1/14

Landman, M. J., & Saffman, P. G. (1987). The three-dimensional instability of strained vortices in a viscous fluid. *Physics of Fluids*, *30*(8), 2339–2342. https://doi.org/10.1063/1.866124

Lavorel, G., & Le Bars, M. (2010). Experimental study of the interaction between convective and elliptical instabilities. *Physics of Fluids*, *22*(11), 114101. https://doi.org/10.1063/1.3508946

Lazovik, Y. A., Barker, A. J., de Vries, N. B., & Astoul, A. (2023). Tidal dissipation in rotating and evolving giant planets with application to exoplanet systems. *Monthly Notices of the Royal Astronomical Society*, *527*(3), 8245–8256. https://doi.org/10.1093/mnras/stad3689

Le Bars, M., Lacaze, L., Le Dizès, S., Le Gal, P., & Rieutord, M. (2010). Tidal instability in stellar and planetary binary systems. *Physics of the Earth and Planetary Interiors*, *178*(1), 48–55. https://doi.org/10.1016/j.pepi.2009.07.005

Le Bars, M., & Le Dizès, S. (2006). Thermo-elliptical instability in a rotating cylindrical shell. *Journal of Fluid Mechanics*, *563*, 189–198. https://doi.org/10.1017/S0022112006001674

Le Bars, M., Cébron, D., & Le Gal, P. (2015). Flows driven by libration, precession, and tides. *Annual Review of Fluid Mechanics*, *47*(1), 163–193. https://doi.org/10.1146/annurev-fluid-010814-014556

Le Reun, T., Favier, B., Barker, A. J., & Le Bars, M. (2017). Inertial wave turbulence driven by elliptical instability. *Physical Review Letters*, *119*, 034502. https://doi.org/10.1103/PhysRevLett.119.034502

Le Reun, T., Favier, B., & Le Bars, M. (2018). Parametric instability and wave turbulence driven by tidal excitation of internal waves. *Journal of Fluid Mechanics*, *840*, 498–529. https://doi.org/10.1017/jfm.2018.18

Le Reun, T., Favier, B., & Le Bars, M. (2019). Experimental study of the nonlinear saturation of the elliptical instability: Inertial wave turbulence versus geostrophic turbulence. *Journal of Fluid Mechanics*, *879*, 296–326. https://doi.org/10.1017/jfm.2019.646

Lesur, G., & Longaretti, P.-Y. (2007). Impact of dimensionless numbers on the efficiency of magnetorotational instability induced turbulent transport. *Monthly Notices of the Royal Astronomical Society*, *378*(4), 1471–1480. https://doi.org/10.1111/j.1365-2966.2007.11888.x

Lesur, G., & Longaretti, P.-Y. (2009). Turbulent resistivity evaluation in magnetorotational instability generated turbulence. *Astronomy & Astrophysics*, *504*(2), 309–320. https://doi.org/10.1051/0004-6361/200912272

Leweke, T., Le Dizès, S., & Williamson, C. H. (2016). Dynamics and instabilities of vortex pairs. *Annual Review of Fluid Mechanics*, *48*(1), 507–541. https://doi.org/10.1146/annurev-fluid-122414-034558

Lin, Y. (2021). Triadic resonances driven by thermal convection in a rotating sphere. *Journal of Fluid Mechanics*, *909*, R3. https://doi.org/10.1017/jfm.2020.1050

Lin, Y. (2023). Dynamical tides in Jupiter and the role of interior structure. *Astronomy & Astrophysics*, *671*, A37. https://doi.org/10.1051/0004-6361/202245112

Lin, Y., & Ogilvie, G. I. (2017a). Tidal dissipation in rotating fluid bodies: The presence of a magnetic field. *Monthly Notices of the Royal Astronomical Society*, *474*(2), 1644–1656. https://doi.org/10.1093/mnras/stx2764

Lin, Y., & Ogilvie, G. I. (2017b). Tidal interactions in spin–orbit misaligned systems. *Monthly Notices of the Royal Astronomical Society*, *468*(2), 1387–1397. https://doi.org/10.1093/mnras/stx540

Lorenzani, S., & Tilgner, A. (2001). Fluid instabilities in precessing spheroidal cavities. *Journal of Fluid Mechanics*, *447*, 111–128. https://doi.org/10.1017/S002211200100581X

Lorenzani, S., & Tilgner, A. (2003). Inertial instabilities of fluid flow in precessing spheroidal shells. *Journal of Fluid Mechanics*, *492*, 363–379. https://doi.org/10.1017/S002211200300572X

Maffei, S., Calkins, M. A., Julien, K., & Marti, P. (2019). Magnetic quenching of the inverse cascade in rapidly rotating convective turbulence. *Physical Review Fluids*, *4*(4), 041801. https://doi.org/10.1103/PhysRevFluids.4.041801

Mak, J., Griffiths, S. D., & Hughes, D. W. (2017). Vortex disruption by magnetohydrodynamic feedback. *Physical Review Fluids*, *2*, 113701. https://doi.org/10.1103/PhysRevFluids.2.113701

Malkus, W. V. R. (1968). Precession of the earth as the cause of geomagnetism. *Science*, *160*(3825), 259–264. https://doi.org/10.1126/science.160.3825.259

Malkus, W. V. R. (1989). An experimental study of global instabilities due to the tidal (elliptical) distortion of a rotating elastic cylinder. *Geophysical & Astrophysical Fluid Dynamics*, *48*(1-3), 123–134. https://doi.org/10.1080/03091928908219529

Mankovich, C. R., & Fuller, J. (2021). A diffuse core in Saturn revealed by ring seismology. *Nature Astronomy*, *5*, 1103–1109. https://doi.org/10.1038/s41550-021-01448-3

Mason, D. M., & Kerswell, R. R. (1999). Nonlinear evolution of the elliptical instability: An example of inertial wave breakdown. *Journal of Fluid Mechanics*, *396*, 73–108. https://doi.org/10.1017/S0022112099005959

Mason, R. M., & Kerswell, R. R. (2002). Chaotic dynamics in a strained rotating flow: A precessing plane fluid layer. *Journal of Fluid Mechanics*, *471*, 71–106. https://doi.org/10.1017/S0022112002001994

Mathis, S., Auclair-Desrotour, P., Guenel, M., Gallet, F., & Le Poncin-Lafitte, C. (2016). The impact of rotation on turbulent tidal friction in stellar and planetary convective regions. *Astronomy & Astrophysics*, *592*, A33. https://doi.org/10.1051/0004-6361/201527545

Mathis, S., & Le Poncin-Lafitte, C. (2009). Tidal dynamics of extended bodies in planetary systems and multiple stars. *Astronomy & Astrophysics*, *497*(3), 889–910. https://doi.org/10.1051/0004-6361/20079054

Mathis, S. (2015). Variation of tidal dissipation in the convective envelope of low-mass stars along their evolution. *Astronomy & Astrophysics*, *580*, L3. https://doi.org/10.1051/0004-6361/201526472

Mayor, M., & Queloz, D. (1995). A Jupiter-mass companion to a solar-type star. *Nature*, *378*(6555), 355–359. https://doi.org/10.1038/378355a0

Militzer, B., Soubiran, F., Wahl, S. M., & Hubbard, W. (2016). Understanding Jupiter's interior. *Journal of Geophysical Research: Planets*, *121*(9), 1552–1572. https://doi.org/10.1002/2016JE005080

Moore, D. W., Saffman, P. G., & Stuart, J. T. (1975). The instability of a straight vortex filament in a strain field. *Proceedings of the Royal Society of London. A. Mathematical and Physical Sciences*, *346*(1646), 413–425. https://doi.org/10.1098/rspa.1975.0183

Müller, S., & Helled, R. (2023). Towards a new era in giant exoplanet characterisation. *Astronomy & Astrophysics*, *669*, A24. https://doi.org/10.1051/0004-6361/202244827

Müller, S., Helled, R., & Cumming, A. (2020). The challenge of forming a fuzzy core in Jupiter. *Astronomy & Astrophysics*, *638*, A121. https://doi.org/10.1051/0004-6361/201937376

Naing, M. M., & Fukumoto, Y. (2011). Local instability of a rotating flow driven by precession of arbitrary frequency. *Fluid Dynamics Research*, *43*(5), 055502. https://doi.org/10.1088/0169-5983/43/5/055502

Naoz, S., Farr, W. M., Lithwick, Y., Rasio, F. A., & Teyssandier, J. (2011). Hot Jupiters from secular planet-planet interactions. *Nature*, *473*(7346), 187–189. https://doi.org/10.1038/nature10076

NASA Exoplanet Archive. (2024). *Planetary Systems Table*. https://doi.org/10.26133/NEA12

Nelson, B. E., Ford, E. B., & Rasio, F. A. (2017). Evidence for two hot-Jupiter formation paths. *The Astronomical Journal*, *154*(3), 106. https://doi.org/10.3847/1538-3881/aa82b3

Noir, J., Brito, D., Aldridge, K., & Cardin, P. (2001). Experimental evidence of inertial waves in a precessing spheroidal cavity. *Geophysical Research Letters*, *28*(19), 3785–3788. https://doi.org/10.1029/2001GL012956

Novi, L., von Hardenberg, J., Hughes, D. W., Provenzale, A., & Spiegel, E. A. (2019). Rapidly rotating Rayleigh-Bénard convection with a tilted axis. *Physical Review E*, *99*(5), 053116. https://doi.org/10.1103/PhysRevE.99.053116

Ogilvie, G. I., & Lin, D. N. C. (2004). Tidal dissipation in rotating giant planets. *The Astrophysical Journal*, *610*(1), 477–509. https://doi.org/10.1086/421454

Ogilvie, G. I. (2013). Tides in rotating barotropic fluid bodies: The contribution of inertial waves and the role of internal structure. *Monthly Notices of the Royal Astronomical Society*, *429*(1), 613–632. https://doi.org/10.1093/mnras/sts362

Ogilvie, G. I. (2014). Tidal dissipation in stars and giant planets. *Annual Review of Astronomy and Astrophysics*, *52*, 171–210. https://doi.org/10.1146/annurev-astro-081913-035941

Ogilvie, G. I., & Lesur, G. (2012). On the interaction between tides and convection. *Monthly Notices of the Royal Astronomical Society*, *422*(3), 1975–1987. https://doi.org/10.1111/j.1365-2966.2012.20630.x

Parodi, A., von Hardenberg, J., Passoni, G., Provenzale, A., & Spiegel, E. A. (2004). Clustering of plumes in turbulent convection. *Physical Review Letters*, *92*, 194503. https://doi.org/10.1103/PhysRevLett.92.194503

Paxton, B., Bildsten, L., Dotter, A., Herwig, F., Lesaffre, P., & Timmes, F. (2011). Modules for Experiments in Stellar Astrophysics (MESA). *The Astrophysical Journal Supplement Series*, *192*, 3. https://doi.org/10.1088/0067-0049/192/1/3

Paxton, B., Cantiello, M., Arras, P., Bildsten, L., Brown, E. F., Dotter, A., Mankovich, C., Montgomery, M. H., Stello, D., Timmes, F. X., & Townsend, R. (2013). Modules

for Experiments in Stellar Astrophysics (MESA): Planets, oscillations, rotation, and massive stars. *The Astrophysical Journal Supplement Series*, *208*, 4. https://doi.org/10.1088/0067-0049/208/1/4

Paxton, B., Marchant, P., Schwab, J., Bauer, E. B., Bildsten, L., Cantiello, M., Dessart, L., Farmer, R., Hu, H., Langer, N., Townsend, R. H. D., Townsley, D. M., & Timmes, F. X. (2015). Modules for Experiments in Stellar Astrophysics (MESA): Binaries, pulsations, and explosions. *The Astrophysical Journal Supplement Series*, *220*, 15. https://doi.org/10.1088/0067-0049/220/1/15

Paxton, B., Schwab, J., Bauer, E. B., Bildsten, L., Blinnikov, S., Duffell, P., Farmer, R., Goldberg, J. A., Marchant, P., Sorokina, E., Thoul, A., Townsend, R. H. D., & Timmes, F. X. (2018). Modules for Experiments in Stellar Astrophysics (MESA): Convective boundaries, element diffusion, and massive star explosions. *The Astrophysical Journal Supplement Series*, *234*, 34. https://doi.org/10.3847/1538-4365/aaa5a8

Paxton, B., Smolec, R., Schwab, J., Gautschy, A., Bildsten, L., Cantiello, M., Dotter, A., Farmer, R., Goldberg, J. A., Jermyn, A. S., Kanbur, S. M., Marchant, P., Thoul, A., Townsend, R. H. D., Wolf, W. M., Zhang, M., & Timmes, F. X. (2019). Modules for Experiments in Stellar Astrophysics (MESA): Pulsating variable stars, rotation, convective boundaries, and energy conservation. *The Astrophysical Journal Supplement Series*, *243*(1), 10. https://doi.org/10.3847/1538-4365/ab2241

Peale, S. J., Cassen, P., & Reynolds, R. T. (1979). Melting of Io by tidal dissipation. *Science*, *203*(4383), 892–894. https://doi.org/10.1126/science.203.4383.892

Penev, K., Barranco, J., & Sasselov, D. (2009a). Direct calculation of the turbulent dissipation efficiency in anelastic convection. *The Astrophysical Journal*, *705*(1), 285–297. https://doi.org/10.1088/0004-637X/705/1/285

Penev, K., Sasselov, D., Robinson, F., & Demarque, P. (2007). On dissipation inside turbulent convection zones from three-dimensional simulations of solar convection. *The Astrophysical Journal*, *655*(2), 1166–1171. https://doi.org/10.1086/507937

Penev, K., Sasselov, D., Robinson, F., & Demarque, P. (2009b). Dissipation efficiency in turbulent convective zones in low-mass stars. *The Astrophysical Journal*, *704*(2), 930–936. https://doi.org/10.1088/0004-637X/704/2/930

Perryman, M. (2018). *The Exoplanet Handbook* (2nd ed.). Cambridge University Press.

Petrovich, C. (2015). Hot Jupiters from coplanar high-eccentricity migration. *The Astrophysical Journal*, *805*(1), 75. https://doi.org/10.1088/0004-637X/805/1/75

Pierrehumbert, R. T. (1986). Universal short-wave instability of two-dimensional eddies in an inviscid fluid. *Physical Review Letters*, *57*, 2157–2159. https://doi.org/10.1103/PhysRevLett.57.2157

Pizzi, F., Mamatsashvili, G., Barker, A. J., Giesecke, A., & Stefani, F. (2022). Interplay between geostrophic vortices and inertial waves in precession-driven turbulence. *Physics of Fluids*, *34*(12), 125135. https://doi.org/10.1063/5.0131035

Poincaré, H. (1910). Sur la précession des corps déformables. *Bulletin Astronomique, Serie I*, *27*, 321–356.

Pontin, C. M., Barker, A. J., Hollerbach, R., André, Q., & Mathis, S. (2020). Wave propagation in semiconvective regions of giant planets. *Monthly Notices of the Royal Astronomical Society*, *493*(4), 5788–5806. https://doi.org/10.1093/mnras/staa664

Pontin, C. M., Barker, A. J., & Hollerbach, R. (2023). Tidal dissipation in stratified and semi-convective regions of giant planets. *The Astrophysical Journal*, *950*(2), 176. https://doi.org/10.3847/1538-4357/accd67

Pontin, C. M., Barker, A. J., & Hollerbach, R. (2024). Tidal dissipation in stably stratified and semiconvective regions of rotating giant planets: Incorporating Coriolis forces. *The Astrophysical Journal*, *960*(1), 32. https://doi.org/10.3847/1538-4357/ad0a90

Pontin, C. M. (2022). *Wave propagation and tidal dissipation in giant planets containing regions of stable stratification* [Doctoral dissertation, University of Leeds]. White Rose eTheses Online. https://etheses.whiterose.ac.uk/31119/.

Prandtl, L. (1925). 7. Bericht über Untersuchungen zur ausgebildeten Turbulenz. *Zeitschrift für Angewandte Mathematik und Mechanik*, *5*(2), 136–139. https://doi.org/10.1002/zamm.19250050212

Rieutord, M. (2004). Evolution of rotation in binaries: Physical processes. In A. Maeder & P. Eenens (Eds.), *Stellar Rotation, Proceedings of IAU Symposium No. 215* (p. 394).

Rieutord, M., & Valdettaro, L. (1997). Inertial waves in a rotating spherical shell. *Journal of Fluid Mechanics*, *341*, 77–99. https://doi.org/10.1017/S0022112097005491

Rubio, A. M., Julien, K., Knobloch, E., & Weiss, J. B. (2014). Upscale energy transfer in three-dimensional rapidly rotating turbulent convection. *Physical Review Letters*, *112*, 144501. https://doi.org/10.1103/PhysRevLett.112.144501

Schaeffer, N., & Le Dizès, S. (2010). Nonlinear dynamics of the elliptic instability. *Journal of Fluid Mechanics*, *646*, 471–480. https://doi.org/10.1017/S002211200999351X

Spiegel, E. A., & Veronis, G. (1960). On the Boussinesq approximation for a compressible fluid. *The Astrophysical Journal*, *131*, 442. https://doi.org/10.1086/146849

Stevenson, D. J. (1979). Turbulent thermal convection in the presence of rotation and a magnetic field: A heuristic theory. *Geophysical & Astrophysical Fluid Dynamics*, *12*(1), 139–169. https://doi.org/10.1080/03091927908242681

Stevenson, D. J. (2020). Jupiter's interior as revealed by Juno. *Annual Review of Earth and Planetary Sciences*, *48*(1), 465–489. https://doi.org/10.1146/annurev-earth-081619-052855

Terquem, C., Papaloizou, J. C. B., Nelson, R. P., & Lin, D. N. C. (1998). On the tidal interaction of a solar-type star with an orbiting companion: Excitation of g-mode oscillation and orbital evolution. *The Astrophysical Journal*, *502*(2), 788–801. https://doi.org/10.1086/305927

Terquem, C. (2021). On a new formulation for energy transfer between convection and fast tides with application to giant planets and solar type stars. *Monthly Notices of the Royal Astronomical Society*, *503*(4), 5789–5806. https://doi.org/10.1093/mnras/stab224

Tilgner, A. (2005). Precession driven dynamos. *Physics of Fluids*, *17*(3), 034104. https://doi.org/10.1063/1.1852576

Tilgner, A., & Busse, F. H. (2001). Fluid flows in precessing spherical shells. *Journal of Fluid Mechanics*, *426*, 387–396. https://doi.org/10.1017/S0022112000002536

Tobias, S. M., & Cattaneo, F. (2013). On the measurement of the turbulent diffusivity of a large-scale magnetic field. *Journal of Fluid Mechanics*, *717*, 347–360. https://doi.org/10.1017/jfm.2012.575

Townsend, R. (2022). *MESA SDK for Mac OS* (Version 22.6.1) [Computer Software]. Zenodo. https://doi.org/10.5281/zenodo.7457723

Turner, J. D., Ridden-Harper, A., & Jayawardhana, R. (2021). Decaying orbit of the hot Jupiter WASP-12b: Confirmation with TESS observations. *The Astronomical Journal*, *161*(2), Article 72, 72. https://doi.org/10.3847/1538-3881/abd178

Verbunt, F., & Phinney, E. S. (1995). Tidal circularization and the eccentricity of binaries containing giant stars. *Astronomy & Astrophysics*, *296*, 709.

Vidal, J., & Barker, A. J. (2020a). Efficiency of tidal dissipation in slowly rotating fully convective stars or planets. *Monthly Notices of the Royal Astronomical Society*, *497*(4), 4472–4485. https://doi.org/10.1093/mnras/staa2239

Vidal, J., & Barker, A. J. (2020b). Turbulent viscosity acting on the equilibrium tidal flow in convective stars. *The Astrophysical Journal Letters*, *888*(2), L31. https://doi.org/10.3847/2041-8213/ab6219

De Vries, N. B., Barker, A. J., & Hollerbach, R. (2023a). The interactions of the elliptical instability and convection. *Physics of Fluids*, *35*(2), 024116. https://doi.org/10.1063/5.0135932

De Vries, N. B., Barker, A. J., & Hollerbach, R. (2023b). Tidal dissipation due to the elliptical instability and turbulent viscosity in convection zones in rotating giant planets and stars. *Monthly Notices of the Royal Astronomical Society*, *524*(2), 2661–2683. https://doi.org/10.1093/mnras/stad1990

Wahl, S. M., Hubbard, W. B., Militzer, B., Guillot, T., Miguel, Y., Movshovitz, N., Kaspi, Y., Helled, R., Reese, D., Galanti, E., Levin, S., Connerney, J. E., & Bolton, S. J. (2017). Comparing Jupiter interior structure models to Juno gravity measurements and the role of a dilute core. *Geophysical Research Letters*, *44*(10), 4649–4659. https://doi.org/10.1002/2017GL073160

Waleffe, F. (1990). On the three-dimensional instability of strained vortices. *Physics of Fluids A: Fluid Dynamics*, *2*(1), 76–80. https://doi.org/10.1063/1.857682

Wei, X. (2022). Magnetic effect on equilibrium tides and its influence on the orbital evolution of binary systems. *Astronomy & Astrophysics*, *664*, A10. https://doi.org/10.1051/0004-6361/202243486

Wei, X., & Tilgner, A. (2013). Stratified precessional flow in spherical geometry. *Journal of Fluid Mechanics*, *718*, R2. https://doi.org/10.1017/jfm.2013.68

Widnall, S. E., Bliss, D. B., & Tsai, C.-Y. (1974). The instability of short waves on a vortex ring. *Journal of Fluid Mechanics*, *66*(1), 35–47. https://doi.org/10.1017/S0022112074000048

Williams, G. E. (2000). Geological constraints on the Precambrian history of Earth's rotation and the Moon's orbit. *Reviews of Geophysics*, *38*(1), 37–59. https://doi.org/10.1029/1999RG900016

Williams, J. G., & Boggs, D. H. (2016). Secular tidal changes in lunar orbit and Earth rotation. *Celestial Mechanics and Dynamical Astronomy*, *126*(1-3), 89–129. https://doi.org/10.1007/s10569-016-9702-3

Wolszczan, A., & Frail, D. A. (1992). A planetary system around the millisecond pulsar PSR1257 + 12. *Nature*, *355*(6356), 145–147. https://doi.org/10.1038/355145a0

Wu, C. C., & Roberts, P. H. (2008). A precessionally-driven dynamo in a plane layer. *Geophysical & Astrophysical Fluid Dynamics*, *102*(1), 1–19. https://doi.org/10.1080/03091920701450333

Wu, Y., & Lithwick, Y. (2011). Secular chaos and the production of hot Jupiters. *The Astrophysical Journal*, *735*(2), 109. https://doi.org/10.1088/0004-637X/735/2/109

Yee, S. W., Winn, J. N., Knutson, H. A., Patra, K. C., Vissapragada, S., Zhang, M. M., Holman, M. J., Shporer, A., & Wright, J. T. (2019). The orbit of WASP-12b is decaying. *The Astrophysical Journal Letters*, *888*(1), L5. https://doi.org/10.3847/2041-8213/ab5c16

Zahn, J.-P. (1966). Les marées dans une étoile double serrée. *Annales d'Astrophysique*, *29*, 313.

Zahn, J.-P. (1989). Tidal evolution of close binary stars. I. Revisiting the theory of the equilibrium tide. *Astronomy & Astrophysics*, *220*(1-2), 112–116.